Technische Universität München

TUM School of Life Sciences

Disentangling the *in vivo* role of ferroptosis in neurodegeneration

Svenja Maria Lorenz

Vollständiger Abdruck der von der TUM School of Life Sciences der Technischen Universität München zur Erlangung des akademischen Grades einer Doktorin der Naturwissenschaften (Dr. rer. nat.) genehmigten Dissertation.

Vorsitz: Prof. Dr. Aphrodite Kapurniotu
Prüfer der Dissertation: 1. Prof. Dr. Wolfgang Wurst
2. Prof. Dr. Jan Lewerenz

Die Dissertation wurde am 31.01.2022 bei der Technischen Universität München eingereicht und durch die TUM School of Life Sciences am 01.06.2022 angenommen.

TABLE OF CONTENTS

ABSTRACT

Due to the steadily increasing life expectancy, the prevalence of age-related neurodegenerative diseases (NDs) including dementia and Alzheimer's disease, Huntington's disease and amyotrophic lateral sclerosis (ALS) is constantly raising worldwide. In addition to the serious health problems for the patients suffering from NDs, the lack of curative therapies represents an enormous burden for healthcare systems. Although the pathophysiological features described among different NDs may vary greatly, the common denominator is neuronal cell death. Emerging evidence, including observations from our laboratory, suggests that ferroptosis, a recently described form of regulated necrotic cell death, might be the underlying cell death mechanisms of neuronal cell death in several NDs. This assumption is based on the presence of peroxidative modification of phospholipids in neuronal tissue, which is the hallmark of ferroptotic cell death. The selenoenzyme glutathione peroxidase 4 (GPX4), as the prime regulator of ferroptosis, plays a central role due to its unique ability to directly reduce peroxides in lipid bilayers, thereby preventing autoxidation and rupturing of cellular membranes.

To investigate the molecular contribution of ferroptosis to neurodegeneration, two mouse models with genetic deletion of *Gpx4* in either glutamatergic or motor neurons (MNs) were generated and comprehensively analyzed in this thesis. The characterization of glutamatergic-neuron-specific *Gpx4* knockout (KO) mice uncovered a series of pathophysiological features reminiscent of dementia, including massive neuronal loss, progressive cortical atrophy and widespread neuroinflammation. Detailed proteomics and lipidomics analyses of cortical tissues of these animals revealed a number of specific signatures characteristic of ND in man. MN-specific deletion of *Gpx4* caused progressive ALS-like symptoms such as altered posture, motor dysfunction and muscle weakness of mice. Neuronal cell death in both mouse models could be prevented by pharmacological and genetic means using the ferroptosis inhibitor liproxstatin-1 and by crossbreeding these mice with transgenic mice expressing a selenium-independent form of GPX4, respectively.

Conclusively, both mouse models generated and analyzed in this work showed substantial parallels to human neuropathology, and the findings presented here imply that ferroptotic cell death emerges to be the underlying cause of neurodegeneration in related diseases. These

animal models thus lay the basis to further explore the role of ferroptosis and associated neuroinflammation in neurodegenerative disorders, including the identification of a specific lethal lipid cell death signal and potential ferroptosis-associated lipid-based biomarkers. Moreover, they will also aid in the identification and development of novel *in vivo* efficacious anti-ferroptotic compounds as potential future drugs for the treatment of NDs. These studies will thus expand our understanding on the role of ferroptosis in neuronal loss, knowledge that should guide us in the design of novel therapies to effectively treat patients suffering from NDs.

ZUSAMMENFASSUNG

In einer zunehmend alternden Gesellschaft steigt die Prävalenz altersbedingter, bisher unheilbarer, neurodegenerativer Erkrankungen, wie Demenzerkrankungen, Alzheimer-und Huntington-Krankheit, oder amyotrophe Lateralsklerose (ALS). Laut Schätzungen des Deutschen Zentrums für Neurodegenerative Erkrankungen dürfte die Gesamtzahl von Demenz-Patientinnen und Patienten in Deutschland bis zum Jahr 2050 als Folge des demographischen Wandels auf drei Millionen oder mehr ansteigen, was das Gesundheitssystem vor große Herausforderungen stellt. Obwohl diese Erkrankungen unterschiedliche pathophysiologische Merkmale aufweisen, besteht die Gemeinsamkeit im fortschreitenden neuronalen Zelltod. Der ferroptotische Zelltod, eine Form des regulierten Zelltods, wurde bereits, auch durch Erkenntnisse aus unserem Labor, mit einer Vielzahl an neurodegenerativen Erkrankungen assoziiert. Ferroptose zeichnet sich durch die eisenabhängige Oxidation von Phospholipiden der Zellmembranen aus, die zur Zerstörung der Membranintegrität und letztendlich zum Zelltod führt. Das Selenoprotein Glutathionperoxidase 4 (GPX4) stellt dabei den Hauptregulator der Ferroptose dar, gekennzeichnet durch seine einzigartige Eigenschaft, Phospholipidhydroperoxide effizient zu reduzieren und so die Autoxidation und das Aufbrechen der Zellmembranen verhindert.

Um der Frage nachzugehen, welche Rolle die Ferroptose in dem Prozess der Neurodegeneration spielt, wurden in dieser Arbeit zwei Mausmodelle mit spezifischer Deletion des Gpx4 Gens in glutamatergen Neuronen und Motoneuronen (MN) etabliert und charakterisiert. Der Knockout (KO) von Gpx4 in glutamatergen Neuronen manifestiert sich in pathophysiologischen Aspekten, wie dem progressiven Verlust von Neuronen, kortikaler Atrophie und einer massiven neuroinflammatorischen Reaktion. Ergebnisse der Omics-Analysen des kortikalen Gewebes zeigen zudem eine Reihe an signifikanten Änderungen im Proteom und Lipidom. Mäuse mit spezifischem Gpx4 KO in den MN entwickeln ALS-ähnliche Symptome, die sich durch eine veränderte Körperhaltung, motorische Dysfunktion und auftretende Muskelschwäche äußerten.

Die Ergebnisse weisen deutliche Ähnlichkeiten mit menschlichen Neuropathologien auf, was folglich untermauert, dass viele neurodegenerative Erkrankungen der Ferroptose unterliegen. Inhibitoren der Ferroptose bergen daher ein großes Potential, neuroprotektiv zu wirken. Der

neuronale Zelltod konnte in den verwendeten Mausmodellen sowohl pharmakologisch durch die Anwendung des Ferroptose-Inhibitors Liproxstatin-1, als auch genetisch verhindert werden. Die zusätzliche Kreuzung mit einer transgenen Mauslinie, die eine selen-unabhängigen Form von GPX4 exprimiert, konnte den auftretenden neuronalen Phänotyp mildern.

Mit der Etablierung dieser Modelle wurde die Grundlage für die weitere Erforschung der Rolle der Ferroptose und die damit verbundenen neuroinflammatorischen Prozesse in neurodegenerativen Erkrankungen gelegt. Sie bieten darüber hinaus die Möglichkeit der Identifizierung spezifischer, ferroptose-assoziierter Lipidsignaturen, die als potenzielle, diagnostische Biomarker in klinischen Studien von enormer Bedeutung sein können und dringend benötigt werden. Folglich lassen sich neue, effizientere Liproxstatine, sowie Studien zu deren Wirksamkeit in vivo entwickeln, die als künftigen Therapieansatz zur Behandlung von Patienten mit neurodegenerativen Erkrankungen eingesetzt werden können.

LIST OF ABBREVIATIONS

%	percent
•	radical
•OH	hydroxyl radical
°C	degree Celsius
μg	microgram
μl	microliter
μM	micromolar
3D	three-dimensional
3D-MRI	three-dimensional magnetic resonance imaging
4F2	SLC3A2
7DHC	7-dehydroxylcholesterol
AA	arachidonic acid
AAR	alternate arm returns
AB	antibody
ABHD12	abhydrolase domain containing 12
ACS	acyl-CoA synthetase
ACSL	acyl-CoA synthetase long-chain family members
AD	Alzheimer's disease
ADI	Alzheimer's Disease International
ADP	adenosine diphosphate
AGC	automatic gain control
AIFM2	apoptosis inducing factor mitochondria associated 2
ALP	alkaline phosphatase
ALS	amyotrophic lateral sclerosis
AMP	adenosine monophosphate
ANOVA	analysis of variance
AO	antioxidants
ApoE	apolipoprotein E
ApoJ	apolipoprotein J
APP	amyloid precursor protein
ATP	adenosine triphosphate
Aβ	amyloid-β
B2M	beta-2-microglobulin
BBB	blood brain barrier
BDNF	brain-derived neurotrophic factor
BH2/BH4	di/tetrahydrobiopterin
BHT	butylated hydroxytoluene
BMC	bone mineral content
BMD	bone mineral density
BOS	base of support
bp	base pairs
BSA	bovine serum albumin
BSO	L-buthionine-sulfoximine
BW	body weight
C	carbon/carbamidomethyl
C1qc	complement C1q C chain

C9orf72	open reading frame of chromosome 9
CAA	2-Chloroacetamide
Camk2a	calcium/calmodulin-dependent protein kinase II alpha
Cas9	CRISPR associated potein 9
CCL12	chemokine (C-C motif) ligand 12
CCL6/C10	chemokine (C-C motif) ligand 6
cDNA	complementary DNA
CE	cholesteryl esters
Cer	ceramide
cGPX4	cytosolic form of GPX4
CHAT	choline acetyltransferase
Clu	clusterin
c-Myc	MYC Proto-Oncogene
CNS	central nervous system
CoA	coenzyme A
COPD	chronic obstructive pulmonary disease
CoQ_{10}	ubiquinone
CRISPR	clustered regularly interspaced short palindromic repeats
CSF	cerebrospinal fluid
CTNF	cerebral dopamine neurotrophic factor
Ctsd	cathepsin D
Ctss	cathepsin S
CW	catwalk
Cys	cysteine
Cyth1	cytohesin-1
DAM	disease-associated microglia
DNA	deoxyribonucleic acid
DAPI	4'-6-diamidino-2-phenylinodole
DDA	data-dependent acquisition
DFO	deferoxamine
DG	diglycerols
DHA	docosahexaenoic acid
DKO	double knockout
DMEM	dubeccos modified eagle medium
DMSO	dimethyl sulfoxide
dNTPs	deoxynucleotides
DTPA	diethylenetriaminepentaacetic acid
DXA	dual energy X-ray absorptiometry
EDL	extensor digitorus longus
EDTA	ethylendiaminetetraacetic acid
EPA	eicosapentaenoic acid
ER	endoplasmic reticulum/estrogen receptor
ESCs	embryonic stem cells
ETC	electron transport chain
EUCOM	european conditional mouse mutagenesis program
FA	fatty acid
Fabp7	fatty acid binding protein 7
fAD	familial AD
fALS	familial amyotrophic lateral sclerosis

FCS	fetal calf serum
FDA	food and drug administration
FDR	false discovery rate
Fe2+	ferrous iron
Fe3+	ferric iron
Fer-1	ferrostatin-1
FP	front paws
FSP1	ferroptosis suppressor protein 1
FTD	frontotemporal dementia
FTLD	frontotemporal lobar degeneration
FUS	fused in sarcoma protein
g	gram/gravitational force
GABA	gamma-aminobutyric acid
Gas	gastrocnemius
Gb	gigabyte
GCH1	GTP cyclohydrolase 1
GCLC	γ-glutamate cysteine ligase catalytic subunit
GFAP	glial fibrillary acidic protein
GFP	green fluorescent protein
GlcCer	glucosylceramide
GMC	German Mouse clinic
GOI	gene of interest
GPX	glutathione peroxidase
GPX4-SO$_{2/3}$H	sulfinic/sulfonic forms of GPX4
GPX-SOH	sulfenic form of GPX4
GR	glutathione reductase
GRN	granulin
GSH	glutathione/γ-glutamylcysteineglycine
GSR	glutathione-disulfide-reductase
GSS	glutathione synthetase
GSSH	oxidized GSH
GTP	guanosine-5'-triphosphate
h	hour
H$_2$O$_2$	hydrogen peroxide
HB9	homebox gene 9
HCD	high energy collisional dissociation
HDL	high-density lipoprotein
HEK cells	human embryonic kidney cells
hESCs	human embryonic stem cells
HESI-II	heated electrospray ionization
Hexb	hexosaminidase subunit beta
hiPSCs	human induced pluripotent stem cells
HMG-CoA	3-hydroxy-3-methylglutaryl-CoA;
HNE	4-hydroxynonenal
HP	hind paws
HPLC	high-performance liquid chromatography
HRP	horseradish peroxidase
Hz	hertz
i.p	intraperitoneal

IBA1	ionized calcium-binding adaptor molecule 1
ICAM-1/CD45	intercellular adhesion molecule-1/ cluster of differentiation 54
iFSP1	FSP1-specific inhibitor
igE	immunoglobulin E
IGF	insulin-like growth factor
IGFBP-2	insulin-like growth factor-binding protein 2
IL-6	interleukin 6
IPP	isopentenyl diphosphate
iPSCs	induced pluripotent stem cells
IRI	ischemia-reperfusion injuries
IVC	individually ventilated cage
kDa	kilo Dalton
kg	kilogram
KIF5a	kinesin superfamily protein 5a
Klf4	kruppel like factor 4
KO	knockout
LB	lysogeny broth
LC/MS	liquid chromatography–mass spectrometry
Lcp1	lymphocyte cytosolic protein1
L-H	lipid
Lip-1/3	liproxstatin-1/3
LIX/CXCL5	CXC chemokine ligand-5
L-O·	alkoxyl radical
L-OH	lipid alcohol
LOOHs	lipid hydroperoxides
LOX	lipoxygenase
loxP	locus of X-over P1
LPC	lysophosphatidylcholine
LPCAT3	lysophosphatidylcholine acyltransferase 3
LPLAT	lysoPL acyltransferase
LPO	lipid peroxidation
lysoPLs	lysophospholipids
M	molar/methionine
m/z	mass-to-charge ratio
MAP2	microtubule-associated protein 2
MAPT/Tau	microtubule-associated protein tau
mbar	millibar
MeCN	acetonitrile
MeSH	medical subject headings
mGPX4	mitochondrial form of GPX4
min	minute
ml	milliliter
mM	millimolar
MN	motor neurons
MNPs	motor neurons progenitors
ms	milli second
MTBE	methyl- tert- butyl ether
MUFA	monounsaturated fatty acid
NAC	N-acetyl-L-cysteine

NaCl	sodium chloride
NADPH	nicotinamide adenine dinucleotide phosphate
NAMPs	neurodegeneration-associated molecular patterns
NaOH	sodium hydroxide
NCE	normalized collision energy
ND	neurodegenerative disease
NEAA	non essential amino acid
Nedd8	ubiquitin-like protein Nedd8
NeuN	neuronal nuclear protein
NfL	neurofilament light
NFTs	neurofibrillary tangles
ng	nanogram
nGPX4	nuclear form of GPX4
NMDA	N-methyl D-aspartate
nNOS	neuronal nitric oxide synthases
NOX	NADP oxidase
NPCs	neuronal progenitor cells
ns	not significant
O_2^-	superoxide anion
OA	oleic acid
Oct3/4	POU Class 5 Homeobox 1/octamer-binding protein 3/4
OF	open field
OH-	hydroxide ion
p.o	per oral
p53	tumor suppressor p53
PAMPs/DAMPs	pathogen-and damage-associated molecular patterns
PBS	phosphate buffered saline
PC	phosphatidylcholine
PCA	principle component analysis
PCR	polymerase chain reaction
PDAC	pancreatic ductal adenocarcinoma
PE	phosphatidylethanolamine
PFA	paraformaldehyd
PFPA	perfluoropentanoic acid
PG	phosphatidylglycerol
pg	picogram
PI	phosphatidylinositol
PL	phospholipid
PL-OO●	lipid radical
PL-OOH	peroxidized phospholipid
POR	cytochrome P450 oxidoreductases
Ppi	inorganic pyrophosphate
PRRs	pattern recognition receptors
PS	phosphatidylserin
PSEN	presenilin
Ptpn6	protein tyrosin phosphatase non-receptor type 6
PUFA	polyunsaturated fatty acid
PV+	parvalbumin-positive
PVDF	polyvinylidene difluoride

RA	retinoic acid
RAS	rat sarcoma virus
ROS	reactive oxygen species
RPMI	Roswell Park Memorial Institute
RP-uHPLC	reversed-phase ultra-high-performance liquid chromatography
RSL3	Ras Selective Lethal 3
RT	room temperature
RTA	radical trapping antioxidant
s	seconds
sALS	sporadic amyotrophic lateral sclerosis
SARs	same arm returns
SDS-PAGE	sodium dodecyl sulfate polyacrylamide gel electrophoresis
Se	selenium
Sec	selenocysteine
SeH	selenol
SHH	sonic hedgehog
SIMOA	single molecule array
SM	sphingomyelin
SOD1	Cu,Zn-superoxide dismutase
Sol	soleus
Sox2	SRY-Box Transcription Factor 2
SPAs	spontaneous alternations
Syn1	synapsin-1
t	time
TA	tibialis anterior
TAM	tamoxifen
TARDBP	TAR DNA-binding protein 43
tBOOH	tert-butylhydroperoxide
TCEP	tris(2-carboxyethyl)phosphine
TE	Tris/EDTA
tet	tetracycline
TF	transferrin
TFR1	transferrin receptor
tg	transgene
TNFα	tumour Necrosis Factor alpha
TREM2	triggering receptor expressed on myeloid cells 2
tRNA	transfer ribonucleic acid
TUJ1	neuron-specific class III beta-tubulin
TUNEL	terminal deoxynucleotideyl transferase dUTP Nick End labeling
TXNRD1	thioredoxin reductase 1
V	voltage
VCP	valosin-containing protein
Vim	vimentin
WT/wt	wildtype
xCT	SLC7A11
α-Toc	α-tocopherol
γ-GCS	γ-glutamylcysteine synthetase

LIST OF FIGURES

LIST OF TABLES

1 INTRODUCTION

1.1 Ferroptosis

1.1.1 Historical considerations and molecular mechanisms

Cell death occurs throughout the entire lifespan of multicellular organisms, and since its first recognition in 1842 it has remained an incessantly researched subject. The traditional illustration of cell death by the German-Swiss scientist Carl Vogt is classified as apoptosis, the first described form of programmed cell death, coined by the discovery of Lockshin and Williams in 1965 [1]. Cell death researchers used morphological criteria to explore different types of cell death, such as for necrotic cell death, which has been initially considered as an unregulated, accidental and proinflammatory form of cell death [1, 2]. Over recent decades, rapid advances in discovering and characterizing the various forms of regulated cell death have been made, highlighting several distinct or even overlapping types of cell death [3].

Roughly twenty years ago, Stockwell's group identified small molecules triggering a "novel", iron-dependent and non-apoptotic form of cell death. One of the compounds was named erastin, after "eradicator of Ras and ST" [4, 5]. In parallel, Conrad's lab working on the selenoenzyme glutathione peroxidase 4 (GPX4) were able to show for the first time that the loss of *Gpx4* causes a non-apoptotic form of cell death [6]. This newly form of cell death was linked to oxidative stress and massive lipid peroxidation in cells, which can be prevented by α-tocopherol (α-Toc). A further breakthrough in the exploration of the function of *Gpx4* was the fact that the deletion of *Gpx4* in neuron-specific *Gpx4* KO mice leads to neurodegeneration [6]. Subsequently, Yang and Stockwell published the discovery of another compound, (1*S*,3*R*) RSL3 ("Ras Selective Lethal 3"), which induces a similar non-apoptotic form of cell death in tumor cells, with the absence of apoptosis-like morphological features such as blebbing of cells or structural changes in nucleus and chromatin and an insensitivity towards pan-caspase inhibitors [5].

In 2012, Dixon *et al.*, published that iron chelators inhibit this type of cell death leading, after all these earlier discoveries, to the term: ferroptosis – an iron-dependent form of nonapoptotic cell death [7]. Yet, some of the morphological features, regulators and cellular processes being involved in ferroptosis had been recognized long before the term ferroptosis was introduced. The retrospective view on the discovery of ferroptosis least traces back to

1

early work by Schubert and Maher, describing a form of programmed cell death in murine hippocampal HT-22 cells, which was associated with oxidative stress in cells, glutamate-induced glutathione (GSH) depletion and an involvement of lipoxygenase coining the name oxytosis, a non-apoptotic, redox-regulated form of cell death [8, 9]. Seemingly, on a molecular level, ferroptosis and oxytosis share the same metabolic changes and molecular pathways and are now regarded as two names describing the same form of cell death [10].

Meanwhile, the underlying mechanisms of ferroptosis have been intensively studied using ferroptosis inducers, inhibitors and different *in vivo* models in mammals, plants and phylogenetically more distant organisms, firmly establishing the concept of ferroptosis (Fig. 1). The ferroptotic cell death pathway includes a series of metabolic and cellular processes including GSH biosynthesis and recycling, cysteine (Cys) metabolism, iron handling, fatty acid (FA) metabolism, anti-oxidants [11, 12], the accumulation of toxic lipid hydroperoxides and oxidative stress [6, 13-15]. There are a number of cellular systems by which ferroptosis can be induced and suppressed, starting with the initially described Cys-GSH-GPX4-axis, including system x_c^-, GSH biosynthesis and the key regulator GPX4, to the NAD(P)H-dependent ferroptosis suppressor protein 1 (FSP1)-ubiquinone (CoQ_{10}) axis, the second main regulator discovered only quite recently [7, 15-18].

System x_c^-, is a heterodimeric amino acid antiporter consisting of two subunits, i.e., SLC7A11 (xCT) light chain and SLC3A2 (4F2) heavy chain. System x_c^- functions as a cystine/glutamate amino acid antiporter, transporting extracellular cystine (the oxidized dimeric form of Cys) in exchange of one molecule of intracellular glutamate into the cell. Reduction of cystine to Cys requires GSH or thioredoxin reductase 1 (TXNRD1). Cys is a building block and a substrate-limiting step for GSH biosynthesis, besides its role in protein synthesis. Next to system x_c^-, Cys can also be supplied via the transsulfurylation pathway at least to some extent. GSH is synthesized in two steps first forming an intermediate metabolite γ-glutamylcysteine catalyzed by γ-glutamylcysteine synthetase (γ-GCS) and second conversion of γ-glutamylcysteine to γ-glutamylcysteinylglycine (GSH) by glutathione synthetase (GSS) [19-22]. GSH is the reducing substrate of many redox enzymes, including GPX4 and therefore represents the most abundant antioxidant in mammalian cells [23]. GPX4, as one of the key players in ferroptosis signaling, prevents lipid peroxidation by converting peroxidized

phospholipids (PL-OOH) to their corresponding alcohols (PL-OH), using two molecules of GSH (see 1.1.2) [13, 20].
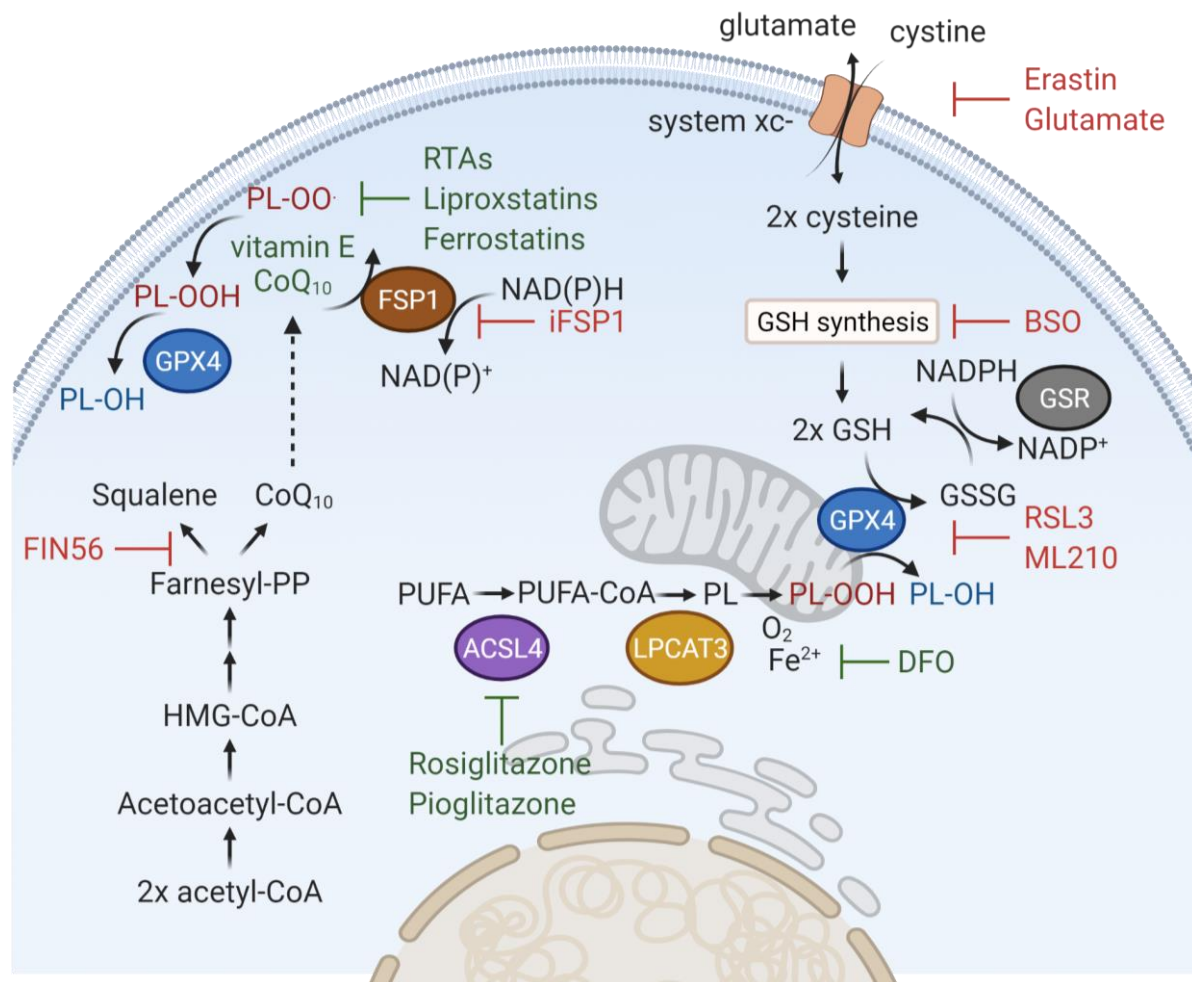
Figure 1| Key cellular processes modulating ferroptosis

Ferroptosis is regulated by two main systems: The cysteine/glutathione (GSH)/glutathione peroxidase 4 (GPX4) axis and the NAD(P)H/ferroptosis suppressor protein 1 (FSP1)/ubiquinone (CoQ$_{10}$) axis. GPX4 as one of the main regulators prevents lipid peroxidation by directly reducing peroxidized phospholipids (PLs) (PL-OOH) to their corresponding alcohols (PL-OH), using two molecules GSH as electron source. For GSH biosynthesis, cystine, the oxidized dimeric form of cysteine, is taken up via system xc-, in exchange of glutamate, and reduced to cysteine inside cells. Oxidized GSH (GSSH) is recycled by glutathione-disulfide-reductase (GSR) in an NADPH-dependent reaction. Acyl-CoA synthetase long-chain family member 4 (ACSL4) activates polyunsaturated fatty acids (PUFAs) before they are esterified in PLs by lysophosphatidylcholine acyltransferase 3 (LPCAT3). FSP1 was identified as the second key regulator of ferroptosis acting via the reduction of extramitochondrial CoQ$_{10}$ to ubiquinol using NAD(P)H/H$^+$ as electron donor. Unlike the GPX4-dependent system, ubiquinol prevents the lipid peroxidation chain reaction on the level of lipid radicals (PL-OO●) by directly reducing them to PLOOH or indirectly using vitamin E (α- tocopherol), a powerful naturally occurring lipophilic antioxidant and ferroptosis inhibitor. The biosynthesis of CoQ$_{10}$ and squalene is linked to the mevalonate pathway, providing essential precursors. Various well-established ferroptosis inducers (red) and inhibitors (green) are marked. Abbreviations: HMG-CoA, 3-hydroxy-3-methylglutaryl-CoA; DFO, deferoxamine; RSL3, Ras Selective Lethal 3; BSO, L-buthionine-sulfoximine; RTA, radical trapping antioxidant; iFSP1, FSP1-specific inhibitor. Figure adapted from [24].

Since Cys and GSH are essential for optimal functioning of GPX4, pharmacological deprivation of a substrate or blocking of any of these processes triggers ferroptosis. Erastin inhibits system x_c^-, leading to Cys starvation and consequently to cellular GSH exhaustion thereby inducing ferroptotic cell death. Further ferroptosis-inducing agents, which share the same mechanism of action, are glutamate or sulfasalazine [7, 18, 25]. In addition, blocking γ-GCS by L-buthionine sulfoximine (BSO) causes GSH deprivation and ferroptosis [13, 23]. In contrast to this class of ferroptosis inducers, the first described ferroptosis-inducing small molecule (1*S*,3*R*)-RSL3 as well as the subsequently discovered small molecules ML-210 act by direct inhibition of GPX4. The covalent modification and irreversible inhibition of the active site selenocysteine (Sec) of GPX4 by this type of ferroptosis inducers effectively triggers ferroptotic cell death by allowing excessive lipid peroxidation and rupture of cellular membranes [13, 26, 27].

Since unrestrained lipid peroxidation of polyunsaturated fatty acids (PUFAs) present in cellular membranes is the hallmark of ferroptosis, the activation of PUFAs by acyl-CoA synthetase long-chain family members (ACSL) and their incorporation into lipid bilayers play a major role in the cell's sensitivity towards ferroptosis. Genome-wide CRISPR/Cas9 screening approaches identified acyl-CoA synthetase long-chain family member 4 (ACSL4) as the first player in the ferroptotic process downstream of genetic *Gpx4* deletion or GPX4 inhibition [28, 29]. ACSL4 ligates CoA to preferably long-chain PUFAs, such as arachidonic acid (AA, 20:4) and adrenic acid (22:4), thereby activating them. When PUFAs are esterified in phospholipids like phosphatidylethanolamine (PE) by LPCAT3 (lysophosphatidylcholine acyltransferase 3), they can generate proximate signals of ferroptotic cell death when they become oxidized [28, 29] (see 1.1.3). Consequently, ferroptosis can be suppressed by genetic knockout (KO) or pharmacological inhibition of ACSL4, since a lower level of PUFAs in membranes decreases the risk of uncontrolled lipid peroxidation and associated ferroptotic cell death [28, 30].

In addition, iron chelators such as deferoxamine (DFO) were found to inhibit this form of cell death, revealing the iron-dependency of ferroptosis and which led to the terminology of ferroptosis (Latin: ferrum = iron; Greek: ptosis = falling leaves). Why is this type of cell death iron-dependent and what role does iron play? Two main hypotheses were initially proposed and are still being discussed: First, ferrous iron (Fe^{2+}) as part of the labile iron pool in cells reacts with hydrogen peroxide(H_2O_2) leading to the formation of the highly reactive hydroxyl radical ($^\bullet$OH), which in turn abstracts a hydrogen atom from a conjugated diene in a PUFA,

leading to formation of a carbon-centered radical (PL$^\bullet$). This reacts with molecular oxygen to form the highly reactive peroxyl radical (PL-OO$^\bullet$), which can further abstract a hydrogen atom from a conjugated diene, thus inciting the lipid peroxidation chain reaction if not counteracted by redox systems as described above [31-34] (Fig. 2). Second, several studies have focused on iron-dependent enzymes including those of the lipoxygenase (LOX) and cytochrome P450 oxidoreductases (POR) family of proteins. LOX family require iron and incorporate molecular oxygen into PUFAs and PUFA-containing lipids, mediating lipid peroxidation in membranes, whereby POR family of proteins mediate lipid peroxidation and subsequent ferroptosis by the production of H_2O_2 [34-37] (Fig. 2). Due to the potentially deleterious roles of iron in sparking ferroptosis, cellular iron homeostasis and the labile iron pool need to be under strict control. Most cells take up iron (Fe^{3+}) bound to transferrin (TF) via specific carriers, such as transferrin receptor (TFR1)-mediated endocytosis or as non-transferrin bound iron. Once inside the cell, ferric iron is reduced to Fe^{2+} and stored in ferritin, which has in turn been proposed to confer greater resistance towards ferroptosis [32, 33]. Beside TF and ferritin, iron can enter the cell as heme iron and non-heme iron, a key research interest with regard to ferroptosis sensitivity or resistance [33, 38, 39]. Recent studies illustrate the association of iron homeostasis and ferroptosis and focus on the imbalance in iron regulation that correlates with impaired development, cardiomyopathy or neurodegenerative disorders [40-43].

The Cys/GSH/GPX4 axis is still regarded as the main system counteracting ferroptosis in mammals. However, two recently published studies reported on the discovery of ferroptosis suppressor protein 1 (FSP1) (formerly named "apoptosis inducing factor mitochondria associated 2", AIFM2) as a GPX4-independent novel ferroptosis regulator. FSP1 acts as a powerful NAD(P)H–oxidoreductase, converting extramitochondrial CoQ$_{10}$ to ubiquinol, which terminates the chain reaction of lipid peroxidation by reducing lipid radicals or by regenerating α-toc radicals [16, 17]. In many ways, the mevalonate pathway is tightly associated with the regulation of ferroptosis. Next to the function in Sec-specific tRNA synthesis or in generating squalene, the biosynthesis of CoQ$_{10}$ is a product of the mevalonate pathway, which is generally responsible for the conversion of acetyl-CoA to isopentenyl diphosphate (IPP) [16, 17, 26, 44]. The first step in the mevalonate pathway generates acetoacetyl-CoA from two molecules acetyl-CoA, before converting them in 3-hydroxy-3-methylglutaryl-CoA (HMG-CoA). This is followed by an irreversible reaction to mevalonate, a new starting point for several enzymatic steps to generate IPP and further downstream metabolites including squalene, CoQ$_{10}$ and 7-

dehydroxylcholesterol (7-DHC) and cholesterol [45-47]. Other studies have reported on the accumulation of squalene, a metabolite of the cholesterol pathway, which tends to have anti-ferroptotic activity [48, 49], or on GTP cyclohydrolase 1 (GCH1), which was reported to be equally linked to ferroptosis resistance independent from the Cys/GSH/GPX4 axis. The metabolic products of GCH1, di/tetrahydrobiopterin (BH_2/BH_4), are on the one hand involved in CoQ_{10} biosynthesis and on the other hand are able to act as so called radical-trapping antioxidants (RTA), thereby blocking the process of lipid peroxidation [50].
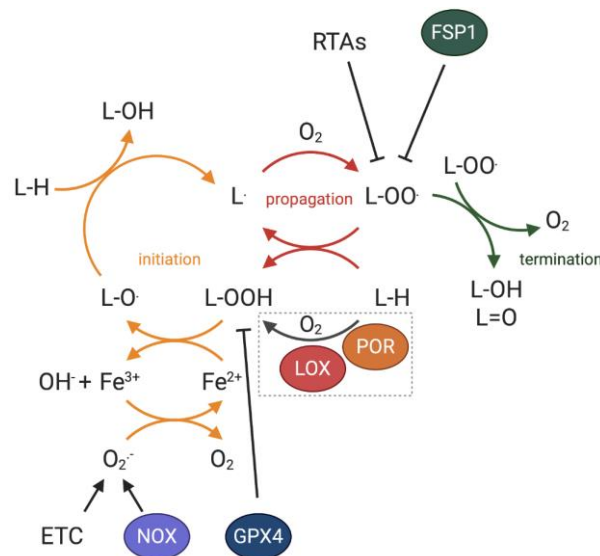
Figure 2| Mechanisms of phospholipid peroxidation
Lipid peroxidation, the hallmark of ferroptosis, occurs in both non-enzymatic and enzymatic ways and can be divided in three phases, i.e., initiation (indicated in orange), propagation (indicated in red) and termination (indicated in green). The initiation process can be mediated via lipoxygenases (LOXs) and/or cytochrome P450 oxidoreductase (POR) (marked by a dashed box) or can be driven by the non-enzymatic reaction through the so-called Fenton reaction, although the exact mechanism still remains to be fully established. Initiation leads to the formation of a lipid radical ($L^\bullet$) which subsequently reacts with molecular oxygen (O_2) forming a lipid peroxyl radical (L-$OO^\bullet$). The propagation phase describes the chain reaction of peroxyl radicals removing hydrogen atoms from neighboring PLs to form lipid hydroperoxides (LOOHs) and $L^\bullet$. In the termination phase, L-$OO^\bullet$ can be converted to the corresponding alcohol (L-OH) or lipid carbonyl (L=O) by either radical-driven by ferroptosis suppressor protein 1 (FSP1) or radical-trapping antioxidants (RTAs). Abbreviations: ETC, electron transport chain; Fe^{2+}, ferrous iron, Fe^{3+}, ferric iron; NOX, NADPH oxidase; L-H, lipid; L-$O^\cdot$, alkoxyl radical; L-OH, lipid alcohol; OH^- hydroxide ion; $O_2^{\cdot-}$, superoxide anion. Figure adapted from [51].

The main driver of ferroptosis is the process of phospholipid peroxidation (Fig. 2); consequently, RTAs are essential as ferroptosis inhibitors. The peroxidation chain reaction can be divided into three phases: initiation, propagation and termination. The propagation of peroxidation chain reaction is directly blocked by adding one electron to lipid radicals. Looking at the chemical structure, RTAs are mostly phenols, quinones and aromatic amines, reacting with peroxyl radicals. The naturally occurring α-toc is the most prominent, biologically active form of the eight variants of the vitamin E class of compounds, with highly efficient radical

scavenger properties [52]. The developed and widely used potent inhibitors of ferroptosis, i.e., ferrostatin-1 [7] and liproxstatin-1 [15], are able to suppress the accumulation of lipid hydroperoxides by acting as potent RTAs. The reactivity of RTAs is dependent on the solvent and on their metabolic stability, resulting in improved versions to be used for *in vivo* application and as the basis for the further development as possible future drugs [53, 54].

Regardless of its initiation, the excessive generation of lipid hydroperoxides directly influences the biological homeostasis, leading to compositional changes and oxidative damage of cell membranes and in toxic process that culminates in cell death. Decomposition of PUFA residues in membranes may also disrupt membrane fluidity affecting membrane-embedded proteins and fatty acids (FA), which can be oxidized by oxygen radicals or by aldehydes, leading to secondary byproducts such as 4-hydroxynonenal (HNE)-protein adducts. HNE as a highly reactive product, originating from the oxidation of n-6 PUFA, such as linoleic acid or γ-linolenic acid, emerges to be a molecule of oxidative stress linked to cell death. Whether HNE, lipid hydroperoxides, all lipid modifications or only a specific subset of oxygenated species actual kill the cell as a final event in ferroptosis still remains unclear and is matter of intense research [55, 56].

1.1.2 The selenoenzyme GPX4 as the guardian of ferroptosis

"The cell sap from pig liver contains a protein which protects phosphatidylcholine liposomes and biomembranes from peroxidative degradation in the presence of glutathione." – this is the initial description of GPX4 by Ursini *et al.* in 1982 [14]. GPX4 is one of 25 selenoproteins in mammals, a family of proteins characterized by incorporating at least one Sec in their polypeptide chain [14]. Selenium (Se) is an essential trace element, historically first considered being a highly toxic or even carcinogenic chemical element, and nowadays regarded as a highly beneficial and essential element for human and animal health [57-59]. Along with the identification of selenoproteins, it has become apparent that Se in its biologically active form in cells is found as the 21th amino acid, i.e., Sec [60, 61]. Selenoproteins are present in diverse organisms, with glutathione peroxidase 1 (GPX1) being the first selenoprotein to be discovered in mammals [62, 63]. Five members of the glutathione peroxidase family of proteins (GPX1- GPX4 and GPX6, only in humans) are Sec-containing enzymes with Sec constituting their catalytic site, whereby GPX5 (and GPX6 in rodents), GPX7 and GPX8 are Cys-containing family members [64, 65]. All GPX show distinct expression levels in different tissues

and cell types and have different protein structures, leading to unique functions and substrate specificities [66, 67]. In general, the majority of selenoproteins, such as GPX and thioredoxin reductases, are redox-active enzymes and act as oxidoreductases. GPX are therefore described as one of the most important family of enzymes for controlling the level of H_2O_2 and other peroxides, in- and outside of cells [59, 60, 68]. Among the GPX family of proteins, GPX4 stands out because of its ability to directly reduce PL or cholesterol hydroperoxides at the expense of GSH or other small molecular weight thiols such as Cys and β-mercaptoethanol [61]. The prevention of peroxidized lipids in membranes, therefore awards GPX4 the title of the "guardian of ferroptosis" [13].

The biochemical mechanism of how GPX4 reduces hydroperoxides or H_2O_2 to their corresponding alcohols or water is depicted in the catalytic cycle of GPX4 (Fig. 3A). During GPX4-mediated reduction of hydroperoxides, the selenolate anion in the catalytic site becomes oxidized to form the selenenic form of GPX4 (GPX4-SeOH). Subsequently, GPX4-SeOH is recycled by two molecules of GSH, first via the formation of an intermediate selenadisulfide form (GPX4-Se-SG) with GSH. A nucleophilic attack of the second GSH molecule towards the GPX4-Se-SG restores fully reduced GPX4 and leads to the formation of GSSG, the oxidized dimeric form of GSH. Glutathione reductase (GR) reduces GSSG to GSH at the expense of two electrons coming from $NADPH/H^+$. Beyond GSH as the prevailing reductant, under limiting GSH conditions - as physiologically evident in maturing spermatozoa - GPX4 can also react with thiol groups in proteins [60, 69, 70]. Even though the difference of the active-site Sec to its homolog Cys is "just" a replacement of selenium with sulfur, the catalytic function of GPX4 is widely changed. For instance, Ingold *et al.* showed by generating a mouse model containing Cys instead of Sec in the active site of GPX4 (*Gpx4$^{cys/cys}$*) that Sec-containing GPX4 is essential for proper embryogenesis in mice when kept on a congenic C57BL/6 genetic background. In the same study, it was further shown that in contrast to Sec-containing enzyme, the Cys mutant of GPX4 is highly susceptible to peroxide-induced overoxidation leading to formation of the sulfinic and sulfonic forms of GPX4 (GPX4-$SO_{2/3}H$). Since, these forms are generally considered to be irreversibly oxidized, inactivation of GPX4 causes unrestrained lipid peroxidation particularly under high cellular peroxide levels finally leading to ferroptotic cell death (Fig. 3B) [44].
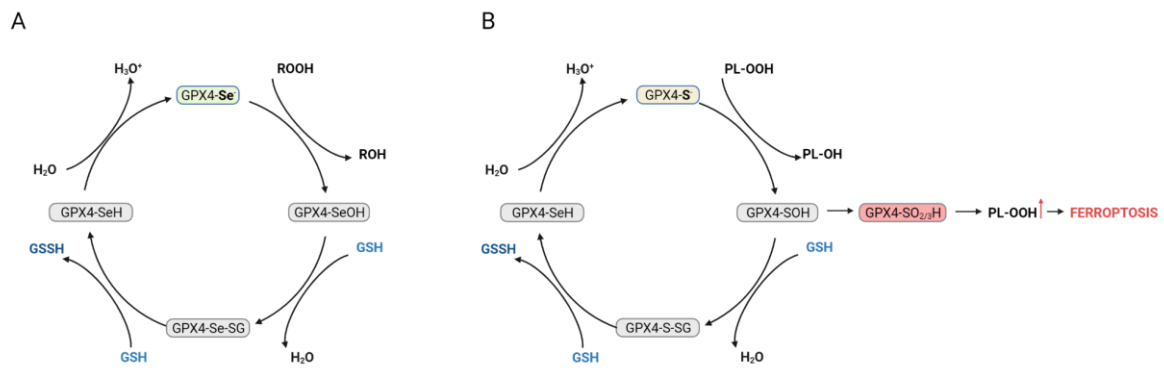
Figure 3| Catalytic cycle of glutathione peroxidase 4 (GPX4)
A| The active-site Sec in GPX4 becomes oxidized to selenenic acid when reducing peroxides to their corresponding alcohols. To regenerate oxidized GPX4, one molecule of GSH reacts with selenenic acid to form an intermediate selenadisulfide bridge, which is resolved by a second molecule of GSH to generate the fully reduced, active form of GPX4 (i.e., selenol (SeH)), with GSSG being formed. B| Like in the wildtype enzyme, the Cys-containing GPX4 becomes oxidized by a peroxide yielding the sulfenic form of GPX4. Since the regenerative step of cysteine containing GPX4 with GSH are kinetically impaired, high cellular levels of lipid peroxides may cause overoxidation of the sulfenic form of GPX4 (GPX-SOH), resulting in sulfinic and sulfonic forms (GPX4-SO$_{2/3}$H), which are considered to be irreversibly oxidized. Impaired GPX4 function in turn leads to the lethal generation of intracellular PLOOH and associated ferroptosis. Figure adapted from [71].

Mammalian GPX4 is expressed as three different forms: a cytosolic (short) form (cGPX4), a mitochondrial form (mGPX4) and a nuclear form (nGPX4). Each variant is encoded by seven exons, whereas the translation initiation site of cGPX4 and mGPX4 is located in exon 1a, while, the translation of nGPX4 is initiated at the alternative exon 1b, which is located between exon 1a and exon 2 [72, 73]. The largest form, i.e., nGPX4 (35 kDa), is almost exclusively expressed in late spermatids in testis, which gave it the original name "sperm nucleus-specific glutathione peroxidase" [72, 74-76]. mGPX4 (23 kDa) contains a cognate mitochondrial leader sequence at its N-terminus, which gets truncated after reaching its location, the mitochondrial matrix in developing spermatozoa. Like nGPX4, mGPX4 is almost exclusively expressed in male germ cells and is essential for forming the so-called mitochondrial capsule surrounding the mitochondria, a keratin-like, structurally rigid capsule that is essential for full structural stability of spermatozoa [77, 78].

The shortest isoform, cGPX4 (19 kDa), is ubiquitously expressed in different tissues, mostly in kidney, brain, liver and testis and described as the essential isoform for mouse development and survival [72, 79, 80]. Before the term ferroptosis was introduced, a number of studies on *Gpx4* showed already the relevance and protective function of GPX4 *in vivo* and *in vitro* [81]. The first mouse model with targeted loss of GPX4 showed early embryonic lethality of *Gpx4*$^{-/-}$ embryos around E7.5, albeit the reasons for embryonic death still remain enigmatic [80, 82,

83]. Therefore, it became evident that mouse models with conditional deletion of *Gpx4* is the preferred way to study the relevance of GPX4 in tissue homeostasis and ferroptosis prevention *in vivo* [6].

1.1.3 Polyunsaturated fatty acid metabolism and the role of fatty acid ligases

GPX4 is one example of an antioxidant enzyme maintaining redox equilibrium, cell function and regulation by its ability to efficiently counteract oxidizing agents like peroxidized PLs. In fact, it is the only enzyme in mammals that can directly reduce peroxides in lipid bilayers without the need to release peroxidized PUFAs by phospholipases and re-esterification of new PUFA residues. PL are the major component of mammalian cell membranes. They are built by a glycerol backbone with two nonpolar fatty acid residues esterified at the *sn-1* and *sn-2* positions, building the nonpolar tail sticking in the membrane and the negatively charged, polar phosphate-containing headgroup, attached at *sn-3* position, directed towards the aqueous environment [84]. The composition and concentration of PLs as well as the reactivity of lipids highly influence the fluidity in cell membrane, cell signaling, oxidative damage and consequently cell death. FA differ based on their chain length and grade of saturation according to the amount and position(s) of carbon double bonds. PUFAs are fatty acids that contain at least two or more double bonds and are mainly localized in cell membranes. Notably, PUFAs are highly reactive towards radicals based on their high rate of autoxidation due to high amount of methylene groups ($-CH_2-$) flanked by C-C double bonds. These C-H bonds are weak and easily broken bonds, allowing the hydrogen atom to be readily abstracted by reactive radical species [54, 85]. The PL composition in cells and tissues varies, whereby phosphatidylcholine (PC) and phosphatidylethanolamine (PE) are the most abundant in mammalian cell membranes [84]. It has been pointed that brain, liver and kidney have a particularly high content of PEs that are highly enriched in long PUFAs, like docosahexaenoic acid (DHA) or AA. Interestingly, it is exactly these tissues that are deemed most susceptible toward lipid peroxidation and ferroptotic cell death [84, 86-89].

Before entering any metabolic pathway, FAs from either exogenous or endogenous sources must first be activated to form an acyl-CoA. ACS enzymes catalyze the activation of FAs to CoA esters in an ATP-dependent manner via a two-step reaction: First, an intermediate fatty acyl-AMP is formed releasing inorganic pyrophosphate (PPi). In the second step, a fatty acyl-CoA is formed releasing AMP [90]. The acyl group can then be re-acylated to lysophospholipids

(lysoPLs) by lysoPL acyltransferase (LPLAT) enzymes or other metabolic reactions. Oxidized PUFAs can be de-acylated from glycerophospholipids before entering the Lands' remodeling cycle, a membrane repair mechanism [90-93]. For example, abhydrolase domain containing 12 (ABHD12) bears different metabolic functions and is involved in PL repair by releasing damaged fatty acyl chains from membrane PLs. In the context of ferroptosis, Kathman *et al.* showed that the inhibition of the lysophosphatidylserine lipase ABHD12 lowers the tendency of cancer cells to undergo ferroptotic cell death [94].

The activation of FAs, catalyzed by ACS, is dependent on the given tissue and cell type and on the FAs itself. Long-chain ACSs are a subgroup of ACS family that activate long-chain FAs fatty acids (C12 to C20). In mammals, *Acsl* genes encode for five distinct gene products: ACSL1, ACSL3, ACSL4, ACSL5 and ACSL6, with differently spliced variants identified for each gene [90, 95-98]. ACSL3 and ACSL4 are the structurally closest homologues according to sequence homology. Nevertheless, they differ in their FA substrate specificities. While ACSL4 preferentially activates PUFAs, ACSL3 prefers monounsaturated fatty acids (MUFAs), inhibiting SFA-induced lipotoxicity. Exogenous supplementation with MUFAs was even shown to protect cells from LPO and ferroptotic cell death by displacing PUFAs from plasma membrane PLs [99]. ACSL4 has a strong preference for AA or EPA. Genetic deletion or pharmacological inhibition of ACSL4 and to some degree LPCAT3 limit the membrane-resident pool of PUFAs, thereby providing strong protection against ferroptosis at least in cultured cells [28]. In addition, ACSL4 has been linked to eicosanoid synthesis. In rat fibroblasts, knockdown of ACSL4 markedly increased free AA levels and eicosanoid biosynthesis [100]. There are two ACSL4 splice variants: ACSL4V1, which is ubiquitously expressed, and ACSL4V2, the longer form exclusively expressed in brain [101].

Compared to other tissues, brain and testis are highly enriched with the essential AA (20:4, n-6) and DHA (22:6, n-3), which cannot be synthesized by mammals due to the absence of desaturase enzymes. AA and DHA are also efficiently activated by ACSL6. Overexpression of ACSL6 in cell models leads to accumulation of DHA-CoA and to some extent oleic acid (OA)-CoA and AA-CoA [102]. In contrast, the knockout of *Acsl6* in mice leads to a reduction in DHA-containing lipids, motor disorder and increased astrogliosis. Furthermore, *Acsl6* KO male mice exhibit a reduction in testicular DHA content causing perturbed spermatogenesis and infertility. These studies thus suggest an essential role for ACSL6 function in lipid and DHA

metabolism for normal brain function and neuroprotection as well as male fertility [103, 104]. The three-dimensional protein structure of mammalian ACSL6 (78 kDa) remains elusive. Yet, first insights at specific structural features that may play an important role in enzyme activity were obtained for the bacterial homologue. Almost one dozen alternatively spliced forms for murine and the human counterpart of ACSL6 are known. The alternative splice variants of ACSL6 mainly differ in 26 amino acid residues in close proximity to the ATP binding site, termed the gate domain [105]. Soupene *et al.* compared the activity of the isoforms towards substrate-specificity of different fatty acids revealing marked differences, which suggest an essential role of fatty acid gait domain motifs for enzyme activity [98].

Under physiological conditions, protection of a PUFA-rich environment in membranes is maintained by RTAs or via the Cys/GSH/GPX4 axis, or others as described in the foregoing. Once this equilibrium is perturbed, either due an impaired antioxidant capacity or due to an increased generation of oxygen radicals, unrestrained lipid peroxidation may proceed with major consequences on the overall cellular lipidome, the latter comprising the structure and function of all lipids. Studying the lipid metabolism and specific lipid oxidation patterns in cells and tissue undergoing ferroptosis by using high-resolution mass spectrometry-based lipidomics technology is thus of great interest not only to identify (oxi)lipid signatures and to compare these results with data obtained from proteomics or metabolomics analyses, but also to unravel relevant pathways with focus on the development of potential biomarkers and pharmacological targets of ferroptosis [106, 107].

1.1.4 Ferroptosis relevance in health and disease

The genetic and pharmacological modulation of ferroptosis is of utmost interest in regard to investigating the potential physiological functions and molecular mechanisms of ferroptosis, as well as for the treatment and clinical benefit of diseases, caused by aberrant cell death or uncontrolled cell proliferation. In recent years, many pharmacological studies and studies with transgenic mouse models were performed, which have helped to gain insights into the *in vivo* relevance of ferroptosis in mammals [24, 54].

Role of ferroptosis in cancer

A series of pathological conditions have been linked to ferroptosis. With the discovery of ferroptosis-inducers in *RAS*-mutant fibrosarcoma cells, several *in vitro* and *in vivo* studies have

shown an important role of ferroptosis in cancer development as well as in the context of cancer treatment [5]. Jiang *et al.* published that p53, one of the main tumor suppressor proteins, can inhibit cystine uptake and repress the expression of *Slc7a11*, thereby sensitizing cells to ferroptosis [108]. Furthermore, the knockout of *xCT* in the highly metastatic mouse B16F10 melanoma cell line and in corresponding *in vivo* tumor transplantation mouse models showed highly promising results, indicating that targeting xCT is a viably approach to abrogate tumor growth and metastasis of melanoma [109]. Systemic depletion of Cys and cystine in mice and non-human primates, induced by the administration of an engineered cyst(e)inase enzyme, caused cell cycle arrest and impaired tumor growth in prostate and breast cancer xenograft models [110]. The genetic deletion of *Slc7a11* further showed that pancreatic ductal adenocarcinoma (PDAC) rely on the Cys import via system x_c^-, inducing ferroptosis in a tumor-selective manner both, in *in vitro* and *in vivo* models [111]. Even though several studies on xCT in tumor growth and tumor metastasis have come to similar conclusions, it should be reinforced that system x_c^- is not ubiquitously expressed in all cancers [16, 112, 113]. Further studies have shown that therapy-resistant cancer cells in a high mesenchymal cell state become strongly depended on GPX4 for their survival and are thus highly sensitive to ferroptosis. Furthermore, in a xenograft model Hangauer *et al.* demonstrated that the knockout of *Gpx4* leads to ferroptosis in selected persister cells and that tumors did not relapse in this mouse model [114, 115].

Although the Cys/GSH/GPX4 axis seems to offer attractive targets for anticancer treatment, one has to remember that GPX4 is essential for embryo development and for many adult tissues, which may severely limit a broad therapeutic window of potential GPX4 inhibitors [82, 83]. In addition, it is known for decades that GPX4 lacks a typical binding pocket for reversible inhibitors, therefore all known GPX4 inhibitors described so far covalently inactivate the enzyme by irreversibly alkylating the active site Sec [51]. With the discovery of FSP1 as a powerful ferroptosis suppressor and the finding that FSP1 is expressed in most tumor cell lines, new opportunities may open up to inhibit this system particularly to target therapy- and ferroptosis- resistant cancer cells [16, 17].

Contribution of ferroptosis to degenerative disease

In contrast to inducers of ferroptosis to prevent uncontrolled cell proliferation, tumor growth and tumor dissemination, the development of ferroptosis inhibitors is crucial, based on their

potential tissue protection functions. The conditional knockout of *Gpx4* in different mouse tissues has afforded to draw a picture, which cell types and tissue in principle depend on functional GPX4 and are generally susceptible to ferroptotic cell death [24]. Ischemia/reperfusion injury (IRI)-related diseases like stroke or ischaemic heart disease remain the leading cause of mortality worldwide with a global steadily increasing numbers in deaths and in disability-adjusted life years [116]. Pathologically, when the blood flow is interrupted for a certain period of time followed by reoxygenation of the tissue the tissues suffer from massive cell death and secondary inflammatory processes. Several studies reported in recent years strongly suggest that ferroptotic cell death is the main contributor underlying IRI-related disease and that ferroptosis inhibitors successfully protects from IRI-induced tissue damage [15, 117, 118]. For instance, using mice with tamoxifen-inducible deletion of *Gpx4* in adult mice in all tissues except brain (using the *ROSA26_CreERT2* deleter mouse) showed that the kidney is one of the most sensitive organs towards *Gpx4* depletion and associated ferroptotic cell death [15]. In the same study, it was demonstrated that the ferroptosis inhibitor liproxstatin-1 (Lip-1) can extend the life span of mice by mitigating acute renal failure [15, 119]. Since then, Lip-1 and improved ferrostatins have provided great promise for the *in vivo* application in various mouse models like models of hepatic IRI or intracerebral hemorrhage model [15, 52, 120-122]. Besides, other forms of tissue injury, for example, chronic obstructive pulmonary disease (COPD), which is associated with an altered inflammatory process in lung epithelial cells, emerges to be a ferroptosis-linked disease. As a study using a cigarette smoke-exposed GPX4 transgenic mouse model mimics COPD phenotype [123].

In addition to IRI-related diseases and organ failure, it is highly likely that ferroptosis is implicated in the loss of neuronal cells and contributes to several neurological disorders like Huntington's disease [124], Parkinson's disease [125-127], amyotrophic lateral sclerosis (ALS) [128] and dementia [6, 129]. Neuronal dysfunction and death can be caused by overstimulation of neurons expressing N-methyl D-aspartate (NMDA) receptors, which are ligand-gated cation channels activated by the excitatory neurotransmitter glutamate, in a process known as glutamate-induced excitotoxicity [130]. High extracellular levels of glutamate (>1 mM), however, can also inhibit system x_c^- thereby triggering ferroptotic cell death, which in turn, can be blocked by ferrostatin. This leads to the assumption that ferroptosis is the underlying type of cell death in these brain diseases [7, 130]. Meanwhile,

certain neuron-specific *Gpx4* knockout models have been established, which allowed to pinpoint the neuronal subtypes being most sensitive to ferroptosis. Parvalbumin-positive (PV$^+$) interneurons regulate cortical network excitability and are sensitive to oxidative stress. In early studies by Seiler *et al.* and Wirth *et al.*, the neuron-specific knockout of *Gpx4* triggered seizures and ataxia, which was caused by a strongly reduced number of PV$^+$ cortical inhibitory interneurons [6, 131]. Similarly, mice homozygous for a targeted mutation of the active site Sec to cysteine in GPX4 (i.e., *Gpx4$^{cys/cys}$*) on a mixed genetic background (C57BL/6x129/Ola), develop severe epileptic seizures also caused by the lack of PV$^+$ cells in the cortex of newborn mice [44]. These studies firmly established that Se-containing GPX is essential for the development and function of GABAergic PV+ interneurons [44, 131]. Besides this type of interneurons, other neuronal cell types like cerebellar neurons, e.g. Purkinje cells or cortical neurons, mostly glutamatergic neurons [6, 131, 132], MNs [128] and photoreceptor cells [133] were shown to be ferroptosis-sensitive. Taken together, the high sensitivity of most neuronal cells toward ferroptosis and the already first *ex vivo* and *in vivo* studies on the neuroprotective effect of ferroptosis inhibitors holds great promise for deciphering the underlining mechanisms of ferroptosis in neuronal demise and for the development of ferroptosis-related inhibitors to prevent or at least ameliorate a fraction of degenerative diseases.

1.2 Neurodegenerative diseases (NDs)

1.2.1 Types of NDs

Neurodegenerative disease (ND) is an umbrella term for a large group of human diseases characterized by the early and progressive loss of the structure and function of neurons in the central or peripheral nervous system. The central nervous system (CNS), which encompasses the brain and spinal cord, is a highly complex organ containing numerous different cell types, whereby neurons are the functional unit responsible for the transmission of information, while glial cells of different identities support and nourish neurons. Known as the longest living cell type in the human body, neurons cannot be sufficiently replaced or repaired once they become severely damaged or even die [134, 135]. Since dysfunction and loss of neurons are usually rather slowly progressing processes, it remains very challenging to define the initial cellular events and molecular mechanisms underlying the initiation and progression of NDs. NDs affect millions of people worldwide with constantly increasing prevalence. One aspect regarding this increasing prevalence is the common risk factor for NDs: aging [136]. Although the genetic basis and specific gene mutations of some NDs have been discovered, the majority of neurological disorders appears sporadic, as a complex interaction between genetic and environmental cues. Furthermore, NDs often share similar symptoms which makes it even more difficult to distinguish and diagnose between the different varieties of NDs. For example, the symptoms of frontotemporal dementia (FTD) or frontotemporal lobar degeneration (FTLD) (both are forms of dementia) are overlapping with characteristic symptoms of amyotrophic lateral sclerosis (ALS). However, various genes and mutations are already known to beg responsible for the familial FTD cases, e.g. microtubule-associated protein tau (MAPT/tau), granulin (GRN) and hexanucleotide expansion repeats in the open reading frame of chromosome 9 (C9orf72) [137, 138].

Alzheimer's disease – the most common form of dementia

Over 50 million people globally have been diagnosed with dementia in 2020 (Alzheimer's Disease International (ADI) marked by difficulties in memory, language and other cognitive skills [139]. The most common form of dementia is Alzheimer's disease (AD), named after Alois Alzheimer who first described a number of symptoms in a case study as a "peculiar severe disease process of the cerebral cortex" [140]. Episodic memory impairment is a hallmark symptom among AD patients. Key pathological features of AD are brain atrophy, extensive

loss of neurons, appearance of intraneuronal neurofibrillary tangles (NFTs) and extracellular amyloid plaques consisting primarily of amyloid-β (Aβ) [140, 141] (Fig. 4).
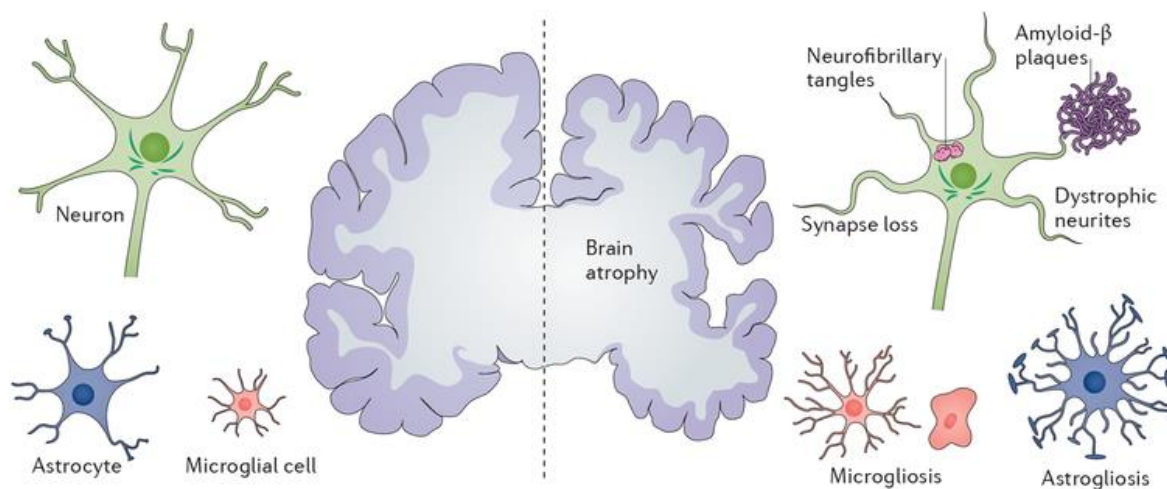
Figure 4| Pathological features of Alzheimer's disease
The comparison of a healthy brain with a brain affected by Alzheimer disease (AD) clearly shows the main characteristics of the disease: massive brain atrophy accompanied by the loss of neuronal synapses, aggregation of neurofibrillary tangles and amyloid β plaques. Furthermore, under normal conditions, microglia and astrocytes are in a quiescent state with small shaped morphology, sensing their surroundings and supporting neurons. Whereby in AD brain, glial cells are activated and found in excessive numbers, a state named as astrogliosis and microgliosis [141].

Like in many other NDs, AD has been linked with oxidative stress in neuronal cells. Increased oxidative stress leads to impaired cell function and the generation of highly toxic intermediates eventually culminating in neuronal cell death and associated neuroinflammatory processes [142, 143]. Since the identification of Aβ, the cleaved form of membrane-bound amyloid precursor protein (APP), a plethora of studies has been performed to examine the role of Aβ in AD progression [144, 145]. For instance, it was frequently shown that formation and accumulation of Aβ fibrils due to misfolding of the improperly processed protein seems to be an early toxic event causing neuronal dysfunction and AD [146, 147]. In other studies, soluble Aβ oligomers have been demonstrated to induce oxidative stress and mitochondrial dysfunction [148], and to bind to different receptors thus triggering neurotoxic signaling [149-152]. In addition to production and aggregation, transport and clearance of Aβ also affect its pathological function. However, all clinical studies aiming to clear up insoluble Aβ in the brain of AD patients in order to improve cognition invariably failed by using for example solanezumab (Eli Lilly), verubecestat (Merck) or lanabecestat (AstraZeneca and Eli Lilly), to name only three anti-amyloid therapies. The actual reason for this massive failure is currently being debated. It can be either due to an impaired reduction of toxic Aβ oligomers

or the amyloid hypothesis does no longer hold true, leading to a shift in the research focus away from the hypothesis Aβ being the underlying cause of ADs [153-155].

The lipid-transport protein, apolipoprotein E (ApoE), is considered a strong genetic risk factor for AD, predominantly in late-onset AD. ApoE is mainly produced by the liver, macrophages and astrocytes. ApoE functions as a key regulator of lipid metabolism and cholesterol homeostasis and is known to be involved in Aβ deposition. Among the three APOE isoforms - ApoE2, ApoE3, and ApoE4 - Aβ deposition appears to be isoform-specific, mainly dependent on ApoE4 followed by ApoE3 over ApoE2 [156, 157]. The difference on amino acid level between the isoforms is restricted to either Cys or arginine being present at positions 112 and 158 [158]. The risk for both, early-onset and late-onset of AD is ~3-fold increased with the presence of one copy of the *ApoE4* allele and even ~12-fold increased having with two copies (www.alzgene.org) [159]. The role of ApoE in AD pathogenesis has been extensively studied in the past. According to several studies, ApoE acts as an Aβ-binding protein thus decreasing Aβ clearance, causing increased formation of amyloid plaques [160, 161]. In addition, ApoE directly influences the formation of NFTs and the phosphorylation of tau responsible for microtubule stabilization.

The role of tau and its phosphorylated forms in AD sparked overwhelming interest among researchers and clinicians worldwide due to the possible role of phosphorylated tau in causing neurodegeneration and inducing neuroinflammation [162, 163]. Human *ApoE* knockin mice expressing APOE specifically in neurons show increased phosphorylation of tau independent of Aβ [157, 164]. Phosphorylation and other site-specific post-translational modifications on tau interfere with correct folding and might induce tau aggregation, which appears to be a molecular characteristic for the diagnosis of AD [141, 165].

In addition to the *APOE4* allele as a genetic risk factor associated with sporadic late-onset AD, a few other genes linked to autosomal dominant familial AD have been identified: *APP*, *PSEN1*, and *PSEN2* (Presenilin 1 and 2). One prominent example are the missense APP "Swedish" mutations (i.e., APPSW, APPK670N, and M671L) that result in increased Aβ production and the development of AD. Mouse models carrying the "Swedish" mutations have been established for the analysis of major AD characteristics including APP and Aβ levels or cognitive impairments [166-168].

So far, the exact mechanism of AD pathogenesis and the interplay between Aβ, tau, ApoE and other players in AD remain incompletely characterized and tools for pharmacological intervention await to be urgently developed. Nowadays, many studies are focusing on the link between neurodegenerative processes and neuroinflammatory cascades. For example, in brain, ApoE is mainly expressed in astrocytes and microglia and was shown to function as classical complement checkpoint inhibitor, postulating ApoE as a main regulator in immune response and neuroinflammation [169-171].

Microglia are the main type of immune cells in CNS. Microglia can proliferate, survey their environment and are in close interaction with neurons, astrocytes and oligodendrocytes, which is pivotal for their morphological and functional change in neurological disorders, referred to as reactive microgliosis. Activated microglia are found in post-mortem brain specimens from people affected by different brain diseases, including AD [172-174]. Microglia show beneficial effects by mediating Aβ clearance, but at same time cause neuroinflammation accompanied by increasing proinflammatory markers and neurotoxic ROS [175-177]. *In vivo* studies demonstrated that APOE and TREM2 (triggering receptor expressed on myeloid cells 2) are directly linked to the activation of microglia [171, 178, 179]. Akin to microglia, astrocytes, another kind of glial cells, can also undergo morphological, functional and molecular changes during neuropathological processes. Thus, disease-causing genetic modifications can prime astrocytic function to a reactive state, characterized by change in morphology, loss of homeostatic function and up- or downregulation of different markers aiming a defensive brain status. For instance, glial fibrillary acidic protein (GFAP) is the major cytoskeletal protein in astrocytes and widely used as a marker for abnormal activation and proliferation of astrocytes [180-182]. Both astrogliosis and microgliosis are typical processes in the different types of dementia, and therefore under great research interest. Notwithstanding, one of the main questions that still need to be explored in the study of ND is whether the reactive state of glial cells is a cause or consequence of dying neurons.

Amyotrophic lateral sclerosis (ALS) – the most devastating neurodegenerative disease

ALS is a rare and one of the most devastating ND, affecting 1 to 2 out of 100.000 people per year. Apart from isolated bulbar palsy or progressive muscular atrophy, ALS makes up about 70 % of motor neuron (MN) diseases [183]. During the pathological process of ALS, the progressive death of both, lower MN and upper MN in the brain and spinal cord, eventually

culminates in severe impairments of voluntary movements, speaking, swallowing and breathing. The upper neurons are glutamatergic neurons originating from the primary motor cortex. The lower MN are located in brainstem and spinal cord and mainly use acetylcholine as neurotransmitter [184, 185]. In spinal cord, the MNs are positioned in the ventral horn and are responsible for the contraction of skeletal muscles and movement as a function of the innervating muscle group [186]. The damage of MNs leads to a major clinical symptom – paralysis, which might be cervical, thoracic, lumbar or sacral, depending on the regions of affected neurons (Fig. 5) [187].
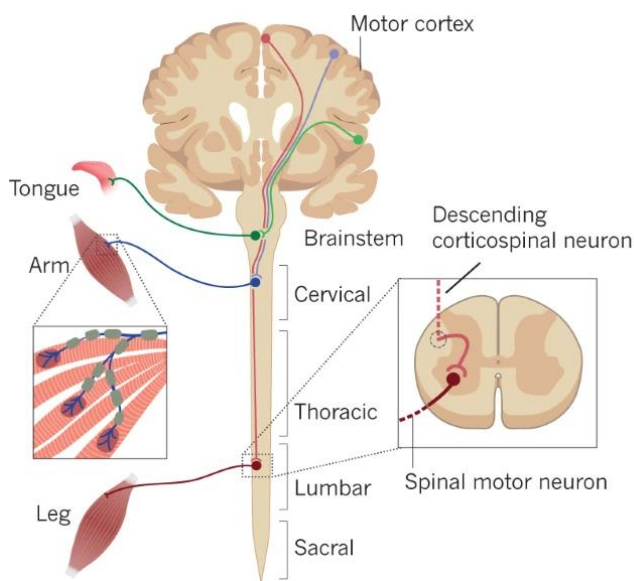
Figure 5| Corticospinal tract, the central scene in ALS
Motor neurons (MNs) are segmented according to the location of their target muscle. MN in motor cortex and brainstem innervate muscles of the face including the tongue. Corticospinal neurons or upper MNs are long distance neurons originating in the motor cortex and are connected to spinal MNs in the grey matter of the spinal cord. Spinal MNs are connected to the limbs and are involved in execution of voluntary movement, thus comprising cervical, thoracic and lumbar spinal cord. Amyotrophic lateral sclerosis (ALS) affects both, upper and lower MN. Progressive degeneration of spinal MNs leads to atrophied target muscles, limbs and eventually paralysis [187].

The reason why people are affected by the disease are only poorly understood, as most ALS cases are sporadic (sALS) with a high prevalence rate in persons aged 50-60, predominantly in males. 5-10 % of cases are familial with the onset peaking at the age of 43-52 [183, 184, 187, 188]. The majority of familial amyotrophic lateral sclerosis (fALS) cases has been linked to different mutations in the gene encoding for the cytosolic Cu,Zn-superoxide dismutase (SOD1). SOD1 is an antioxidant enzyme, which detoxifies superoxides by converting them in hydrogen peroxide and oxygen. One of the most known mutations that is widely used to study the disease-related processes is the alanine substitution SOD1G93A, which is the cause for one form of familial dominantly inherited ALS. Transgenic mouse models carrying SOD1G93A mutation develop ALS-like symptoms, including paralysis in hind limbs due to MN loss, inflammasome activation and in some cases even death within few months [184, 187, 189, 190]. The accumulation of abnormal SOD1 and the dysregulation of intracellular calcium homeostasis have been shown to be sufficient for triggering a pathological phenotype in mice,

albeit clinical trials in ALS patients targeting SOD1 have not been effective and successful so far [191]. The example of other genes in which modifications have been identified in familiar ALS cases include *TARDBP*, encoding for TAR DNA-binding protein 43 [192], *FUS*, encoding for fused in sarcoma protein [193], or the expansion of a noncoding GGGGCC hexanucleotide repeat in the *C9ORF72* gene [194]. Mutations in these genes lead to a different vulnerability of MNs in ALS patients and transgenic mouse models, implying that ALS is a multifactorial disease where genetic changes of both, neuronal and non-neural cell types contribute to disease development and progression [184, 195]. Furthermore, one study showed that environmental factors might also affect the pathology, as the phenotype of this *C9ORF72*-mutant mouse model was shown to be dependent on the environment, whereby the exposure of these mice to a less immune-stimulating gut microbiome ameliorated the phenotype [196].

Studies on post-mortem tissue of ALS patients demonstrated increased endoplasmic reticulum (ER) stress, iron accumulation and increased sensitivity to oxidative stress accumulating in oxidative damage of proteins and lipids [197]. Since cellular membranes of neurons and glial cells are highly enriched in PUFAs, oxidative stress has been linked to lipid peroxidation and neurotoxicity [198]. Iron accumulation in the spinal cord or dysregulation of mitochondria might be additional factors for ROS generation and toxicity leading to the loss of MNs and associated inflammatory responses [142, 199, 200]. Several studies revealed a link between oxidative stress and the pathogenesis of ALS; however, questions as to whether oxidative stress is cause or consequence of neuronal dysfunction remain unclear. Although treatment with different antioxidant compounds, such as vitamin E or N-acetyl-l-cysteine (NAC), was reported to slow down disease progression and to prolong survival of transgenic SOD1-mice [201, 202], none of the tested compounds demonstrated beneficial effects in human studies [203, 204]. This scenario is recurrent for a multitude of experimental pharmaceutical therapies providing promising results in transgenic ALS animal models, but with little or usually no effects in clinical trials.

To date, there are only two FDA approved drugs, i.e., riluzole and edaravone that are used for the treatment of ALS. Riluzole is a glutamate receptor antagonist, which blocks glutamate excitotoxicity. Edaravone acts as a poor RTA preventing lipid peroxidation and ferroptosis [205]. Even though the progression of symptoms is slightly delayed with both drugs, ALS still remains incurable and most patients eventually die from the inability to breathe that usually

occurs after 2-5 years from the onset of the first symptoms [206, 207]. Diverse phenotypes and heterogeneity among patients paired with the lack of appropriate mouse models are considered to be main issues in devolving new and efficacious drugs against ALS.

To sum up, the inspiring and appropriate words about the disease of Mitch Albom (Tuesdays with Morrie: An Old Man, a Young Man, and Life's Greatest Lesson) are very descriptive [208]:

"ALS is like a lit candle: it melts your nerves and leaves your body a pile of wax. You cannot support yourself standing. You cannot sit up straight. By the end, if you are still alive, your soul, perfectly awake, is imprisoned inside a limp husk. Like something from a science fiction movie, the man frozen inside his own flesh."

1.2.2 Cell-based models for the study of NDs

Our understanding of the true mechanisms of neurodegeneration still remains very limited despite decades of intensive research worldwide. A number of *in vitro* approaches including optimization, culturing and modification of neuronal cells have been established to investigate the molecular and functional aspects of NDs and to develop novel tools for pharmacological intervention.

Cultured neuronal cells derived from embryonic rat spinal cord and ganglia have been used in electrophysiological studies, however, their preparation and maintenance of those cells in a good, rather "physiological" state remains difficult [209, 210]. In contrast, the establishment of mouse and human embryonic stem cells (hESCs) and their differentiation to neuronal cells have been more successful in recent years. hESCs derived from the inner cell mass of the human blastocysts grow mainly on a layer of murine feeder cells [211]; however, this technique comes along with major ethical considerations. Some of these ethical issues have been resolved by the possibility of reprogramming adult somatic cells to virtually unlimited numbers of so-called human induced pluripotent stem cells (hiPSCs). The conversion of somatic cell to hiPSCs was successfully accomplished by the pioneering work by Takahashi and Yamanaka using four well-defined genetic factors: octamer-binding protein 3/4 (Oct3/4), SRY-Box Transcription Factor 2 (Sox2), MYC Proto-Oncogene c-Myc and kruppel like factor 4 (Klf4) [212, 213]. Based on their work, different protocols for reprogramming patient-specific cells have been implemented to study pathological processes, especially for neurological disorders. For instance, Yagi *et al.* established iPSCs derived from familial AD (fAD) patients carrying

mutations in both variants of presenilin, PSEN1 (A246E) and PSEN2 (N141I), which sufficiently recapitulate an increase of Aβ secretion as one of the major hallmarks of AD [214]. In another study by Lee *et al.*, hiPSc were generated from patients, suffering from familial dysautonomia, a disease characterized by the loss of autonomic and sensory neurons. Those cells were reprogrammed in different kind of cells, which were used for transcriptome analysis and for validating potent drug candidates [215]. Similarly, fibroblasts from schizophrenia patients were reprogrammed and subsequently differentiated in neurons to gain novel insights in the underlying cellular and molecular mechanisms [216]. Furthermore, the Eggan lab established and characterized MNs and glia derived from reprogrammed ALS-patient-specific stem cells [217, 218]. Apart from the generation of patient-specific hiPSCs, CRISPR/Cas9 based genome-editing offered novel possibilities to study NDs, for example by introducing AD-causing mutations, like "Swedish" mutations and presenilin 1 PSEN1M146V mutation in hiPSCs [219, 220]. These cell-based technologies are continuously expanding and improving with the implementation of three-dimensional (3D) matrices or even brain organoids to better mimic the neuro-microenvironment [221-223], that can significantly result in in-depth investigations answering specific questions on the underlying mechanisms of ND.

1.2.3 Transgenic mouse models for the study of NDs

The success rate in discovery of new drugs for the treatment of NDs is incredibly low and very daunting, as best illustrated by the fact that less than 1 % of the developed drugs against AD have been applied in clinics for patient treatment. Besides the lack of knowledge of the true underlying mechanism causing NDs, one of the key factors are complications of the interpretation and translation of data derived from animal models into human-oriented studies, including characteristics of the correct drug target, usage of the correct dose of the drug or design of the appropriate trial [224].

Mouse (*Mus musculus*) models are the most frequently used animal models in science, mainly because of the ease of breeding, short generation and availability of various tools for genetic modifications. Rat models might be another good option in regard to ND research with the advantage to study such disease symptoms as behavioral impairments and cognitive functions in AD. In addition, rats similar to humans have six isoforms of tau protein, leading to higher similarity in hyperphosphorylation of tau and formation of tangles, although subsequent formation of plaques, another hallmark of AD, is absent in rats [225, 226].

The first transgenic mouse models used for study of NDs have been generated by overexpressing known human mutations of ND-related genes. Previously identified in familial cases of ND, mice carrying SOD1G93A mutation are used for studying ALS and animals carrying APP mutations were used for the study of AD-related processes, respectively. Next to the introduction of similar genetic changes, an efficient mouse model should also simulate disease characteristics and might enable drug testing and treatment. Animal studies have often been criticized for their poor design including standardization and insufficient transparency that might compromise reliability of the data [224, 227]. The number of mouse models has increased significantly throughout the years, which included not only well known or likely causative genes. For example, APOE or TREM2, which are linked to the activation of microglia, have been demonstrated to play a major role in AD progression in several transgenic mouse models. In addition, the specific overexpression of proteins associated with motor function such as dynamitin resembles ALS in mouse models [161, 179, 228].

Since NDs have been frequently linked with increased oxidative stress and lipid peroxidation, distinct players in the ferroptosis pathway might be of paramount interest in establishing adequate animal models. For example, depletion of GSH due to the specific knockout of γ-glutamate cysteine ligase catalytic subunit (GCLC) in neurons leads to gait and motoric abnormalities and neurodegeneration [229]. GPX4, as one key regulator of ferroptosis, is highly expressed in neurons of cortex, cerebellum and hippocampus. In-deed, neuron-specific tamoxifen-inducible GPX4 KO mice show increased lipid peroxidation, ferroptosis and neurodegeneration [6, 129]. Another model of conditional deletion of GPX4 using *Thy1* Cre mice demonstrated that these mice develop severe muscle atrophy, paralysis and quickly die within 8 days. While being informative, this mouse model, however, does not facilitate longitudinal studies and does not reflect long-term neurodegenerative processes as evident in ND patients [128]. In contrast to loss of GPX4, overexpressing GPX4 in SOD1G93A transgenic mice provided a mild rescuing effect characterized by a delay of disease onset, a reduction of spinal motor neuron degeneration and an extended overall survival of compound mutant mice [230].

Yet, all these approaches have their intrinsic limitations, such as they only recapitulate certain aspects of neurodegenerative disorder or show limitations regarding the therapeutic window. The ideal mouse model for ND should mimic synaptic dysfunction and loss, overall neuronal abnormalities followed by the death of neurons, as the main biochemical and cellular features.

Furthermore, a progressive impairment of these processes would be part of an ideal model. In addition, a contribution of aging, an involvement of glial cells and the innate immune system would increase the translational potential of mouse studies to human [227]. Thus, the one animal model closely recapitulating all aspects of ND does not exist and there is an ongoing and pressing need to overcome these limitations on the path to the development of efficacious drug to combat these often devastating and fatal NDs.

1.3 Aim of the study

NDs affect millions of people worldwide with constantly increasing prevalence. Why and how those neurons degenerate is still not fully understood with the exception of some familial mutations, known to be linked to AD or ALS. The investigation of the mechanisms underlying NDs has been severely hampered by a lack of appropriate *in vitro* and *in vivo* models mimicking the main hallmarks of ND. These, in turn, are however urgently needed for the development of both diagnostic biomarkers and for novel therapeutics to effectively treat ND, as no cure for any of these diseases is available yet. A number of cellular processes including oxidative damage, mitochondrial dysfunction, deregulated iron handling or calcium homeostasis have been already associated with NDs, but, how these aberrant processes culminate in early neuronal death processes is not well understood. Ferroptosis, as a novel form of regulated cell death, appears to play a predominant role in NDs. One of the key regulators of this form of cell death is the selenoenzyme GPX4, which has the unique ability to restrain uncontrolled lipid peroxidation in cellular membranes by directly reducing phospholipid hydroperoxides to the corresponding alcohols.

Hence, the overall goal of this thesis was to investigate the molecular underpinnings of ferroptosis in the development of ND *in vivo* and how it impacts on neuroinflammatory processes. To this end, two mouse models with spatiotemporal, neuron-specific deletion of *Gpx4* either in glutamatergic neurons or in MNs were conceived allowing for a comprehensive and longitudinal analysis of the cellular mechanisms contributing to neuronal ferroptosis *in vivo*, as well the discovery of specific molecular signatures that may recapitulate a fraction of NDs. Second, genetic and pharmacological approaches were envisioned to study whether neurodegeneration induced by neuron-specific loss of GPX4 can be mitigated by genetic means or by next generation ferroptosis inhibitors. Moreover, to model neurological disorders *in vitro*, the differentiation of hiPSCs have opened new opportunities to determine sensitivity of neurons. ALS-patient derived hiPSCs will be differentiated in MNs, and used to determine sensitivity or resistance against ferroptosis induction.

2 MATERIAL

2.1 Instruments

Instruments	Company
Chemi Doc™ MP Imaging System	BioRad, Munich, Germany
Mini-PROTEAN® Tetra electrophoresis chamber	BioRad, Munich, Germany
TC20 automated cell counter	BioRad, Munich, Germany
Trans-Blot Turbo Transfer System™	BioRad, Munich, Germany
Axioplan 2 Microscope	Carl Zeiss AG, Oberkochen, Germany
LSM 880	Carl Zeiss AG, Oberkochen, Germany
Centrifuge 5424R	Eppendorf, Hamburg, Germany
Centrifuge 5430R	Eppendorf, Hamburg, Germany
Thermo Mixer C	Eppendorf, Hamburg, Germany
Thermal Cylcer	G-Storm, Somerton, United Kingdom
Roller 10 digital	IKA Labortechnik, Staufen, Germany
T 25 digital ULTRA-TURRAX® Dispergierer	IKA®-Werke GmbH & CO. KG, Staufen, Germany
Centrifuge Combi Spin FVl-2400N	Kisker Biotech GmbH & Co. KG, Steinfurt, Germany
Centrivap Cold Trap	Labconco Corporation, Kansas City, USA
RapidVap Vacuum Evaporation System	Labconco Corporation, Kansas City, USA
Leica CM3050 S Cryostat	Leica Biosystems Nussloch GmbH, Nussloch, Germany
Leica DFC3000G Microscope	Leica Microsystems GmbH, Wetzlar, Germany
Hemocytometer (Neubauer chamber)	Marienfeld, Lauda Königshofen, Germany
Mettler Toledo™ FiveEasy™ Plus FP20 pH/mV Meters	Mettler Toledo, Columbus, Ohio, USA
Spectrophotometer UV5Nano	Mettler Toledo, Columbus, Ohio, USA
XA205 Dual Range	Mettler Toledo, Columbus, Ohio, USA
SpectraMax M5 Microplate Reader	Molecular Devices, Sunnyvale, CA, USA
Nikon Eclipse microscope	Nikon, Tokyo, Japan
Multi-Tube Vortex Mixers VXMTDG	OHAUS Europe GmbH, Nänikon, Switzerland
Electrophoresis power supply	PEQLAB Biotechnologie GmbH, Erlangen, Deutschland
NanoDrop 1000 Spectrophotometer	PEQLAB Biotechnologie GmbH, Erlangen, Deutschland
Mixer Mill MM 400	Retsch GmBH, Haan, Germany
Vortex Genie 2	Scientific industries, Bohemia, New York, USA
Sharp-R-941-BK-W-Inverter-Microwave	Sharp, Osaka, Japan
Mr. Frosty™ freezing container	Thermo Fischer, Bonn, Germany
Thermo Scientific™ Fresco™ 17 Microcentrifuge	Thermo Fisher Scientific, Waltham, USA
Fisherbrand™ GT4 Benchtop Centrifuge	Thermo Fisher Scientific, Waltham, USA
Waterbath VWB 12	VWR, Radnor, USA

2.2 Chemicals

Chemical	Company	Catalog no.
(1S,3R)-RSL3	Cayman Europe, Michigan, USA	19288
0.9 % Sodium Chloride injection solution	B. Braun Melsungen AG, Melsungen, Germany	-
10X PCR buffer	Thermo Fisher, Bonn, Germany	10342020
2-Mercaptoethanol 50 mM	Life Technologies, Carlsbad, USA	31350-010

2-Propanol	Merck KGaA, Darmstadt, Germany	1096342500
2-Propanol	Thermo Fisher Scientific, Waltham, USA	P/7508/17
3-Methyl-1-phenyl-2-pyrazoline-5-one (edaravone)	Sigma-Aldrich GmbH, Taufkirchen, Germany	M70800
4',6-Diamidino-2-phenylindole dihydrochloride (DAPI)	Sigma-Aldrich GmbH, Taufkirchen, Germany	D9542-10MG
AquaBluer ™ Cell Viability Assay Solution	MultiTarget Pharmaceuticals LLC, Salt Lake City, USA	6015
B-27 Supplement (50X)	Life Technologies, Carlsbad, USA	17504044
B-27 Supplement (50X), minus antioxidants (-AO)	Life Technologies, Carlsbad, USA	10889038
Bambanker	VWR International , Radnor, USA	WAKO30214681
Blasticidin S hydrochloride	Thermo Fisher, Bonn, Germany	A1113903
BSA, fatty acid free	Sigma-Aldrich GmbH, Taufkirchen, Germany	A8806-5G
Butylated hydroxytoluene (BHT)	Sigma-Aldrich GmbH, Taufkirchen, Germany	W218405
Ceramide/Sphingoid Internal Standard Mixture II	Avanti Polar Lipids, Birmingham, USA	LM6005-1EA
CHIR 99021	Tocris Bioscience, Bristol, UK	4423/10
Chloroform	Thermo Fisher Scientific, Waltham, USA	C/4966/17
CryoStor® CS10	Stemcell Technologies, Vancouver, Canada	7930
Cumene hydroperoxide	Sigma-Aldrich GmbH, Taufkirchen, Germany	247502
D+Saccarose	Carl Roth GmbH & Co, Karlsruhe, Germany	46211
DAPT	Miltenyi Biotec B.V. & CO. KG, Bergisch Gladbach, Germany	130-110-489
Diethylenetriaminepentaacetic acid (DTPA)	Sigma-Aldrich GmbH, Taufkirchen, Germany	D6518405
Dimethylsulfoxide (DMSO)	Agilent, Santa Clara, USA	600675
DMEM (1x)	Thermo Fisher, Bonn, Germany	21969035
DMEM/F-12-500 mL	Life Technologies, Carlsbad, USA	11320-074
DMH1	Tocris Bioscience, Bristol, UK	4126/10
DMSO	Sigma-Aldrich GmbH, Taufkirchen, Germany	D2650
DNA Agarose	Biozym Scientific GmbH, Hessisch Oldendorf, Germany	870055
DNA Loading Dye 6x	Sigma-Aldrich GmbH, Taufkirchen, Germany	R0611
Doxycycline hyclate	Sigma-Aldrich GmbH, Taufkirchen, Germany	D9891-1G
Dulbecco's Phosphate Buffered Saline (DPBS)	Thermo Fisher, Bonn, Germany	14190094
Erastin	Merck KGaA, Darmstadt, Germany	329600-5MG
Ethanol (EtOH)	Merck KGaA, Darmstadt, Germany	1009831000
Ethyleneglycol	Carl Roth GmbH & Co, Karlsruhe, Germany	9516.3
Fetal Bovine Serum (FBS)	Thermo Fisher, Bonn, Germany	10270106
Geltrex, reduced growth factor basement membrane matrix	Life Technologies, Carlsbad, USA	A1413302
GeneRuler 1 kb Plus DNA Ladder-5 x 50 µg	Life Technologies, Carlsbad, USA	SM1331
Geneticin® Selective Antibiotic (G418 Sulfate) (50 mg/mL)	Thermo Fisher, Bonn, Germany	10131035
Gentamicin sulfate	Sigma-Aldrich GmbH, Taufkirchen, Germany	G1914-250MG
GlutaMAX Supplement-100 mL	Thermo Fisher, Bonn, Germany	35050038
Glycerin	Carl Roth GmbH & Co, Karlsruhe, Germany	3783.2

Human BDNF, research grade	Miltenyi Biotec B.V. & CO. KG, Bergisch Gladbach, Germany	130-093-811
Human CNTF, research grade	Miltenyi Biotec B.V. & CO. KG, Bergisch Gladbach, Germany	130-096-336
Human IGF-1, research grade	Miltenyi Biotec B.V. & CO. KG, Bergisch Gladbach, Germany	130-093-885
Insulin Solution, Human recombinant	Sigma-Aldrich GmbH, Taufkirchen, Germany	I9278-5ML
Ketamin 10 %	Veterinärarzneimittel	-
L-buthionine sulfoximine (BSO)	Sigma-Aldrich GmbH, Taufkirchen, Germany	B2515
L-Glutamine	Thermo Fisher, Bonn, Germany	25030081
Liproxstatin	Selleck Chemicals GmbH, Berlin, Germany	S7699
Liproxstatin 3rd generation	customized order	
Lonza™ AccuGENE™ Molecular Biology Water	Thermo Fisher Scientific, Waltham, USA	BE51200
Magnesium Chloride	Sigma-Aldrich GmbH, Taufkirchen, Germany	1374248-1G
Magnesium Chloride (50 mM)	Thermo Fisher, Bonn, Germany	10342020
Meloxicam (Melosus) 1.5mg/ml	Veterinärarzneimittel	-
MEM non-essential amino acid NEAA (100X)	Sigma-Aldrich GmbH, Taufkirchen, Germany	M7145-100ML
Methanol	Thermo Fisher Scientific, Waltham, USA	M/4056/17
Methyl-Tert-Butyl Ether	Thermo Fisher Scientific, Waltham, USA	M/4496/17
Mygliol	ChemTik, Berlin, Germany	CTK5E4513
N2 SUPPLEMENT 5ML	Thermo Fisher, Bonn, Germany	17502048
Neurobasal Medium-500 mL	Life Technologies, Carlsbad, USA	21103-049
Paraformaldehyd	Carl Roth GmbH & Co, Karlsruhe, Germany	0335.3
Penicillin/Streptomycin	Thermo Fisher, Bonn, Germany	15140122
Protamine sulfate	Sigma-Aldrich GmbH, Taufkirchen, Germany	P3369-10G
Proteinase K	Carl Roth GmbH & Co, Karlsruhe, Germany	7528.1
Puromycin dihydrochloride	Sigma-Aldrich GmbH, Taufkirchen, Germany	P9620-10ML
Retinoic acid	Miltenyi Biotec B.V. & CO. KG, Bergisch Gladbach, Germany	130-117-339
Roti®-Phenol/Chloroform/Isoamylalkohol	Carl Roth GmbH & Co, Karlsruhe, Germany	A156.2
Skim Milk Powder	Carl Roth GmbH & Co, Karlsruhe, Germany	T145.2
SOC-Medium	Thermo Fisher, Bonn, Germany	15544034
Sodium Chloride (NaCl)	Sigma-Aldrich GmbH, Taufkirchen, Germany	W302600
Sodium dodecyl sulfate (SDS)	Carl Roth GmbH & Co, Karlsruhe, Germany	2326.2
Sodium hydroxide (NaOH)	Carl Roth GmbH & Co, Karlsruhe, Germany	6771.1
SPLASH® LIPIDOMIX® Mass Spec Standard	Avanti Polar Lipids, Birmingham, USA	330707-1EA
StemFlex medium	Thermo Fisher, Bonn, Germany	A3349401
StemMACS Purmorphamine	Miltenyi Biotec B.V. & CO. KG, Bergisch Gladbach, Germany	130-104-465
StemMACS SB431542	Miltenyi Biotec B.V. & CO. KG, Bergisch Gladbach, Germany	130-106-275
StemPro Accutase Cell Dissociation Reagent	Life Technologies, Carlsbad, USA	A1110501
Sybr® Safe DNA gel stain	Invitrogen, Karlsruhe, Germany	S33102
Tamoxifen	Sigma-Aldrich GmbH, Taufkirchen, Germany	T5648-1G
tertiary-butyl hydroperoxide	Sigma-Aldrich GmbH, Taufkirchen, Germany	C6628
Tris (Trizma-Base)	Carl Roth GmbH & Co, Karlsruhe, Germany	2449.2
Trisodium citrate dihydrate	Sigma-Aldrich GmbH, Taufkirchen, Germany	S1804
Triton-X	Sigma-Aldrich GmbH, Taufkirchen, Germany	T9284-10ml
Trypsin 0,05% EDTA	Thermo Fisher, Bonn, Germany	25300054

Tween ® 20	Sigma-Aldrich GmbH, Taufkirchen, Germany	P9416
Tween20	Sigma-Aldrich GmbH, Taufkirchen, Germany	P9416
Valporic acid	Tocris Bioscience, Bristol, UK	2815
Water	Thermo Fisher Scientific, Waltham, USA	W/0106/17
X-tremeGene HP DNA Transfection Reagent	Roche Diagnostics, Mannheim, Germany	6366236001
Xylazin 20 mg/ml	Veterinärarzneimittel	-
Y-27632 dihydrochloride; 10 mg	Tocris Bioscience, Bristol, UK	1254/10

2.3 Disposals and Kits

Disposals and Kits	Company	Catalog no.
µ-Dish 35 mm, low	ibidi GmbH, Gräfelfing, Germany	80136
Disposable Vinyl Specimen Molds	Weckert Labortechnik, Kitzingen, Germany	4557
Tissue Tek® Compound Embedding Medium	Weckert Labortechnik, Kitzingen, Germany	4583
Costar® reagent reservoirs	Sigma-Aldrich GmbH, Taufkirchen, Germany	4870
Roti®-Histokitt	Carl Roth GmbH & Co, Karlsruhe, Germany	6638.1
Pierce BCA Protein Assay	Thermo Fisher, Bonn, Germany	23225
PageRuler prestained protein ladder	Thermo Fisher, Bonn, Germany	26616
SuperSignal West Femto Maximum Sensitivity Kit	Life Technologies, Carlsbad, USA	34095
Cell culture dish 100 x 20 mm	Greiner Bio-One, Kremsmünster, Austria	664160
Cell Counter Slides for TC20™	Bio-Rad, Munich, Germany	1450011
Clarity ™ Western ECL Blotting Substrate	Bio-Rad, Munich, Germany	1705061
Lysing Matrix S	MP Biomedicals, Santa Ana, USA	6925100
Corning Tubes with Cap 14 ml	Thermo Fisher Scientific, Waltham, USA	9401352
Nunc 96 well plates	Thermo Fisher, Bonn, Germany	9407473
Nunc 60 x 15 mm plates	Thermo Fisher, Bonn, Germany	9476940
Nunc 6 well plates	Thermo Fisher, Bonn, Germany	9477145
Parafilm M®	Thermo Fisher, Bonn, Germany	12378039
Chromacol™ 10mL screw top round bottom vial	Thermo Fisher Scientific, Waltham, USA	71210135501
Fisherbrand™ Pasteur Pipets	Thermo Fisher Scientific, Waltham, USA	1154-6963
Trans-Blot Turbo Transfer Pack, PVDF	Bio-Rad, Munich, Germany	170-4156
Aqua-Poly/Mount	Polysciences, Inc., Warrington, USA	18606-20
Micro tube 0.5ml 9NC	Sarstedt AG & Co.KG, Nümbrecht, Germany	411.506.002
Cell Scraper with 2-position blade	Sarstedt AG & Co.KG, Nümbrecht, Germany	422-83.1832
Precellys Keramik-kit 1.4 mm 2 ml Tubes	VWR International , Radnor, USA	432-3751
12 % Mini-PROTEAN® TGX Stain-Free™ Precast Gels	Bio-Rad, Munich, Germany	456-8043
DNA Loading Dye 6x	Thermo Fisher, Bonn, Germany	R0611
ApopTag® Fluorescein In Situ Apoptosis Detection Kit	MilliporeSigma, Massachusetts, USA	S7110
Millex GP Filter 0,22µm	MilliporeSigma, Massachusetts, USA	SLGP033RS
Millex GP Filter 0,45µm	MilliporeSigma, Massachusetts, USA	SLHP033RS
CryoTubes®	Thermo Fisher, Bonn, Germany	V7634-500EA

2.4 Enzymes

Enzymes	Company	Catalog no.
cOmplete™ Protease Inhibitor Cocktail	Roche Diagnostics, Mannheim, Germany	1697498
PhosSTOP™Phosphatase inhibitor cocktail	Roche Diagnostics, Mannheim, Germany	4906837001

Proteinase K	Carl Roth GmbH & Co, Karlsruhe, Germany	7528.1
RNase A	Thermo Fisher, Bonn, Germany	10777019
Taq Polymerase	Thermo Fisher, Bonn, Germany	10342020

2.5 Antibodies

Primary antibodies	species	Company	Catalog no.
ACSL4	mouse	Santa Cruz Biotechnologies, Heidelberg, Germany	sc-365230
CHAT	goat	MilliporeSigma, Massachusetts, USA	MAB144P
GFAP	rabbit	Abcam, Cambridge, UK	ab7260
GPX4	rabbit	Abcam, Cambridge, UK	ab125066
HB9	mouse	Santa Cruz Biotechnologies, Heidelberg, Germany	sc-515769
IBA1	rabbit	Genetex, Irvine, USA	GTX100042
KIF5A	rabbit	Abcam, Cambridge, UK	ab5628
MAP2	mouse	MilliporeSigma, Massachusetts, USA	M9942
NeuN	mouse	MilliporeSigma, Massachusetts, USA	MAB377
TUJ1 (beta III tubulin)	mouse	Sigma-Aldrich GmbH, Taufkirchen, Germany	T5076
VCP	mouse	Abcam, Cambridge, UK	ab11433
β-Actin	mouse	Sigma-Aldrich GmbH, Taufkirchen, Germany	A5441
β-Actin-peroxidase	mouse	Sigma-Aldrich GmbH, Taufkirchen, Germany	A3854

Secondary antibodies	species	Company	Catalog no.
Alexa Fluor 488 donkey anti-goat	donkey	Life Technologies, Carlsbad, USA	A32814
Alexa Fluor 488 donkey anti-rabbit	donkey	Life Technologies, Carlsbad, USA	A21206
Alexa Fluor 488 goat anti-mouse	goat	Life Technologies, Carlsbad, USA	A32723
Alexa Fluor 546 goat anti-mouse	goat	Life Technologies, Carlsbad, USA	A11003
Alexa Fluor 594 donkey anti-rabbit	donkey	Life Technologies, Carlsbad, USA	A21207
goat anti-mouse IgG-HRP	goat	Santa Cruz Biotechnologies, Heidelberg, Germany	SC-2031
goat anti-rabbit IgG-HRP	goat	Santa Cruz Biotechnologies, Heidelberg, Germany	SC-2030

2.6 Oligonucleotides

Oligonucleotides were synthesized by Life Technologies or Sigma Aldrich. The stock solutions were diluted with a corresponding volume of H_2O to give a final concentration of 100 µM.

Genotyping primer	sequence
Gpx4_PF_for	CGTGGAACTGTGAGCTTTGTG
Gpx4_PF_rev	AAGGA CACAGAGCTGAGGCTG
Gpx4_1_for	GTTTAAGGATGGTGGTGGTAACCTGCTAG
Gpx4_3_rev	ACTTAGCCCATAGTCCTAAGATCAC
Acsl4_flox_for	TCTAATGCCATTGGTGACCTC
Acsl4_flox_rev	AGGTCCTCATA GGCACCATCA
Cre D	CACGACCAAGTGACAGCAATGCTG
Cre E	CAGGTAGTTATTCGGATCATCAGC
CreER1	GGTTCTCCGTTTGCACTCAGGA
CreER2	CTGCATGCACGGGACAGCTCT
CreER3	GCTTGCAGGTACAGGAGGTAGT

2.7 Cell lines

Human IPSCs HMGU#1 (ISFi001-A): Human iPSCs were derived from neonatal fibroblasts BJ (ATCC®CRL2522™) using the CoMiP system and were purchased from the Helmholtz Zentrum München.

Human iPSCs SOD1 mutations: hIPS cell line #27e originates from dermal fibroblast from a 29 age-old ALS patient carrying SOD1G85S mutation and #29d was obtained from an 82 age-old patient carrying SOD1L144F mutation. hIPSCs were generated via viral integration of Oct4, Sox2, KLF4 Acsl4 and obtained from Harvard University, Stem Cell Core Facility (MEW-2564).

2.8 Mouse lines

Gpx4tm2Marc (Gpx4^{fl/fl})

This mouse strain carries *Gpx4* alleles with two loxP sites flanking exons 5-7 and was generated and described in Seiler *et al.* [6].

Gpx4^{cys/fl}

This mouse strain carries a *Gpx4* allele with site-directed mutation of Sec to Cys (GPX4U46C) in the active site and was generated and described in Ingold *et al.* [44].

Acsl4tm1c/tm1c (Acsl4^{fl/fl})

The conditional mouse strain *Acsl4^{tm1c}* (*Acsl4^{fl/fl}*) originates from the *Acsl4^{tm1a(EUCOMM)wtsi}* strain (MGI:1354713) produced by EUCOMM. The generation of conditional "*tm1c*" strain was made by crossing so-called "tm1a" with mice, expressing Flp recombinase as described by Dr. Sebastian Doll [231].

CaMK2aCreERT2 transgenic mouse

This TAM-inducible Cre line *Camk2a-CreERT2_TG* mice was originally provided by Dr. Günther Schütz (German Cancer Research Center, Heidelberg, Germany). The transgenic mice express Cre recombinase driven by calcium/calmodulin-dependent protein kinase II alpha (Camk2a) promoter, leading to Cre recombinase expression in the forebrain of adult mice. By TAM application, CreER^{T2}, the fusion of mutated estrogen receptor (ER) and Cre becomes activated and allows robust activation of Cre/Lox recombination-mediated conditional gene knockout [232, 233].

Gpx4^{fl/fl} CaMK2aCreERT2 transgenic mouse

For the specific deletion of *Gpx4* in glutamatergic neurons, *Gpx4^{fl/fl}* mice were bred with *CaMK2aCreERT2* transgenic mouse. This generates a mouse carrying one or two loxP-flanked (fl) Gpx4 alleles and a TAM-inducible CreER^{T2} protein in cells, where the *CaMK2a* gene is expressed.

Acsl4^{fl/fl} x Gpx4^{fl/fl} CaMK2aCreERT2 transgenic mouse

To generate an *Acsl4/Gpx4* double knockout mouse line, *Acsl4^{fl/fl}* mice were bred with the *Gpx4^{fl/fl;CaMK2aCreERT2}*, described by Dr. Sebastian Doll [231].

Gpx4^{cys/fl} x Gpx4^{fl/fl} CaMK2aCreERT2 transgenic mouse

By crossing *Gpx4^{wt/cys}* (GPX4U46C) mice with *Gpx4^{fl/fl;CaMK2aCreERT2}* mice *Gpx4^{cys/fl;CaMK2aCreERT2}* were generated. After TAM application, the floxed *Gpx4* allele is deleted, while the Cys variant of GPX4 is still being expressed.

Hb9Cre transgenic mouse

The *Hb9Cre* line was provided by Dr. Andrea Huber-Brösamle (Institute of Developmental Genetics, HMGU). Cre expression is restricted to *Mnx1* (HB9) expressing cells, mainly motor neurons, making the mice a useful line for studies of neuromuscular disease and motor neurons function. *Homebox gene 9 (Hb9)* is expressed in developmental spinal cord between E9-E9.5 and completed by E10.5-E11 [234].

Gpx4^{fl/fl} Hb9Cre transgenic mouse

When *Gpx4^{fl/fl}* mice were bred with *Hb9-Cre* line, Cre-mediated recombination in the resulting offspring leads to deletion of *Gpx4* in *Mnx1 (Hb9)* expressing cells, mainly in motor neurons.

2.9 Software and online tools

Software	Supplier
BioMart	[235]
Biorender	BioRender, Toronto, Canada
Catwalk XT 10.6	Noldus, Wageningen, Netherlands
EndNote X8	Clarivate Analytics, Philadelphia, USA
FinchTV 1.4	Geospiza, Inc., free software
Geneious Prime	Geneious, Auckland, New Zealand
GeneRanker [236]	Precigen Bioinformatics Germany GmbH, Germany
Genomatrix	Precigen Bioinformatics Germany GmbH, Germany
GraphPad Prism 8.0	GraphPad Software Inc., USA
Image Lab	Bio-Rad, Munich, Germany
MetaboAnalystR	Xia Lab
multalin.toulouse.inra.fr	INRAE Institute
netScope®	Net-Base Software GmbH
QR-Code Studio 2.0	TEC-IT Datenverarbeitung GmbH, Steyr, Austria
R & R Studio	R Studio, Boston, USA
Vector NTI	Thermo Fisher, Bonn, Germany
ZEN	Carl Zeiss AG, Oberkochen, Germany

QR-Code Scan

To view the attached videos, open the QR Code reader/camera on your phone and hold it over the QR code. After scanning, you need to log in with name: review-lorenz and password: DK78_dvT.

3 METHODS

3.1 General methods working with DNA

3.1.1 Isolation of genomic DNA from mouse ear punches

Mouse ear punches were lysed overnight in 250 µl DNA lysis buffer containing 50 µg/ml proteinase K in a thermo shaker at 55°C. 250 µl of phenol/chloroform/isoamyl alcohol were added to the lysed solution. Upon vortexing and centrifugation for 10 min at 18,400 × g at room temperature, this results in phase separation of DNA fraction and protein fraction. After the centrifugation step, the upper aqueous phase containing the DNA was transferred into a new tube and DNA was precipitated by adding 500 µl (2.5 x volume of aqueous phase) of 100 % ethanol containing 75 mM NaCl. After centrifugation at 18,400 × g for 10 min at 4 °C, followed by a washing step with 200 µl 70 % ethanol, precipitated DNA was allowed to dry at room temperature (RT). DNA pellets were resuspended in 100 µl TE buffer and stored at -20 °C for long term storage. For re-genotyping of sacrificed mice, same protocol was used for tail clips.

Alternatively, genomic DNA can be extracted from ear punches or tail clips by a short lysis protocol. Small amount of mouse tissue was directly lysed in 100 µl 50 mM NaOH for 10 min at 95 °C. Samples were briefly centrifuged and were directly used for genotyping by genomic PCR.

DNA Lysis buffer: 10 mM Tris (pH 7.6), 10 mM EDTA, 0.5 % SDS, 10 mM NaCl
TE buffer: 10 mM Tris, 1 mM EDTA (pH 8)

3.1.2 Agarose gel electrophoresis

Agarose gel electrophoresis is a routine method for DNA separation according to its size. DNA fragments were separated in 0.9 %, 1 % or 2 % agarose gel, made of agarose in 1 x TAE buffer containing SYBR® Safe DNA stains in a ratio of 1:10,000. The gel running chamber contains 1 x TAE buffer and voltage was applied to enable the separation of the fragments. Before filling the DNA samples in the gel pockets, they were mixed with 6x DNA loading dye (Thermo Fisher). For visualization of the DNA fragments, the ChemiDoc™ UV transilluminator (BioRad) was used.

TAE buffer (10 ×): 200 mM Tris, 100 mM sodium acetate, 6 mM EDTA (pH 7.5)

3.1.3   DNA Fragments for mouse genotyping

To amplify specific DNA fragments and to discriminate between mice carrying targeted or wildtype (wt) alleles, the standard PCR technique was used. For each mouse strain, specific oligonucleotides were designed, resulting in small PCR products of different sizes allowing to distinguish the different genotypes. PCR reactions were set up in 25 µl containing 2 µl gDNA isolated from ear clips (see 3.1.1), 10 × PCR buffer, 1.5 mM MgCl2, 0.2 mM dNTP mix, 0.5 µM of the specific primers and recombinant Taq polymerase. PCR reactions were performed in a G-Storm thermo cycler or BioRad C1000 Touch Thermal Cycler. As different oligonucleotides require different annealing and elongation temperatures, the PCR programs with the corresponding mouse strains and primers are listed below. PCR products were separated and visualized on a 2 % agarose gel (see 3.1.2).

Hb9Cre: Primer: Cre D/Cre E; °C$_{Annealing}$: 63 °C, t$_{Elongation}$: 50 sec; PCR products: 500 bp

CamK2aCreERT2: Primer: CreER1 (sense)/ CreER2 (antisense)/CreER3 (antisense); °C$_{Annealing}$: 63°C, t$_{Elongation}$: 60sec; PCR products: wt 290 bp; CamK2aCreERT2 (transgene,tg) 375 bp

Gpx4 fl/fl: Primer: Gpx4_PF_for/Gpx4_PF_rev; °C$_{Annealing}$: 65 °C, t$_{Elongation}$: 50 sec; PCR products: wt 180 bp; floxed 240 bp

Gpx4 wt/cys: Primer: Gpx4_1/Gpx4_3; °C$_{Annealing}$: 60 °C, t$_{Elongation}$: 30 sec; PCR products: wt 256 bp; tg/floxed: 310 bp

Acsl4 fl/fl: Primer: Acsl4_flox_for/Acsl4_flox_rev; °C$_{Annealing}$: 61 °C, t$_{Elongation}$: 60 sec; PCR products: wt 225 bp; floxed: 363 bp

3.2 General methods working with protein

3.2.1   Protein purification from tissues

Freshly dissected mouse tissues were snap frozen in liquid nitrogen and stored at -80 °C until required. For protein extraction, tissue was transferred in 400- 1000 µl LCW lysis buffer, containing a protease and phosphatase inhibitor cocktail (both Roche) and homogenized using the Eurostar RW16 (IKALabortechnik). After incubation on ice for 30 min, cell debris was removed by centrifugation (18,400 × g, 4°C, 45 min). The supernatant was transferred to a new tube and protein quantification was performed by using the Pierce™ BCA Protein Assay Kit (Thermo Fisher) according to manufacturer`s instructions. 6 × loading dye was added to 20 µg of the protein samples in a 25 µl volume stored at -20 °C. Before applying the samples

to SDS-PAGE, the protein samples were boiled for 5 min 95°C or at 55°C for analyzing transmembrane proteins.

LCW Lysis Buffer: 0.5 % TritonX-100, 0.5 % sodium deoxycholate salt, 150 mM NaCl, 20 mM TRIS, 10 mM EDTA, 30 mM Na-Pyrophosphate, pH 7.5.

Sample Loading Dye (6x): 9 % SDS, 50 % glycerol, 0.03 % Bromophenol Blue, 9 % ß-Me, 375 mM Tris pH 6.8.

3.2.2   Sodium dodecyl sulfate polyacrylamide gel electrophoresis (SDS PAGE)

Protein samples were separated on precast 12 % Mini-PROTEAN® TGX Stain-Free™ Protein Gels (BioRad) at 80-100 V for ~1.5 h in a Mini-PROTEAN® Tetra (Bio-Rad) electrophoresis chamber filled with running buffer. Protein ladder (Prestained Protein Page Ruler) was used along with the protein samples to determine the size. For protein transfer, SDS gels were removed from their plastic scaffold and placed on a Trans-Blot® Turbo™ PVDF (polyvinylidene difluoride) membrane (Bio-Rad) for western blot analysis. The standard semi-dry transfer was performed at 25 V for 30 min using Trans-Blot® Turbo™ System (protocol: Standard SD, 30 min, 25 V, Bio-Rad).

Running buffer (10 ×): 250 mM Tris-HCl, 2.5 M glycine, 1 % SDS

3.2.3   Western Blot Analysis

The membrane was blocked with 5 % skim milk powder in TBST for 60 min at room temperature under constant motion. Membranes were cut depending on the desired size of protein. After blocking, appropriate diluted primary antibodies were applied according to the manufacturer`s protocol in blocking solution, incubating overnight 4 °C under constant rotating. On the next day, primary antibody was removed and membranes were washed 3 times for 5 min with TBST before incubation with a horseradish peroxidase (HRP)-conjugated secondary antibody for ~1.5 h diluted in the corresponding blocking solution. Membranes were washed again three times with TBST. For visualizing proteins, Clarity™ Western ECL Blotting Substrate (Bio-Rad) or for antibodies with faint signal Thermo Scientific™ Super Signal West Femto (Thermo Fisher) was applied on the membranes and visualized by ChemiDocTM Imaging system (Bio-Rad).

If necessary, antibodies can be stripped from the PVDF membrane with 0.5 M NaOH for 7 min at RT. After three washing steps and membrane blocking with blocking solution, a different primary antibody can be applied.

TBST: 25 mM TRIS, 125 mM NaCl, 0.1 % Tween-20, pH 7.6

Blocking buffer: TBST, 5 % skim milk

3.2.4   Proteomics analysis

All experiments regarding the proteomics analysis were performed by Dr. Ashok Kumar Jayavelu, Max Planck Institute of Biochemistry Munich. Data analysis were accomplished by Dr. Ashok Kumar Jayavelu and Dr. Dietrich Trümbach.

3.2.5   Label free proteome sample preparation

GPX4 conditional KO and WT mouse cortex was lysed in 1 % SDC buffer, incubated on ice for 20 min, boiled at 95 °C, sonicated for 10 min on a Biorupter plus and heated again for 5 min at 95 °C as describe previously [237]. Proteins in the cortex sample were digested with LysC (1:100 ratio) for 2 h followed by trypsin (1:100 ratio) for overnight at 37 °C. For the proteome, to the protease digested samples, 5 times the volume isopropanol/1 % TFA was added and vortexed to stop the digestion. The peptides were de-salted on equilibrated styrenedivinylbenzene-reversed phase sulfonated (SDB-RPS) StageTips, washed once in isopropanol/1 % TFA and twice with 0.2 % TFA. Purified peptides were eluted with 60 µl of elution buffer. The dried elutes were resuspended in MS loading buffer and stored at -20°C until MS measurement.

SDC buffer: 1 % SDC, 100 mM Tris pH 8.5, 40 mM CAA and 10 mM TCEP

Elution buffer: 80 % MeCN, 1.25 % NH_4OH

MS loading buffer: 3 % MeCN, 0.3 % TFA

3.2.6   Single shot LC-MS/MS measurements

A nanoflow HPLC (EASY-nLC1000, Thermo Fisher Scientific) coupled online to an Exploris 480-Orbitrap Mass Spectrometer (Thermo Fischer Scientific) via a nano electrospray ion source was utilized for the sample analysis. Approximately, for proteome measurements, 300 ng of peptides were loaded onto a 50-cm column with 75-µM diameter, packed in house with 1.9 µM C18 ReproSil particles (Dr. Maisch GmbH). The column temperature was maintained using a homemade column oven at 60 °C. The peptides were separated with the binary buffer system of 0.1 % formic acid (buffer A) and 60 % MeCN plus 0.1 % formic acid (buffer B), at a flow rate of 300 nl/min. Peptides were eluted on a duration of 120 min with a gradient of 30 % buffer B over 95 mins and increased to 60 % over for 5 min. This was followed by a quick ramp up to 95 % over 5 min and declined back to 5 % over 5 min to re-equilibrate the column. Mass

spectra was acquired in a data dependent mode. Briefly, with one full scan at a target of 3e6 ions (300-1650 m/z, R=60,000 at 200 m/z), followed by Top15 MS/MS scans with HCD (high energy collisional dissociation) (target 1e5 ions, maximum filling time 28 ms, Isolation window 1.4 *m/z*, and normalized collision energy 27), detected in the Orbitrap at a resolution of 15.000. Dynamic exclusion 30 s and charge inclusion (2-5) were enabled.

3.2.7 Data-dependent acquisition (DDA) of proteome samples

Peptides were eluted on a duration of 140 min with a gradient of 20 % buffer B over 85 min and increased to 40 % over for 35 min. This was followed by a quick ramp up to 65 % over 10 min, 80 % over 5 min, and declined back to 5 % over 5 min to re-equilibrate the column. The Exploris 480 was operated with a scan range set to 350-1450 *m/z* at a resolution of 120,000. The AGC was set to 3e6 at a maximum injection time of 54 ms. HCD (NCE 27 %) was used for precursor fragmentation and fragment ions were analyzed in 32 DIA windows at a resolution of 30,000, while the AGC was kept at 3e6.

3.2.8 DDA-MS data analysis and bioinformatics

MS raw files were processed using Maxquant [238] version 1.5.5.2 supported by Andromeda search engine. The data was searched for proteins and peptides using a target-decoy approach with a reverse database against Uniprot Human (version 2016) FASTA file with a false discovery rate of less than 1% at the levels of protein and peptide. No changes were made to the enabled default settings such as oxidized methionine (M), acetylation (protein N-term), and carbamidomethyl (C) as fixed modification and Trypsin as enzyme specificity. A maximum of 2 missed cleavages were allowed, and a minimum peptide length of seven amino acids set. The proteins were assigned to the same protein groups if two proteins could not be discriminated by unique peptides. The label-free quantification was performed using the MaxLFQ algorithm [239] and match between run feature was enabled for identification of peptide across runs based on mass accuracy and normalized retention times. For label free protein quantification, minimum ratio count was set to 2. The Maxquant output table was analyzed in Perseus [240], prior to the analysis contaminants marked as reverse hits, contaminants and only identified by site-modification were filtered out.

3.2.9 Heat map

One way ANOVA was applied to normalized log2 transformed intensities of proteins from single shot LC-MS/MS measurements of Gpx4 KO and WT mice samples (cortex) from one,

two and four weeks after KO induction containing four replicates for each condition. ANOVA was performed by using the lm function in R statistical software (www.r-project.org), version 4.0.5. Subsequently, calculation of the false discovery rate (FDR) according to Benjamini and Hochberg with the R function p.adjust was applied [241]. Significantly changed protein levels over all experimental conditions (P adjusted < 0.05) were represented by a heat map. For the generation of the heat map we used the heat map function within the ComplexHeatmap package in R. Protein levels (rows) were scaled and centered before with the scale function in R and k-means clustering was set on rows (km = 2 within the Heatmap function). Agglomerative hierarchical clustering by the hclust function (method = "ward.D2") was applied to group experimental conditions (columns) as well as to each row slice of protein intensities (rows) for the heat map. A dendrogram is shown for columns as well as rows, whereby the column dendrogram was reordered. To assign protein levels to biological functions an enrichment analysis of significantly changed proteins with help of the GeneRanker program (Genomatix, Germany) was done separately. Protein levels which are annotated to significantly enriched categories of Gene Ontology biological process and Disease (Genomatix Literature Mining and Medical Subject Headings, i.e. MeSH terms) were highlighted next to the row dendrogram/heat map by lines in different grey colors.

3.2.10 Principal component analysis

Based on the protein levels of significantly regulated proteins according to the one way ANOVA of Gpx4 KO and WT cortex samples (P adjusted < 0.05) a principal component analysis (PCA) was performed by usage of the FactoMineR package in R. For the PCA the data were scaled to unit variance.

3.2.11 Enrichment analysis

UniProtKB identifier of significantly changed proteins from the one way ANOVA of Gpx4 KO and WT cortex samples (P adjusted < 0.05) were converted into NCBI gene identifier by using BioMart (GRCm39) [235] Gene IDs were used as input for the GeneRanker program (Genomatix, Germany) that is based on the ElDorado 04-2021 and Genomatix Literature Mining 01-2021 database.[242] Distribution of P values, which were calculated according to Fisher's Exact test, of the top significantly enriched terms from the category MeSH Disease were represented by R using the barplot function. In the output of the GeneRanker program also the adjusted P value is given which is estimated by the determination of the false positive

rate from 1,000 randomly selected genes according to Berriz *et al.* [236]. Column headings of Supplementary Tables 2, 3 and 4 (Appendix): "GO-Term", "Disease" or "Mesh-Term" denotes annotation term; "GO-Term id", "Disease id" or "Mesh-Term id" is a unique identifier; "P-value" (based on Fisher´s Exact Test) is the probability of overrepresentation calculated for each annotation term; "adjusted P-value" is estimated by the determination of the false positive rate from 1,000 randomly selected genes [236];"# Genes (observed)" number of genes from the input set expected to have a given annotation; "#Genes (expected)" number of genes expected to have a given annotation; "#Genes (total)" are number of genes from entire genome with a given annotation; "List of observed genes" summarizes gene symbols from the input set with assigned annotation; "Gene ids" list the corresponding Entrez gene identifiers from the input set ("List of observed genes").

3.2.12 Vulcano plot

Unpaired two-sided t-test assuming unequal variance were performed on log2 transformed protein intensities of Gpx4 KO versus WT samples (cortex) from one, two and four weeks after KO induction, respectively, by using the t-test function in R with the parameter alternative = "two.sided" and var.equal = "FALSE". Multiple testing correction was applied with the p.adjust function in R to adjust individual *P* value of each protein by the Benjamini and Hochberg method [241]. Volcano plots were generated with help of the EnhancedVolcano package in R by plotting –log10(adjusted *P*) versus log2(fold change) on the y and x axis, respectively.

3.3 General methods working with lipids

3.3.1 Lipid extraction from tissue

Lipids from brain samples were extracted using biphasic, chloroform/methanol methods, according to Folch *et al.* [243]). To avoid oxidation, all solvents were treated with 0.1 w/v BHT and cooled on ice during use. 10 µl SPLASH® Lipidomix mass spec standard (Avanti Polar Lipids) and 15 µl Ceramide/Sphingoid Internal Standard Mixture II (Avanti Polar Lipids) per 50 mg tissue were mixed as standard. For quality control, triplicates of one tissue were used. 1 ml ice-cold methanol was added to lysis matrix tubes, before frozen samples were transferred and spiked with 12.5 µl of standard mixture. Then, samples were homogenized by cryomilling in 4 intervals of 1.5 min at 30/s frequency. For extracting lipids, samples were transferred in 10 ml glass tube, lysis beads were first washed with 400 µl methanol then with 1000 µl chloroform. Additional 1.8 ml chloroform were added before vortexing for 2 min at 2500 rpm.

Sample mixtures were incubated for 1 h at 4 °C under rotation (32 rpm). Phase separation was induced by adding 840 µl water. Samples were mixed by vortexing and incubated for 10 min 4 °C under rotation, before centrifugation (10 min, 1000 × g, 4°C). The upper phase contains non-lipidic material; the lower, organic phase containing lipids was collected to new glass vial. For re-extraction, 2.8 ml chloroform were added, mixed by vortexing and incubated (1 h, 4 °C, and 32 rpm), as described above. The organic phases, combined from both extractions, were dried in a vacuum evaporator (~ 1 h, 100-150 mbar, max. 12 % speed). For reconstitution of lipids, 250 µl isopropanol were added, samples were vortexed for 30 s and transferred to a new tube. After drying samples in a vacuum evaporator (~ 45 min, 80-100 mbar, max 12% speed), samples were stored in -80°C until further analysis.

3.3.2 Liquid chromatography

All experiments regarding the lipidomics analysis were performed by Dr. Maria Fedorova, TU Leipzig/TU Dresden. Data analysis were accomplished by Dr. Maria Fedorova, Palina Nepochelovich, Dr. Dietrich Trümbach and Dr. Maceler Aldrovandi.

Reversed-phase ultra-high-performance liquid chromatography (RP-uHPLC) was carried out on a Vanquish Horizon (Thermo Fisher Scientific, Germering, Germany) equipped with an Accucore C18 column (150 x 2.1 mm: 2.6 µm, 150 Å, Thermo Fisher Scientific, Sunnyvale, CA, USA). Lipids were separated by gradient elution with solvent A (MeCN/H_2O, 1:1, v/v) and B (*i*- PrOH/MeCN/H_2O, 85:10:5, v/v/v) both containing 5 mM $HCOONH_4$ and 0.1% (v/v) formic acid. The separation was performed at 50°C with a flow rate of 0.3 ml/min using the following gradient: 0-20 min – 10 to 86 % B, 20-22 min – 86 to 95 % B, 22-26 min –95 % B (isocratic), 26-26.1 min – 95 to 10 % B, 26.1-34.0 min – 10 % B (isocratic, column re-equilibration).

Solvent A: MeCN/H_2O, 1:1, v/v, 5 mM $HCOONH_4$ and 0.1% (v/v) formic acid

Solvent B: *i*-PrOH/MeCN/H_2O, 85:10:5, v/v/v, 5 mM $HCOONH_4$ and 0.1% (v/v) formic acid

3.3.3 Mass spectrometry

RP-uHPLC was coupled on-line to a Thermo Scientific Q Exactive Plus Quadrupole-Orbitrap mass spectrometer (Thermo Fisher Scientific, Bremen, Germany) equipped with a heated electrospray (HESI) source with the following parameters: sheath gas – 40 arbitrary units, auxiliary gas – 10 arbitrary units, sweep gas – 1 arbitrary unit, spray voltage – +3.5 kV and -2.5

kV, capillary temperature – 300 °C, S-lens RF level – 35 %, and aux gas heater temperature – 370 °C.

3.3.4 Data-dependent acquisition method for lipidomics

Full MS spectra were acquired at the resolution 140,000 at m/z 200, scan range 200 – 1000 m/z (negative ion mode, 0-18 min) and 380 – 1200 m/z (positive ion mode, 18-34 min), automatic gain control (AGC) target 10^6 counts, maximum injection time (max IT) 100 ms. Each sample was measured twice – once in positive and once in negative modes. MS/MS events were triggered for top 10 most abundant precursor ions at each RT point.

Data dependent MS/MS were acquired with resolution settings of 17500 at 200 m/z, AGC target 10^5 counts, maximum IT 60 ms, loop count 15, isolation window 1.2 m/z and stepped normalized collision energies of 10, 20 and 30 %. A data dependent MS/MS was triggered when an AGC target of $2 \cdot 10^2$ was reached followed by a dynamic exclusion for 10 s. All isotopes and charge states > 1 were excluded. All data was acquired in profile mode.

3.3.5 Identification and quantification of lipids

For identification and relative quantification of unmodified lipidome, raw files were imported into Lipostar v.1.3.3 (Molecular Discovery LTD) [244]. Automatic peak picking was performed with built in peak alignment and peak integration algorithm. Lipid identification was done on the averaged MS/MS spectra using LIPID MAPS LMSD database (version 20210212, https://www.lipidmaps.org/data/structure/) together with default identification rules integrated by Lipostar.

The identification results were first filtered using the automatic filter to keep only high confidence annotations (3 stars and 4 stars hits only), and further manually reviewed to keep only the best assignment of each feature. During manual revision, peak integrations were also checked and manually corrected, multiple shoulder peaks which belongs to the same lipid at molecular species level were merged into one feature.

The manually reviewed feature matrix were then normalized using a calculated normalization factor. This normalization factor (NF_i) was calculated using peak areas of internal standard PC(15:0/18:1)(d7) across the samples as the reference compound. The peak areas were extracted using Skyline v. 20.2.0.343 (MacCoss Lab) [245] from the same set of spectra with manual correction of the peak boundaries.

The normalization factor of each sample NFi was calculated using equation (1):

$$NF_i = \frac{\overline{PeakArea}}{PeakArea_i} \times \frac{\overline{SampleAmount}}{SampleAmount_i} \qquad (1)$$

where $PeakArea_i$ is the area under the curve (AUC) for PC(15:0/18:1)(d7) in each i (i =1…36) sample, $\overline{PeakArea}$ is the average AUC for PC(15:0/18:1)(d7) identified across the samples, $SampleAmount_i$ is the amount of i (i =1…36) sample aliquot (mg for cortex tissues), and $\overline{SampleAmount}$ is the average amount of sample aliquote within the set.

The NF_i was then imported into Lipostar as the metadata information and using the normalization function within Lipostar for area normalization with formula option that utilized the peak area of internal standards and sample amount. The basic principle of normalization is to use equation (2) to normalize raw peak areas A^{raw} to normalized peak area A^{norm}:

$$A_i^{norm} = \frac{A_i^{raw}}{NF_i} \qquad (2)$$

where A_i^{norm} is the normalized AUC for a given lipid in sample i (i =1…36), and A_i^{raw} the raw AUC for a given lipid in sample i (i =1…36).

The normalized data matrix in both positive and negative mode were exported as CSV table. An in-house Python script was used for automatic matching and overwrite the assignment of PL in positive mode by corresponding negative mode assignment that have same neutral elemental composition and eluted in the RT windows within +/- 10 seconds. For PLs identified in the negative mode only, the final AUC used for further analysis was calculated by multiplying A_i^{norm} identified in the negative mode by an amplification factor f_{amp} calculated by formula (3):

$$f_{amp} = \frac{\overline{PeakArea_{positive}}}{\overline{PeakArea_{negative}}}, \qquad (3)$$

where $\overline{PeakArea_{positive}}$ is the average AUC identified in the positive mode, and $\overline{PeakArea_{negative}}$ is the average AUC identified in the negative mode calculated for lipids identified in both modes. f_{amp} are calculated for blood plasma, cerebellum and cortex sample sets separately.

Then the amplified peak area of the PLs identified only in negative were used for further statistical analysis with PLs identified in positive mode and both modes. Lipid annotations

were also converted from structure defined level to molecular species level for PLs and to bulk level for GLs. The final matrix was manually reviewed, and the feature labels were updated before export into csv table before submitting to MetaboAnalyst v. 5.0 (https://www.metaboanalyst.ca/, Xia Lab) [246] for statistical analysis.

3.3.6   Data analysis and visualization

Normalized peak areas from lipidomics and epilipidomics datasets were median-centered and log-transformed in MetaboAnalyst v.5 (https://www.metaboanalyst.ca, Xia Lab) [246]. A univariate statistical analysis was employed for each pair of conditions (KO vs WT) of week 1, week 2, and week 4 separately. Data processed by MetaboAnalyst were exported as CSV files and used in other software for visualization.

Lipids with statistically significant difference in KO/WT were selected for creating in heat maps. The latter were created in Genesis v. 1.8.1 (Bioinformatics TU-Graz) [247], where the features were auto-scaled. Samples were clustered by average linkage WPGMA agglomeration rule. Other graphs were also created in OriginPro 2019 unless otherwise stated. PCA was created in MetaboAnalyst R.

3.4 Cell culturing

3.4.1   Geltrex™ Coating

For Geltrex™ coating, dishes were coated at least 1 h at 37 °C with Geltrex™ solution, diluted 1:100 in DMEM/F12. Coating solution was aspirated and dishes were directly used for culture of cells.

3.4.2   Cryoconservation and thawing of cells

Cryo-conserved cell stocks, for long-term storage in liquid nitrogen, could be prepared when cells reached roughly 80 % confluency. After trypsinizing, the cells were harvested by centrifugation at 400 x g for 5 min at RT. hiPSCs and NPCs were frozen either as cell clumps or as single cells in Cryostor® cell cryo preservation media CS10. After dissociation to clumps or single cells as described above at a confluence of 80 %, cells were resuspended in freezing medium (3 ml per 6 cm dish) and transferred as 1 ml aliquots to cryo vials. Subsequently, cryo vials were transferred to freezing container, before they were stored in liquid nitrogen.

For thawing, cells cryo-vials were placed in a waterbath at 37°C. After being defrosted, the cell suspension was immediately transferred into a tube, containing 10 ml of pre-warmed standard DMEM/F12 to remove residual DMSO or StemFlex for hiPS. After centrifugation (200 × g for 5 min at RT, or 200 × g for 3 min at RT, for hiPS), cells pellets were resuspended in StemFlex with the addition of 10 µM Rock inhibitor (Y-27632), and seeded onto appropriate Geltrex™ coated cell culture plates.

3.4.3   Determination of cell numbers (Neubauer chamber)

Cell numbers can be determined via the Neubauer chamber cell. To this end, cells were split as single cells and diluted in 10 ml of StemFlex or in the appropriate medium. 10 µl of the cell suspension was used to determine cell number using the Neubauer chamber. Alternatively, TC20™ (Bio-Rad) automated cell counter was used.

3.4.4   Culture of hiPSCs

hiPSCs were cultured on Geltrex™ coated plates in StemFlex medium at 37 °C with 5 % CO_2. Medium change was done daily and cells were split on a regular basis every 3 to 4 days at a confluence of 80 %. For splitting in cell clumps, hiPS were washed once with DPBS and incubated with 0.5 mM EDTA (2 ml per 6 cm dish) for 5 min at RT. Cells were detached by tapping the cell culture dish and collected in a 15 ml tube containing 4 ml StemFlex. After cell clumps were allowed to settle down, medium was aspired and cell clumps were gently resuspended in fresh medium and splitted in a ratio of 1:4 to 1:8 on Geltrex™ coated dishes. For splitting single cells, hIPS were washed once with DPBS and incubated with Accutase (2 ml per 6 cm dish) for 10 min at 37 °C. By pipetting, cells were dissociated and transferred to a 15 ml tube containing 4 ml StemFlex, before centrifugation at 200 x g for 5 min at RT. Cell pellet were resuspended in fresh medium supplemented with 10 µM Rock inhibitor (Y-27632) and seeded on coated plates.

3.4.5   Differentiation of hiPSCs to motor neurons

hiPSCs are differentiated to MNs via motor neuron progenitors (MNP) using a combination of small molecules adapted from Du *et al.* [248]. A schematic protocol for the differentiation is given in Figure 6. Geltrex™-coated plates were used to seed hiPSC in StemFlex+ 10 µM Y27632 at a density of 7 x 10^4 cells/cm^2. Neuronal induction is started by changing to neural induction medium (day 0 of differentiation). Neuronal induction medium is a 1:1 mixture of N2 media and B-27 media supplemented with 3 µM CHIR99021, 2 µM DMH- 1 and 2 µM SB431542 to

maintain cell proliferation. It was changed every day over a period of 6 days. On day 7 of differentiation, cells were expanded 1:6 as single cells and medium was changed to MNP specification medium plus, containing 5 supplements: 0.1 µM retinoic acid (RA), 1 µM CHIR99021, 2 µM DMH-1, 2 µM SB431542 and 0.5 µM purmorphamine. After another 6 days of incubation, MNP were frozen in Cryostor® cell cryopreservation media CS10 or plated as single cells supplemented with 0.5 mM valproic acid for expansion. To induce MN differentiation, cells were cultured for day 14-19 in MN specification medium (i.e., 1:1 mixture of N2 media and B-27 media supplemented with 0.5 µM RA and 0.1 µM purmorphamine). The medium was changed every other day. Starting from day 20 of differentiation onwards, the medium was replaced with MN maturation medium containing following neurotrophic supplements: 0.1 µM DAPT, 10 ng/ml IGF-1, 10 ng/ml BDNF and 10 ng/ml CTNF.

Every medium is supplemented with B27 as it is an optimized serum-free supplement for neuronal cell culture. In regard to cell viability assays and the characterization of motor neurons susceptibility to ferroptosis, B27 was replaced by B27-AO on day 14 of differentiation.

N2-medium: DMEM/F12, 1x N2, 5 µg/ml Insulin, 1x GlutaMaxx, 100 µM non-essential amino acid (NEAA), 100 µM 2-mercaptoethanol, 500 U/ml penicillin, 50 µg/ml streptomycin

B27 medium: Neuobasal, 1x B27, 1x GlutaMaxx, 500 U/ml penicillin, 50 µg/ml streptomycin

MNP specification medium (Day 0-6): 50 % N2-medium, 50 % B27 medium, 1 µM CHIR99021, 2 µM DMH-1, 2 µM SB431542

MNP specification medium plus (Day 7-12): 50 % N2-medium, 50 % B27 medium, 0.1 µM retinoic acid (RA), 1 µM CHIR99021, 2 µM DMH-1, 2 µM SB431542, 0.5 µM purmorphamine

MNP specification medium expansion (Day 13): 50 % N2-medium, 50 % B27 medium, 0.1 µM RA, 1 µM CHIR99021, 2 µM DMH-1, 2 µM SB431542, 0.5 µM purmorphamine, 0.5 mM valproic acid

MN differentiation medium (Day 14-19): 50 % N2-medium, 50 % B27 medium, 0.5 µM RA and 0.1 µM purmorphamine

MN maturation medium (Day 20-29): 50 % N2-medium, 50 % B27 medium/50 % B27-AO, 0.5 µM RA and 0.1 µM purmorphamine, 0.1 µM DAPT, 10 ng/ml IGF-1, 10 ng/ml BDNF and 10 ng/ml CTNF
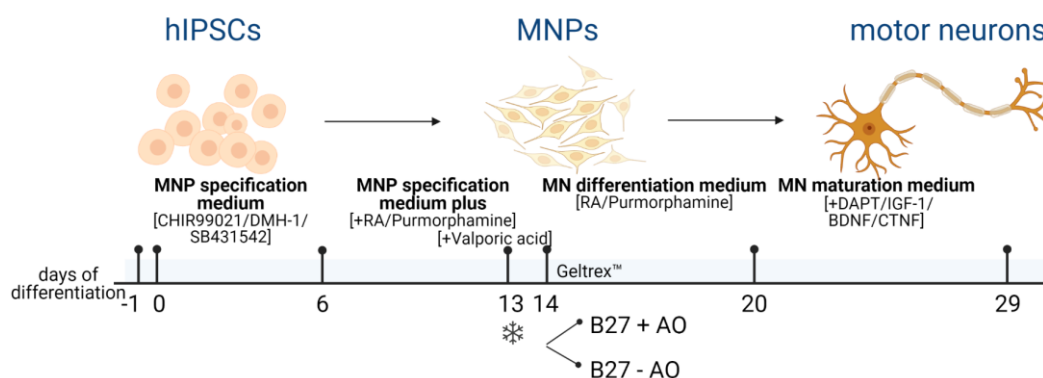
Figure 6| Outline of the differentiation of hiPSCS to motor neurons via MNPs

3.4.6 Cell viability assay

The redox indicator AquaBluer™ can be used as a quick proxy for the viability of cells. 20.000 cells/well for hiPS derived MN were seeded on 96-well plates one day prior to treatment with a usually 7-point dilution of the compound to be tested. In this thesis, several compounds were used: *(1S,3R)*-RSL3, erastin, L-buthionine sulfoximine (BSO), staurosporine, edaravone, hydrogen peroxide (H_2O_2), cumine, tert-butylhydroperoxide (tBOOH), liproxstatins (Lip-1, Lip-3) and iFSP1. After an incubation time of 24-72 h, AquaBluer™ (1:100) (MultiTarget Pharmaceuticals, LLC) was added to each well according to manufacturer's instruction. Viable cells reduce the oxidized form of AquaBluer™, which can be measured by a change in fluorescence at 540ex/590em using a SpectraMax microplate reader (Molecular Device GmbH).

To record the cell death process over time, differentiated MNs cells were plated on Geltrex™-coated 35mm μ-ibidi dish and treated with 10 nM RSL3. Live cell imaging was performed using 3D Cell Explorer Nanolive microscope (Grid Scan: 3x3, 180 cycle, 1 cycle: 4 min 20 s, RI only). Nanolive's technology is based on the 3D refractive index distribution of cells, resulting in long-term imaging.

3.5 Histopathological methods

3.5.1 Staining of cells by immunocytochemistry

Adherent cells were fixed in 4 % PFA in PBS for 10 min at RT, followed by three washing steps with PBS. Fixed cells were blocked and permeabilized with 1 % BSA and 0.3 % Triton X-100 in PBS for 10 min at RT, before adding the primary antibody (AB), diluted in 1 % BSA and 0.1 % Triton X-100 in PBS, for an overnight incubation at 4 °C. On the following day, cells were washed three times with PBS and incubated in the dark with the respective fluorophore-

conjugated secondary antibodies diluted in 1 % BSA, 0.1 % Triton X-100 in PBS for 1 h at RT. After a 10 min counterstain with 4'-6-diamidino-2-phenylinodole (DAPI) (1:1,000 diluted in PBS), followed by three washing steps with PBS, stained cells were stored in PBS (with 0.002 % sodium acid for long term storage) at 4 °C, protected from light. Immunofluorescence staining was analyzed by fluorescence microscopy on an EVOS FL Cell Imaging System (Thermo Fisher Scientific) or on Nikon Eclipse microscope using the corresponding wavelength of used antibodies.

3.5.2 Cryosections

Freshly dissected tissue, like brain and spinal cord, were fixed overnight in 4% PFA, followed by an overnight incubation in 20 % sucrose in PBS to maintain cellular structures and prevent ice crystal formation. For embedding, tissue was placed into disposable vinyl specimen molds filled with Tissue Tek® medium or for spinal cord into silicone molds and placed on dry ice until Tissue Tek® medium was completely frozen. Embedded tissue was stored at -80 °C. Brain tissues were cut in 40 µm free-floating sections. Brain samples were cut in 12 series using cryostat (CM3050S Cryostat, Leica) and stored in cryo protection solution at -20 °C. Spinal cord samples were cut in 20 µm thick sections and store at -80 °C until further proceed.

Cryo protection solution: 50 % PBS, 25 % glycerol, 25 % ethylene glycol

3.5.3 Immunohistochemistry of cryosections

3.5.3.1 Free-floating sections

Free-floating immunohistochemistry can be used for thick slides, because it allows double-sided penetration of antibodies. Brain slices were stored in cell strainer in 6-well plate to reduce tissue handling. After storage in cryo protection solution, slides were washed in PBS overnight, before incubated in blocking solution for 1.5 h. Primary antibodies (see 2.5) were diluted according to manufacturer's instruction in blocking solution, and slides were incubated overnight at 4 °C with primary antibody. Following day, slides were washed three times for 10 min with PBS and incubated for 1.5 h with secondary antibody, diluted in blocking solution, at RT protected from light. After three more washing steps with PBS for 10 min, 1 x DAPI in PBS staining for 3-5 min was performed. Slides were washed again (3 x 10 min, PBS) and mounted on superfrost plus slides using Aqua-Poly/Mount. After drying, slides were store at 4 °C, protected from light.

Blocking solution: PBS, 5 % goat serum, 0.3 % Triton X-100

3.5.3.2 Slide-mounted sections

For antibody-based staining, slide-mounted cryosections stored at -80 °C were thawed for 15 min at RT, fixed in 1 % PFA for 10 min, washed twice with PBS (5 min) and post-fixed in 100 % ethanol containing acetic acid (2:1) for 5 min at -20°C. After two washing steps (2 x 5min, PBS), slides were incubated with blocking solution for 1 h at RT. Primary antibody solution was diluted according to manufacturer's instruction and added onto the slides for overnight incubation at 4 °C. On the next day, slides were washed three times with PBS (5 min) and incubated with the corresponding fluorophore-conjugated secondary antibody (1.5 h, RT, protected from light). DAPI staining was performed as described above and slides were mounted using Aqua-Poly/Mount.

Antibody staining was visualized using Nikon Eclipse microscope or confocal microscope LSM880 (Zeiss) using the laser 405 nm, 488 nm and 595 nm.

Blocking solution: PBS, 1 % BSA, 0.3 % Triton X-100

Nissl staining

Nissl staining is widely used to assess overall morphology of brain tissue. Slide-mounted sections were thawed for 15 min at RT, before stained for 1 min in cresyl violet solution, followed by washing in dH$_2$O for 2 min. Then, slides were incubated in increasing concentrations of ethanol for 2 min each (70 %, 70 %, 96 %, 96 %, 100 %, 100 %) and finally in xylol for 5 min, before mounting the slide with Rothi-Histo-Kit.

Cresylviolet solution: 2.5 g cresyl violet, 0.102 g Na-acetate in 500 ml dH$_2$O, adjust pH to 3.5 with acetic acid, filtered through 22 µm filter

Terminal Deoxynucleotideyl transferase dUTP Nick End labeling (TUNEL) staining

For the detection of dead cells, TUNEL staining was performed using ApopTag® Fluorescein in situ Apoptosis Detection Kit (Millipore). As pretreatment, cryosections were immersed in preheated PBST and incubate at 85 °C for 20 min, followed by three washing steps with PBS. Cryosections were incubated with equilibration buffer, working Strength TdT enzyme, Stop/Wash Buffer and Anti-Digoxigenin Conjugate according to manufacturer`s instructions. Counterstaining of nuclei was performed with 1x DAPI for 3-5 min as described before and slides were mounted using Aqua-Poly/Mount.

3.6 Animal Husbandry and analysis

3.6.1   Animal facility

All mice were kept under SPF-IVC standard conditions with food (#1314 Altromin) and water *ab libitum* in the animal facility of the Helmholtz Zentrum München. Mice were bred and maintained in a controlled environment (22 ± 2 °C, 55 ± 5 % humidity, 12 h light/dark cycle) with a group size of 2-5 animals per cage, supplied with nesting material and enrichment, like wood pieces and housing. All animal experiments were performed in compliance with the German Animal Welfare Law and have been approved by the institutional committee on animal experimentation and the government of Upper Bavaria (AZ 02-14-205, AZ 02-20-51, AZ 02-18-13). Offspring was weaned from the mothers around 3 weeks after birth and marked by ear punch for identification and subsequent DNA extraction for genotyping.

3.6.2   Cross-breeding of *Gpx4^{fl/fl}* mice with different Cre-expressing strains

3.6.2.1   *Gpx4^{fl/fl; Camk2aCreERT2}*

For the specific deletion of *Gpx4* in glutamatergic neurons, *Gpx4^{fl/fl}* mice (*Gpx4^{tm2Marc}*, previously described in detail [6]) were cross-bred with a tamoxifen (TAM)-inducible Cre line *Camk2a-CreERT2_TG* mice (Dr. Günther Schütz, German Cancer Research Center, Heidelberg, Germany [232]). Due to the expression of the Cre recombinase in sperm cells, only Cre recombinase positive females were mated with Cre negative males.

By cross-breeding of *Gpx4^{fl/fl;Camk2aCreERT2}* with conditional *Acsl4^{fl/fl}* mice [28], an inducible double KO mouse line for *Gpx4* and *Acsl4* in glutamatergic neurons was generated. To investigate the Cys-variant of GPX4, *Gpx4^{cys/wt}* (Gpx4U46C, previously described in detail [44]) was used to breed with *Gpx4^{fl/fl;Camk2aCreERT2mice}*, yielding *Gpx4^{cys/fl:Camk2aCreERT2}*mice.

To induce the deletion of *Gpx4* allele in adult mice, TAM application was performed (see 3.6.3).

3.6.2.2   *Gpx4^{fl/fl;Hb9Cre}*

The generation of conditional motor-neuron specific KO mice results from cross-breeding of *Gpx4^{fl/fl}* mice (*Gpx4^{tm2Marc}*, previously described in detail [6]) with *Hb9Cre* mice (B6.129S1-Mnx1tm4(cre)Tmj/J). Akin to *Gpx4^{fl/fl;Camk2aCreERT2}* mice, double KO of ACSL4 and GPX4, as well as the Cys-variant *Gpx4^{cys/wt}* were cross-bred to investigate whether additional deletion of ACSL4 or the Cys variant of GPX4 rescues the phenotype induced by GPX4 loss. GPX4 KO mice

are viable at birth and indistinguishable from wildtype littermates, therefore, KO mice were identified by genotyping and grouped in KO and WT cohorts.

3.6.3 Tamoxifen (TAM)-inducible gene KO

GPX4 conditional KO mice carry loxP sites flanking the last three exons of *Gpx4*, allowing induction of the KO via TAM application. Adult mice, around 10-12 weeks of age expressing *Camk2aCreERT2_TG*$^{+/-}$, were injected three times (on day 0; 2; 4) intraperitoneally (i.p) with 2 mg TAM dissolved in miglyol (100 µl of 20 mg/ml). The control group consists of either *Gpx4*$^{fl/fl;Camk2aCreERT2}$ mice injected with miglyol or *Gpx4*$^{fl/fl}$ mice injected with TAM in the same manner. 5 mg/kg meloxicam for 6 days were administered *p.o* for general anesthesia after injection.

3.6.4 *In vivo* treatment of GPX4 KO mice with liproxstatins

To generate animals for the pharmacological inhibitor experiments, mating of male *Gpx4*$^{fl/fl}$ mice with female *Gpx4*$^{fl/fl;Camk2aCreERT2}$ mice were performed. All cohorts contain equal number of females/males (n>3) of the same age between 10-12 weeks. For the pharmacological in vivo studies, liproxstatin-1 (dissolved in PEG400/Solutol/PBS) was administrated daily i.p alongside with TAM on days 0, 2 and 4. Liproxstatin or vehicle injection starts two days prior TAM for a total duration of 12 days.

Non-inducible, MN-specific GPX4 KO mice were treated with 3rd generation liproxstatin p.o. via the diet. Mice were kept on 2 mg/kg BW liproxstatin, directly after weaning, starting from 4 weeks of age. Concentration of liproxstatin was calculated for average mouse with 30 g BW and 4.5 g food intake per day. Mice were analyzed at 4 months of age.

3.6.5 Sample collection

Cohorts were grouped for analysis at different time points after KO induction or for specific age, with a comparable distribution of females/males. Animals were anesthetized to collect blood by retrobulbar bleeding as a final blood withdrawal in plasma tubes (0.5 ml 9NC, Sarstedt). After centrifugation (2500 × g, 15 min, RT), plasma samples were stored at -80 °C until further analysis. Thereafter, animals were perfused with PBS or AntiOx buffer, containing diethylenetriaminepentaacetic acid (DTPA), butylated hydroxytoluene (BHT) and trisodium citrate before freshly dissected tissue was frozen in liquid nitrogen and stored at -80°C until use.

AntiOx buffer: 500 ml DPBS (Gibco©, prewarmed 37°C), 5 ml 10 mM DTPA, 100 µl 500 mM BHT, 19 g trisodium citrate

3.6.6   3D MRI Scan

Three-dimensional magnetic resonance imaging (3D MRI) of brains from $Gpx4^{fl/fl; Camk2aCreERT2}$ mice after KO induction was performed using a Bruker BioSpin multi-purpose MR scanner (FLASH-3D technology, 9.4 Tesla magnet) in collaboration with Dr. Gil Westmeyer, IDG.

3.6.7   Gait and behavior analysis: $Gpx4^{fl/fl;Camk2aCreERT2}$

3.6.7.1 $Gpx4^{fl/fl;Camk2aCreERT2}$: Open field

The Open Field (OF) was assessed at 2 weeks after TAM injection and carried out as described previously [249]. The arena was made of transparent and infrared light-permeable acrylic with a smooth floor (internal measurements: 45.5 x 45.5 x 39.5 cm). Illumination levels for the measurement were set at approx. 150 lux in the corners and 200 lux in the middle of the test arena. Data were recorded and analyzed using the ActiMot system (TSE, Germany) over a 20-minute period.

3.6.7.2 $Gpx4^{fl/fl;Camk2aCreERT2}$: Rotarod

The rotarod (Bioseb, Chaville, France) for measuring motor coordination and balance is equipped with a computer-controlled motor-driven rotating rod. The unit consists of a rotating spindle and five individual lanes for each mouse. The mice were placed perpendicular to the axis of rotation at an accelerating speed from 4 to 40 rpm for 300 sec with 15 min between each trial. Mice were given three trials at the accelerating speed at one day. The mean latency to fall off the Rotarod during the trials was recorded and used in subsequent analysis. In addition, the reason for the trial end (falling, jumping or rotating passively) was recorded.

3.6.7.3 $Gpx4^{fl/fl;Camk2aCreERT2}$: Y-maze

This test evaluates spatial working memory and was performed as previously described [250-252]. In brief, the Y-maze test apparatus consists of three identical arms (30 x 5 x 15 cm) placed at a 120° angle from each other, made of opaque light grey PVC. To assess spontaneous alternation, defined as consecutive entries into all three maze arms, mice are placed

individually at the end of one arm and allowed to freely explore the Y-Maze for 5 min. Arm entries are monitored by a trained observer. The ratio of actual to possible arm alternations (total number of triplets) multiplied by 100 is calculated as % spontaneous alternations (SPAs), and a ratio of alternate arm returns (AARs) and same arm returns (SARs) is calculated likewise.

3.6.7.4 *Gpx4$^{fl/fl;Camk2aCreERT2}$*: Balance beam

Mice were trained to traverse a one meter long round wooden beam. After a training period, animals were placed on the beam for three testing trials. The time needed to traverse the beam, the number of foot slips (both front and hind paw slips), and number of falls from the beam were measured [253].

3.6.7.5 *Gpx4$^{fl/fl;Camk2aCreERT2}$*: Hanging wire

Mice were placed with front paws on a bar (clothes hanger) 26 cm above surface for a maximal duration of 1 min. The time to fall is recorded giving hints for motor function of mice.

3.6.7.6 *Gpx4$^{fl/fl;Camk2aCreERT2}$*: Catalepsy

To test muscle rigidity and catalepsy, fore limbs are placed on a wooden bar (0.7 cm in diameter) elevated 4.5 cm above surface as externally imposed posture. Time to correct this position were measured (max time: 3 min).

3.7 Gait and behavior analysis by German Mouse Clinic (GMC)

German mouse clinic (GMC) established large scale standardized and comprehensive phenotypic analysis of mouse mutants. Mice were maintained in IVC cages with water and standard mouse chow according to the directive 2010/63/EU, German laws and GMC housing conditions (www.mouseclinic.de). All tests were approved by the responsible authority of the district government of Upper Bavaria.

3.7.1 Gait and behavior analysis: *Gpx4$^{fl/fl;Hb9Cre}$*

Gpx4$^{fl/fl;Hb9Cre}$ cohorts were bred, genotyped and transferred to animal facility of GMC. In total, 58 knockout mice (15 males, 14 females) and wild-type control littermates (14 males, 15 females) underwent a specialized phenotyping screen by the German Mouse Clinic at the Helmholtz Zentrum München (http://www.mouseclinic.de) as previously described [249, 254-256]. This screen started at the age of 17 weeks and covered multiple parameters in the areas

of behavior, neurology, nociception, eye analysis and vision, hematology and Clinical Chemistry as well as transcriptome analysis. As the final test, SHIRPA, rotarod and grip strength analysis, were performed at 52 weeks of age to observe the progression of motoric phenotype.

If not stated otherwise, data that was generated by the German Mouse Clinic was analyzed using R (Version 3.2.3). Tests for genotype effects were made by using t-test, Wilcoxon rank sum test, linear models, or ANOVA and posthoc tests, or Fisher's exact test depending on the assumed distribution of the parameter and the questions addressed to the data. A p-value < 0.05 has been used as level of significance; a correction for multiple testing has not been performed.

3.7.1.1 *Gpx4$^{fl/fl;Hb9Cre}$*: Open field

The Open field (OF) test was assessed at 17 weeks of age and carried out as described previously [249]. (see 3.6.7.1)

3.7.1.2 *Gpx4$^{fl/fl;Hb9Cre}$*: SHIRPA

SHIRPA test was used for the evaluation of pronounced physical characteristics, behaviors and morphological aberrations at 18 and 48 weeks of age. For neurobehavioral assessment, a series of parameters reflecting abnormal locomotion, appearance, behavior and reflex reactions were chosen including contact righting, vocalization, aggression, head bobbing, startle response, unexpected behaviors, trunk curl, limb grasp, gait, locomotor activity, activity (body position), head morphology, and tremor. Defined rating scales (as expected/not as expected, present/absent, reduced/normal/increased) were used to categorize alterations. The number of squares crossed in the viewing arena (3 x 5 squares of 10 cm^2) during the first 30 seconds after transfer indexed locomotor activity.

3.7.1.3 *Gpx4$^{fl/fl;Hb9Cre}$*: Beam walk

In the beam walk test (also known as the raised-beam test), 25-weeks old mice were trained to traverse a distance of 90 cm on series of elevated, narrow beams (diameters beams 1-4: square 20 mm, round 22 mm, square 12 mm, round 15 mm) to reach an enclosed escape platform. The traversing time and numbers of falls, foot slips, and stops were recorded. The

mouse performed three trials each consecutively, and the average time of these three trials was calculated.

3.7.1.4 *Gpx4$^{fl/fl;Hb9Cre}$*: Ladder beam

The beam ladder consists of two Plexiglas screens connected with several metal beams of variable distance. The test is used to evaluate skilled walking of the mice. Mice (26 weeks old) traverse the ladder and foot slips of fore paws and hind paws are counted separately, as well as the time to traverse the beam.

3.7.1.5 *Gpx4$^{fl/fl;Hb9Cre}$*: Grip strength

The grip strength test was performed with a grip strength meter (Bioseb, France) having the mice grasping a grid attached to the force sensor of the device. The maximum force the mice apply to attach to the grid when slowly pulled away by its tail is recorded. The mouse is allowed to catch the grid with either 2 or 4 paws. Three trials were done for each mouse and measurement were done within one minute. The mean values are used to represent the grip strength of a mouse. Grip strength test was performed with 18- and 48-weeks old mice.

3.7.1.6 *Gpx4$^{fl/fl;Hb9Cre}$*: Rotarod

See 3.6.7.2. Rotarod measurement was performed with 19- and 49-weeks old mice.

3.7.1.7 *Gpx4$^{fl/fl;Hb9Cre}$*: Catwalk

Animals were tested in Catwalk (CW) XT system (Noldus Information Technology, Wageningen, Netherlands, [257]) from the age of 28 weeks. In this system, the mouse traverses an elevated glass walkway bordered by Plexiglas walls in a dark room. A camera beneath the walkway tracks the illuminated footprints which is analyzed with the CW software. For each animal the mean of 2 to 4 continuous runs (each included approx. 4-6 step cycles) were calculated and used for the analysis. The camera captured the footprints with a high-speed camera at a rate of up to 100 Hz. The CW system measures aspects of paw floor contact dynamics and calculates a vast number of spatial and temporal gait parameters. These include (i) individual paw print parameters, such as the width and length, with a calculation for the front and hind paws (FP and HP, respectively); (ii) paw print position with respect to each other parameters, such as the stride length and the base of support (BOS), indexing the

width between the two FPs and the two HPs respectively; and (iii) parameters related to time-based relationships between paw pairs (couplings and phase dispersion) and their variation.

3.7.1.8 *Gpx4*$^{fl/fl;Hb9Cre}$: **X-ray and DXA analysis**

The bone mineral content (BMC) and density (BMD) as well as the body composition (lean and fat mass) were assessed using the DXA (Dual Energy X-ray Absorptiometry) analyser UltraFocus^{DXA} by Faxitron® at the age of 53 weeks. Mice were measured immediately after being sacrificed. The same equipment was used for X-ray analyses. Body length was measured with a ruler. The kyphotic index from 53-week-old mice was calculated according to Laws et al., [258] using lateral X-rays and Fiji (ImageJ 1.52p) software [259].

3.7.1.9 *Gpx4*$^{fl/fl;Hb9Cre}$: **Muscle phenotyping**

In cooperation with the group of Prof. Wackerhage (Exercise Biology, TU München) the cohort of 12-months old mice were used to analyze hind limb phenotype. Dissecting of TA (tibialis anterior), EDL (extensor digitorus longus), Sol (Soleus) and Gas (Gastrocnemius) muscles from hind limbs was followed by weighing and snap freezing in liquid nitrogen until sectioning. 10 µm thick cryosections were taken in a 90° angle to the muscle fiber orientation and stored at -20 °C until staining. Slides were warm to RT for about 10-15 min before staining.

Hematoxylin & Eosin staining

Sections were stained for 10 min in Mayer's hematoxylin followed by a 5 min washing step under tab water for blueing. Then, sections were stained for 1 min in 1 % eosin solution followed by a short washing step. Finally, sections were dehydrated in a graded series of ethanol (30 s 70 % ethanol; 30 s 100 % ethanol; 1 min Xylene; 30 sec 100 % ethanol; 1 min Xylene; 1 min Xylene before they were mounted and covered with DPX Mounting Medium.

NADH-TR staining

TA sections were incubated for 30-45 min in a solution of nitroblue tetrazolium (1 mg NADH-disodium salt per 1 ml nitroblue tetrazolium basic solution) in a humidified chamber at RT. After rinsing in dH$_2$O, slides were dehydrated in a graded series of ethanol (30 s 70 % ethanol; 30 s 100 % ethanol; 1 min Xylene; 30 sec 100 % ethanol; 1 min Xylene; 1 min Xylene before they were mounted and covered with DPX Mounting Medium.

NADH-TR basic solution (NBT-solution): 0.34 g Tris base, 1.26 g Tris HCl, 0.05 g nitro blue tetrazolium, (Sigma-Aldrich), dissolve in 40 ml dH$_2$O, adjust pH to 7.4, fill up to 50 ml with dH$_2$O

ATPase staining

Standard ATPase staining allows the identification of fiber types. Sol sections were incubated for 5 min in solution 1. After a washing step in dH$_2$O, slides were incubated in solution 2 for 30 min. Then, slides were washed with dH$_2$O and incubated for 3 min in CaCl$_2$ (solution 3). After a washing step, slides were incubated for 1 min in CoCl$_2$ (solution 4). Next, slides were washed again and incubate for 1 min in ammonium sulfide solution (solution 5). Finally, sections were dehydrated in a graded series of ethanol (30 s 70 % ethanol; 30 s 100 % ethanol; 1 min Xylene; 30 sec 100 % ethanol; 1 min Xylene; 1 min Xylene before they were mounted and covered with DPX mounting medium.

Solution1 (acid pre incubation medium; pH 4.47): 3.9 g Na-acetate, 3.7 g KCl, dissolve in 400 ml dH$_2$O, adjust pH to 4.47, fill up to 500 ml with dH$_2$O, readjust pH on the day of use and add 0.085g ATP, stir until ATP is dissolved.
Solution 2 (ATPase reaction): 2.253 g glycine, 2.4 g CaCl$_2$, 1.755 g NaCl, 300 ml dH$_2$O, mix well and then add 200 ml NaOH-Solution (0.6 g of NaOH in 200 ml dH$_2$O). On the day of the experiment: adjust pH of 50 ml solution 2 to pH 9.4 and add 0.085 g ATP (-20°C).
Solution 3 (1 % CaCl$_2$): 5 g CaCl$_2$, fill up to 500 ml with dH$_2$O
Solution 4 (2 % CoCl$_2$): 10 g CoCl$_2$, fill up to 500 ml with dH$_2$O
Solution 5 (1 % S(NH$_4$)$_2$, ammonium sulphide): 2 ml 20 % ammonium sulphide, fill up to 40 ml with dH$_2$O

3.7.1.10 *Gpx4$^{fl/fl;Hb9Cre}$*: **Blood collection**

Blood samples were collected under isoflurane anesthesia by retrobulbar puncture as a final blood withdrawal. Blood samples for clinical chemistry analyses were collected in Li-heparin-coated tubes and stored on ice until centrifugation (4500 x g, 10 min) and separation of plasma aliquots for further analyses.

3.7.1.11 *Gpx4$^{fl/fl;Hb9Cre}$*: **Biomarker panel**

A multiplex assay platform was used to measure the concentration of IgE, IL-6, TNFα Leptin, FGF-21 and insulin in plasma samples. The platform is an electroluminescence-linked immunosorbent assay based on the Mesoscale Discovery technology (U-Plex). A 10 spot MSD plate is coated with anti-IgE, anti-insulin, anti-IL6, anti-TNFα antibodies (previously treated with the corresponding spot-linkers). Plasma samples were diluted 1:2 and incubated for 1 h. Thereafter, the samples were incubated for 1 h with sulfotag-conjugated detection antibodies

(second antibodies) before they were analyzed in the MSD plate reader. Antibodies for IL-6 and TNFα were provided as U-plex antibodies from MSD. MSD discovery workbench is used as analysis software.

3.7.1.12 *Gpx4$^{fl/fl;Hb9Cre}$*: Clinical chemistry

The clinical chemistry analyses of circulating biochemical parameters in non-fasted blood was performed using a clinical chemistry analyzer (Beckman Coulter AU 480 autoanalyzer, Krefeld, Germany) at the age of 16 weeks. A broad set of parameters was measured using the respective kits provided by Beckman Coulter, including various enzyme activities as well as plasma concentrations of specific substrates and electrolytes in *ad libitum* fed mice [260].

3.7.1.13 *Gpx4$^{fl/fl;Hb9Cre}$*: Transcriptome analysis

Total RNA from spinal cord (cervical, thoracic, and lumbar) was isolated employing the RNeasy Mini kit (Qiagen, Hilden, Germany) including Trizol treatment. The Agilent 2100 Bioanalyzer was used to assess RNA quality and RNA with RIN>7 was used for transcriptome analysis.

Total RNA was analyzed by RNA sequencing done by Novogene on an Illumina NovaSeq 6000 with a PE150 stranded protocol resulting in 5-10 Gb of data per sample. Paired-end data was generated and analyzed by a RNAseq pipeline consisting of quality control (FastQC, MultiQC), read trimming (trim_galore), genome alignment (STAR, [261]), and gene-level read counting (summarizeOverlaps, mode = 'Union').

Significantly regulated genes were determined with deseq2 [262] after excluding low expressed genes. Sets of regulated genes were determined after multiple testing correction with Benjamini-Hochberg (padj<0.1). For the biological interpretation of the observed gene regulation we performed pathway and GO term enrichment analyses through the use of QIAGEN's Ingenuity Pathway Analysis software (IPA®, QIAGEN Redwood City, www.qiagen.com/ingenuity) and by g:profiler (https://biit.cs.ut.ee/gprofiler/gost).

3.8 Cytokine Assay- Proteome Profiler™ Array

The relative level of selected mouse cytokines was determined using Mouse XL Cytokine Array Kit (RnD Systems). Proteins from cortex samples were extracted according to manufacturer's protocol. Samples from *Gpx4$^{fl/fl}$* mice were used as control for comparison with cortex samples from *Gpx4$^{fl/fl;Camk2aCreERT2}$* mice 2 and 4 weeks after KO induction.

3.9 Single molecule array Simoa®

Plasma neurofilament light (NfL) analysis was conducted on a single molecule array HD-1 Analyzer using single molecule array (Simoa) NF-light reagent kit (Quanterix®, Lexington, MA, USA) according to the manufacturer's instructions. Simoa NF-light® assay is a digital immunoassay for the quantitative determination of NfL level in liquid samples. Mouse plasma samples were centrifuged (2000 x g, 5 min, RT) and diluted 1:6.67 with sample diluent before measurement. NfL measurements were performed in collaboration with Dr. Petra Steinacker and Prof. Jan Lewerenz, Universität Ulm.

3.10 Isolation of CNS-Infiltrating immune cells and flow cytometry

Mice were perfused intracardially with ice-cold PBS immediately after sacrificed by CO_2 to remove blood from the intracranial vessels. The brain was prepared with sterile instruments, minced with a scalpel and incubated with agitation in RPMI (Roswell Park Memorial Institute) medium 1640 (PAA) containing 1 mg ml^{-1} collagenase A (Roche) and 0.1 mg ml^{-1} DNase I recombinant, RNase-free (Roche) for 45 min at 37 °C. Tissue was triturated through a 100-μm cell strainer and washed with PBS (pellet was centrifuged at 300 x g for 10 min at 4 °C). The homogenized tissue was resuspended in 30 % isotonic Percoll (GE Healthcare) and carefully underlaid with 78 % isotonic Percoll. After gradient centrifugation (1500 x g for 30 min at 4 °C), CNS-infiltrating immune cells were recovered from the gradient interphase and washed in ice-cold PBS. Single-cell suspension was divided into two tubes for an immune-cell and microglia panel and staining was performed in brilliant stain buffer (BD Biosciences) for 30 min at 4 °C. Fixable Dead Cell stain V500 (Thermo-Fisher) was used for live/dead discrimination. Total cell numbers of infiltrating immune cells were measured from total brain hemispheres with 123 count eBeads (Thermo-Fisher). For quantification of microglia activation marker, expression levels of single living cells gated for CD45-low and CD11b-positive cell populations were measured. The antibodies and the respective antigen, host species, supplier, catalogue number, clone and dilution are listed in the attached table. Data was acquired on an LSR II FACS analyzer (BD Biosciences). Data analysis was performed with the FlowJo v.10 analysis software (FlowJo LLC). Flow cytometry gating strategy for immune cells and microglia is shown in the Appendix. The isolation and analysis were carried out in close collaboration with Prof. Manuel Friese and Nicola Rothammer (Zentrum für Molekulare Neurobiologie Hamburg (ZMNH), Institut für Neuroimmunologie und Multiple Sklerose (INIMS), Universitätsklinikum Hamburg-Eppendorf).

Table 1| Immune cell panel

Antigen	Host species	Company	Catalog no.	Clone	Ig fraction	Fluorophore	Dilution FACS
CD3e	Armenian hamster	BioLegend	100305	145-2C11	IgG	FITC	0.111111111
CD8a	Rat	BioLegend	100750	53-6.7	IgG	BV786	0.180555556
CD11b	Rat	BioLegend	101228	M1/70	IgG	PerCP-Cy5.5	0.319444444
CD11c	Armenian hamster	BioLegend	117318	N418	IgG	PE-Cy7	0.25
CD45	Rat	BioLegend	103127	30-F11	IgG	AF700	0.180555556
NK1.1	Mouse	eBioscience	12-5941-82	PK136	IgG	PE	0.111111111
F4/80	Rat	BD	565411	T45-2342	IgG	BV421	0.111111111
CD19	Rat	BioLegend	115539	6D5	IgG	BV650	0.319444444
MHCII	Rat	BioLegend	107643	M5/114.15.2	IgG	BV711	0.319444444
CD317	Rat	BioLegend	127015	927	IgG	APC	0.111111111
Ly6G	Rat	BioLegend	127623	1A8	IgG	APC-Cy7	0.180555556

Table 2| Microglia panel

Antigen	Host species	Company	Catalog no.	Clone	Ig fraction	Fluorophore	Dilution FACS
MHCII	Rat	BioLegend	107635	M5/114.15.2	IgG	PacBlue	0.319444444
B2M	Mouse	BD	745120	S19.8	IgG	BV605	1:50
CD206	Rat	BioLegend	141727	C068C2	IgG	BV711	1:50
Ly6C	Rat	BioLegend	128041	HK1.4	IgG	BV785	0.180555556
CD80	Hamster	BioLegend	104705	16-10A1	IgG	FITC	0.111111111
CD11b	Rat	BioLegend	101228	M1/70	IgG	PerCP-Cy5.5	0.319444444
P2RY12	Rat	BioLegend	848003	S16007D	IgG	PE	0.180555556
CX3CR1	Mouse	BioLegend	149015	SA011F11	IgG	PE-Cy7	0.736111111
TREM2	Rat	R&D	FAB17291A	237920	IgG	APC	1:20
CD45	Rat	BioLegend	103128	30F11	IgG	AF700	0.180555556
Ly6G	Rat	BioLegend	127623	1A8	IgG	APC-Cy7	0.180555556

4 RESULTS

4.1 Analysis of mice with spatiotemporal deletion of GPX4 in glutamatergic neurons of cortex and hippocampus

4.1.1 Generation of mice with TAM-inducible deletion of *Gpx4* KO in glutamatergic neurons of cortex and hippocampus

In order to generate a mouse line with TAM-inducible glutamatergic neuron-specific *Gpx4* KO, *Gpx4fl/fl*, mice were crossbred with a *Camk2aCreERT2* mouse line until homozygosity of the loxP-flanked (floxed, fl) *Gpx4* locus and heterozygosity for the transgene (tg) *Camk2a* locus was established (Fig. 7A). PCR analysis of ear punch DNA was used to distinguish between floxed (240 bp) and wildtype (180 bp) alleles of *Gpx4*. The presence of the Cre recombinase tg (*Camk2aCreERT2*) was confirmed by two bands 290 bp for wt and 375 bp for the tg band (Fig. 7B). The functional KO of *Gpx4* in glutamatergic neurons was induced by three consecutive i.p. injections of mice with TAM. *Gpx4fl/fl* mice served as a control group. To analyze the effect of the KO in glutamatergic neurons, animals were sacrificed at predefined time points (Fig. 7C).
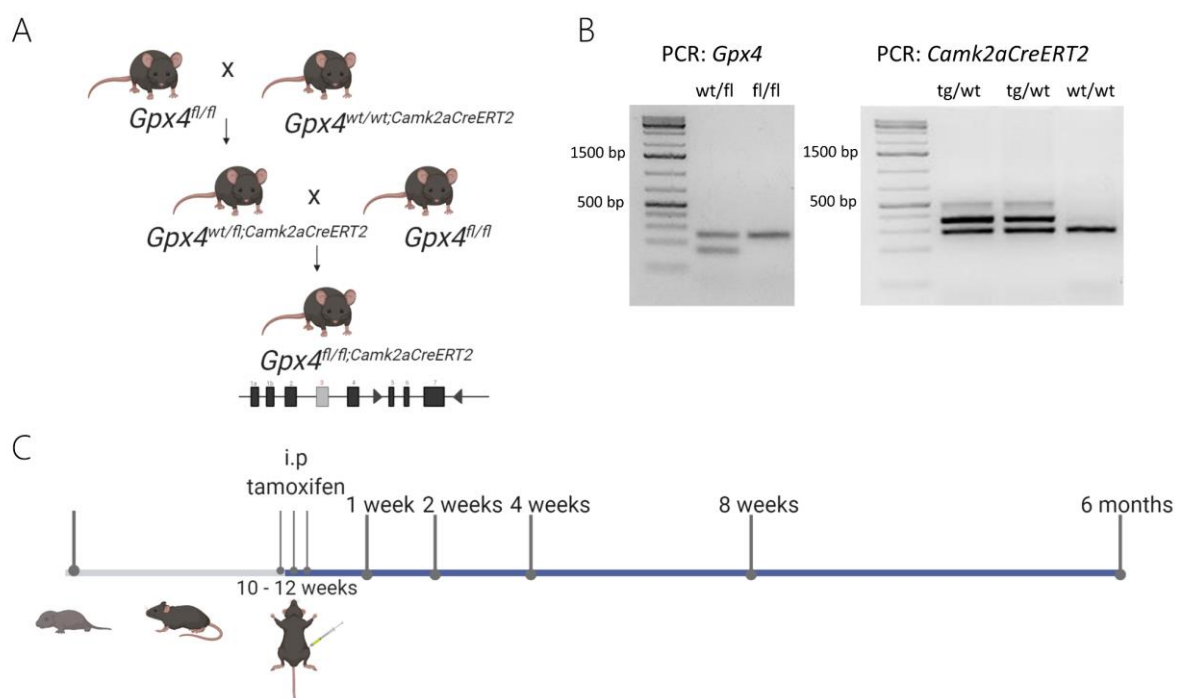
Figure 7| Generation and genotyping of the TAM-inducible *Gpx4* KO mouse line in glutamatergic neurons of cortex and hippocampus using the *Camk2aCreERT2* mouse line

A| Breeding scheme for the generation of tamoxifen (TAM)-inducible glutamatergic neuron-specific *Gpx4* KO mice by crossbreeding *Gpx4fl/fl* mice with the *Camk2aCreERT2* mouse line. B| Mice were genotyped by PCR of ear punch DNA. The primer pair for genotyping the *Gpx4* locus are designed surrounding the loxP site 5' of exon 7, resulting in a 240 bp length product, which represents the floxed allele (fl/fl) for *Gpx4* or a 180 bp length product, which represents the wildtype allele (wt/wt). Two products of *Camk2aCreERT2* PCR products (290 bp and 375

bp) indicate heterozygosity for the *Camk2a* locus (tg/wt). C| Workflow illustrates the induction of the *Gpx4* KO in adult animals via three times i.p injection with 2 mg/ml TAM. Samples were collected at different time points (i.e., 1, 2, 4, 8 weeks and 6 months) after TAM injection.

4.1.2 Gait and behavioral analyses of neuron-specific *Gpx4* KO mice reveal massive impairment in coordination and cognitive deficiencies

After KO induction, body weight was recorded for 24 weeks. While a gradually lower body weight was observed in *Gpx4$^{fl/fl;Camk2aCreERT2}$* mice, no acute body weight loss was noticed in these animals as compared to control animals (Fig. 8A). Two weeks after TAM injection, extensive behavior analyses were performed in order to obtain a general assessment of the neurological phenotype of TAM-treated *Gpx4$^{fl/fl;Camk2aCreERT2}$* mice. The behavioral changes were evident in both genders, indicating a clear genotype effect. Open field analysis is one of the most common tests to monitor the general behavior and activity of mice. Here, the observation period is set for 20 min (Fig. 8B). In comparison with control mice, *Gpx4* KO mice showed a significant decrease in average traveled distance, time spent in center and average speed, indicating a severely comprised locomotor activity and willingness to move. In addition, *Gpx4* KO mice exhibited significantly fewer rears and increased resting time, corroborating the impairment in body activity. Due to this apparent deficiency in rearing, *Gpx4* KO mice require to be fed with chow directly in the cage from one week after TAM administration. Further, analysis of traveled distance over each 5 min periods demonstrated decreased activity in *Gpx4* KO mice, which was independent of sex (Fig. 8B). Rotarod analysis, a test used to determine coordination, clearly displayed an impairment of motoric skills in *Gpx4* KO mice (Fig. 8C). To further assess short-time memory in those cohorts, Y-maze test was performed revealing significantly increased latency time and less numbers of entries of *Gpx4* KO mice (Fig. 8D). This test therefore shows that KO mice had a decreased willingness to explore new environments, indicating cognitive deficits already two weeks after KO induction. In order to evaluate motor function, beam and hanging wire tests were conducted. *Gpx4* KO mice required significantly longer times with increased numbers of hind limb slips for crossing the beam as compared to control mice (Fig. 8E). In the hanging wire test, the latency of animals to fall was recorded which revealed a strong decline in the *Gpx4* KO group (Fig. 8F), indicating impaired motor function and balance of *Gpx4* KO mice. Finally, the catalepsy test is a measure for muscle rigidity by determining the time needed to correct for an abnormal position. The measured time varied between each tested animal, but there was a clear tendency showing that *Gpx4* KO mice are impaired in correcting their position (Fig. 8G).

Conclusively, *Gpx4*^{fl/fl;Camk2aCreERT2} mice display severe behavioral abnormalities with highly significant differences and impairments in motor coordination and balance resulting from the inducible deletion of *Gpx4* in glutamatergic neurons.
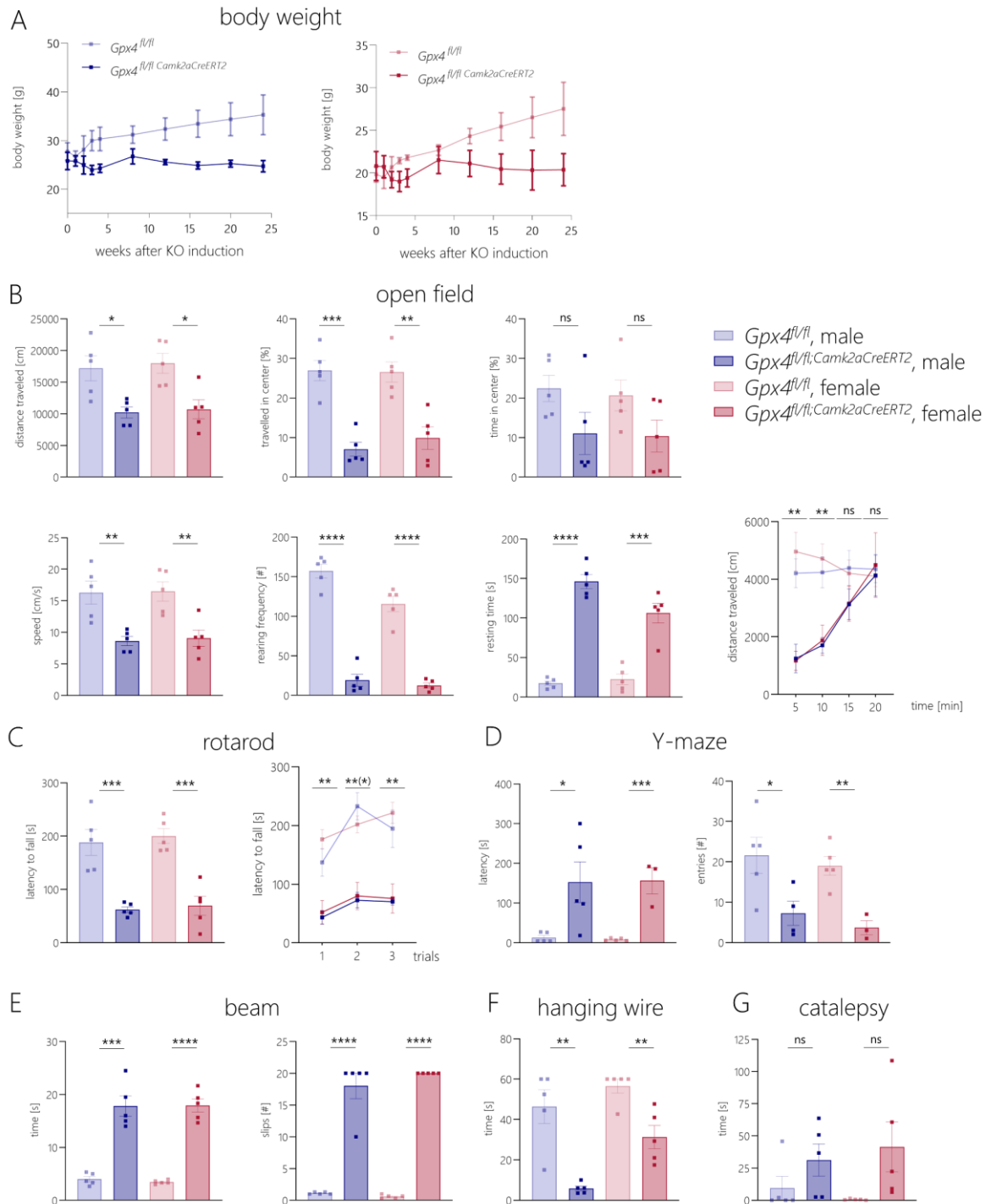
Figure 8| *Gpx4*^{fl/fl;Camk2aCreERT2} **mice show massive impairment in gait and behavior**

A| *Gpx4*^{fl/fl;Camk2aCreERT2} mice showed decreased body weight gain after TAM injections (left: males, right: females). Two weeks after TAM injections, a series of behavior analyses were performed to compare *Gpx4*^{fl/fl;Camk2aCreERT2} and *Gpx4*^{fl/f} control mice. Male and female mice were separately analyzed to unveil potential sex-specific differences. B| Open field analysis displayed significant differences in average traveled distance, time spent in

center, average speed, number of rearing and resting time. The observed differences indicated impaired locomotor activity and movement. C| Rotarod performance was measured over three trials as latency to fall, which clearly showed a deficiency in motoric skills of *Gpx4* KO mice. D| Increased latency time and less numbers of entries of *Gpx4* KO mice in the Y-maze imply a decreased willingness to explore new environments, cognitive and short time memory deficits. F| Motoric function and balance were tested via beam analysis (E) and hanging wire test (F). Both tests showed significant alterations in the time required. G| *Gpx4* KO mice tend to be slower in correcting their positions recorded by the catalepsy test. Data shown represents the mean ± SEM of n=5 animals. Statistical analysis was performed using t-test, p < 0.05 (*), p < 0.01 (**), p < 0.001 (***), p < 0.0001 (***), n.s. = not significant.

4.1.3   *Gpx4$^{fl/fl;Camk2aCreERT2}$* mice develop progressive and massive cortical atrophy

For a longitudinal analysis of possible morphological changes of *Gpx4$^{fl/fl;Camk2aCreERT2}$* mice, several time points after the TAM injections were chosen (i.e., 1, 2, 4, and 8 weeks, as well as 6 months). These analyses revealed massive cortex atrophy, especially in animals that were analyzed 6 months after KO induction. The overall brain weight at 6 months after KO induction showed an approximately 55 % reduction in *Gpx4$^{fl/fl;Camk2aCreERT2}$* mice (0.5 ± 0.045 g) as compared to WT mice (0.27 ± 0.046 g) (Fig. 9A). This was supported by magnetic resonance imaging (MRI) demonstrating a progressive loss of cortical mass, which coincided with a 2.5-fold increased volume of ventricles already 2 months after KO induction (Fig. 9B).
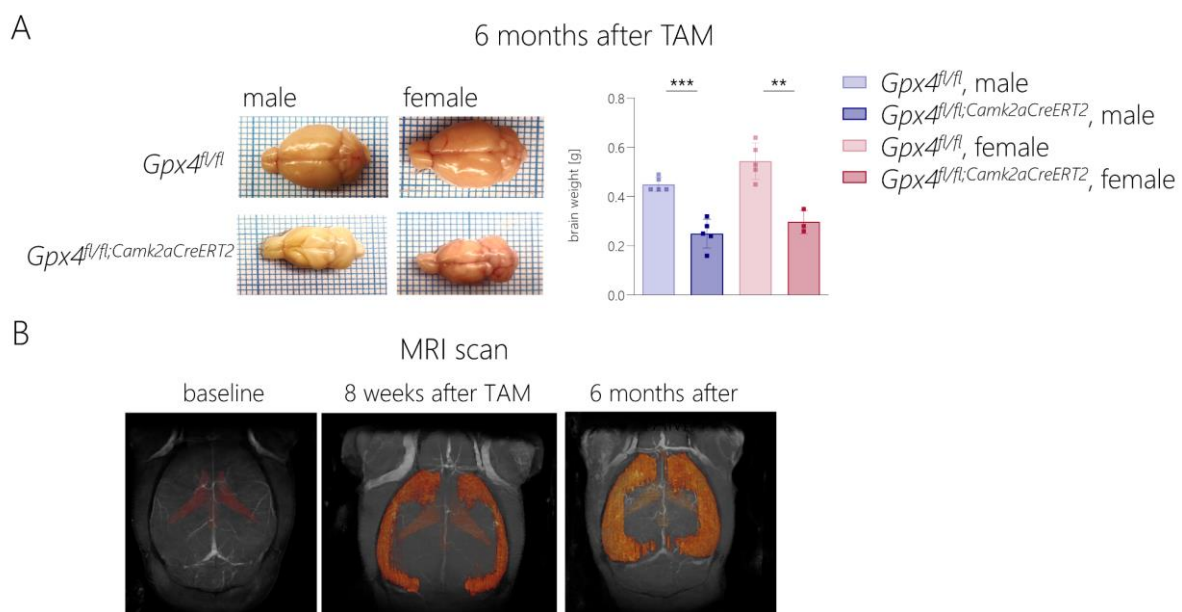
Figure 9| *Gpx4$^{fl/fl;Camk2aCreERT2}$* mice develop massive cortical atrophy
A| *Gpx4$^{fl/fl;Camk2aCreERT2}$* mice at 6 months after TAM induction showed massive cortical atrophy as mirrored by an approximately 55 % reduction in brain weight. Statistical analysis was performed using t-test, p < 0.01 (**), p < 0.001 (***). B| Magnetic resonance imaging (MRI) illustrates a marked loss of cortical mass already 2 months after KO induction coinciding with an increase in the volume of the lateral ventricles.

Histopathological analysis of sagittal brain sections revealed widespread neurodegeneration and progressive loss of cortical neurons in *Gpx4fl/fl;Camk2aCreERT2* mice using Nissl-staining, a commonly used method to stain for neuronal tissue.
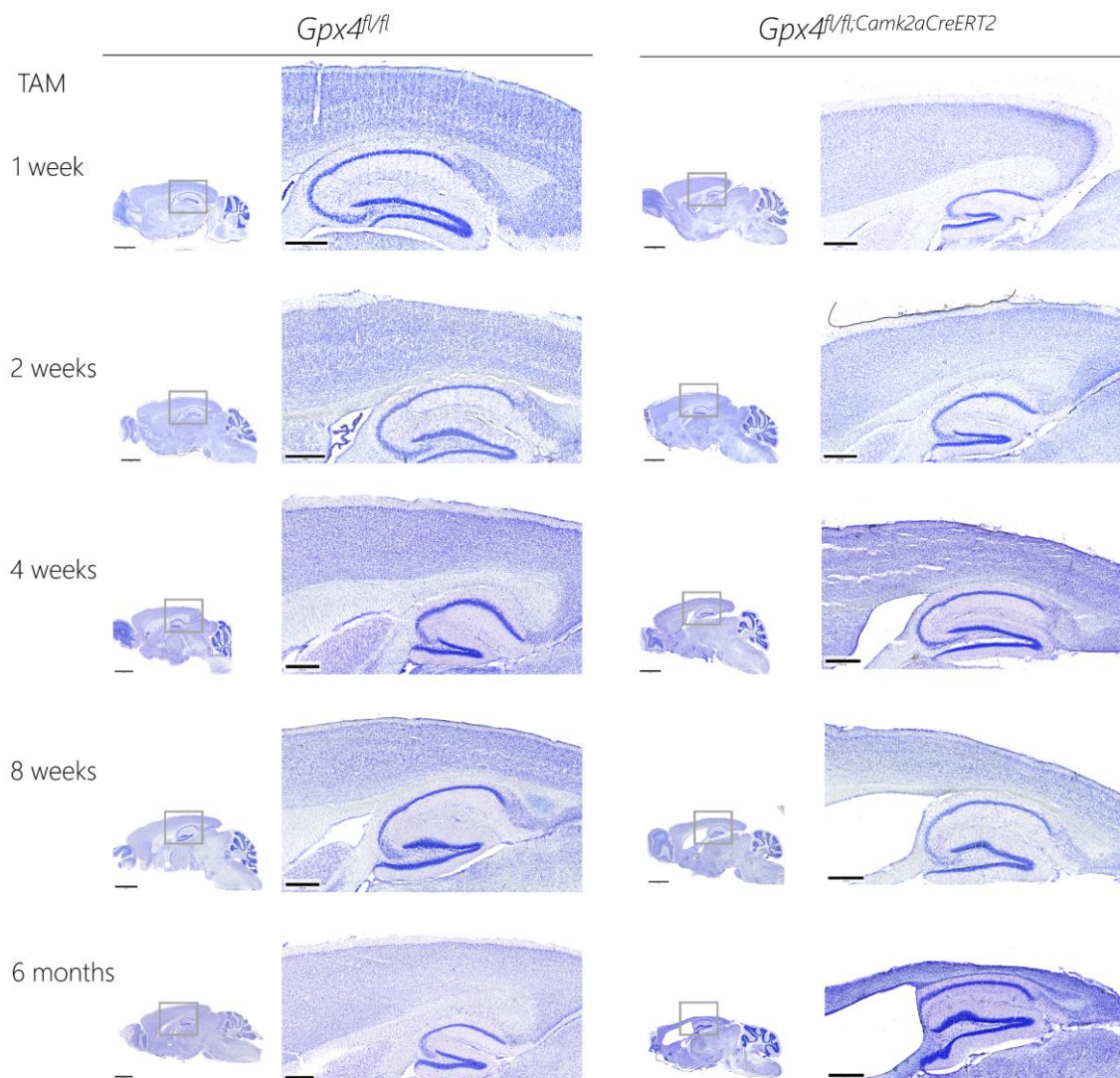
Figure 10| Nissl staining of brain illustrates a massive loss of cortical layers and cortical atrophy in GPX4 KO brains
Nissl staining of sagittal brain sections of *Gpx4* KO mice demonstrated a massive loss of cortical layers, cortical atrophy and an increase in the volume of the ventricles, whereas hippocampus remained unaffected. Pictures were taken with an AxioScan.Z1 microscope; scale bar indicates 2 mm in overview picture, in cortex blow-up 500 µm.

WT mice showed typical lamination of six cortical layers and no overt alterations in ventricle volume. In contrast, staining of KO brain tissues displayed a gradual loss of cortical layers coinciding with an increased lateral ventricle volume, which was evident already 4 weeks after KO induction. Furthermore, dramatic cortical atrophy with approximately 80 % loss of cortical mass was observed at 6 months after KO induction explaining the decrease in overall brain weight. These findings demonstrate regio-specific neurodegeneration of cortical structures,

whereby the hippocampus remained unaffected (Fig. 10). This is highly intriguing as expression of the *Camk2a* transgene is confined to glutamatergic neurons of the cortex and the hippocampus [232], the latter seemingly being resistant to *Gpx4* deletion. As expected, other structures of the brain including cerebellum and olfactory bulb remained unaffected in these mice.

4.1.4   Massive cortical neuron loss in response to spatiotemporal deletion of *Gpx4*

For a further characterization of the altered cortical layers, immunocytochemical analysis was performed. Expression of GPX4 and neuronal nuclei (NeuN) was determined by immunoblotting in cortex and cerebellum of WT and KO mice at 1, 2, 4 and 8 weeks after TAM treatment (Fig. 11 A). NeuN is a nuclear protein exclusively expressed in neurons [263]. At each time point, the GPX4 expression was found to be decreased in cortex of *Gpx4$^{fl/fl;Camk2aCreERT2}$* mice as compared to cerebellum and *Gpx4$^{fl/fl}$* control animals. Figure 11B shows representative examples of cortical regions, 2 weeks after KO induction, co-stained with NeuN and GFAP, showing an increase of GFAP-positive cells and a decrease of NeuN-positive cells. GFAP is an astrocyte-specific marker frequently used to detect astrogliosis, which is known to occur secondary to neuronal cell death and a marker for neuroinflammation. To address whether the loss of GPX4 in neurons causes increased cell death, staining for dying cells was performed using TUNEL labeling, which detects fragmented DNA. In fact, an increased number of dead cells was noticeable in cortical regions of *Gpx4$^{fl/fl;Camk2aCreERT2}$* mice (Fig. 11B).

In sum, the cortical neuron-specific deletion of GPX4 causes loss of neurons after KO induction, as determined by consistently reduced numbers of NeuN-positive cells and increased numbers of TUNEL-positive cells coinciding with an increased number of GFAP-positive staining, indicating the induction of neuroinflammatory processes.
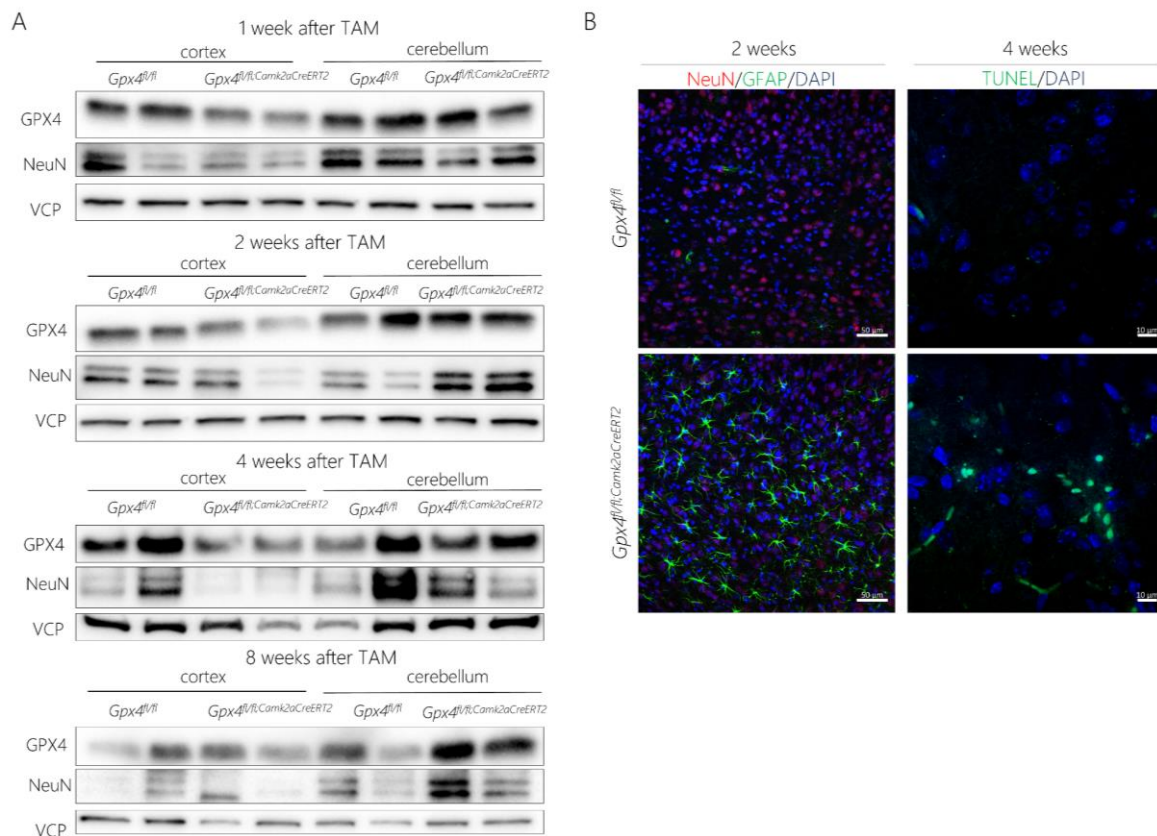
Figure 11| Cortical neuron-specific deletion of *Gpx4* causes neuronal cell death and reactive astrogliosis
A| Immunoblot analysis of GPX4 and NeuN in cortex and cerebellum at 1, 2, 4 and 8 weeks after TAM injection. As expected, *Gpx4*^{fl/fl;Camk2aCreERT2} cortex samples showed decreased expression of GPX4 following KO induction. Low expression of NeuN was detected 4 weeks after TAM treatment. No changes in expression levels of the aforementioned protein were detected in cerebellum as expected. VCP expression was used as loading control.
B| Double-staining of NeuN, and GFAP revealed increased numbers of reactive astrocytes accompanied by a loss of NeuN positive cells in *Gpx4*^{fl/fl;Camk2aCreERT2} mice as compared to *Gpx4*^{fl/fl} mice 2 weeks after KO induction. Alongside, TUNEL (Terminal deoxynucleotideyl transferase dUTP nick end labeling)-positive cells were detected, in cortical structures indicating neuronal cell death. Pictures were taken with LSM880, Examiner Z1 microscope (Carl Zeiss NTS Ltd.); scale bar GFAP/NeuN/DAPI indicates 50 µm, in TUNEL/DAPI staining 10 µm.

4.1.5 Progressive astro-and microgliosis in glutamatergic neuron-specific *Gpx4* KO mice

To investigate in more detail the neuroinflammatory processes secondary to massive ferroptosis in cortex of mice, expression of ionized calcium-binding adaptor molecule 1 (IBA1), a microglia-specific marker and GFAP, were compared over time using immunoblot and immunohistochemical analyses (Fig. 12). Already one week after KO induction, IBA1 (~17 kDa) protein levels were slightly elevated in cortex of *Gpx4*^{fl/fl;Camk2aCreERT2} mice compared to WT samples, with strongest IBA1 signals observed 4 weeks after KO induction. GFAP expression (~55 kDa) in cortex was detected to varying degree in each sample, however in samples from KO mice, a double band could be observed already one week after KO induction, indicating a breakdown product of activated GFAP [264]. In contrast to IBA1 expression, the expression

level of GFAP remained high in cortex samples of KO animals even 8 weeks after TAM injection (Fig. 12A).
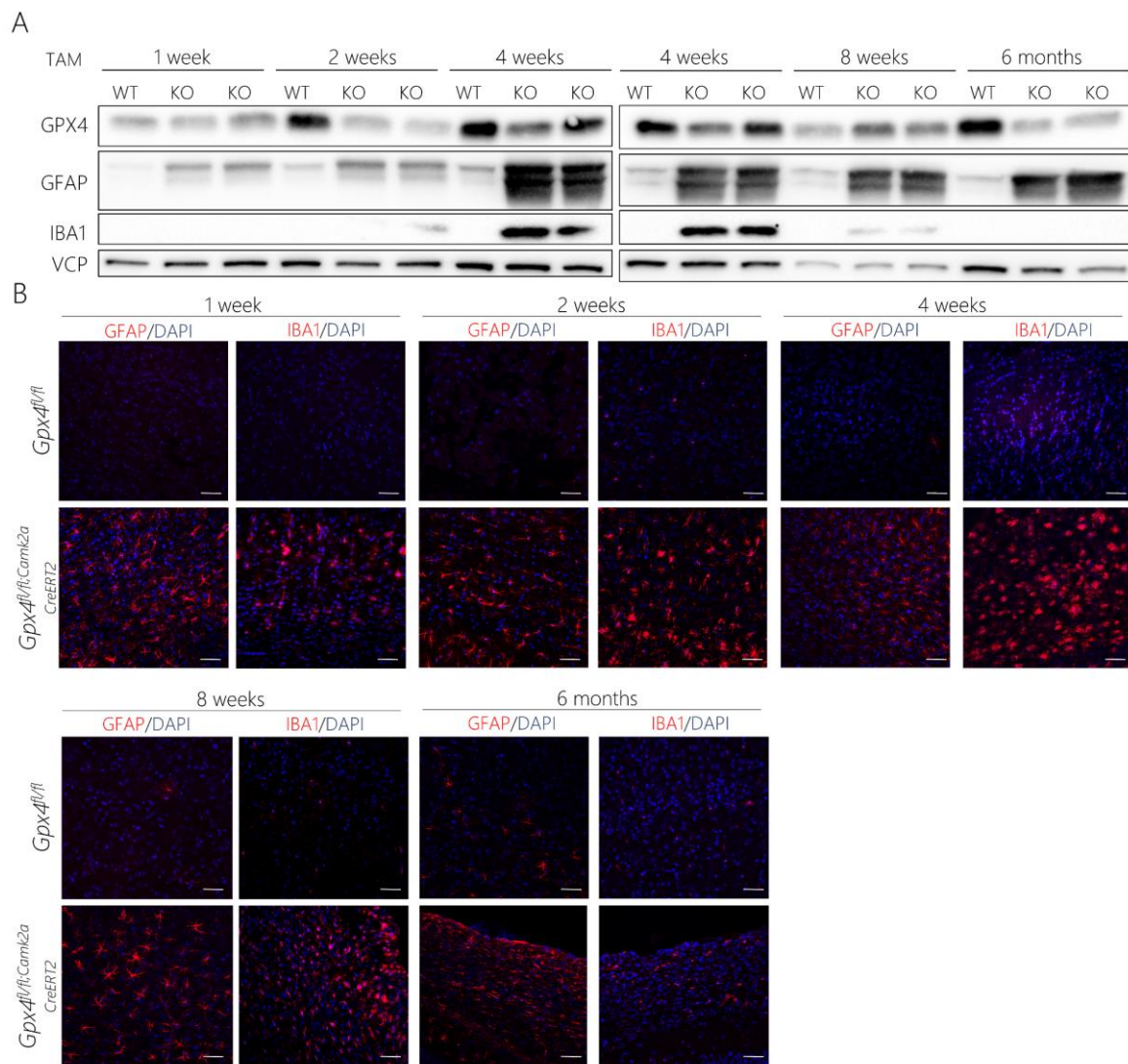
Figure 12| Induction of neuroinflammatory processes as determined by staining against GFAP and IBA1
A| Expression analysis of GPX4, GFAP and IBA1 in cortex samples at 1, 2, 4, 8 weeks and 6 months after TAM injection. Loss of GPX4 expression caused massive activation of astrocytes (GFAP) followed by microglia (IBA1) activation. VCP expression was used as loading control. B| Immunohistochemical analysis confirmed occurrence astrogliosis and microgliosis in GPX4 KO tissue. Pictures were taken with LSM880, Examiner Z1 microscope (Carl Zeiss NTS Ltd.); scale bar indicates 50 μm.

A very similar pattern was observed analyzing GFAP and IBA1 expression in immunohistochemical staining, revealing significantly elevated levels of GFAP and IBA1 in KO as compared to WT animals (Fig. 12B). Thus, these results suggest that astrocytes become strongly activated with highest levels already at 4 weeks after KO induction. Unlike GFAP the number of IBA1-positive cells declined 4 weeks after KO induction. These findings indicate that

the induction of *Gpx4* KO in cortical neurons causes widespread ferroptosis in cortical structures leading to first massive astrogliosis followed by microgliosis.

4.1.6 Cytokine profiling and immune cell infiltration in cortex reveals a pro-inflammatory state in brain of neuron-specific *Gpx4* KO mice

Since the *Gpx4* KO in cortical neurons triggered massive necroinflammatory processes, brain extracts were used to study in detail the cytokine profiles and the infiltration of distinct immune cell populations in response to GPX4 loss. First, cortical extracts were subjected to the Proteome Profiler Mouse XL Cytokine Array (R&D Systems), a membrane-based antibody array that allows for the relative detection of selected chemokines and cytokines in protein extracts from mouse tissue. Pooled tissues from three animals per group were extracted and lysates are probed on the membranes. Blots were developed with the same exposure times allowing for a direct comparison between each array (Fig. 13A).

The levels of specific cytokines and chemokines were dynamically altered in *Gpx4*$^{fl/fl;Camk2aCreERT2}$ mice upon KO induction as compared to WT controls (Fig. 13B). CCL6/C10 (Chemokine (C-C motif) ligand 6), a member of the CC chemokine family in rodents, was largely absent in control tissue, but clearly increased over time from 2 to 4 weeks after KO induction. Murine CCL6/C10 is known to play a role in attracting and activating macrophage infiltration [265].

A similar pattern of regulation was observed for insulin-like growth factor-binding protein 2 (IGFBP-2), and intercellular adhesion molecule-1/ cluster of differentiation 54 (ICAM-1/CD45). Such an increase points to a stimulation of cytokine release and neuroinflammatory responses and an altered signaling of microglia and macrophages after *Gpx4* KO induction [266-269]. Unlike these rather early responses, some cytokines were only detectable 4-weeks after KO induction. These include osteopontin, CCL12, chitinase 3-like 1 and LIX (CXCL5, CXC chemokine ligand 5). These cytokines are also associated with microglia activation and neuroinflammatory responses. Importantly, several studies suggest their roles as potential biomarkers of certain inflammatory disease conditions [270-272].
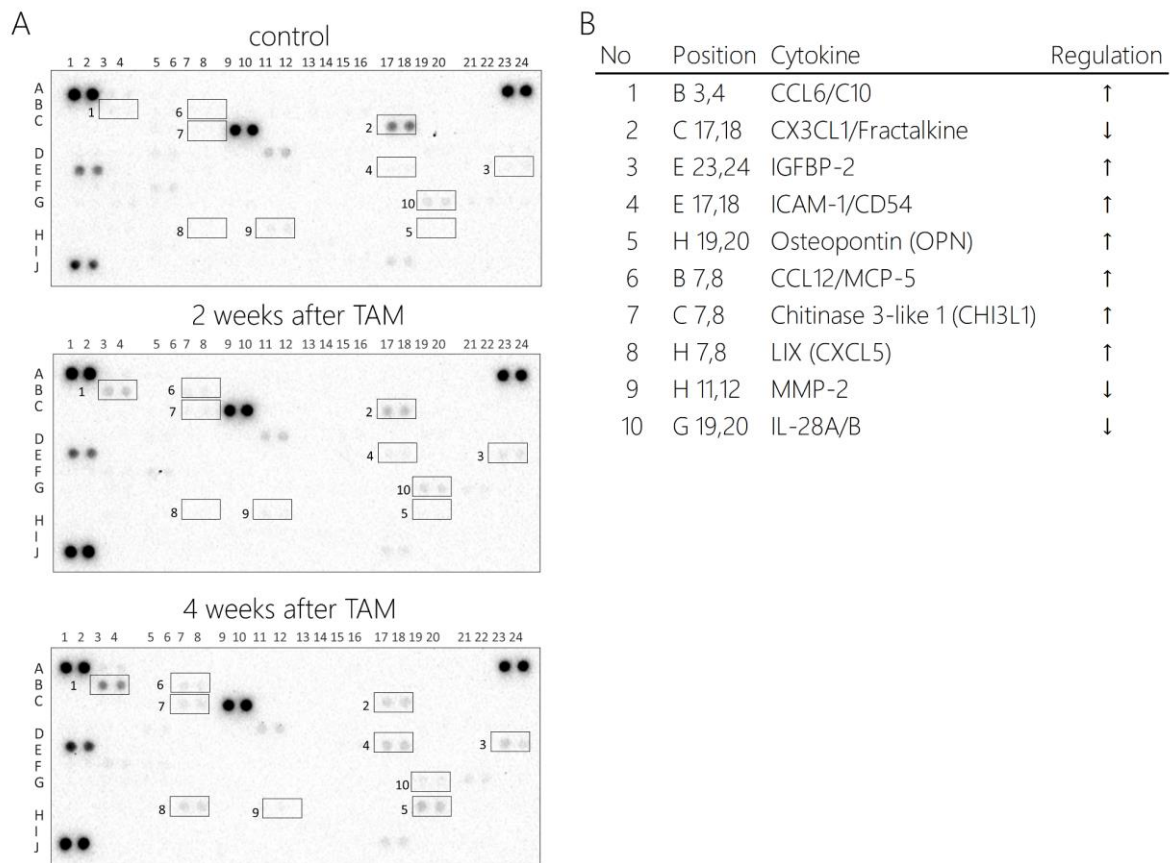
Figure 13| Cytokine arrays revealed that KO of GPX4 triggers a pro-inflammatory response in the cortex
A| Proteome Profiler Mouse XL Cytokine Array (R&D Systems) using homogenized cortex samples detected selected chemokines and cytokines, which are differently regulated upon *Gpx4* KO induction over time. Every capture antibody is spotted in duplicate on the array. Positions A1, A2, J1, J2 and A23, A24 are reference spots; J23, J24 is the negative control. Exposure time was set to 600 s, pooled cortex samples n=3 were used. B| List of the cytokines, which were found to be up- or downregulated. Arrows illustrate up-(↑) or downregulation (↓) of specific cytokines in cortex samples over time. Abbreviations: CCL6/C10, Chemokine (C-C motif) ligand 6; CX3CL1/fractalkine, C-X3-C motif chemokine ligand 1; IGFBP-2, Insulin-like growth factor-binding protein 2; ICAM-1/CD45, Intercellular adhesion molecule-1/Cluster of differentiation 54; OPN, osteopontin, CCL12, Chemokine (C-C motif) ligand 12; CHI3L1, Chitinase 3-like 1; LIX/CXCL5, CXC chemokine ligand 5; MMP2, matrix metallopeptidase 2; IL-28A/B, Interleukin 28A/B

In contrast to an upregulation of mostly microglia- and macrophage-associated factors, some cytokines/chemokines disappeared upon KO induction. For instance, fractalkine (CX3CL1) showed a strong signal in control tissue, which decreased 2 and 4 weeks after loss of GPX4. Fractalkine is strongly expressed in neurons interacting with its cognate receptor CX3CR1, expressed on microglial cells. A decrease of fractalkine was described to be associated with microglia activation in NDs such as Alzheimer's disease [273]. Also, MMP-2, a member of matrix metalloproteinase family of proteins and interleukin-28A/B (IL-28A/B), were found to be downregulated in *Gpx4* KO samples.

Thus, by studying the dynamic changes and patterns of the different cytokines in control versus *Gpx4* KO cortex tissue over time, it emerges that the neuron-specific KO of *Gpx4*

triggers a pro-inflammatory response which is likely related to the rupture of neuronal cells by ferroptosis and the release of neurodegeneration-associated molecular patterns (NAMPs) [175, 274, 275]. These results therefore lay the basis for future studies focusing on ferroptosis and associated neuroinflammatory responses as the underlying mechanisms contributing to neurodegenerative disorders.

Based on these results, the immune cell populations in freshly dissected whole brains from *Gpx4^{fl/fl;Camk2aCreERT2}* mice were investigated using flow cytometry (experiments performed in collaboration with the group of Prof. Manuel Friese, Universitätsklinikum Hamburg-Eppendorf). Two time points after KO induction were chosen, i.e., 12 days and 4 weeks after KO induction (Fig. 14). The panel of immune cells that were specifically analyzed included granulocytes, macrophages, NK T cells, B cells, CD8^+ T cells, and CD4^+ T cells. At 12 days after KO induction, there were no discernable differences in the specific immune cell populations in the brain tissue of TAM-treated *Gpx4^{fl/fl;Camk2aCreERT2}* mice and *Gpx4^{fl/fl}* control mice. By contrast, 4 weeks after *Gpx4* KO induction, a general increase in the number of immune cells was detected. Except for B cells, the absolute numbers of each analyzed immune cell type were significantly higher in KO animals, assuming massive infiltration of immune cells into the brain of *Gpx4^{fl/fl;Camk2aCreERT2}* mice. CD45^+ cells were used for normalization of the immune cells in brains. The calculated percentage (%) of live CD45^{hi} cells value represents the composition of immune cells, which remained mainly stable in brain samples. A significant increase was only notable among NK T cells and a decrease among B cells 4 weeks after KO induction (Fig. 14A, lower graph). Figure 14B illustrates the alterations in microglia markers. Already at day 12 after KO induction, microglial markers, such as beta-2-microglobulin (B2M) or purinergic receptor P2Y12 (P2RY12), were significantly altered when comparing WT and *Gpx4* KO animals. These changes became even more profound at 4 weeks after *Gpx4* deletion. In particular, an increased staining for TREM2, B2M and CD80 was evident in *Gpx4^{fl/fl;Camk2aCreERT2}* mice, whereas several microglia markers, including CD206, Lc6C, MHCII, P2RY12 and CXCR1, were found to be significantly decreased.
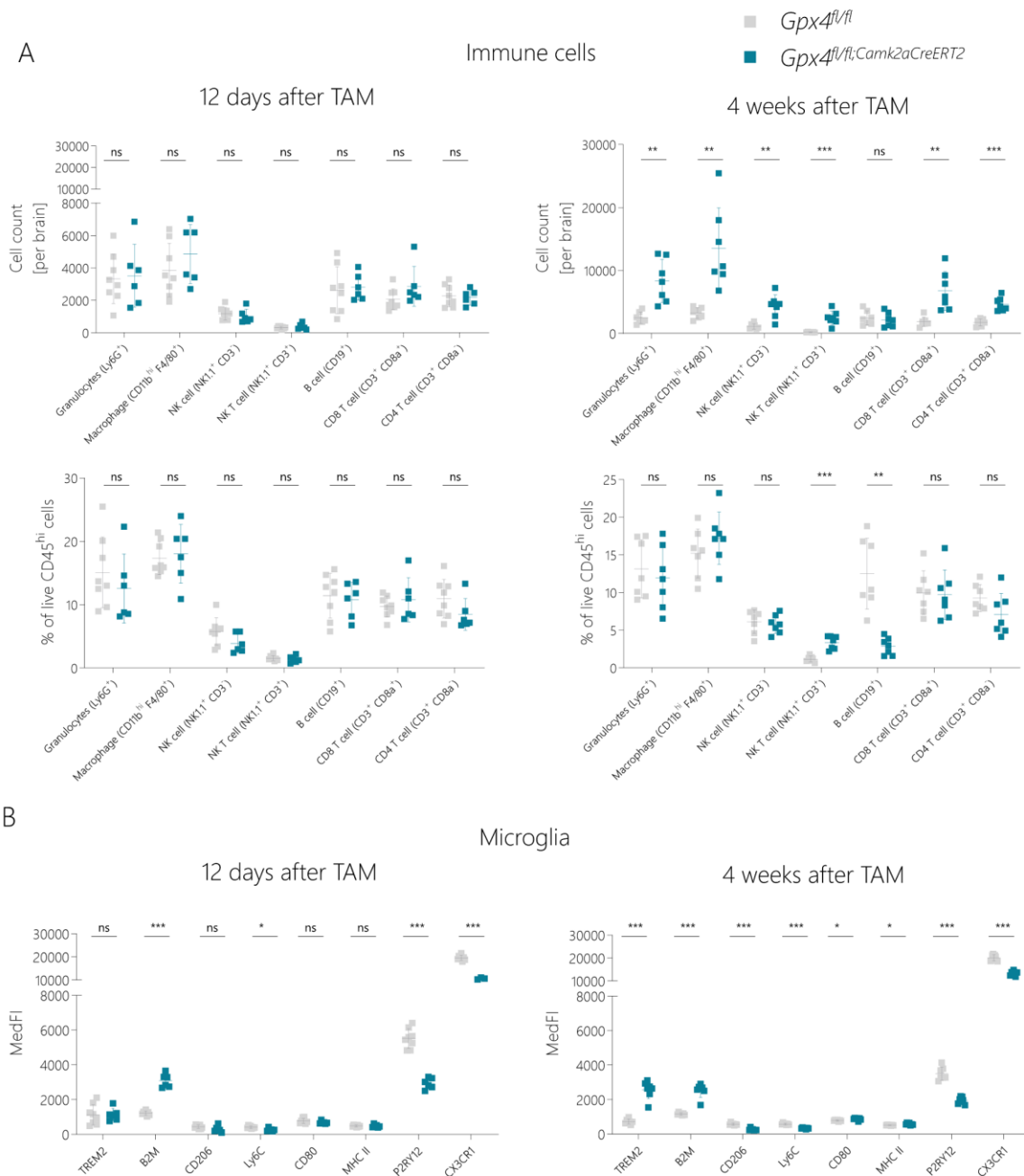
Figure 14| Analysis of CNS-infiltration using flow cytometry indicates a massive increase in immune cells and microglia in brain tissue of *Gpx4fl/fl;Camk2aCreERT2* mice

A| The total number of infiltrating immune cells was measured from total brain hemispheres using flow cytometry. Cell counts for immune cells clearly showed significant alterations 4 weeks after TAM in *Gpx4fl/fl;Camk2aCreERT2* mice compared to control mice. The amount of infiltrating immune cells, normalized to total immune cells (% of live CD45 cells) showed an overall stable ratio of immune cells in brain, except for NK T cells and B-cells. B| The intensity of microglia activation markers in *Gpx4fl/fl;Camk2aCreERT2* was increased for TREM2, B2M and CD80, whereas the intensity for CD206, Lc6C, MHCII, P2RY12 and CXCR1 were found to be significantly decreased. Statistical analysis was performed using multiple t-test, adj.p < 0.05(*), adj.p < 0.01 (**), adj.p < 0.001 (***), adj.p < 0.0001 (****). n.s. = not significant.

Abbreviations: TREM2, triggering receptor expressed on myeloid cells 2; B2M, beta-2-microglobulin; CD206, cluster of differentiation 206; Ly6C, lymphocyte antigen 6 complex; CD80, cluster of differentiation 80; MHC II, class of major histocompatibility complex II; P2RY12, purinergic receptor P2Y12; CX3CR1, C-X-3-C motif chemokine receptor 1

4.1.7 The extent of neuronal ferroptosis can be measured and quantified in plasma of neuron-specific *Gpx4* KO mice

Neurofilament light (NfL) is a 68 kDa cytoskeletal intermediate protein expressed only in the axons of neurons [271]. Therefore, NfL is a valid biomarker for the diagnosis of patients suffering from ND, as it is released into the plasma and cerebrospinal fluid (CSF) as a direct result from neuronal cell death or axonal damage [271]. Consequently, Simoa NF-light® assay was used to study whether NfL levels can be quantitatively determined in plasma samples of mice at 1, 2, 4 and 8 weeks after TAM injection (in collaboration with Dr. Petra Steinacker, Universität Ulm).
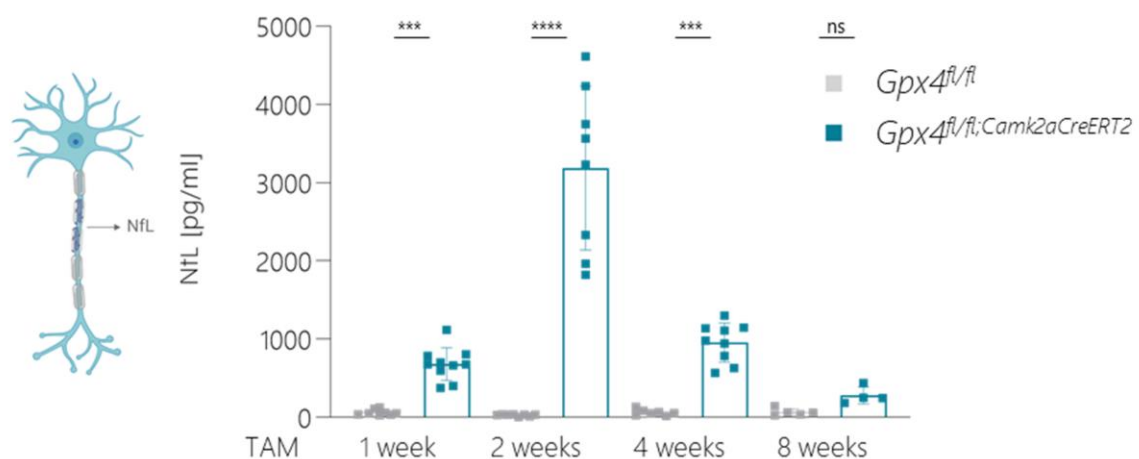
Figure 15| Progressive neurodegeneration can be detected by measuring circulating levels of NfL in plasma of *Gpx4fl/fl;Camk2aCreERT2* mice

Neurofilament light (NfL) level analysis in *Gpx4fl/fl;Camk2aCreERT2* animals was conducted using Simoa NF-light® assay. A marked (10-fold) increase of NfL level was apparent already 1 week after the inducible deletion of GPX4. This culminated in an approximate 100-fold increase at 2 weeks, while thereafter NfL levels dropped down to 15-fold by 4 weeks after TAM injection. It needs to mentioned that based on the sensitivity and dynamic range for plasma of this assay, values >1800 pg/ml should not be considered as absolute quantification The levels of NfL remained unchanged in control mice being generally below 100 pg/ml. Statistical analysis was performed using t-test, $p < 0.001$ (***), $p < 0.0001$ (***). n.s. = not significant.

One week after KO induction circulating NfL levels in plasma of *Gpx4fl/fl;Camk2aCreERT2* mice were already 10-fold higher than control mice with an average level of 680.8 (±198.7) pg/ml. At 2 weeks after TAM injection, the NfL level exceeded to about 100-fold in KO animals versus WT controls. These high NfL levels dropped by 4 weeks after KO induction to an around 15-fold increase in KO samples, with an average level of 957 (±234.9) pg/ml. Plasma samples of animals 8 weeks after TAM injection showed no significant differences in NfL levels, although the average level in *Gpx4fl/fl;Camk2aCreERT2* samples remained still slightly higher at 281.75 pg/ml

(Fig. 15). These data indicate a progressive neurodegenerative process induced by ferroptotic cell death in cortical neurons of *Gpx4$^{fl/fl;Camk2aCreERT2}$* mice with highest levels between 2 and 4 weeks after KO induction.

4.2 Proteomics analysis uncovers protein expression signatures reminiscent of human neuronal disorders

Although the histopathological analysis showed that ferroptosis of neuronal cells and associated neuroinflammatory processes underlie massive and progressive cortical atrophy, the molecular mechanisms remained unclear. To shed light into possible proteomic changes associated with neuronal ferroptosis, untargeted mass spectrometry-based proteomics analysis of cortex samples was performed at 1, 2 and 4 weeks after TAM treatment of mice (proteomics study was performed by Dr. Ashok Kumar Jayavelu, Max Planck Institute of Biochemistry, Munich).

In total, 4676 proteins were detected, of which 2952 were significantly altered in the cortex of *Gpx4* KO animals (Appendix Table 1). Analysis of proteomics results by principal component analysis (PCA) revealed clear segregation of *Gpx4* KO samples, particularly at later time points (Fig. 16A). A clear time-dependent change in the expression level of a vast number of proteins was observed following TAM treatment in the cortex of *Gpx4* KO, as shown in figure 16B. Unsupervised hierarchical clustering analysis showed both up- and downregulation of protein expression levels, which were more pronounced at 4 weeks after KO induction (Fig. 16B). Clustering of the samples revealed that samples from 4 weeks of TAM-induced *Gpx4$^{fl/fl;Camk2aCreERT2}$* mice clearly separated from all other groups. The finding that samples from 1 week TAM-induced *Gpx4$^{fl/fl;Camk2aCreERT2}$* mice are grouped with 1 week TAM-treated control mice demonstrated that only minor proteomic changes are evident at this time point.

Remarkably, the great majority of these regulated proteins had been previously linked to AD, dementia, neurodegeneration, inflammation or the immune system (Fig. 16C). A complete list of the proteins and their corresponding match categories, including gene ontology (GO) category 'immune system' (Appendix Table 2), literature mining (lit) via Genomatix (Appendix Table 3) and medical subject headings (MeSH) terms (Appendix Table 4) are available in the supplementary material section. Interestingly, the enriched proteins are equally distributed over all regulated proteins independent of their expression levels. According to the enrichment analysis via MeSH term diseases, most regulated proteins detected in the cortex of *Gpx4$^{fl/fl;Camk2aCreERT2}$* mice were linked to neurodegeneration, brain and CNS diseases, as

wells as dementia and Alzheimer's disease, which are the top 10 appearing MeSH-Terms (Fig. 16C).
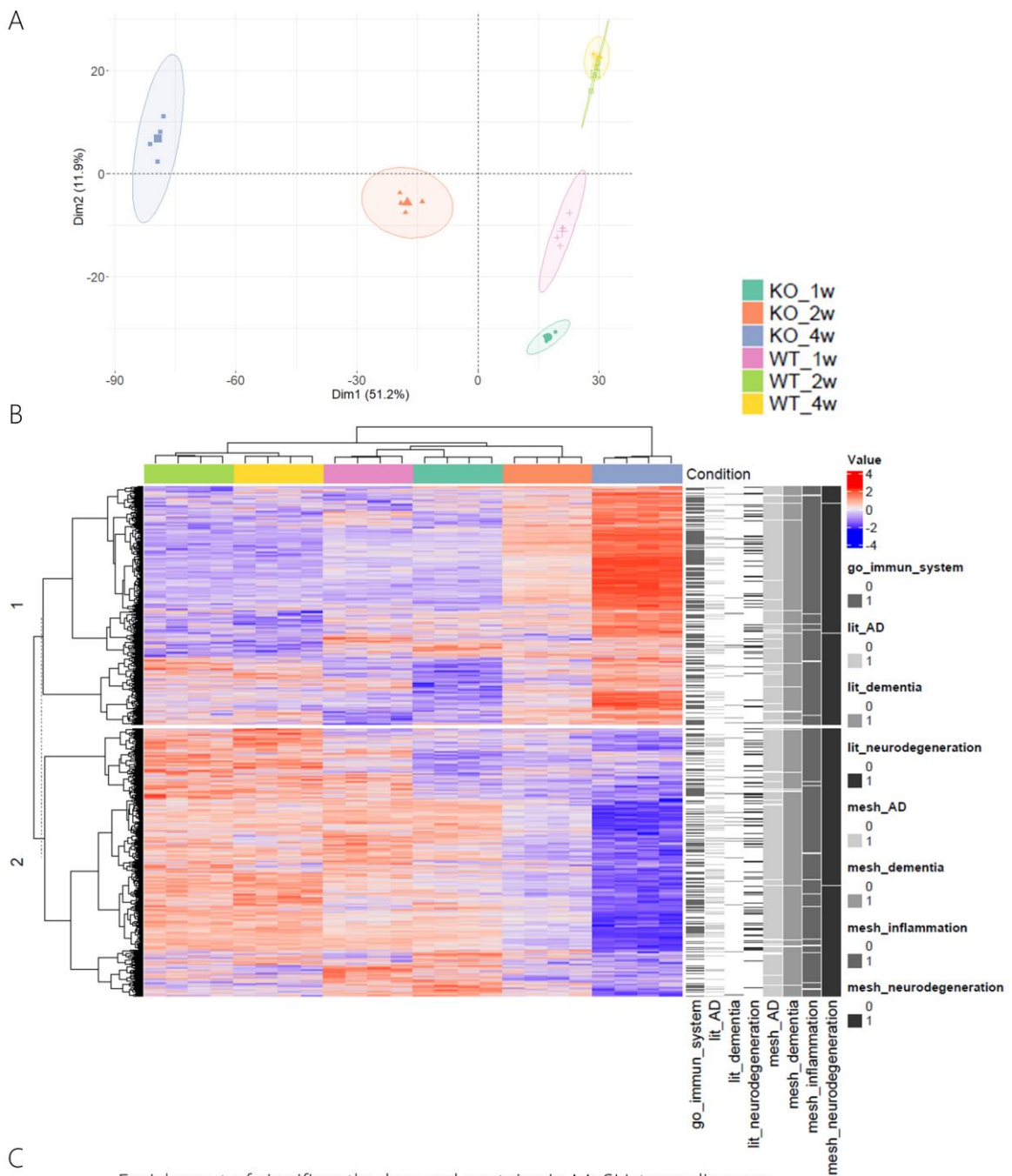
Figure 16| Proteomic changes associated with neuronal ferroptosis are tightly linked to neurodegenerative diseases

A| Based on the protein levels of significantly regulated proteins according to the one-way ANOVA of *Gpx4* KO and WT cortex samples (P adjusted < 0.05) a principal component analysis (PCA) was performed by using the FactoMineR package in R. For the PCA, the data were scaled to unit variance. B| Profound proteomic time-dependent changes in the cortex following neuron-specific deletion of *Gpx4*. Unsupervised cluster analysis of significantly altered protein levels (one-way ANOVA) after *Gpx4* KO induction are represented by a heat map. Hierarchical clustering of mouse cortex samples after 1, 2 and 4 weeks TAM treatment is displayed by the top dendrogram. Cortex samples of *Gpx4*^{fl/fl;Camk2aCreERT2} mice 4 weeks after KO induction ("KO_4w") clearly separate from all other conditions. The dendrogram on the left shows clustering of protein expression levels. Increased protein levels are shown in red, while decreased protein levels are indicated in blue. Significantly regulated proteins were classified according to MeSH disease categories (annotated by "mesh_neurodegeneration", "mesh_inflammation", "mesh_dementia" and "mesh_AD" (Alzheimer's Disease)), literature mining ("lit_neurodegeneration", "lit_dementia" and "lit_AD") or to the Gene Ontology term "go_immun_system", as displayed on the right. B| Regulated proteins are tightly linked to brain and CNS diseases. Pathway enrichment analysis of significantly altered protein levels across all GPX4 KO and WT samples (one-way ANOVA) in the category MeSH Disease of the GeneRanker (Genomatix, Germany). Diseases of the top mostly overrepresented terms are shown in descending order on the y-axis and the corresponding -log10 transformed P values on the x-axis.

Furthermore, volcano plots generated using individual data sets of each specific time point revealed the top regulated proteins (Fig. 17 and Appendix Table 5-7). After 1 week of *Gpx4* KO induction, the neuron-specific cytoskeletal protein microtubule-associated protein 2 (MAP2) was significantly downregulated (Fig. 17A). Similarly, the neuronal phosphoprotein synapsin-1 (Syn1) expression was considerably downregulated after 2 weeks after KO induction (Fig. 17B). Whereas, Hexb (hexosaminidase subunit beta), Apoe, Gfap, C1qc (complement C1q C chain), Clu (clusterin) were the top upregulated hits. After 4 weeks of *Gpx4* KO induction, a vast array of proteins were upregulated, including Vim (vimentin), Fabp7 (fatty acid binding protein 7), Lcp1 (lymphocyte cytosolic protein1), Ctss and Ctsd (cathepsin S and D) as well as Ptpn6 (protein tyrosin phosphatase non-receptor type 6) (Fig. 17C). In contrast, Nedd8 (ubiquitin-like protein Nedd8) and cytohesin-1 (Cyth1) were significantly decreased.
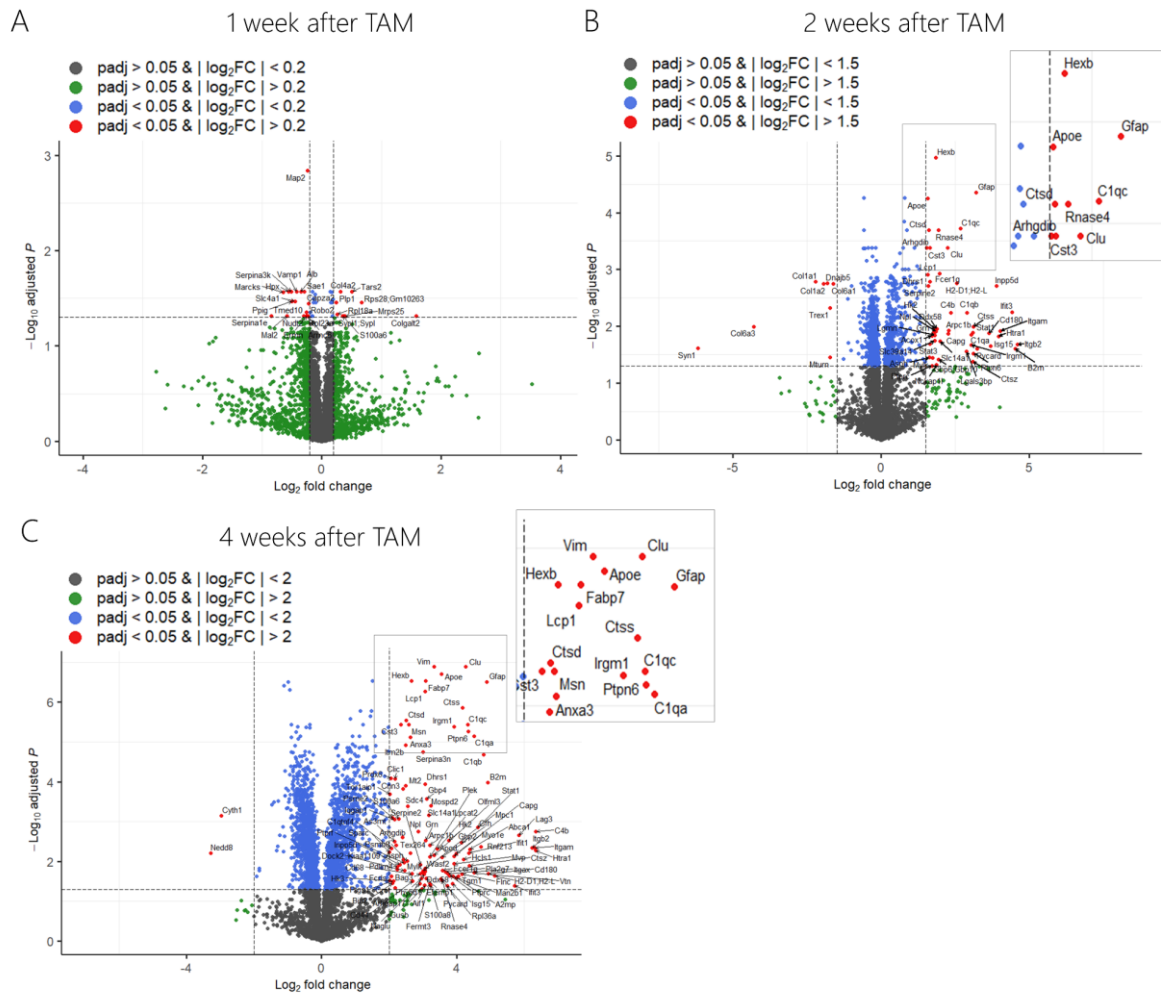
Figure 17| Proteomic signature in response to ferroptotic neuronal cell death
Volcano plots summarizing the proteomic changes in the cortex of *Gpx4* KO versus WT mice. A one-way ANOVA between Gpx4 KO and WT tissue was performed; volcano plots were calculated using log$_2$ fold changes (FC) and log$_{10}$-transformed p-values for each individual time point. The threshold value of adjusted p-value was set to p<0.05 and the log$_2$ FC was set individually for each time point due to the huge number of upregulated proteins. Red circles show proteins significantly altered in *Gpx4$^{fl/fl;Camk2aCreERT2}$* cortex compared to WT animals. A| MAP2 was drastically downregulated after 1 week of *Gpx4* deletion. The vertical line denotes log$_2$ FC =0.2. B| Expression levels of Hexb, Apoe, Gfap, C1qc and Clu were the top most upregulated proteins 2 weeks after *Gpx4* KO induction. The vertical line denotes log$_2$ FC =1.5. C| Massive upregulation of distinct proteins 4 weeks after *Gpx4* deletion. Vertical line denotes log$_2$ FC =2. Unpaired two-sided t-test assuming unequal variance was performed on log$_2$ transformed protein expression levels of GPX4 KO versus WT samples after KO induction. P-value correction was performed using the Benjamini and Hochberg method (Appendix table 5-7).

4.3 Lipidomics analysis reveals different lipid class distribution in neuron-specific *Gpx4* KO mouse cortex

Considering that lipids comprise half of the brain mass, predominantly found in neuronal cells [276, 277], and that lipid peroxidation of cellular membranes is the hallmark of ferroptosis [54], a detailed lipidomics analysis of the *Gpx4$^{fl/fl;Camk2aCreERT2}$* mouse line was performed.

A

B

C

PLs

1 week after TAM   2 weeks after TAM   4 weeks after TAM

(continued on next page)
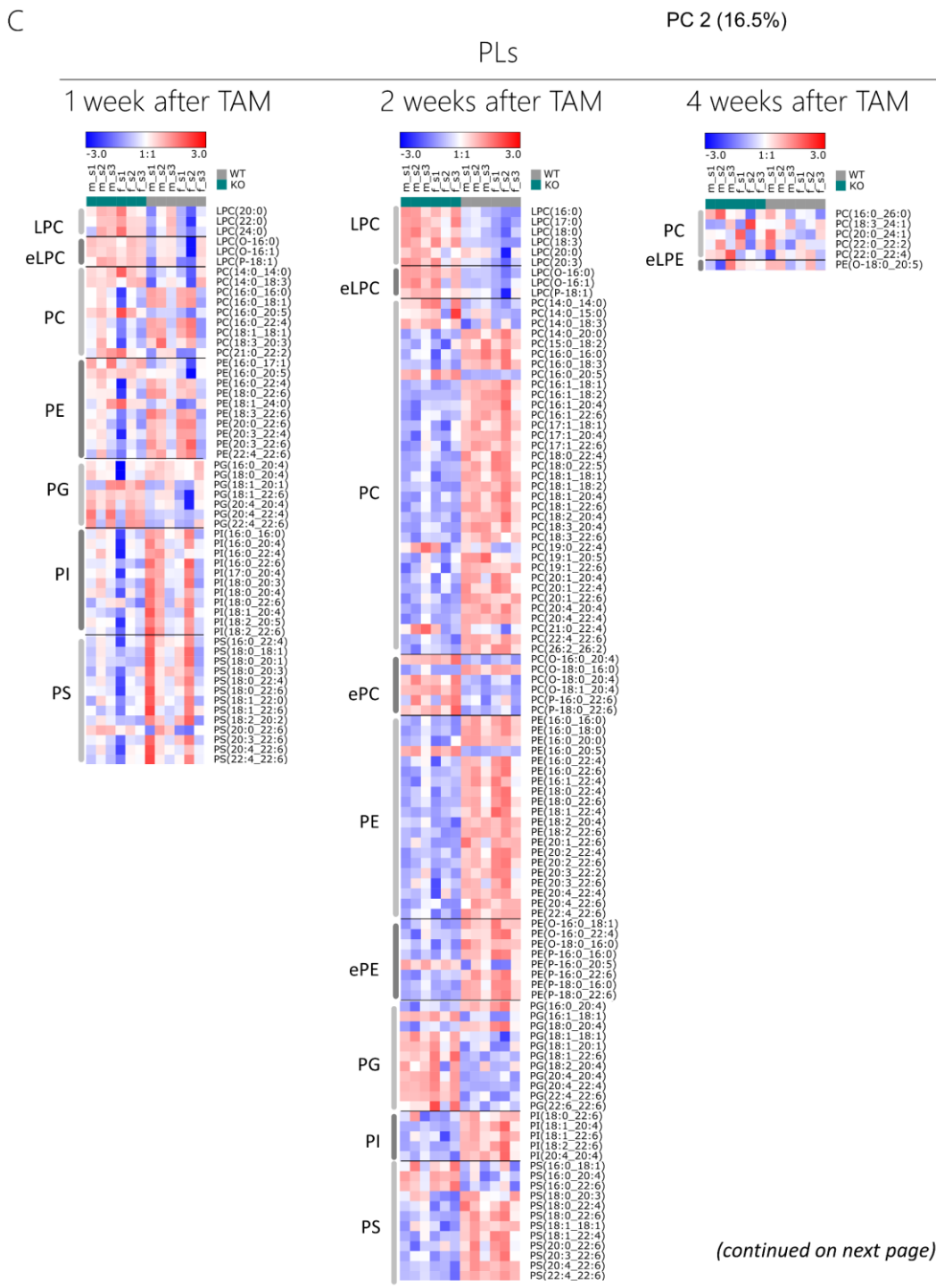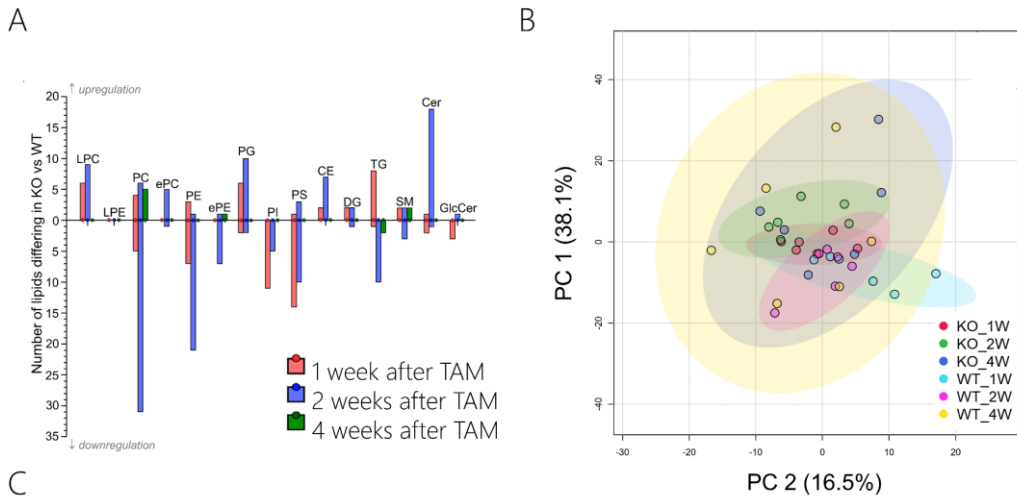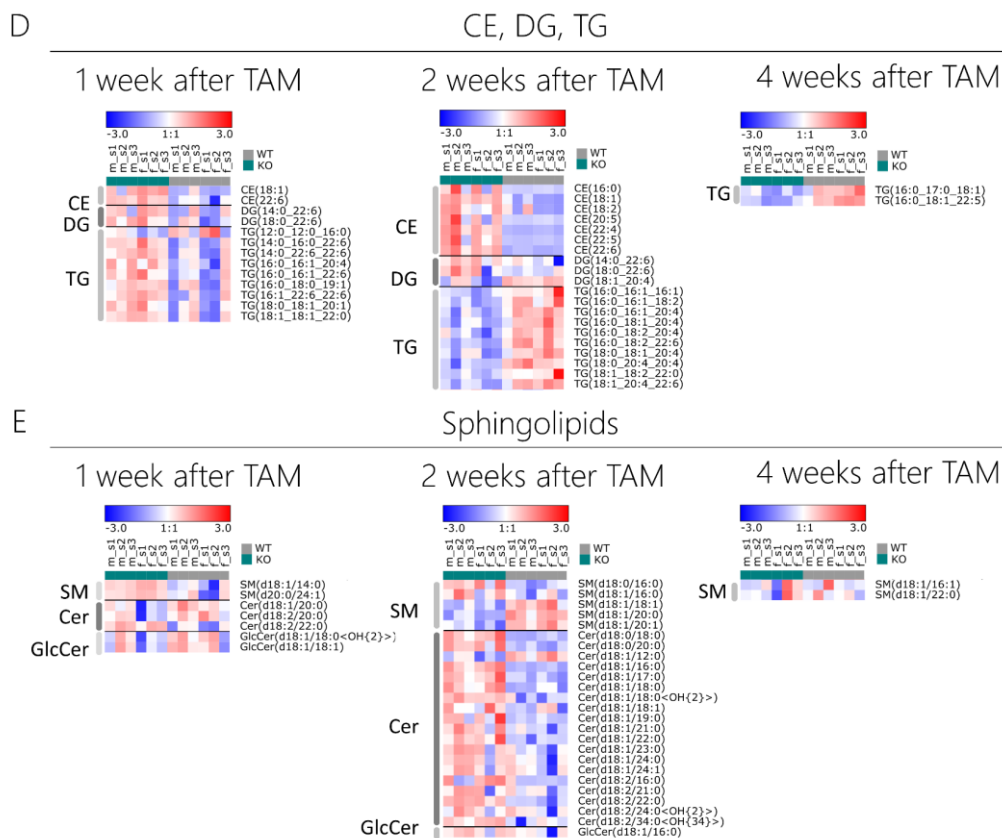
Figure 18| Lipidomic signatures in response to glutamatergic neuron-specific deletion of *Gpx4*

A|. Glycerophospholipids are predominantly regulated in cortex of neuron-specific *Gpx4* KO mice. Fold change analysis was performed with normalized lipidome data of cortex samples indicating massive remodeling in lipidome two weeks after KO induction. Color code illustrates samples at 1 (red), 2 (blue), and 4 (green) weeks after KO induction. B| Based on the normalized levels of significantly regulated lipids of *Gpx4* KO and WT cortex samples a PCA was performed using MetaboAnalystR. Clear separation was only observed at two weeks after KO induction. C-E| Significantly regulated PL species; such as CE, DG, TGs and sphingolipids, after KO induction are illustrated in the heat maps. Lipid extracts were analyzed using LC-MS and normalized to tissue weight. Data were normalized by mean centering and divided by the standard deviation. Mean values are represented by white squares (1:1, no change), red and blue indicate up- and downregulation compared to the mean value, respectively. Corresponding FC and P-value (FDR) cutoffs are 1.3 and 0.1, respectively. Abbreviations: PL, phospholipids; LPC, lysophosphatidylcholine; LPE, lysophosphatidylethanolamine; PC, phosphatidylcholine; ePC, ether PC; PE, phosphatidylethanolamine; ePE, ether PE; PG, phosphatidylglycerol ;PI, phosphatidylinositol; PS, phosphatidylserine; CE, cholesteryl ester; DG, diglycerol; TG, triglyceride; SM, sphingomyelin; Cer, ceramide; GlcCer, glucosylceramide

A comprehensive non-targeted lipidomics profiling workflow was established, along with our close collaborator Dr. Maria Fedorova (University of Dresden/Leipzig) to investigate the effect of *Gpx4* deletion in mouse cortex lipidome. After TAM treatment (1, 2 and 4 weeks) of animals, lipid extracts from cortex samples were analyzed using LC-MS/MS (performed by Fedorova's group). Non-targeted lipidomic analysis identified 556 different lipid species from distinct lipid categories and classes. The most prominent changes in the lipidome occurred 2 weeks after KO induction in cortical tissue of *Gpx4^fl/fl;Camk2aCreERT2* mice, in which the level of 157 lipid species were significantly altered (Fig. 18A). PCA assessing differences in the cortex lipidome

showed segregation between *Gpx4* KO and WT 2 weeks after KO induction (Fig. 18B). *Gpx4* deletion induced a moderate change in cortex lipidome after one week, whereas after 4 weeks only mild alterations in the level of a distinct number of lipid species were detected (Fig. 18C-E).

The most pronounced PL changes after 2 weeks of KO induction is shown in figure 18C. At this time point, phosphatidylcholine (PC), the most abundant PL in biological membranes [278], as well as phosphatidylethanolamine (PE) and ether PE (ePE) were mostly decreased in *Gpx4* KO mice. Noticeably, only PC(16:0_20:5) and PE(16:0_20:5) were higher in cortex of *Gpx4^{fl/fl;Camk2aCreERT2}* mice. PCs and PEs are generally enriched in neurons, and thus the reduction of these lipids is in line with the specific loss of cortical neurons in *Gpx4* KO mice [277]. In contrast, lysophosphatidylcholine (LPC), which are mainly produced from PC by phospholipase A2 [279], and eLPC were significantly more abundant in *Gpx4* KO animals.

Changes in the level of phosphatidylglycerol (PG), phosphatidylinositols (PI) and phosphatidylserines (PS) were evident at 1 and 2 weeks after KO induction, whereas at 4 weeks, no significantly regulated lipids of these groups were detected (Fig. 18C). Levels of PUFA containing PG were particularly higher in *Gpx4* KO animals 2 weeks after KO induction. In contrast, PUFA containing PI and PS were less abundant in *Gpx4* KO animals.

Next, comparing cholesteryl esters (CE), triglycerides (TG) and diglycerols (DG) (Fig. 18E), TG were predominantly enriched in cortex 1 week after KO induction. This pattern changed over time, as TGs (most likely C20 and C22 containing TGs) were significantly lower in 2 and 4 weeks after KO induction. A strong effect was observed for CEs, which are highly abundant in *Gpx4* KO animals. CEs do not contribute to membrane structures but collect and store free FA [278].

The regulation pattern of sphingomyelin (SM) species 2 weeks after KO induction showed a higher abundance of two palmitoyl-containing SMs, namely SM(d18:0/16:0) and SM(d18:1/16:0) and a lower abundance of longer-chain SMs. Furthermore, ceramides (Cer) serve as a bioactive sphingolipid and are centered in the so-called "salvage pathway", which describes a recycling pathway to generate Cer [280-282]. The great majority of Cer species were elevated in *Gpx4* KO animals. The regulation patterns of DG and glucosylceramide (GlcCer) were not distinct in the cortex samples.

In brain, (phospho)lipid metabolism plays a central role in energy storage, the functional unit of cellular membranes and as signaling molecules [283]. Overall, the lipidomics analysis

uncovered significantly regulated lipid species in cortex, mainly 2 weeks after KO induction, suggesting lipidome remodeling upon *Gpx4* deletion probably as an early event.

4.4 Cortical atrophy can be rescued by the Cys-variant of GPX4, but not by the knockout of ACSL4

Previously, our laboratory identified and characterized ACSL4 as an important fatty acid ligase essential for the ferroptotic process at least in cultured cells [28]. Pharmacological inhibition or genetic deletion of ACSL4 conferred an unprecedented protection against ferroptosis induced by ferroptosis inducing agents or by genetic ablation of *Gpx4* in cultured cells. To address whether the progressive phenotype and cortical atrophy can be rescued by loss of ACSL4 *in vivo*, *Gpx4$^{fl/fl;Camk2aCreERT2}$* mice were crossbred with *Acsl4$^{fl/fl}$ x Gpx4$^{fl/fl}$* double transgenic mice. Since the *Acsl4* gene is located on the X-chromosome, male *Acsl4$^{y/fl}$ x Gpx4$^{fl/fl}$* double transgenic mice (generated by Dr. Sebastian Doll [231]) were crossbred with female *Gpx4$^{fl/fl;Camk2aCreERT2}$* mice. In order to achieve homozygosity of both alleles, *Acsl4$^{wt/fl}$ x Gpx4$^{fl/fl;Camk2aCreERT2}$* were again crossed with *Acsl4$^{y/fl}$ x Gpx4$^{fl/fl}$* double transgenic mice, resulting in homozygous *Acsl4$^{fl/fl}$ x Gpx4$^{fl/fl;Camk2aCreERT2}$* mice (Fig. 19A). TAM treatment of these mice thus causes simultaneously deletion of both genes in the same cell type.

TAM-treated *Acsl4$^{fl/fl}$ x Gpx4$^{fl/fl;Camk2aCreERT2}$* double KO (DKO) mice were surprisingly indistinguishable from neuron-specific *Gpx4$^{fl/fl;Camk2aCreERT2}$* mice in their overall phenotype and behavior. Tissue and plasma samples from *Acsl4$^{fl/fl}$ x Gpx4$^{fl/fl;Camk2aCreERT2}$* were collected at 1, 2 and 4 weeks after TAM injection in order to compare with samples derived from *Gpx4$^{fl/fl;Camk2aCreERT2}$* mice. Comparing the expression levels of GPX4 and other CNS markers mentioned in the foregoing (see 4.1.4), expression of GFAP and IBA1 remained unchanged in KO and DKO cortical tissue (Fig. 19B). Furthermore, histopathological analysis of sagittal brain sections did not reveal any overt differences between *Acsl4$^{fl/fl}$ x Gpx4$^{fl/fl;Camk2aCreERT2}$* mice and *Gpx4$^{fl/fl;Camk2aCreERT2}$* mice, with a loss of cortical layers and massive cortical atrophy of DKO mice (Fig. 19C). The comparison of NfL plasma levels from GPX4 KO and ACSL4/GPX4 DKO mice only showed a slight yet significant improvement in DKO mice (difference 220 ±71.23 pg/ml) 1 week after TAM, whereas at 2 and 4 weeks after KO induction, NfL plasma levels were massively increased in DKO mice indistinguishable from KO mice (Fig. 19D). Thus, it can be concluded that the additional KO of *Acsl4* in glutamatergic neuron-specific *Gpx4* KO mice does not allow rescue of the profound histopathological phenotype in brain tissue of *Gpx4$^{fl/fl;Camk2aCreERT2}$* mice, which is in stark contrast to what was reported in cultured cells [28].

According to Ingold *et al.* mice expressing one allele of the Cys-variant of GPX4 (Gpx4U46C: targeted replacement of the catalytically active selenocysteine to Cys) were protected against acute kidney injury induced by TAM-inducible systemic deletion of wt *Gpx4* in adult mice [44]. To address if the expression of the *Gpx4* allele carrying this Gpx4U46C mutation [44] may suffice to rescue the described phenotype, conditional mice expressing the hypomorphous GPX4 variant were generated. To this end, *Gpx4^{cys/wt}* mice [44] were mated with cortical neuron-specific *Gpx4^{fl/fl;Camk2aCreERT2}* mice, yielding *Gpx4^{cys/fl;Camk2aCreERT2}* mice. *Gpx4^{cys/fl;Camk2aCreERT2}* mice were then treated with TAM, causing deletion of the floxed *Gpx4* allele, while maintaining expression of the Cys-variant of GPX4 expressed by the second allele (Fig. 19A). In contrast to *Gpx4^{fl/fl;Camk2aCreERT2}* and *Acsl4^{fl/fl}*x *Gpx4^{fl/fl;Camk2aCreERT2}* double mutant mice, *Gpx4^{cys/fl;Camk2aCreERT2}* mice showed no striking phenotype or altered behavior upon KO induction. This strongly suggests that the Cys variant of GPX4 can largely prevent neuronal cell death of WT GPX4-deprived glutamatergic neurons of the cortex. This was corroborated by immunoblotting against GFAP, IBA1 and NeuN, which showed similar expression level compared to *Gpx4^{fl/fl}* control cortex (Fig. 19B). GPX4 expression level is high in *Gpx4^{cys/fl;Camk2aCreERT2}* mice, which was expected due to the facilitated co-translational incorporation of Cys in GPX4 (Fig. 19B). In addition, brain sections of *Gpx4^{cys/fl;Camk2aCreERT2}* cortex area displayed an unaltered layered cortex and no increase in the volume of the ventricles. Only at the latest time point, 6 months after KO induction, a decrease in cortical mass could be detected (Fig. 19C). However, overall the analysis of *Gpx4^{cys/fl;Camk2aCreERT2}* cortex indicates a clear rescuing effect of the described progressive cortical atrophy in *Gpx4^{fl/fl;Camk2aCreERT2}* mice. When studying the level of NfL in plasma samples of the different compound mutant mice, *Gpx4^{cys/fl;Camk2aCreERT2}* mice showed significantly lower levels of NfL at 1 and 2 weeks after TAM injection compared to *Gpx4* KO animals (Fig. 19D). Yet, at 4 weeks after TAM treatment, an increase of NfL could also be noticed in *Gpx4^{cys/fl;Camk2aCreERT2}* mice reaching the same levels as *Gpx4* KO and *Acsl4/Gpx4* KO animals. These results suggest that the expression of the Cys variant of GPX4 rather slows down the development of the phenotype but fails to entirely prevent neurodegeneration.
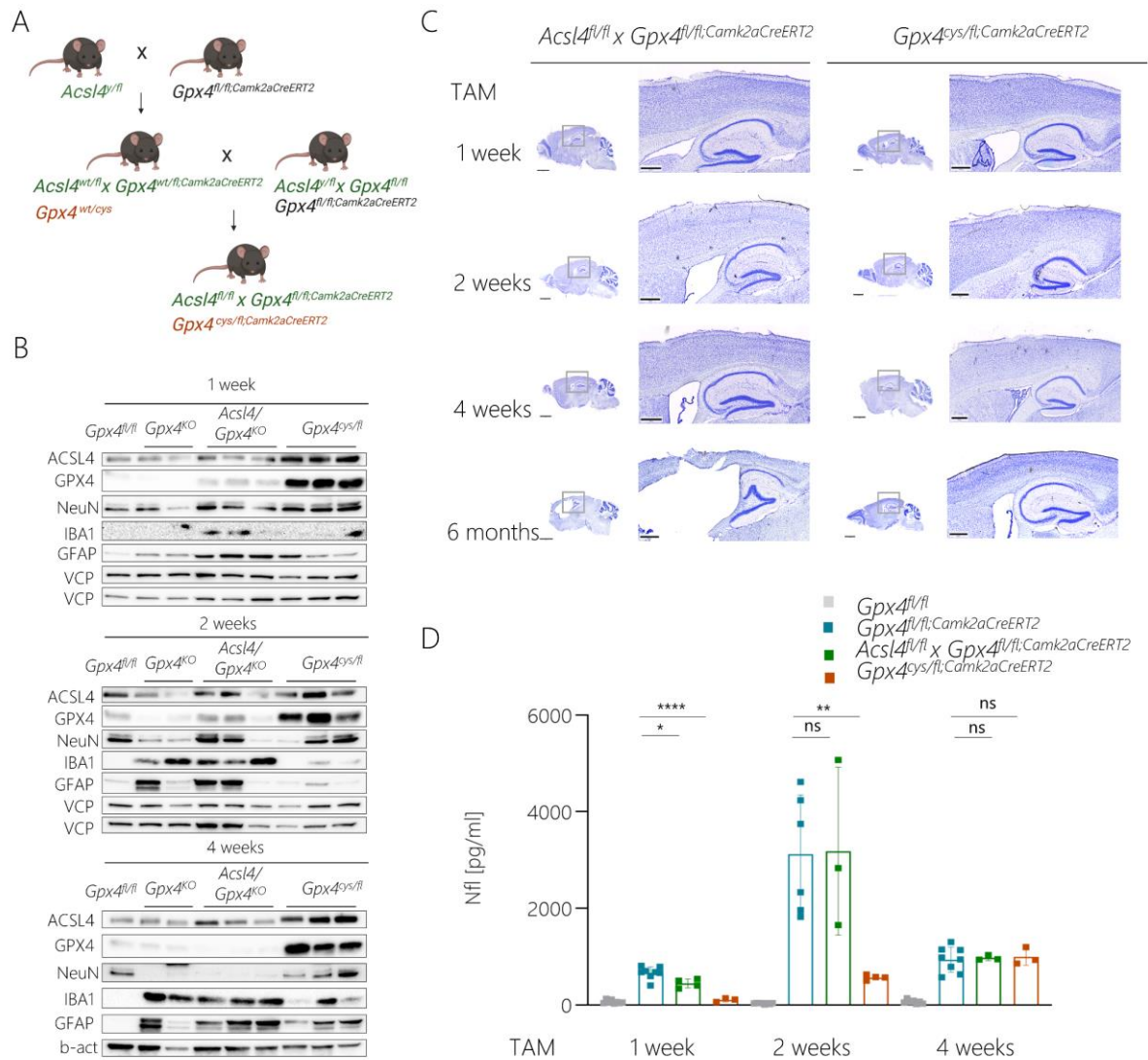
Figure 19| The GPX4U46C variant of GPX4, but not the KO of ACSL4 can rescue progressive cortical atrophy of *Gpx4^fl/fl;Camk2aCreERT2* mice

A| Breeding scheme for the generation of inducible glutamatergic neuron-specific *Acsl4^fl/fl xGpx4^fl/fl;Camk2aCreERT2* mice by crossbreeding *Gpx4^fl/fl* mice with the conditional *Acsl4^fl/fl* mouse line (green). Generation of *Gpx4^cys/fl;Camk2aCreERT2* mice by crossbreeding *Gpx4^fl/fl;Camk2aCreERT2* mice with *Gpx4^cys/wt* mice, expressing one allele of the Cys-variant of GPX4 (orange). B| Nissl staining of brain samples illustrates a progressive loss of cortical layers and cortical atrophy in *Acsl4^fl/fl x Gpx4^fl/fl;Camk2aCreERT2* mice. This progressive phenotype is rescued in *Gpx4^cys/fl;Camk2aCreERT2* mice. C| Immunoblot analysis of GPX4, ACSL4, NeuN, IBA1, GFAP and VCP/b-act of cortex samples at 1, 2 and 4 weeks after TAM was performed comparing *Gpx4^fl/fl*, *Gpx4^fl/fl;Camk2aCreERT2*, *Acsl4^fl/fl x Gpx4^fl/fl;Camk2aCreERT2* and *Gpx4^cys/fl;Camk2aCreERT2* . D| NfL levels in plasma of *Acsl4^fl/fl x Gpx4^fl/fl;Camk2aCreERT2* mice exhibit a moderate increase at 1 week after TAM treatment (unlike *Gpx4^cys/fl;Camk2aCreERT2* mice), which is followed by a massive increase at 2 weeks after TAM application, indistinguishable from *Gpx4^fl/fl;Camk2aCreERT2* mice. At 4 weeks after KO induction, the NfL levels were clearly reduced in plasma samples of *Acsl4^fl/fl x Gpx4^fl/fl;Camk2aCreERT2* and *Gpx4^fl/fl;Camk2aCreERT2* mice, comparable to those of *Gpx4^cys/fl;Camk2aCreERT2* mice. Statistical analysis was performed using t-test, $p < 0.05$ (*), $p < 0.01$ (**), $p < 0.001$ (***) $p < 0.0001$ (****). n.s. = not significant.

4.5 The ferroptosis inhibitor Lip-1 partially prevents neuronal demise of *Gpx4^{fl/fl;Camk2aCreERT2}* mice

The development of *in vivo* efficacious ferroptosis inhibitors is an essential step towards novel pharmacotherapies to combat neurodegenerative disorders, such as AD, FTD and ALS, which might be ultimately linked to ferroptosis. This is even more relevant in light of the data presented in this thesis (see 4.2), where it was shown that cortical neurons dying by ferroptosis yielded molecular signatures highly reminiscent of AD and other NDs. To this end, *Gpx4^{fl/fl;Camk2aCreERT2}* mice were pharmacologically treated with the small molecule Lip-1, a spiroquinoxalinamine and highly efficient ferroptosis inhibitor. Initially shown to ameliorate tissue damage inflicted by transient IRI in liver and in a genetic model of *Gpx4* deficiency (i.e., *Gpx4^{fl/fl;Rosa26CreERT2}* mice), Lip-1 has been repeatedly shown to be tissue-protective in a series tissues and diseases scenarios [15, 24]. Although Lip-1 only moderately crosses the blood brain barrier (BBB) (unpublished data), it was nonetheless put to test whether Lip-1 might mitigate neuronal loss in TAM-treated *Gpx4^{fl/fl;Camk2aCreERT2}* mice. *Gpx4^{fl/fl;Camk2aCreERT2}* mice were injected daily with 20 mg/kg BW Lip-1, starting two days prior to TAM injection for a period of 12 days (Fig. 20A). *Gpx4^{fl/fl;Camk2aCreERT2}* mice treated with vehicle and *Gpx4^{fl/fl}* mice with Lip-1 served as control groups. In order to investigate if Lip-1 administration can rescue at this early time point, the expression of neuronal and astrocyte markers, as well as the levels of circulating NfL in plasma of Lip-1 treated animals were analyzed.
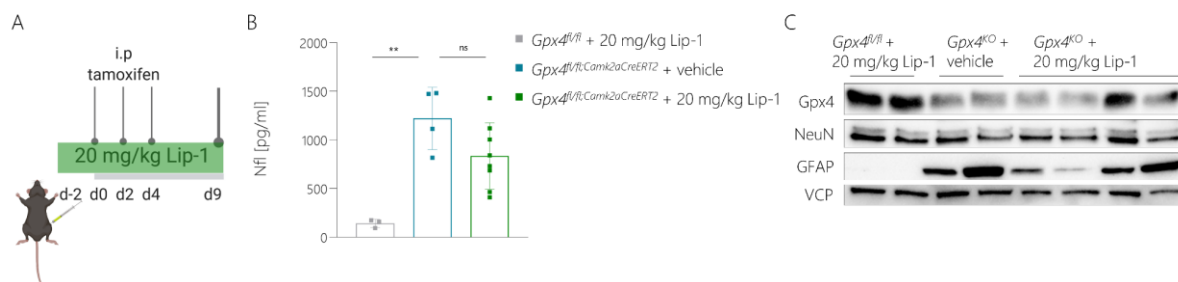
Figure 20| The ferroptosis inhibitor Lip-1 tends to protect against neuronal demise of *Gpx4^{fl/fl;Camk2aCreERT2}* mice
A| The treatment paradigm illustrating daily i.p. injections of 20 mg/kg BW Lip-1 for a period of 12 days in addition to the KO induction by administration of TAM at days 0, 2 and 4. B| Although NfL level analysis did not show significant changes upon Lip-1 treatment, there was a clear tendency towards lower levels of NfL in Lip-1 treated animals. Statistical analysis was performed using t-test, $p < 0.01$ (**); n.s. = not significant. C| Immunoblot analysis of GPX4, NeuN and GFAP of cortex samples showed no significant differences of GFAP and NeuN expression levels among the untreated and Lip-1 treated groups.

The pharmacological treatment of *Gpx4^{fl/fl;Camk2aCreERT2}* mice with 20 mg/kg Lip-1 did not reach a statistically significant rescue of neuronal cell death as determined by measuring NfL levels in plasma of mice (Fig. 20B). Despite the high variation of NfL in plasma samples, there was,

however, a clear yet not significant difference in the means of untreated animals (1223 pg/ml) versus treated animals (837.3 pg/ml). Although, the expressions levels of GFAP and NeuN were not different between treated and untreated groups at this time point, plasma NfL levels and GFAP expression levels in cortex seem to be promising for the validation of further pharmacological studies (Fig. 20C).

4.6 hiPSCs-derived motor neurons are sensitive towards ferroptosis

The ability to differentiate hiPSCs opens up new opportunities for modeling cellular mechanisms of numerous human disorders, such as ALS, *in vitro*. In this regard, hiPSCs-derived MNs from ALS patients were used as a tool to study the impact of SOD1 mutations in the context of ferroptosis sensitivity and signaling in MN death. After establishing a suitable protocol for the differentiation of hiPSCs to MNs, pharmacological treatment was performed in order to investigate the sensitivity of MNs towards cell death inducing compounds. The differentiation protocol used herein forces hiPSCs via neuronal precursor cells (NPCs) to a highly enriched population of matured MNs by using a combination of small molecules in a defined medium based on the protocol by Du *et al.* [248] (see 3.3.5). This intermediated differentiation step to motor neuron precursors (MNPs) thus allows for the expansion of different batches of mature MN for cellular studies originating from same MNPs.

In most differentiation protocols, the medium is supplemented with B27, because it is an optimized serum-free supplement for neuronal cell culture. B27, however, contains several antioxidants (AO) (vitamin E, vitamin E acetate, superoxide dismutase, catalase, and glutathione) in high concentrations to reduce oxidative stress of cultured neuronal cells. In order to study cell viability and the susceptibility of MN to ferroptosis, B27 supplement was therefore replaced by B27-AO (i.e., B27 supplement lacking AO) on day 14 of differentiation. hiPSCs, derived from a 29-years-old fALS patient carrying a SOD1G85R mutation were used (MEW-2564, Harvard University) and further referred to as "Mut SOD1". WT MNs served as a control cell line, which was differentiated from an HMGU-internal cell line, referred to as hiPSCs HMGU#1 clone. The established protocol was further applied to another hiPSCs clone (#29d) from an 82-age-old patient carrying the SOD1L144F mutation. However, the cell proliferation rates and the differentiation efficiency of this clone were insufficient to include this mutant cell line in subsequent studies.

Fully matured MNs were obtained at day 30 of differentiation, which was validated by a fluorescent staining for different neuronal markers (Fig. 21). Comparing WT and SOD1 mutant cells, the differentiation efficiency was equally high, independent of B27 supplementation, as almost all cells were HB9- and choline acetyltransferase (CHAT)-positive, both of which are MN-specific markers (Fig. 21A). Furthermore, immunocytochemical analysis revealed an equal expression of microtubule-associated protein 2 (MAP2), neuron-specific class III beta-tubulin (TUJ1), which are mainly expressed in neuronal extensions, and kinesin superfamily protein

5a (KIF5a) (Fig. 21B-D). The immunocytochemical data showed that the differentiation of WT and SOD1 mutant derived hiPSCs resulted in pure MN cultures, which can be further utilized for cellular assays.
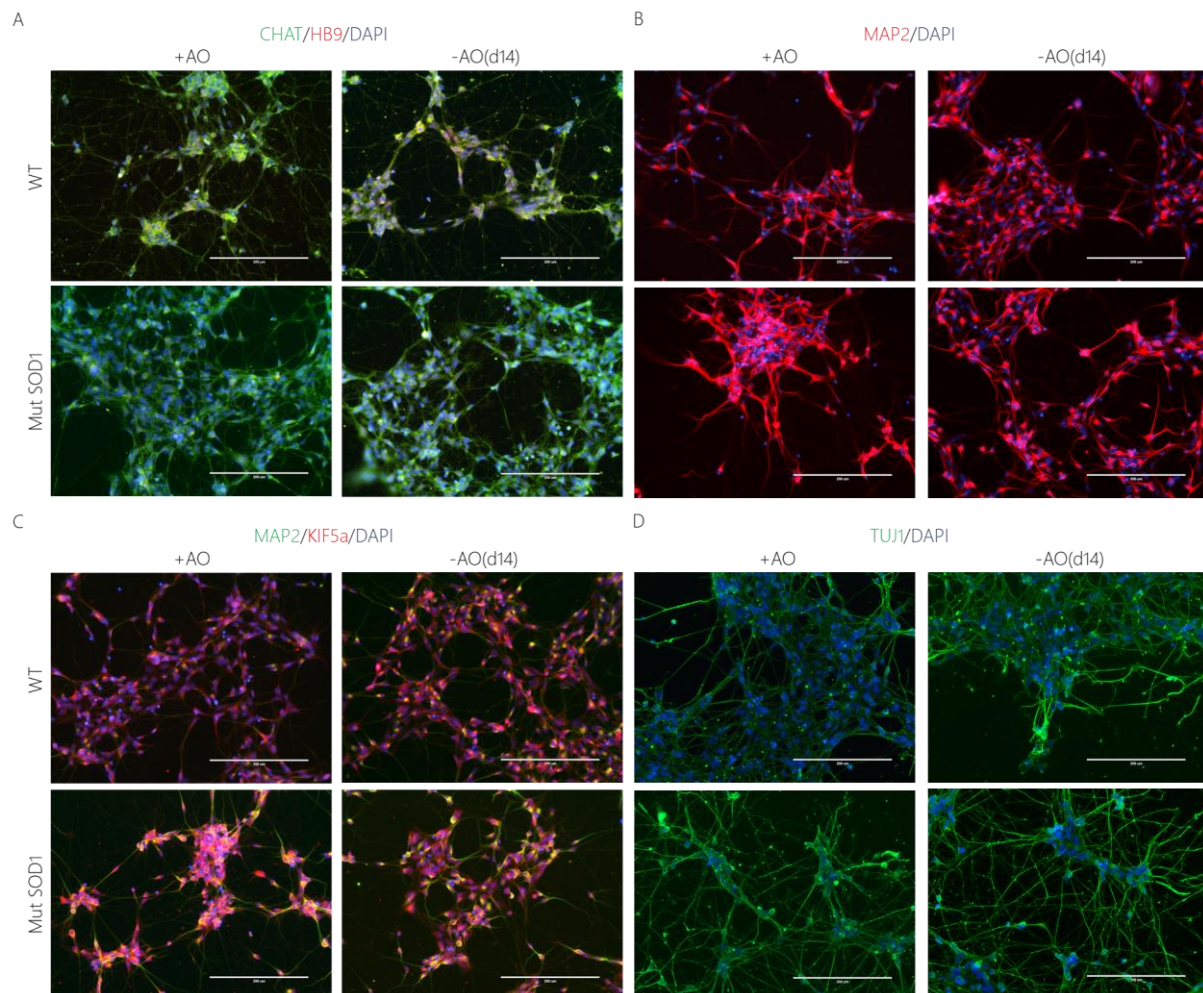
Figure 21| The expression of certain neuronal markers confirms the efficient differentiation of hiPSCs into MNs, regardless of B27 supplement and their genetic background

A| hiPSCs from WT or patient-derived hiPSCs carrying the SOD1L144F mutation (Mut SOD1) were differentiated in MNs. To confirm the proper differentiation under the different conditions, MNs were stained with neuronal markers such as CHAT/HB9/DAPI, (B) MAP2/DAPI, (C) MAP2/KIF5a/DAPI and (D) TUJ1/DAPI. Scale bar indicates 200 μm; pictures were taken by EVOS FL auto imaging, Thermo Fisher Scientific. Abbreviation: CHAT, choline acetyltransferase; HB9, homebox gene 9, DAPI, 4'-6-diamidino-2-phenylinodole; MAP2, microtubule-associated protein 2; KIF5a, kinesin superfamily protein 5a; TUJ1, neuron-specific class III beta-tubulin.

In order to challenge the differentiated MNs with different ferroptosis inducing agents and cytotoxic compounds, a broad panel of small molecules was used for the treatment of differentiated MNs. To this end, both, WT and SOD1 mutant cells were seeded in 96-well plates under AO-supplemented and AO-free conditions (B27+/- AO supplement from day 14) and incubated for three days prior to treatment in order to achieve proper attaching and connecting of neuronal cells. Cell viability was assessed after the treatment using Aquabluer™.

Canonical ferroptosis inducing agents included RSL3 (24 h), BSO (48 h) and erastin (48 h). Compared to WT cells, Mut SOD1 MNs were highly sensitive towards RSL3 and BSO treatment (Fig. 22). Furthermore, RSL3 treatment showed that Mut SOD1 MN were even more sensitive after the withdrawal of B27 supplementation at day 14 of differentiation. As expected, erastin treatment had no effect on cell viability of MNs, since the expression level of xCT, the main target of erastin, in neurons is known to be very low or even absent [284]. Similarly, MNs were resistant towards staurosporine treatment. The small difference between the groups might be due to slight variations in plating of differentiated cells lines. Hydroperoxide induced cell death was triggered by the treatment of cells with cumene and tBOOH, as well as H_2O_2, the latter a widely used tool to trigger necrotic cell death. In general, MNs were sensitive towards these inducers (Fig. 22), with Mut SOD1 derived MNs being significantly more sensitive compared to corresponding WT cells.

Since Mut SOD1 MN were found to be sensitive toward ferroptosis inducers, it was next addressed whether cell death can be inhibited by ferroptosis inhibitors or edaravone, a ROS-scavenger and FDA-approved drug used to treat ALS patients. Both, Lip-1 and a 3rd generation liproxstatin Lip-3 ameliorated RSL3-induced cell death already at nanomolar concentrations. Also, higher concentrations of edaravone could rescue ferroptosis in Mut SOD1 MNs. In addition, iFSP1, an inhibitor of FSP1 and sensitizer of ferroptosis in numerous human cancer cell lines [16], was used to treat MNs. While no toxic effects were observed when using iFSP1 alone, surprisingly it rescued RSL3-induced ferroptosis cell death at higher concentrations. Due to the observation that Mut SOD1 MNs in the absence of AO (-AO) could be rescued only with higher concentration of iFSP1, this suggests that iFSP1 may have some antioxidative effects at higher concentrations (Fig. 22). In sum, this data suggests that Mut SOD1 sensitizes differentiated MN towards ferroptosis, although additional cell lines from different patients are required to draw strong conclusions on a possible contribution of ferroptosis in familiar ALS.
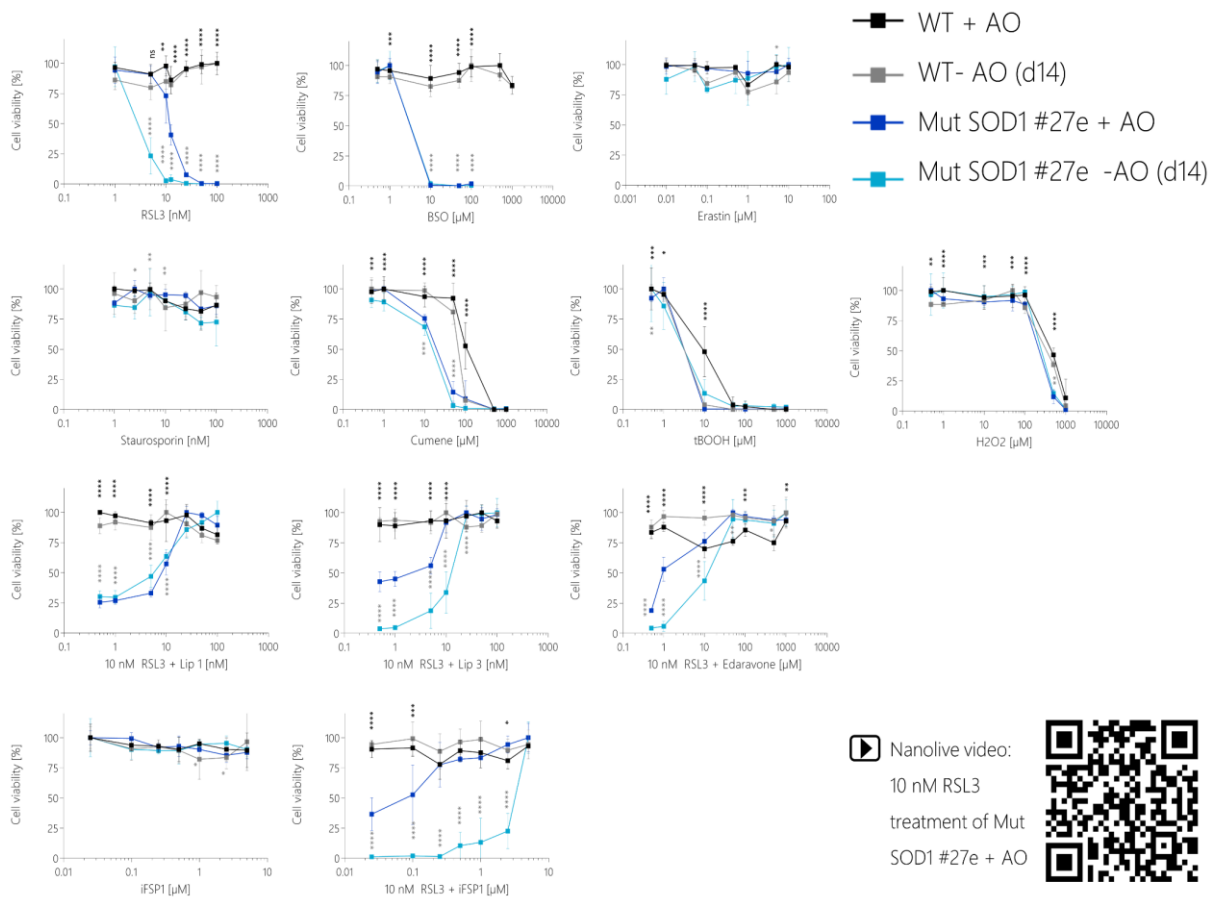
Figure 22| ALS patient-derived MNs are highly sensitive towards ferroptosis induction
A panel of small molecules was tested on WT and SOD1 mutant MNs (B27+/- AO supplementation at day 14 of differentiation). Ferroptotic cell death was induced using RSL3, BSO and erastin treatment. Staurosporin was used to trigger apoptosis. Hydroperoxide-induced ferroptosis was triggered by the treatment with cumene hydroperoxide and tBOOH. H_2O_2 was used as a general compound to trigger necrotic cell death. For the rescue experiments, RSL3-treated MNs were co-treated with Lip-1, Lip-3 and edaravone. In addition, iFSP1 and co-treatment of RSL3 and iFSP1 treatment were included to explore possible synergistic effects. The sensitivity of cells towards small molecule induced cell death was measured using Aquabluer™ assay. Statistical analysis was performed using t-test (WT vs. Mut SOD1), $p < 0.05$ (*), $p < 0.01$ (**), $p < 0.001$ (***), $p < 0.0001$ (****). n.s. = not significant. To open the video, scan the QR code and log in at mediatum.de (name: review-lorenz; password: DK78_dvT).

4.7 Analysis of *Gpx4* KO in motor neurons (MN) - a mouse model to study MN degeneration *in vivo*

4.7.1 Generation of MN-specific *Gpx4* KO mice

Mice with MN-specific deletion of *Gpx4* were generated by breeding *Gpx4$^{fl/fl}$* mice with transgenic mice expressing a constitutively active *Hb9Cre*. Heterozygous offspring were intercrossed to achieve homozygosity for both floxed *Gpx4* alleles and heterozygosity for the *Hb9Cre* allele. The *motor neuron and pancreas homeobox 1 gene, Mnx1* (Hb9) is selectively expressed at E9.25–E9.5 in MNs of the developing CNS [234]. Although MN-specific *Gpx4* KO mice are viable at birth and phenotypically indistinguishable from their WT littermates, a longitudinal analysis of the animals revealed progressive anatomic alterations in the KO animals. Weight determination showed that *Gpx4$^{fl/fl;Hb9Cre}$* mice gained less weight as compared to control mice over a time period of 100 weeks (Fig. 23A). At the age of 6 weeks, *Gpx4$^{fl/fl;Hb9Cre}$* mice failed to move up their tail from the ground, which further developed to a wavy and dragging tail by the age of 6 months (Fig. 23B). This apparent phenotype is illustrated in two short videos showing representative mice at the age of 6 and 17 months, respectively (Fig. 23C). Besides the wavy and dragging tail, *Gpx4$^{fl/fl;Hb9Cre}$* mice developed progressive kyphosis, illustrated in the lateral view by X-ray imaging of 12-months-old mice (Fig. 23E). The kyphosis index was then determined, which represents the ratio of the distance between caudal margin of the last cervical vertebra to the caudal margin of the sixth lumbar vertebra (distance AB) and the distance perpendicular to this line to the point of greatest curvature (distance CD). Both sexes of *Gpx4$^{fl/fl;Hb9Cre}$* mice tended to have a lower kyphotic index (Fig. 23F). Although these differences were not significant using t-test, it must be taking into account that the measured body length of 12-months-old mice still indicated significant changes; the kyphosis index has to be examined in relative terms. The body length of *Gpx4$^{fl/fl;Hb9Cre}$* mice was reduced by about 0.5 cm in both sexes compared to controls (Fig. 23G). Dual energy X-ray absorptiometry (DXA) scan of 1-year-old animals confirmed the significant difference in body weight. This technique was also used to perform bone mineral content (BMC) and density analysis, as well as to define fat and lean mass of the transgenic mice. BMC was significantly reduced in females (-19.7 %) and in males by around 15 % compared to age-matched controls (Fig. 23H).
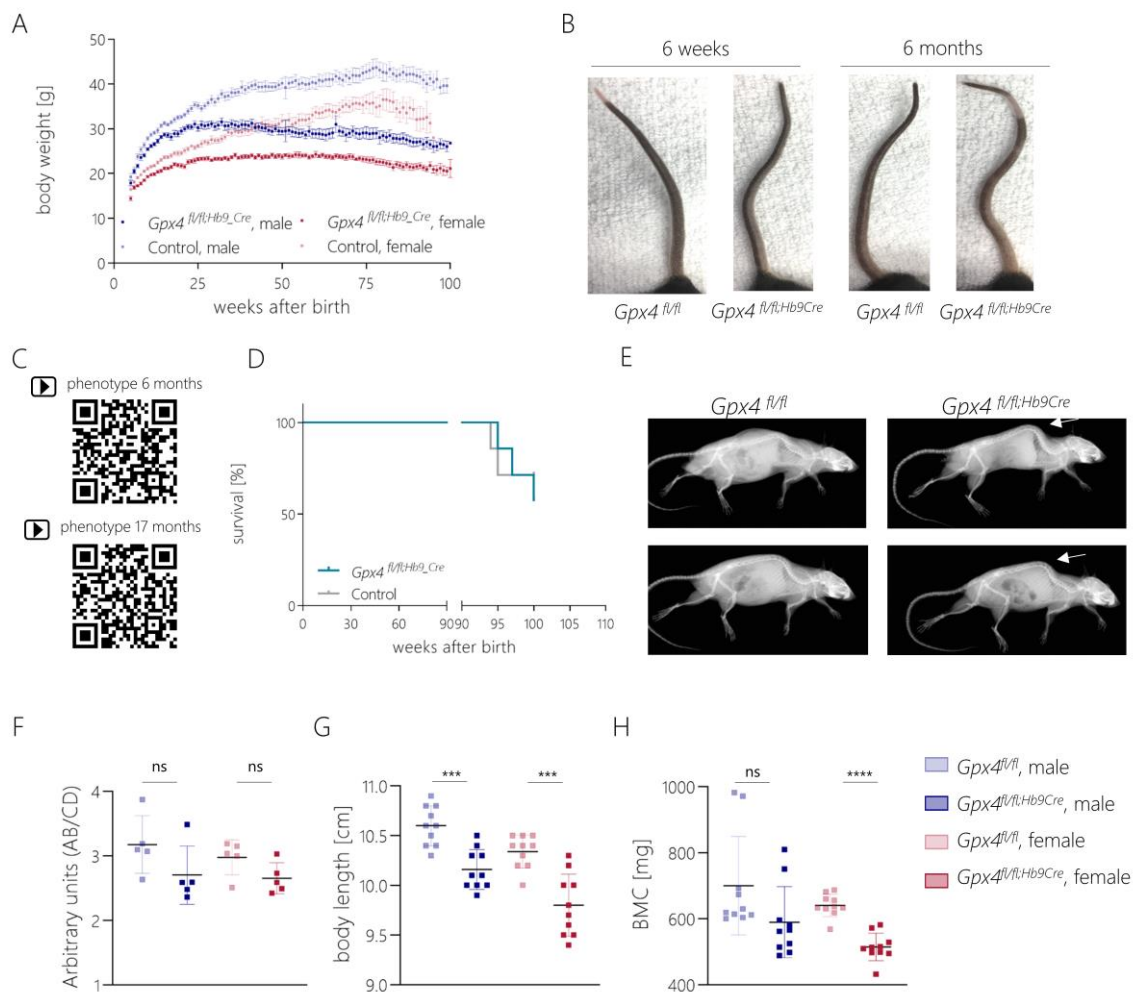
Figure 23| MN-specific *Gpx4* KO mice show skeletal abnormalities, decrease in body weight, abnormalities in tail lifting and body posture

A| MN-specific *Gpx4* KO mice showed less body weight gain as compared to WT mice, resulting in a markedly reduced body weight. B| *Gpx4fl/fl;Hb9Cre* mice developed a dragging and wavy tail over time, however overall survival was not affected D|. C| Videos from 6 months and 17 months old animals illustrate the changes in overall phenotype (name: review-lorenz and password: DK78_dvT to log in at mediatum to open the video sequences). E| The development of kyphosis was analyzed in X-ray scan with 12-months aged animals. F|. Kyphosis index was calculated at 12 months of age, showing no significant difference, despite clear signs of kyphosis. G| In contrast, body length was significantly reduced in *Gpx4* KO animals at 12 months of age. H| Bone mineral content (BMC) was reduced in *Gpx4fl/fl;Hb9Cre* mice. Statistical analysis was performed using t-test, $p < 0.001$ (***), $p < 0.0001$ (***). n.s. = not significant.

DXA analysis of fat and lean mass of a 12-months old cohort revealed a strong reduction in both, fat and lean mass in *Gpx4fl/fl;Hb9Cre* mice, resulting in a markedly reduced body weight. The ratio of lean and fat mass versus body weight showed that *Gpx4fl/fl;Hb9Cre* mice had an around 10 % decreased fat mass (Fig. 24A, B), and a nearly 15 % increased lean mass (Fig. 24D). A direct comparison of these ratios resulted in 60 % lean mass/body mass ratio for control animals and approximately 75 % in KO animals. The reduction in fat mass/body mass ratio manifested 30 % in controls and close to 21 % in *Gpx4* KO animals. The ratios were

independent from body mass (Fig. 24 C, E). Despite these changes in fat distribution, body size and weight, the overall survival was not altered between WT and KO animals. The maximal observation period was set to 100 weeks of age, when the first animals started to die due to general ageing (Fig. 23D).
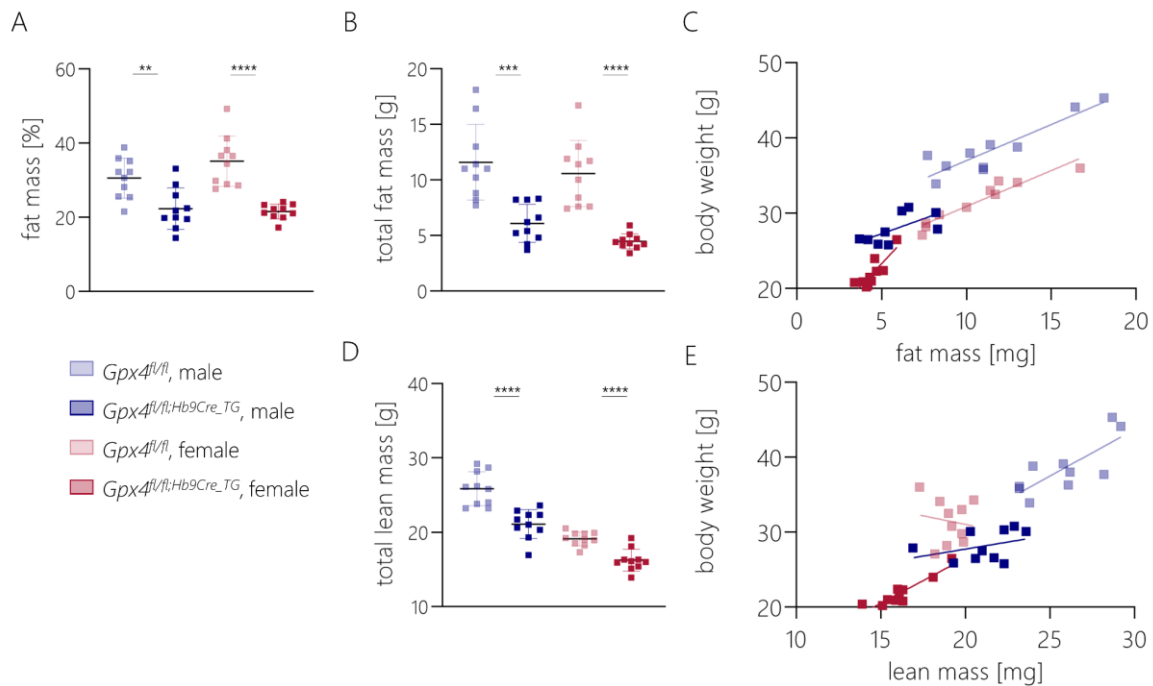
Figure 24| DXA (dual energy X-ray absorptiometry) scan of 1-year old mice show massive alterations in fat, but also lean mass of 12-months old *Gpx4$^{fl/fl;Hb9Cre}$* mice

A-C| The amount of fat was reduced nearly by 10 % in 12-months old *Gpx4$^{fl/fl;Hb9Cre}$* mice, independently from body mass as seen by determination of the content of fat mass(A) and total fat mass(B), as well as of body weight (C). D,E| Similarly, lean mass was significantly reduced in these mice compared to age-matched control. Statistical analysis was performed using t-test, $p < 0.01$ (**), $p < 0.001$ (***), $p < 0.0001$ (***). n.s. = not significant.

4.7.2 MN-specific *Gpx4* KO mice develop gait and behavioral abnormalities

Overall behavior and gait of MN-specific *Gpx4* KO mice were analyzed by a thorough neuro-behavioral screen at the GMC (German Mouse Clinic at the Helmholtz Zentrum München). The first analysis of this cohort was conducted with animals at the age of 4-5 months. Open field analysis showed a decreased activity, measured by distance traveled, and speed of movement in a novel environment, indicating reduced locomotor activity of *Gpx4$^{fl/fl;Hb9Cre}$* KO animals. Whereby, time in center and resting time were not significantly altered between groups. *Gpx4$^{fl/fl;Hb9Cre}$* KO animals further showed decreased rearing frequency, which was significantly reduced in females. The open field analysis exhibited reduced locomotor activity and movement, although *Gpx4$^{fl/fl;Hb9Cre}$* mice showed no change in anxiety at 4 months of age (Fig. 25A). SHIRPA, a primary observation protocol for general phenotype assessment (named

by SmithKline Beecham Pharmaceuticals; Harwell, MRC Mouse Genome Centre and Mammalian Genetics Unit; Imperial College School of Medicine at St Mary's; Royal London Hospital, St Bartholomew's and the Royal London School of Medicine; Phenotype Assessment [285]), confirmed the reduced locomotor activity of KO animals. Observations on posture and movement provided insights about emerging tics and tremor, abnormal gait and changes in tail elevation (Fig. 25B).

In order to investigate motor coordination and balance, balance and ladder beam analyses of $Gpx4^{fl/fl;Hb9Cre}$ mice were performed. While traversing four different beams (i.e., 1-4: square 20 mm, round 22 mm, square 12 mm, round 15 mm), the time required and the number of slips and stops were recorded. $Gpx4^{fl/fl;Hb9Cre}$ mice needed significantly more time to cross the beams, independent from the shape of the beams. The number of slips, while traversing beam no. 2 and beam no. 4, was increased for KO animals compared to the control group. For the number of stops, the same pattern occurred for the first and second beam (Fig. 25C). Similar observations were recorded for ladder beam analysis. $Gpx4^{fl/fl;Hb9Cre}$ mice required significantly more time to cross the beam and they stopped more frequently, which, however, reached statistical significance only in males (Fig. 25D).

In order to assess coordination, balance and muscle strength, rotarod and grip strength analyses were conducted. The time spent on an accelerating rotarod (Fig. 25E), as well as the mean force of fore limbs and combined fore and hind limbs remained unchanged as compared to the $Gpx4^{fl/fl}$ control group (Fig. 25F). To calculate the mean force, a linear regression of body weight and mean force were set up for each animal. This analysis showed that mice with a lower body weight displayed reduced mean force, which reached statistical significance only taking into account genotype and body weight interaction. In conclusion, $Gpx4^{fl/fl;Hb9Cre}$ mice developed an abnormal motoric phenotype, corroborated by a general decreased locomotor activity, reduced movement with abnormal gait and altered tail posture, as well as an impaired balance coordination.
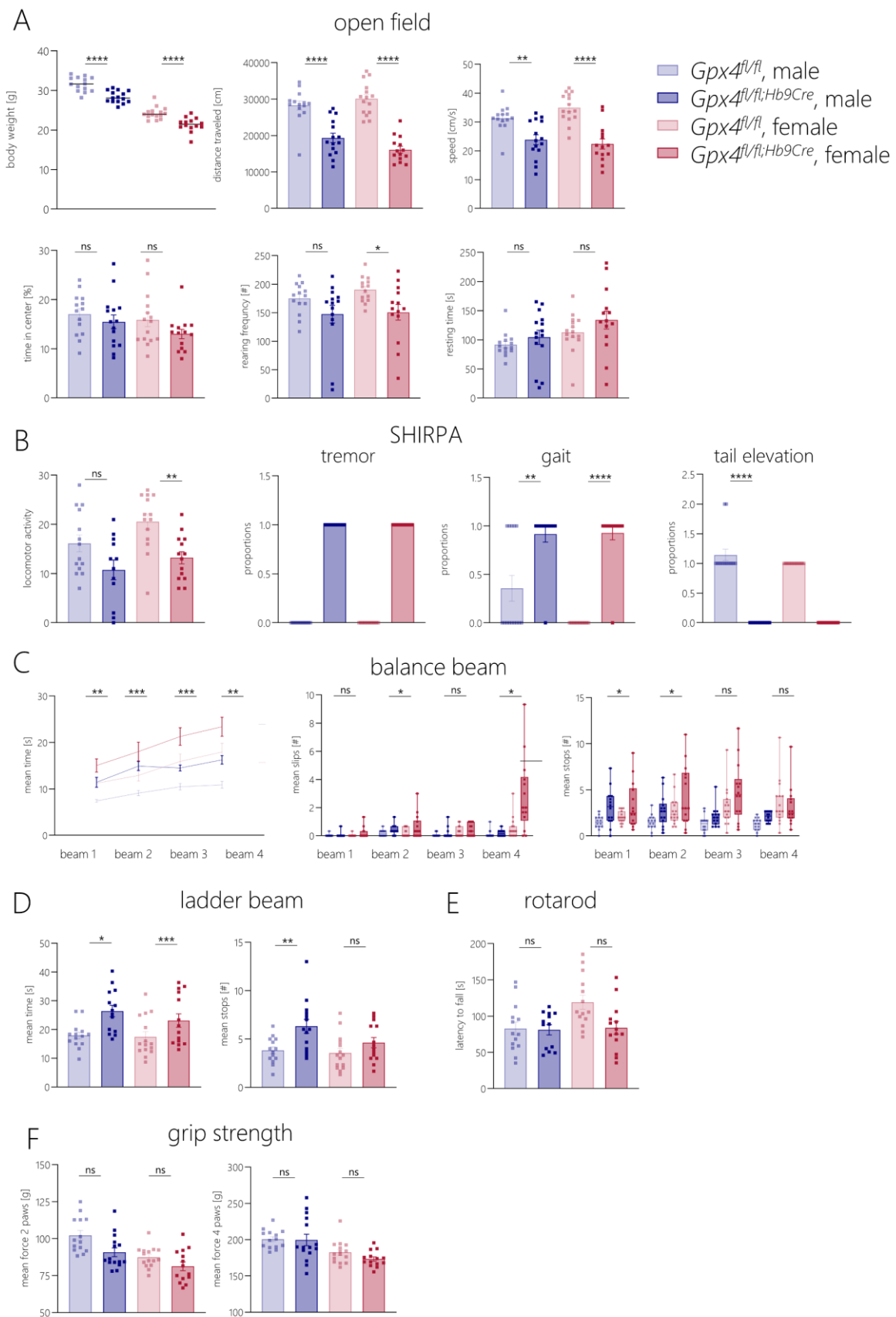
Figure 25| Gait and behavior analysis unveiled an abnormal locomotor phenotype of *Gpx4^fl/fl;Hb9Cre*^ mice

A| Besides a decrease in body weight, *Gpx4^fl/fl;Hb9Cre*^ mice showed impairments in several behavioral tests. Open field analysis showed reduced locomotor activity of MN-specific *Gpx4* KO mice, as determined by the distance

traveled, and speed of movement in a novel environment. B| SHIRPA analysis revealed the appearance of tics and tremor, abnormal gait and changes in tail elevation of $Gpx4^{fl/fl;Hb9Cre}$ mice. The coordination and balance were investigated using balance beam (C) and ladder beam (D). Both tests showed impaired coordination of $Gpx4^{fl/fl;Hb9Cre}$ mice. E,F| Rotarod and grip strength performance were conducted to test muscle strength, which was not altered between $Gpx4^{fl/fl;Hb9Cre}$ mice and age matched-controls. Statistical analysis A-E| was performed using t-test, p < 0.05 (*) p < 0.01 (**), p < 0.001 (***), p < 0.0001 (****). n.s. = not significant, (F, grip strength analysis) was performed by GMC using a linear regression model.

4.7.3 $Gpx4^{fl/fl;Hb9Cre}$ mice try to compensate for motoric impairments

The Noldus CatWalk XT is a completely automated gait analysis tool for the quantitative assessment of footfalls, motor function and the gait of animals. By recording videos the way the mice move on a glass platform, several parameters of the gait can be measured and analyzed. These recordings revealed a clear genotype-related effect, showing that $Gpx4^{fl/fl;Hb9Cre}$ mice were slower in crossing the walkaway, along with a reduced walking speed (Fig. 26A, B). The base of support (BOS) is a parameter which measures the average width between the paws while crossing the walkaway. Both, the front paws (FP) and hind paws (HP) were significantly wider in $Gpx4^{fl/fl;Hb9Cre}$ KO mice, independent from gender (Fig. 26C).
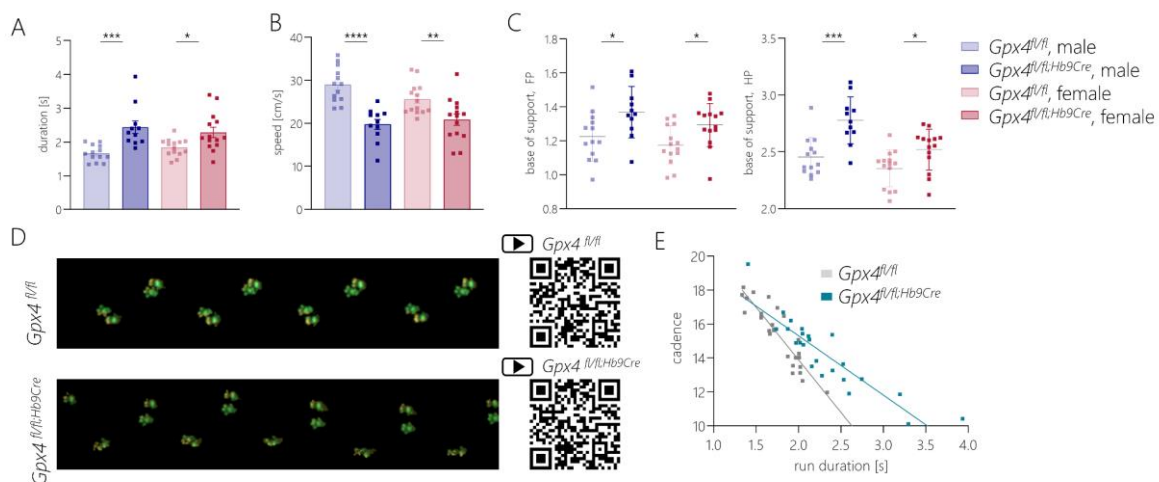
Figure 26| Catwalk XT analysis of $Gpx4^{fl/fl;Hb9Cre}$ mice illustrated abnormal gait and motoric impairments
A, B| $Gpx4^{fl/fl;Hb9Cre}$ mice showed a significant increase in the duration of crossing the walkaway and a decrease in overall speed. C| The base of support (BOS) measures the average width between the paws. Both, front paws (FP) and hind paws (HP) were significantly wider in $Gpx4^{fl/fl;Hb9Cre}$ mice. D| The pattern of paws and cadence is shown in footprint image and attached videos (name: review-lorenz and password: DK78_dvT to log-in at media.tum and to open the video sequences). E| The correlation of cadence with average run duration illustrated that $Gpx4^{fl/fl;Hb9Cre}$ mice took more steps per second. Statistical analysis was performed using t-test, p < 0.05 (*) p < 0.01 (**), p < 0.001 (***), p < 0.0001 (****). n.s. = not significant

Beside the BOS, the cadence (the steps taken per second) was recorded and was correlated with average run duration. This analysis showed that, with the same run duration, $Gpx4$ KO mice exhibited a higher cadence, meaning $Gpx4^{fl/fl;Hb9Cre}$ mice took more steps per second (Fig.

26E). Further parameters such as shorter stride length and shorter swing phase, confirmed this gait phenotype as illustrated in Figure 26D (scan QR code for catwalk video). The catwalk analysis therefore indicates that *Gpx4$^{fl/fl;Hb9Cre}$* KO mice try to cope with their general instability and motor deficiencies by slowing down the walking speed with smaller steps and widening their BOS.

4.7.4 *Gpx4$^{fl/fl;Hb9Cre}$* mice show reduced activity at advanced age

In order to analyze the progression of the motoric phenotype, SHIRPA, rotarod and grip strength analyses were repeated with an aged mouse cohort at the age of 12 months. Locomotor activity further decreased in aged *Gpx4* KO mice, resulting in significant differences between *Gpx4$^{fl/fl;Hb9Cre}$* mice and aged controls (Fig. 27B). The initially observed tics in younger mice progressed to tremors. The tail posture was even more wavy and dragging in *Gpx4$^{fl/fl;Hb9Cre}$* mice. In contrast, performance on accelerating rotarod showed no progressive decline in 12-months-old *Gpx4$^{fl/fl;Hb9Cre}$* mice, while a reduction in latency to fall was observed in female mice (Fig. 27C). The performance on grip strength was calculated by linear regression of body weight (Fig. 26A) and mean force per genotype and sex (Fig. 27D). Thereby, no significant genotype effect was observed, although small effects occurred for genotype and body weight interaction, meaning *Gpx4$^{fl/fl;Hb9Cre}$* mice are lighter in body weight and show less mean force simultaneously. Overall, 12-months-old *Gpx4$^{fl/fl;Hb9Cre}$* mice showed reduced activity and abnormities in gait and different motor tasks; however, most behavior tests were normalized for body weight of mice, which was markedly reduced in aged cohort of *Gpx4* KO mice.
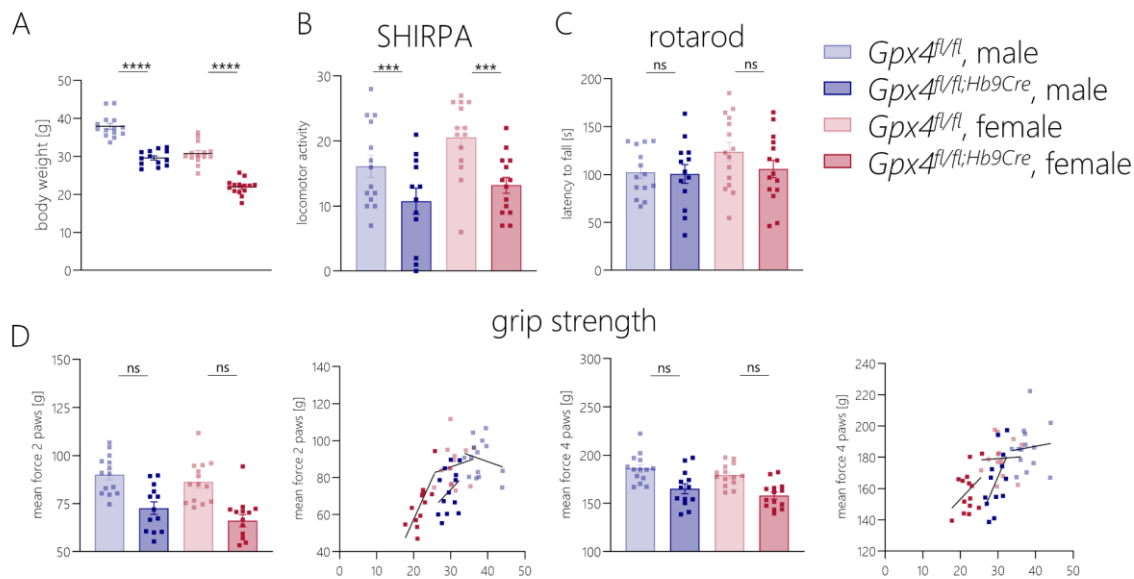
Figure 27| Locomotor activity is decreased in 12-months old *Gpx4^{fl/fl;Hb9Cre}* mice
A| Significant differences in body weight of *Gpx4^{fl/fl;Hb9Cre}* mice were observed at 12-months of age. B| SHIRPA analysis of aged *Gpx4* KO mice showed a significantly reduced locomotor activity. C| Performance on rotarod showed a reduction of KO female latencies, but no general significant impairment in *Gpx4^{fl/fl;Hb9Cre}* mice. D| Repeated grip strength analysis with aged mice showed no significant genotype effect. Small effects were based on body weight and genotype interaction. Statistical analysis was performed using ANOVA test and a linear regression model, $p < 0.001$ (***), $p < 0.0001$ (****). n.s. = not significant.

4.7.5 Motor neuron loss and elevated NfL levels in plasma of *Gpx4^{fl/fl;Hb9Cre}* mice

In addition to the behavioral studies, *Gpx4^{fl/fl;Hb9Cre}* mice were analyzed with regard to the number of MNs, which are essential for muscle innervation and coordination. To determine whether *Gpx4* deletion leads to the loss of MNs, lumbar spinal cord cryosections (20 µm) were stained with cresyl violet. MNs can be easily recognized as they are large neurons in the ventral horn region of the spinal cord. As illustrated in Figure 28A, the number of MN were found to be clearly reduced in *Gpx4^{fl/fl;Hb9Cre}* mice, which aggravated over time. Consistent with these findings, immunohistochemical staining against NeuN and GFAP illustrated a loss of large NeuN-positive cells, as well as an increase in GFAP-positive cells in lumbar spinal cord region (Fig. 28B).

Simoa NF-light® assay was used to quantitatively determine NfL levels in pre-diluted plasma samples at various time points (measurement was performed by Dr. Petra Steinacker, Universität Ulm). MN-specific *Gpx4* KO animals showed a robust and progressive increase in plasma NfL concentrations over time. Already at an age of 4 weeks, *Gpx4^{fl/fl;Hb9Cre}* mice demonstrated a 10-fold increase in NfL levels compared to control mice. At the age of 16 weeks, the biggest difference in NfL levels was observed. At 2 years of age, elevated NfL levels

were detected in all mice independent of their genotype, which likely represents a general aging effect (Fig. 28C). These results confirmed a progressive loss of MNs in $Gpx4^{fl/fl;Hb9Cre}$ animals leading to an increase in plasma NfL levels and reactive astrogliosis in spinal cord.
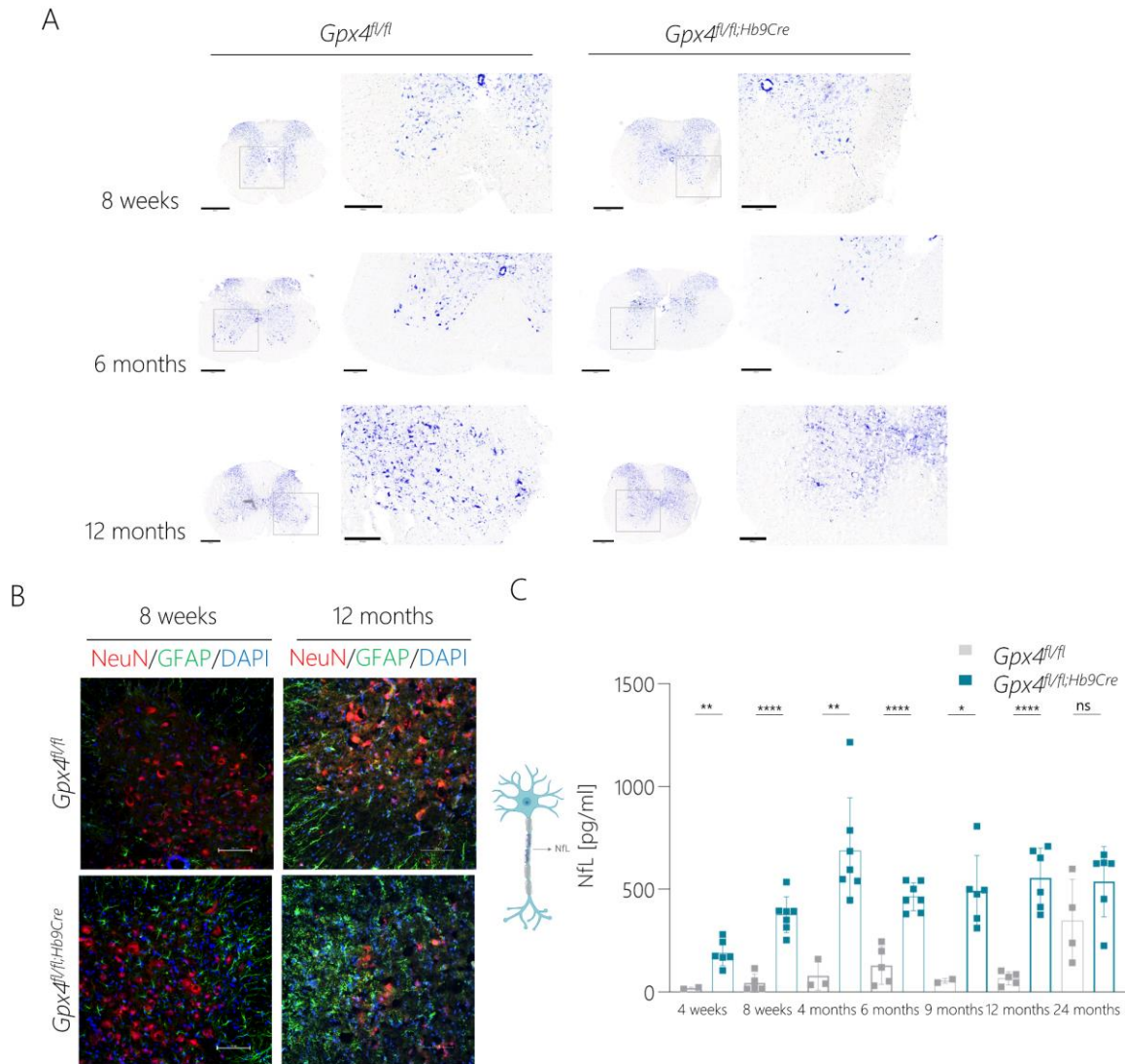
Figure 28| Progressive loss of MNs in $Gpx4^{fl/fl;Hb9Cre}$ mice leads to a marked increase in plasma NfL levels
A| A robust increase of plasma NfL levels was evident starting at 4 weeks of age in *Gpx4* KO animals. B| Cresyl violet staining of lumbar region of spinal cord (20 µm) at various ages illustrated a loss of MNs in $Gpx4^{fl/fl;Hb9Cre}$ mice. Pictures were taken with an AxioScan microscope; scale bar in overview picture indicates 500 µm, in ventral horn blowup 200 µm. C| Immunohistochemistry analysis showed a loss of NeuN-positive cells, as well as an increase in GFAP-positive cells in lumbar spinal cord region. Pictures were taken with Nikon eclipse microscope; scale bar indicates 100 µm. Statistical analysis was performed using t-test, p < 0.05 (*) p < 0.01 (**), p < 0.001 (***), p < 0.0001 (****). n.s. = not significant.

4.7.6 *Gpx4^{fl/fl;Hb9Cre}* mice exhibit a muscle fiber shift

Hind limbs of 12 months old mice were dissected and analyzed through muscle phenotyping in cooperation with the group of Prof. Wackerhage (Exercise Biology, TU München). Tibialis anterior (TA), extensor digitorum longus (EDL), gastrocnemius (GAS), and soleus (SOL) were dissected and weighted (Fig. 29A).
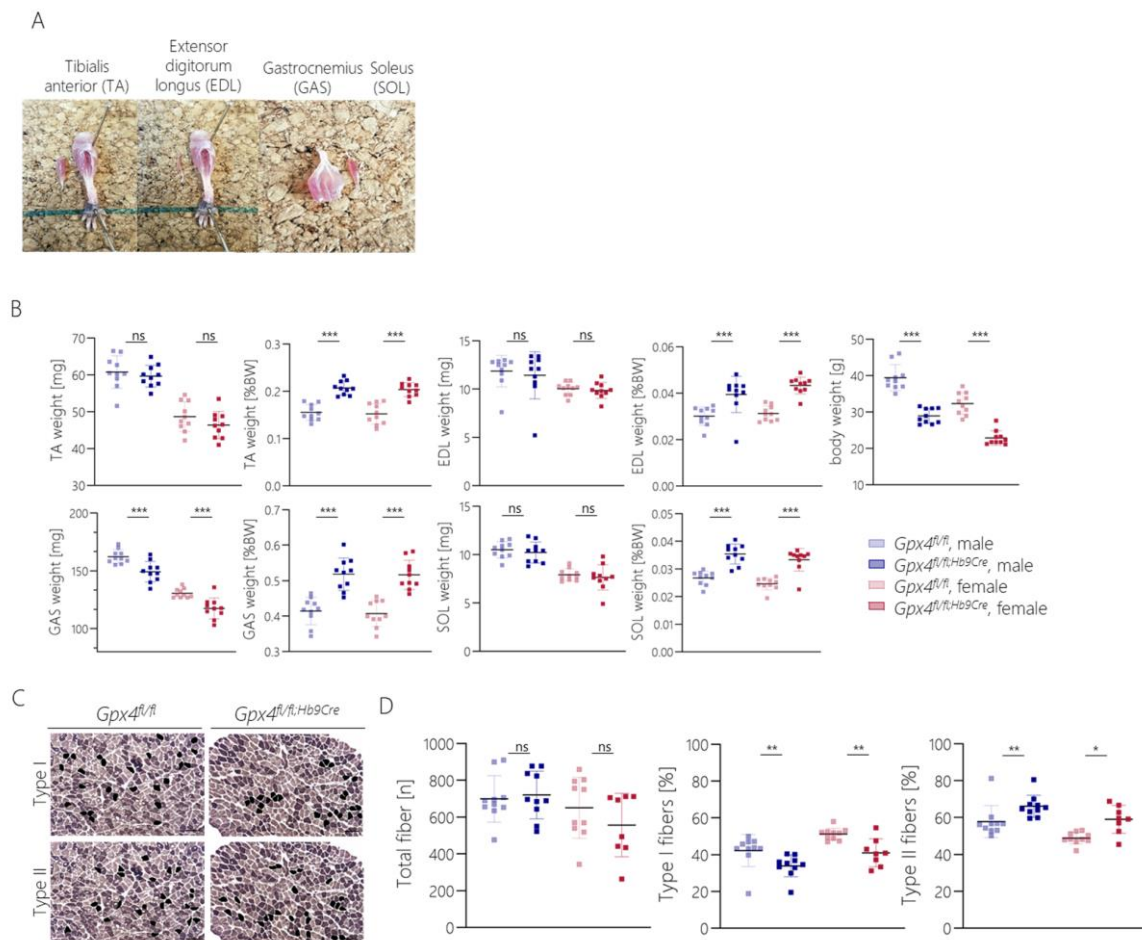
Figure 29| Lower proportion of type I and higher II fibers indicate a muscle fiber shift in *Gpx4^{fl/fl;Hb9Cre}* mice
A| Hind limbs were dissected in tibialis anterior (TA), extensor digitorum longus (EDL), gastrocnemius (GAS), and soleus (SOL). B| Determination of the weight of muscles showed an absolute lower GAS weight in *Gpx4* KO animals. Relative weights to body weight indicated global differences between *Gpx4* KO and WT, whereby *Gpx4* KO showed a higher relative muscle weight. C| ATPase staining of soleus analyzed cross sectional area of fibers. Measured fibers are marked in black. Scale bar in cross section picture indicates 100 µm D| Total fiber count in soleus illustrated no significant alterations; however, *Gpx4^{fl/fl;Hb9Cre}* exhibited less type I fibers (slow-twitch fibers) and a higher proportion of type II fibers (fast-twitch fibers). Statistical analysis was performed using two way ANOVA (Pairwise multiple comparison: Student-Newman-Keul method), $p < 0.05$ (*), $p < 0.01$ (**), $p < 0.001$ (***), n.s. = not significant.

Absolute weights of TA, EDL and SOL did not show differences with regard to a potential genotype effect between WT and *Gpx4* KO animals. However, male and female animals differed over all groups and muscle types as expected (p<0.001). In contrast, the absolute

weight of GAS indicated a significantly lower muscle weight between $Gpx4^{fl/fl;Hb9Cre}$ mice and $Gpx4$ controls (p<0.001), regardless of gender (males and females over all groups p<0.001) (Fig. 29B). This weight analysis showed that GAS of 12-months old $Gpx4^{fl/fl;Hb9Cre}$ mice differ from their WT controls. Furthermore, muscle weights were set in relation to body weight. Due to major differences in body weight, the relative muscle weight for TA, EDL, SOL and GAS showed a higher relative weight without gender-specific differences (Fig. 29B).

To further investigate the type of muscle fiber, the total number of fibers and the number of type I and type II muscle fibers were counted in ATPase-stained SOL sections (Fig. 29C). Total fiber count indicated small differences between WT and mutant mice, which, however failed to reach statistical significance (p=0.458). In contrast, the analysis of type I and II muscle fibers revealed significantly different gender and genotype effects. $Gpx4^{fl/fl;Hb9Cre}$ exhibited less type I fibers (slow-twitch fibers, aerobic fiber) as compared to WT, in both genders (males: p=0.008, females: p=0.003). When comparing genders, females had a higher proportion of type I fibers than males regardless of genotype. Consistent with this, $Gpx4^{fl/fl;Hb9Cre}$ mice had more type II fibers (fast-twitch-fibers, anaerobic fiber) (males: p=0.008, females: p=0.003). ATPase staining of SOL illustrated a higher amount of type II fibers in $Gpx4$ KO mice and a lower amount of brown stained type I fibers (Fig. 29D). This analysis provides evidence for a muscle fiber shift in $Gpx4^{fl/fl;Hb9Cre}$ mice towards glycolytic, fast twitch muscle fiber type II associated with an alteration in energy consumption.

4.7.7 Plasma analysis uncovered altered lipoprotein metabolism in $Gpx4^{fl/fl;Hb9Cre}$

In order to analyze systemic inflammation or an altered metabolism in $Gpx4^{fl/fl;Hb9Cre}$ mice, plasma samples isolated from 12-months old animals were screened for related cytokines, hormonal and metabolic markers via multiplex assay platform (Meso QuickPlex®) or a clinical chemistry analyzer (Olympus AU480).

Pro-inflammatory cytokines such as interleukin 6 (IL-6) and tumor necrosis factor alpha (TNFα) were found to be unaltered in KO versus WT mice (Fig. 29A). Nevertheless, insulin and leptin plasma levels were significantly reduced in both female and male $Gpx4^{fl/fl;Hb9Cre}$ mice. The plasma levels of fibroblast growth factor 21 (FGF21), however, were not different between KO and WT mice (Fig. 30A).

Plasma lipid concentrations were assessed by measuring cholesterol, high-density lipoprotein (HDL)-cholesterol and triglyceride levels (Fig. 30B). These metabolic parameters were strongly reduced in $Gpx4^{fl/fl;Hb9Cre}$ mice as compared to control mice. Although some of the control mice

showed low values, the difference in cholesterol and HDL-cholesterol levels were still significantly lower in *Gpx4*^{fl/fl;Hb9Cre} females. Triglyceride levels were 1.5-fold higher in WT animals compared to *Gpx4*^{fl/fl;Hb9Cre}. These values indicated a major effect on general metabolic pathway, mainly affecting lipoprotein metabolism. Furthermore, an increase of alkaline phosphatase (ALP) activity was observed in *Gpx4* KO animals. In contrast, alpha-amylase activity was decreased predominantly in female KOs, while lipase activity appeared unaffected Fig. 30C). Even though only one time point was chosen for plasma analysis, apparent patterns of an altered lipoprotein metabolism were observed in MN-specific *Gpx4* KO mice.
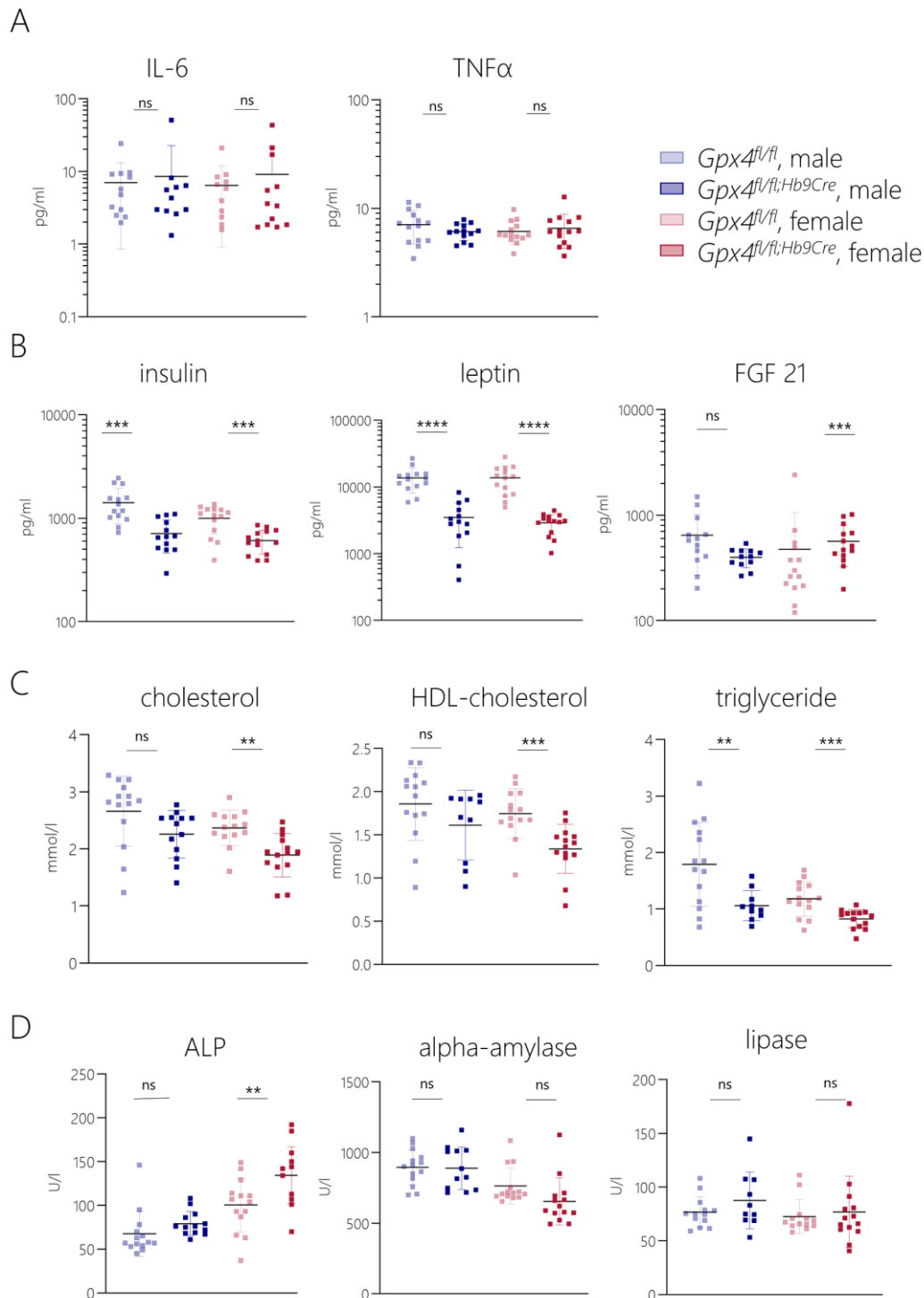
Figure 30| Plasma sample analysis reveals profound effects in lipid metabolism of *Gpx4^{fl/fl;Hb9Cre}* mice
A| Several clinical parameters were measured in plasma samples of 12-months old cohort. No difference in pro-inflammatory cytokines, interleukin 6 (IL-6) and tumor necrosis factor alpha (TNFα) were found in *Gpx4^{fl/fl;Hb9Cre}* mice. B| By contrast, *Gpx4^{fl/fl;Hb9Cre}* mice showed a marked decrease in insulin and leptin levels in plasma, whereby the levels of fibroblast growth factor 21 (FGF21) were not consistently different between *Gpx4* KO and WT animals. C| Cholesterol, high-density lipoprotein (HDL)-cholesterol and triglyceride levels were clearly decreased in *Gpx4^{fl/fl;Hb9Cre}* mice, implying an alteration in lipid metabolism of GPX4 KO mice at 12-months of age. D| A clear difference was also observed for alkaline phosphatase (ALP) activity, which was increased in mutant animals, while alpha-amylase activity and lipase activity remained unaffected. Statistical analysis was performed using t-test, $p < 0.001$ (***), $p < 0.0001$ (***). n.s. = not significant.

4.7.8 Gene expression profiling of spinal cord tissue resulted in 1754 differently regulated genes related to immune system, metabolism and neuronal function

A genome-wide transcriptome analysis of spinal cord tissue from 12-months-old *Gpx4*^{fl/fl;Hb9Cre} and *Gpx4*^{fl/fl} control animals was performed using RNA sequencing (data provided in collaboration with GMC, done by Dr. Martin Irmler). Statistical analyses with deseq2 were completed for both sexes together and separate for females and males. 1754 genes were found to be regulated (padj < 0.1, Fig. 31A) in *Gpx4*^{fl/fl;Hb9Cre} mice as compared to *Gpx4*^{fl/fl} controls (Appendix Table 9). Overall, genes regulated by the KO of *Gpx4* were mostly similar in females and males; therefore, the set of 1754 regulated genes was used for further analysis. The heat map illustrates the expression level (higher expression levels in yellow; lower expression levels in blue) and clustering along genes and genotype. A consistent regulation of genes was observed based on genotype (KO vs WT). The top 10 differently regulated genes by padj were *Clec7a, Lyz2, Calca*, *Vgf*, *Kif5a, Apoe, Serpina3n, Slc11a1, Fcgr2b* and *C4a.* Except for *Kif5a*, all of these genes were found to be up regulated and are illustrated in the heat map of 40 top regulated genes (Fig. 31B). Genotype-dependent differences in the expression of *Gpx4* were not generally detected in this transcriptome analysis, only some spinal cord samples showed reduced levels of the exonic region comprising exons 5-7 of the *Gpx4* gene (Fig. 31C). However, when considering that non-neuron to neuron ratio in spinal cord is about four in murine spinal cord, the knockout of *Gpx4* is very likely masked by other cell types in the samples [286]. *Chat*, as a marker of cholinergic neurons and mainly expressed in MN, was among the significantly regulated between genotypes, whereby *Gpx4*^{fl/fl;Hb9Cre} samples showed reduced expression levels. In addition, *Gfap* was significantly upregulated in *Gpx4*^{fl/fl;Hb9Cre} samples, indicating astrogliosis resulting from the MN-specific *Gpx4* KO followed by a loss of MN in spinal cord samples (Fig. 31C; see also Fig. 28).

A

B

C
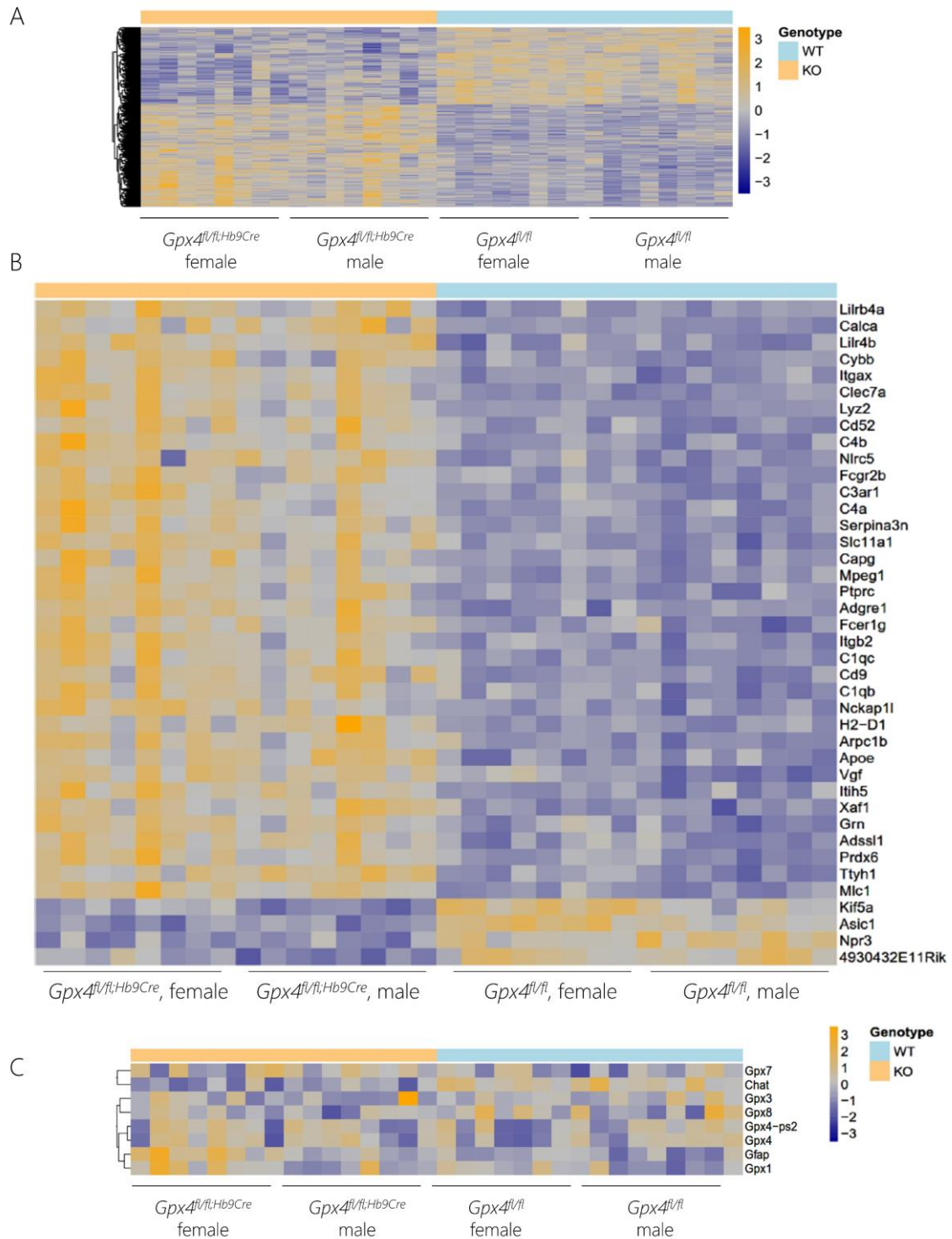
D

Enrichment of differentially expressed genes in Ingenuity canonical pathway
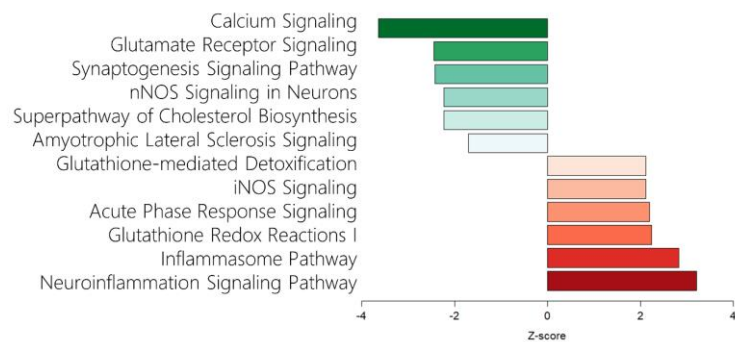
Figure 31| Gene expression profiling of spinal cord tissue from *Gpx4^fl/fl;Hb9Cre* mice identified metabolic alterations, impaired neuronal function and signaling, as well as activation of the innate immune system
Spinal cord samples from 12-months old *Gpx4^fl/fl;Hb9Cre* mice were used for RNA sequencing analysis. A| The combined analysis of female and male *Gpx4^fl/fl;Hb9Cre* mice resulted in a consistently altered gene regulation of 1754 genes (padj<0.1). Orange indicates higher and blue lower expression levels. B| The heat map illustrates the top 40 regulated genes by padj, sorted by fold-change. B| Specific gene expression levels were chosen manually, whereby only *Chat* and *Gfap* were significantly regulated between genotypes (padj < 0.1 for females and males). Expression levels of *Gpx5, Gpx6, Gpx2-ps1, Gpx4-ps1, Gpx2* and *Chit1* were low and not significantly altered. D| Selected significantly enriched canonical pathways (p<0.05) argue for an activated innate immune system and for impaired neuronal function and signaling. z-scores >2 (<-2) indicate activated (inactivated) terms (Appendix Table 10) .

To assess the biological consequences of the observed gene regulation, enrichment analyses were performed on the 1754 regulated genes by using the Ingenuity Pathway Analysis (IPA) software and g:Profiler (Fig. 31D, Appendix Table 10). This enrichment analysis unraveled significantly enriched terms, which are related to the innate immune system, observed to be activated in *Gpx4^fl/fl;Hb9Cre* spinal cord samples. In contrast, metabolic pathways and pathways related to neuronal function and signaling were found to be impaired in KO samples. For example, inhibited terms included calcium signaling, synaptogenesis signaling pathway, nNOS signaling in neurons, superpathway of cholesterol biosynthesis and ALS signaling. By contrast, activated terms include neuroinflammatory processes and the inflammasome pathway, glutathione-dependent redox reactions and glutathione-mediated detoxification. Beside the enriched canonical pathway terms, enriched terms in function and disease as well as in upstream regulators suggest that regulated genes are strongly associated with an altered immune response.

4.7.9 Generation of transgenic compound mutant mice and pharmacological treatment of MN-specific *Gpx4* KO mice to rescue progressive motoric impairment

With the aim to study whether the loss of *Acsl4* or the expression of the Cys variant of GPX4 (U46C_GPX4 mice [44]) ameliorates MN degeneration in *Gpx4^fl/fl;Hb9Cre* mice, *Gpx4^fl/fl;Hb9Cre* mice were cross-bred with *Acsl4^fl/fl* mice or with *Gpx4^wt/cys* mice, in analogy to the strategy described in 4.4. Although a first observation of *Acsl4^fl/fl x Gpx4^fl/fl;Hb9Cre* mice suggested a slightly delayed occurrence of the overall phenotype of *Gpx4^fl/fl;Hb9Cre* mice, such as dragging and wavy tail, the development of the motoric phenotype of *Gpx4/Acsl4* DKO mice was comparable to *Gpx4^fl/fl;Hb9Cre* mice. As a more quantitative measure, plasma samples were taken at different ages to determine plasma NfL levels. The comparison of NfL levels showed a substantial decrease at 8 weeks of age in *Acsl4^fl/fl x Gpx4^fl/fl;Hb9Cre* double KO mice (377.1 pg/ml) compared to *Gpx4^fl/fl;Hb9Cre* mice (240.3 pg/ml) (Fig. 32A). However, at each other

time point, no alterations in NfL levels between these groups could be detected (Fig. 32A). From these findings, it follows that the loss of *Acsl4* does not provide robust protection against MN loss induced by *Gpx4* deletion.

Next, *Gpx4^cys/fl;Hb9Cre^* mice were analyzed, which express exclusively the U46C variant of GPX4 in MN. In contrast to the MN-specific *Gpx4/Acsl4* DKO mice, the Cys variant of GPX4 was sufficient to rescue the main pathology of *Gpx4^fl/fl;Hb9Cre^* mice, which are the phenotypical abnormalities in anatomy and behavior as described above. Furthermore, the NfL levels of *Gpx4^cys/fl;Hb9Cre^* mice were significantly lower as compared to *Gpx4^fl/fl;Hb9Cre^* mice (Fig. 32B). At 4 weeks of age, NfL levels of *Gpx4^cys/fl;Hb9Cre^* were around 194 pg/ml, in contrast to an average NfL level of 377.1 pg/ml in plasma of *Gpx4^fl/fl;Hb9Cre^* mice. The difference in plasma NfL concentrations at 4 months of age, however, failed to reach statistical significance due to a high variation within the groups, although the plasma NfL values of *Gpx4^cys/fl;Hb9Cre^* mice were clearly reduced. At one year of age, *Gpx4^cys/fl;Hb9Cre^* mice showed markedly reduced level of circulating NfL. The NfL value of aged *Gpx4^fl/fl;Hb9Cre^* mice was about 554.5 pg/ml as compared to 204.5 pg/ml for aged *Gpx4^cys/fl;Hb9Cre^* mice. Nevertheless, the plasma NfL concentrations of *Gpx4^cys/fl;Hb9Cre^* mice were constantly reduced, but NfL values never reached the levels of WT animals. These findings indicate that expression of the Cys variant of GPX4 is sufficient to ameliorate MN loss and associated symptoms of *Gpx4^fl/fl;Hb9Cre^* mice in a manner, which is similar to what was already observed for *Gpx4^cys/fl;Camk2aCreERT2^* mice (see 4.4). (Fig. 32B).

To investigate whether MN loss can be halted by pharmacological means, MN-specific *Gpx4* KO animals were treated with 3rd generation liproxstatins (Lip-3). 3rd generation liproxstatin was established in our laboratory and optimized for higher efficacy in preventing ferroptosis and for an increased blood brain barrier-permeability. To test these, 3rd generation Lip was provided to the *Gpx4^cys/fl;Hb9Cre^* mice via food pellets, starting at the age of 4 weeks. Plasma NfL level analysis of treated mice were determined at 4 months of age to analyze potential *in vivo* efficacy of Lip-3. The comparison of treated versus untreated animals only showed a slight decrease of NfL levels which failed to reach statistical significance (Fig. 32C).
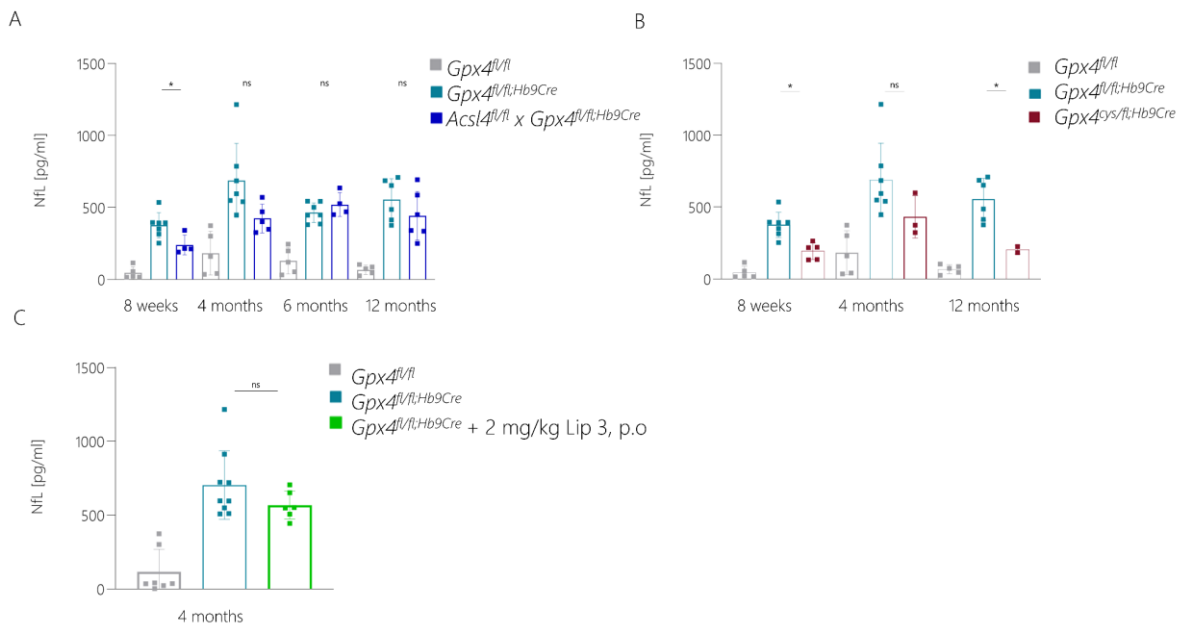
Figure 32| Genetic and pharmacological studies to rescue MN death and associated symptoms of *Gpx4^{fl/fl;Hb9Cre}* mice

A| As shown, plasma NfL levels were not grossly reduced in *Acsl4^{fl/fl} x Gpx4^{fl/fl;Hb9Cre}* mice as compared to *Gpx4^{fl/fl;Hb9Cre}* mice, except at 2 months of age. B| In contrast, plasma NfL levels were clearly reduced in *Gpx4 ^{cys/fl;Hb9Cre}* mice. C| Pharmacological treatment of *Gpx4^{fl/fl;Hb9Cre}* mice with a 3rd generation Lip (Lip-3) only provided a mild yet statistically insignificant protection in *Gpx4^{fl/fl;Hb9Cre}* mice as determined by measuring NfL levels in plasma. Statistical analysis was performed using t-test, p < 0.05 (*), n.s. = not significant.

5 DISCUSSION

NDs affect millions of people worldwide with constantly increasing prevalence. Currently, there is no cure for any of these diseases, no matter which neurons are destined to die [134]. Why, how and when those neuros degenerate is still not fully understood with the exception of some familial mutations, known to be linked to AD or ALS. NDs cause a variety of neurological symptoms like cognitive impairments, speech disabilities, movement disorder, paralysis and death of patients. Furthermore, reliable mouse models to study the underlying molecular mechanism of neurodegeneration are not available since most of the existing mouse models fail to mimic most aspects of the human pathology so far.

Ferroptosis, as a recently discovered form of regulated cell death, has been linked to various diseases, including NDs [24]. Ferroptosis is characterized by excessive lipid peroxidation and an oxidative destruction of cellular membranes. NDs as well as ferroptotic cell death have been associated with a number of cellular processes including oxidative stress, mitochondrial dysfunction, deregulated iron handling and/or calcium homeostasis. The selenoprotein GPX4 is the key regulator of this form of cell death due to its unique activity to efficiently reduce peroxidized phospholipids to the corresponding alcohol to restrain overwhelming lipid peroxidation in phospholipid bilayers [7, 13, 15]. Since mice with neuron-specific inactivation of *Gpx4* (as characterized in this PhD thesis) present common hallmarks of human NDs, these transgenic models may serve as an ideal tool to investigate a possible link between ferroptotic cell death and neurodegeneration. Earlier studies using *Gpx4* KO mice unraveled specific neuronal subpopulations that are generally prone to undergo ferroptosis and have shown the importance of GPX4 for cortical neuron survival and neuroprotection. Yet, considering the progression of neurodegeneration over time, *Gpx4* KO mice studies have been insufficient as almost all previous studies relied on non-inducible KO or deletion of *Gpx4* which resulted in early death of mice.

5.1 Phenotype of glutamatergic neuron specific inducible *Gpx4* KO model is reminiscent of dementia-associated symptoms including cortical atrophy and neuroinflammation

To be able to study the underlying molecular contribution of ferroptosis to neurodegeneration, an inducible neuron-specific *Gpx4* KO model, *Gpx4*$^{fl/fl;Camk2aCreERT2}$, has

been generated. The time-resolved induction of *Gpx4* deletion in glutamatergic neurons of adult mice by the i.p. administration of TAM thus, permits a longitudinal study on the process of phenotype progression. At first, mice were analyzed through relevant behavior and gait analyses revealing severe behavioral abnormalities in locomotor activity, coordination, balance and short-time memory upon *Gpx4* deletion. Furthermore, the cortical structure was found to lose its integrity over time, coinciding with an enlargement of both ventricles and an approximately 80 % loss of brain mass 6 months after KO induction. In brief, this initial analysis of the *Gpx4* KO mouse model demonstrated massive brain atrophy, loss of cortical layers and progressive degeneration of cortical mass in KO animals. These observations are highly reminiscent of symptoms of patients suffering from dementia or AD. In fact, impairment in cognitive abilities and daily activities caused by the degeneration of hippocampal, cortical and subcortical neurons in the brain, as well as alterations in behavior and personality are the first clinical symptoms of dementia [139, 140, 287].

To monitor the progression of this dementia-associated phenotype in the inducible mouse model, NfL levels in plasma were quantitatively determined. NfL is a structural protein of the axonal cytoskeleton, mainly present in the large myelinated axons. NfL is an established blood and CSF biomarker in the diagnostic of NDs as it is released in the CSF and plasma due to neuroaxonal damage or neurodegeneration. Although NfL is a non-specific marker of neurodegeneration, various studies on NfL in different types of NDs indicated a clear correlation of NfL levels with disease progression rates [271, 288]. This correlation was evident when measuring NfL levels in the established mouse line, where the massive increase in plasma NfL peaked already 2 weeks after TAM treatment. To evaluate the neuronal damage upon *Gpx4* deletion, NfL was thus validated as a robust biomarker in this mouse model. Taken together, the established *Gpx4fl/fl;Camk2aCreERT2* model notably mimics patterns of dementia and can be defined as a novel mouse model to study the underlying molecular mechanisms of ferroptotic cell death in cortical neurons.

On the cellular level, *Gpx4fl/fl;Camk2aCreERT2* mice also presented an increase in astrocyte activation as measured by the expression of the astrocytic marker GFAP shortly after KO induction. Reactive astrogliosis has been frequently described in different transgenic animal models recapitulating AD [289, 290]. The term "reactive astrogliosis" describes the reactionary remodeling of astrocytes upon pathological conditions in the CNS [181]. Furthermore, severe

reactive astrocytes are found to be sufficient to cause irreversible neurodegeneration in an *in vivo* mouse model [291]. Further studies on human patient samples reported elevated GFAP levels in blood samples from early and late-onset AD patients. In addition, GFAP levels markedly correlate with the severity of gliosis during disease progression, indicating GFAP as a promising blood biomarker in the diagnosis of AD [292-294]. Pathological conditions, including inflammatory defense reaction, may trigger changes in the expression levels of GFAP, as well as morphological and functional properties of astrocytes, albeit GFAP expression levels may vary in different brain regions and physiological stimuli can alter the GFAP content [295, 296]. Therefore, a higher number of GFAP-positive cells alone is not sufficient to serve as a robust marker for neuroinflammatory processes or even neurodegeneration.

Next to an increased level of GFAP, immunostaining of brain tissue showed a loss of neurons and an increase in microglia upon *Gpx4* KO induction. NeuN is predominantly expressed in the nucleus of neurons and therefore a widely used marker protein to specifically detect neuronal cells [263]. Double staining of NeuN and GFAP underpinned the findings of cortical degeneration and reactive astrogliosis, since NeuN-positive cells in brain decreased, while at the same time the number of GFAP-positive cells increased. This was also accompanied by highly increased numbers of IBA1-positive cells. IBA1 is expressed in microglia, a specified type of macrophages in the CNS. It is known that under NDs conditions, microglia cells can lose their homeostatic state and function in sensing their environment, thereby transitioning to disease-associated microglia (DAM) [175].

DAM are known to upregulate typical microglial markers, such as *Iba1, Cst3* and *Hexb*, and to downregulate genes like *P2ry12, P2ry13, Cx3cr1, CD33* and *Tmem119.* It is hypothesized that neurodegeneration-associated molecular patterns (NAMPs), being recognized by various receptors on microglia, trigger the transition of resident microglia to DAM. This is in analogy to what is known for the peripheral immune system, which is activated upon the detection of pathogen- and damage-associated molecular patterns (PAMPs and DAMPs, respectively) by pattern recognition receptors (PRRs) [175, 297]. High abundance of microglia in the cortex of KO animals indicates their function in removing the damage initialized by NAMPs originating from for instance dying cells and lipid degradation products. The results presented here thus show that the activation of astrocytes is followed by the activation of microglia or even DAM, leading to a neuroinflammatory response circuit initialized by the neuron-specific KO of *Gpx4*.

The regulation of typical microglia markers are in line with the results obtained from the $Gpx4^{fl/fl;Camk2aCreERT2}$ mouse model, where flow cytometry was used to identify specific microglia patterns. At the earlier time point, *B2M*, which is part of the DAM program was significantly upregulated in $Gpx4^{fl/fl;Camk2aCreERT2}$ mice, whereas *P2ry12* and *Cx3cr1* were decreased in intensity. These findings imply that the homeostatic function of microglia cells is skewed already 12 days after TAM. Decreased expression of checkpoint genes characterizing the homeostatic state of microglia coinciding with upregulation of markers for DAM, like TREM2, B2M, CD80 and MHCII was apparent 4 weeks after TAM treatment of mice. The DAM phenotype thus seems to be shared across different neurological disorders as it has been postulated in different studies using models for AD, tauopathy and ALS [175, 177, 298-300]. In general, TREM2 signaling is essential for microglia response towards CNS pathology and is highly linked to AD [161, 178, 179, 301]. The study by Keren-Shaul *et al.* postulates a two-step activation mechanism regulating DAM. In the first TREM2-independent step, an activation of *Tyrobp*, *Apoe*, and *B2M*, as well as the downregulation of *Cx3cr1* and *P2ry12/13* was observed. This is followed by the second TREM2-dependent stage, which involves the induction of lipid metabolism and phagocytic pathways [302]. In line with this hypothesis are the results of the cytokine assay performed in this work that showed a progressive downregulation of Cx3cl1/fractalkine, which is the ligand to Cx3cr1. The observed upregulation of chemokines, such as CHI3L1 or CXCL5, is in line with previous data linking microglia activation and inflammatory cells as a common reaction in neuroinflammatory conditions [271, 272], and even ALS [303]. In addition, as reported by Abu-Rumeileh *et al.,* CHI3L1 was investigated in a clinicopathological study where it was shown to be highly increased among CSF samples from different ND patients [271].

Besides the detailed analysis of microglia and chemokine regulation in cortex samples, immune cell infiltration was investigated in the same manner. Similar to the pattern of microglia, immune cell count uncovered a slight alteration after 12 days of KO induction, which progressed to a significant increase 4 weeks after TAM injection. In a healthy state, different cells of the innate and adaptive immune system, such as granulocytes, macrophages, NK cells, B cells, CD8 or CD4 T cells control mainly the periphery of the brain [304, 305]. Except for B-cells, all immune cells investigated here populated neuron-specific *Gpx4* KO brains 4 weeks after KO induction. This progressive increased infiltration of immune cells suggests that damaged neuronal structures activate an inflammatory response and the secretion of

cytokines, which can cross the BBB, followed by migration and infiltration of immune cells from the periphery into the brain. Microglia and infiltrated macrophages share the ability for phagocytosis to clear tissue from dead cells, cellular debris, and protein aggregates to maintain tissue homeostasis. Infiltration of immune cells into the brain and microglial phagocytosis have been implicated in a variety of ND studies [300, 306-308]. For example, a study on *tau* transgenic mice revealed infiltration of CD8+ T cells into the brain, which was linked to an early chemokine response [308].

In sum, the data presented in this work provide strong evidence that the glutamatergic neuron-specific KO of *Gpx4* causes progressive loss of neurons in the cortex, leading to a vicious cycle of both astrocytosis and microgliosis, release of pro-inflammatory cytokines and chemokines and the infiltration of peripheral immune cells culminating in brain atrophy, all hallmarks frequently being described in neurodegenerative disorders, such as AD.

5.2 Omics analysis identifies pathway alterations associated with human neurodegenerative diseases

A comprehensive characterization of ferroptosis-associated modified peptides and lipid species in the mouse model described in the foregoing was conceived to enable the identification of specific protein patterns and lipid alterations affected by the inducible deletion of *Gpx4* in glutamatergic neurons.

Indeed, a detailed proteomics analysis of mouse cortex clearly showed a hierarchical clustering between *Gpx4* KO and WT samples and a progression in peptide abundance, strongly suggesting that the protein levels specifically altered in response to *Gpx4* deletion and its downstream events described in chapter 4.2. Remarkably, the differently changed proteins have been linked to various brain disorders, including ND, CNS diseases, dementia, tauopathies and AD, supporting the notion of the $Gpx4^{fl/fl;Camk2aCreERT2}$ model as a promising model to study ferroptotic neuronal cell death.

Specifically, *Gpx4* deletion significantly decreased MAP2 expression level shortly after TAM treatment. MAP2 is mainly expressed in neurons, but it can also be expressed in reactive astrocytes [309, 310]. GFAP, Vim, Serpina3n and Fabp7 were significantly upregulated and are known as astrocyte-expressed proteins [181]. The high abundance and significant upregulation of astrocyte-expressed proteins are consistent with the aforementioned results. HexB has been linked to DAM, correlating well with massive astrogliosis and microgliosis in

Gpx4^{fl/fl;Camk2aCreERT2} mice [175]. Proteomics analysis revealed Clu (also known as apolipoprotein J, ApoJ) among the top abundant proteins. In the past years, several studies have been focusing on Clu, which was originally described as a chaperone being highly expressed in the brain, mostly in astrocytes and neurons. *In vivo* studies revealed that deletion of Clu leads to impaired glutamatergic synaptic transmission, whereas overexpression of Clu was shown to ameliorate the neuropathological phenotype [311, 312]. Interestingly, secreted Clu co-localizes with protein aggregates such as Aβ-plaques or Lewy bodies and is ranked as the third most significant genetic risk factor for late-onset AD [312]. Clu was highly abundant in the cortex of *Gpx4^{fl/fl;Camk2aCreERT2}* mice despite the absence of neurodegenerative disease-associated mutations forming Aβ-plaques. In addition, human studies, analyzing the apolipoprotein fractions, showed Clu in CSF and plasma [313, 314], leading to a possible neuroprotective role of Clu by the inhibition and clearance of deposits or lipids aggregation as a consequence of neuroinflammatory processes or oxidative stress [315, 316].

The strong genetic risk factor of AD, ApoE, was also significantly abundant in the brain of *Gpx4^{fl/fl;Camk2aCreERT2}* mice. Similar to ApoJ, many studies have suggested a link between ApoE, deposition of Aβ-plaques and impaired synaptic function. The impact and function of ApoE in the pathology of neurodegenerative disorders, especially in AD, have been widely studied. ApoE is reported to influence Aβ pathology, triggering cortical atrophy or being upregulated upon a pro-inflammatory response [157, 159, 317, 318], although the precise mechanism remains elusive.

The subunits of complement protein C1qc and C1qa were also highly increased upon *Gpx4* deletion. C1q is known as the recognition and activation protein of the classical complement pathway. Complement activation is triggered upon recognition of molecular patterns associated with microorganisms and is necessary for the clearance of apoptotic cells [319]. Upon neuron-specific deletion of *Gpx4*, a time-dependent association between microglia activation, increased levels of C1q and release of pro-inflammatory cytokines was observed. This is in line with previous studies showing a correlation between microglia activation and increased level of C1q, which is associated with the release of pro-inflammatory cytokines and enhanced phagocytosis of damaged cells and cellular debris by microglia [319, 320]. Once complement activation is triggered, it drives a vicious cycle of pro-inflammatory processes and the disruption of the BBB [320]. Overall, these studies put forward the concept that the

induction of ferroptotic cell death by the loss of *Gpx4* in neurons induces activation of astrocytes and microglia, eliciting a pro-inflammatory state similar to that described in neurodegenerative disorders, such as AD. Remarkably, the longitudinal analysis of the *Gpx4*^{fl/fl;Camk2aCreERT2} mice uncovered multiple parallels to dementia-linked pathologies, although none of the known causative or genetic risk factors, such as APP, PSEN1/2 or APOE were actively modified in cortical neurons.

Despite a multitude of studies connecting lipid peroxidation to ferroptosis, only few have attempted to identify and characterize a lipid death signature imprinted by ferroptosis. Therefore, the cortical-neuron specific *Gpx4* KO mouse model was used to conduct a non-targeted lipidomic study, aiming to uncover significantly altered native lipids, driving ferroptotic cell death and neural demise, with potential for biomarker development.

The brain is highly enriched with PUFAs including AA (20:4n–6) and DHA (22:6n–3), which are found to be mainly esterified in PLs of the cellular membrane [89]. Deletion of *Gpx4* induced significant changes in lipid metabolism in mouse cortex, mainly in PUFA-containing PLs. Fitzner *et al.* reported that primary cultures of CNS cell types and all major brain regions contain a high proportion of PCs [277]. Our lipidomics analysis showed downregulation of most PC species, whereas LPCs were highly abundant in cortex of *Gpx4* KO animals. These reciprocal changes can be explained by an increased activity of phospholipase A$_2$ (PLA$_2$). PLA$_2$ is a class of enzymes catalyzing the generation of lysoPCs and free FA by hydrolyzing the FA in sn-2 position of PLs. Many studies have linked PLA$_2$ activity and LPCs to cardiovascular diseases, neurological disorders and inflammation. Elevated PLA$_2$ activity was also reported in CSF from patients suffering from AD [279, 321, 322]. PLA$_2$ activity is further involved in the generation of oxylipins. Oxylipins are highly active lipid mediators derived from oxidized PUFAs, exhibiting a pro-inflammatory effect for instance in cardiovascular disease, such as atherosclerosis [323-325], and also NDs including AD [326]. These bioactive lipids might serve as messengers or precursors for mediators activating pro-inflammatory reactions and modulating regulatory brain functions [327]. In order to establish a link between an altered PC/LPCs ratio and an increased neuroinflammatory response as shown here, further studies including

metabolomics analysis are planned with focus on an altered PUFA metabolism, especially on eicosanoids.

To avoid excessive toxic free FAs in cytoplasm, free FAs are stored in lipid droplets and may be used by mitochondria for energy production during nutrient deprivation. However, neurons show a minimum capacity to consume FAs, which leads to a high sensitivity towards mitochondrial membrane rupture and FA toxicity upon excessive free FAs [328]. To control lipotoxicity, neurons sequester free FAs in lipid droplets, which are taken up by glial cells [328-330]. Several studies have shown that oxidative stress and elevated levels of ROS in neurons cause lipid droplet accumulation in neighboring glia cells, showing a close cross-talk between neurons and astrocytes in lipid metabolism [330, 331]. ApoE is a lipid-binding protein that facilitates lipid transport between different cell types of the brain and is primarily expressed by astrocytes and microglia [332]. Qi *et al.* hypothesized that ApoE4 triggers neuronal dysfunction by reducing FA sequestering and lipid droplet transport efficiency [333]. Furthermore, Fitzner *et al.* observed that PGs are more abundant in cultured microglia compared to neurons or astrocytes [277]. Although neuron-specific deletion of *Gpx4* resulted in upregulation of both ApoE and PG species, further analysis concerning a neuron-astrocyte/microglia coupling effect associated to neuronal ferroptotic cell death in this animal model is required. This would then further support the presumption that ApoE, besides being upregulated in a pro-inflammatory response, also plays an important role in lipid metabolism upon neuron-specific *Gpx4* KO induction.

Cer metabolism plays an important role in brain homeostasis and is associated with neurodegenerative processes [283]. Cer can be synthesized via different pathways: the sphingomyelinase (SMase) pathway, the *de novo* synthesis, starting with serine and palminoyl-CoA or the salvage pathway [282]. Cutler *et al.* reported increased levels in long-chain Cer in AD patients, suffering from mild to moderate symptoms, and that lipid peroxidation triggered by iron exposure leads to increased levels of Cer and cholesterol in cultured neurons [334]. Similar findings were reported by Satoi *et al.* showing significantly elevated Cer levels in the CSF of AD patients and co-localization of Cer and astrocytes [335]. Comparing the lipids in cortical tissue of *Gpx4* KO mice, Cer were the most upregulated lipids after KO induction. The impact of *Gpx4* deletion on Cer metabolism is further evident from the significantly upregulated proteins unraveled in the proteomics study, including enzymes such as

ceramidase (acid ceramidase, glucosylceramidase, non-lysosomal glucosylceramidase) and sphingomyelinase (sphingomyelin phosphodiesterase), which is consistent with the elevated Cer levels in KO tissue. *Gpx4* deletion in cortical neurons induces significant changes in Cer metabolism, which might be associated with the neuroinflammation and neurodegeneration observed in our mouse model. The results provided here are in line with previous studies showing that sphingolipids and high levels of Cer are associated with the induction of neuronal cell death and the inflammatory response triggered by activated glial cells [281, 336, 337]. Yet, to resolve the complex interplay between ferroptotic neuronal cell death, oxidative stress and phospholipid peroxidation, an oxilipidomics approach to identify modified lipid species, including oxidized PLs, is mandatory. A recent study by Dong *et al.* uncovered oxidized phosphatidylcholines (oxPCs) as toxic species, triggering demyelination and neurodegeneration *in vivo* [338].

Overall, in-depth characterization of the molecular pattern of the brain is crucial to understand alterations in (patho)physiological conditions. The omics results presented herein clearly demonstrates a remarkable effect of the neuron-specific deletion of *Gpx4* on a vast number of proteins and lipid species in the cortex. However, region-specific protein and lipid content are related to different types of brain cells, such as glia and neurons, and specific cellular processes, such as cytoskeleton structure, regulation and metabolism, which might be only partially explored using standard MS analysis tools. In order to identify the underpinning lipidome changes and to understand the complexity of the system, including astro- and microgliosis as well as the infiltration of immune cells over time, brain samples of neuron-specific deletion of *Gpx4* mice should be ideally analyzed on a single-cell level.

Over the last decade, the possibility of high-throughput omics technology revolutionized the methodology and data generation in research. The application of different individual omics studies, primarily aiming at the global non-targeted analysis of proteins (proteomics), metabolites (metabolomics) and more recently lipids ((oxi)lipidomics), have been applied for a greater understanding of (patho)physiological processes and in biomarker discovery. Therefore, a global metabolome and (oxi)lipidome analysis of *Gpx4* KO mouse cortex should be performed next. Together with the proteomics and lipidomics results, these future studies are expected to aid the discovery of uncharacterized altered metabolic pathways elicited by the neuron-specific loss of *Gpx4* and to provide more definite insights into the molecular

mechanisms underlying NDs. Moreover, these studies are expected to enable the identification of a ferroptosis-specific marker with potential for future development of diagnostic biomarkers for NDs and other ferroptosis-associated brain pathologies. NDs have an enormous impact on quality of life, and thus, potential biomarker candidates and novel therapeutic targets are urgently awaiting to be established. As plasma NfL level is a general marker for neuronal damage in clinics, a ferroptosis-specific biomarker is of utmost importance to unequivocally demonstrate that ferroptotic cell death indeed underlies at least a fraction of neuropathologies.

5.3 Motor neurons are highly sensitive towards ferroptosis

The early death of MNs is the main characteristics of ALS [184]. While oxidative damage of cellular membranes is a known factor leading to neuronal death, the investigation of MN sensibility towards ferroptotic cell death was the second main topic of this thesis. The technology of hiPSCs and the differentiation of patient-derived hIPSCs create new possibilities to study the pathology of ALS *in vivo* and to identify and to test potential therapeutic approaches [339, 340]. The herein applied protocol for MN differentiation is based on an intermediate step of MNPs, followed by neuronal patterning by retinoic acid and purmorphamine treatment, which forces MNPs to MN by activating the sonic hedgehog (SHH) pathway. SHH signaling has been shown to be required for the induction and differentiation of MNs [341].

Two different hiPSC lines derived from ALS patients and one healthy control hiPSC clone were used for this study. However, the cell line originating from an 82 age-old patient carrying a rare *L144F* dominant mutation in the *SOD1* gene was excluded due to strongly impaired proliferation and poor differentiation rates. One possible reason for this might be the age of the patient as the donor is among the oldest patients carrying an ALS-causative *SOD1* allele. Second, a correlation between the *L144F* mutation in *SOD1* and a generally slow progression of ALS phenotype as well as unusual respiratory impairment onset can explain the difficulties of impaired differentiation [342, 343]. The second hiPSC line was generated from primary dermal fibroblasts from a 29 age-old ALS patient carrying a *SOD1G85S* mutation. Differentiated MNs from this Mut SOD1 and a control line were stained positive for HB9, CHAT, TUJ1, MAP2, confirming the efficient differentiation to MNs. Cell death induction and the use of specific cell death inhibitors were used to clarify the vulnerability of differentiated MNs and to explain what kind of cell death is predominant. The cell viability assays indicated a high sensitivity against ferroptosis-inducing agents and a susceptibility towards ferroptosis inhibitors in hiPSCs-derived MNs from the ALS patient. This increased sensitivity towards ferroptosis is in accordance with the previously reported link between oxidative stress and the pathogenesis of ALS [128, 142, 201]. Edaravone, an approved drug for the treatment of ALS patients, was included in the study. As an RTA preventing lipid peroxidation, it exhibited a rescuing effect against RSL3-induced ferroptosis at micromolar concentrations in the differentiated MN cells expressing the SOD1G85S mutation. Moreover, the protective effects of both liproxstatin compounds at nanomolar dosage uncovers these molecules as highly

promising tools targeting lipid peroxidation in dying MNs. This result supports the concept that MNs carrying an ALS-causing mutation are highly sensitive towards ferroptotic cell death. However, in order to strengthen and broaden these findings, additional patient-derived cell lines, including those from fALS as well as sALS cases, need to be included in similar assays in the future. Although the underlying molecular mechanisms of MN death remain enigmatic, the marked sensitivity of MNs carrying an ALS-causing mutation towards ferroptosis pave the way for studying the efficacy of novel ferroptosis inhibitors in models of ALS *in vivo*.

5.4 Motor neuron-specific deletion of *Gpx4* reveals long-term progression of ALS-like symptoms

In parallel to the cellular study using ALS-derived hiPSCs, a MN-specific GPX4 mouse model using *Gpx4^{fl/fl;Hb9Cre}* mice was established to investigate the *in vivo* mechanisms of ferroptosis. A constitutive MN-specific deletion of *Gpx4* leads to the development of progressive ALS-like symptoms in mice, including wavy and dragging tail, kyphosis, motor dysfunction and muscle weakness. A large cohort of the *Gpx4^{fl/fl;Hb9Cre}* mice was then used to assess the overall phenotype and survival of this mouse line. Various tests investigating balance and gait clearly indicated an impairment in coordination of *Gpx4* KO animals. These observations mirror the classical symptoms of patients suffering from ALS, including weaknesses in limbs and muscle atrophy [187]. The motoric alterations in KO mice were most likely driven by a degeneration of MNs and inflammasome activation in the lumbar part of spinal cord, as shown through staining for MNs and GFAP-positive cells in spinal cord sections.

MN degeneration ultimately causes progressive muscle weakness and paralysis of ALS patients, which is mirrored by elevated levels of NfL in CSF and plasma [271, 288]. As described above, NfL levels were found to be high in several neurological disorders [271]. In the clinics, NfL concentration is determined in CSF and serum samples in order to diagnose MN disease [288, 344]. The plasma NfL level in the established *Gpx4^{fl/fl;Hb9Cre}* mouse line correlated well with patient studies, showing higher NfL levels in ALS in comparison to control groups and a positive correlation with disease progression and survival. A further correlation is noticeable between age and circulating NfL levels, indicating that serum NfL level are generally higher in aged persons [288, 345], which is in accordance with the plasma NfL levels of the 24-months aged mice cohort as shown here. The results on spinal cord tissue revealed that the MN specific KO of *Gpx4* causes progressive neuronal loss and neuroinflammatory response,

leading to a progressive ALS-like phenotype including motoric impairments and increased plasma NfL levels.

An earlier study reported a striking phenotype and early death within 8 days after TAM treatment in a conditional GPX4 mouse model using single-neuron labeling inducible Cre-mediated knockout (Slick)-H transgenic mice, allowing neuron-specific conditional KO in Thy1-expressing cells, the majority of neurons population in CNS [128]. Although this study showed a delayed onset of paralysis by vitamin E supplementation, this model is hardly suitable to study disease progression as it fails to reflect long-term disease progression in human ALS patients [126]. This limitation was overcome here by the generation and characterization of the $Gpx4^{fl/fl;Hb9Cre}$ mouse line, showing a progressive impairment of the phenotype, allowing to further study the contribution to aging and immune system response. Hence, it supports the translational potential of this mouse studies to the pathology of ALS in patients.

The loss of MNs in the described $Gpx4^{fl/fl;Hb9Cre}$ mouse line was associated with alterations of the innervated skeletal muscles. Skeletal muscles are quite heterogeneous in nature allowing for a high flexibility. They are mainly grouped in type I and type II muscle fibers based on their contractile properties: slow-twitch muscles (type I), characterized by oxidative enzymes and fast-twitch muscle fibers (type II) mainly depending on glycolytic metabolism [346, 347]. An alteration or adaption of the composition of muscle fiber types upon deletion of $Gpx4$ in MNs as well as a shift towards lower proportion of type I and higher type II fibers was noticed in MN-specific $Gpx4$ KO animals. These results are consistent with those reported by Biering-Sorensen *et al.* suggesting a slow-to fast fiber transition when muscles become denervated and the observation of muscle fiber type switches in patients suffering from MN diseases [348]. Changes in muscle fiber types can be seen as a protective mechanism based on abnormal conditions including glucose and lipid metabolism, cytoskeletal functions and physical strength by the regulation of gene expression pattern or calcium release [348, 349]. Many studies are focusing on skeletal muscle and muscle fiber type alterations in the context of obesity and type 2 diabetes. It is known that insulin-mediated glucose uptake is related to the composition of muscle fiber types. It is suggested that insulin signaling and glucose metabolism is mainly present in type I fibers [350]. The observed muscle fiber switch in the MN-specific $Gpx4$ KO animals may therefore be linked to denervated muscles and alterations in glucose and lipid metabolism.

121

In order to gain first insights into an altered cell metabolism, plasma samples from 12-months old cohort were analyzed regarding parameters, such as inflammatory signals, insulin, cholesterol or triglycerides. The plasma analysis revealed alterations in lipid metabolism, indicated by a decrease of insulin and leptin concentrations and a decrease in cholesterol and triglycerides. Since the MN -specific *Gpx4* mouse model further reflects lower body weight, less fat and lean mass and less proportion of muscle fiber type I, the interplay of insulin and leptin secretion and their effect on skeletal muscle and adipose tissue [350-352] might be a first hint to the underlying mechanism controlling body weight. However, to gain more insights in this complex regulatory machinery, implication of metabolic cages, which enable the measurement of metabolism-related parameters, including food and energy consumption of mice, would be a very helpful tool.

Since lipid peroxidation is the hallmark of ferroptotic cell death and oxidative stress is seen as one of the causative factors of ALS, alterations in lipid metabolism were expected in the MN-specific *Gpx4* KO mouse model. The results from plasma parameter analysis showed reduced concentrations in cholesterol, HDL cholesterol and triglyceride in 12-months old KO animals, indicating dyshomeostasis of cholesterol metabolism, which is proposed to be closely linked to ALS pathogenesis [353, 354]. Shown in the study from Dorst *et al.*, effects of triglyceride and cholesterol levels are closely related to body weight and even survival in ALS patients [353]. In order to explore the role of ferroptotic cell death and its contribution to an altered lipid metabolism, those clinical parameters should be monitored in plasma samples of the GPX4 mouse model over time. In addition, to determine specific lethal lipid death signatures and to include alterations in FA composition, plasma samples as well as spinal cord tissue samples can be used to perform a detailed (epi)lipidomics analysis. The association of alterations in lipid metabolism and ALS disease progression are currently of great interest. Lipidomics studies on ALS patients and the transgenic *SOD1* mouse model have already shown increased levels of sphingomyelin, ceramides and cholesteryl esters in spinal cord tissue [355, 356]. To address the question concerning the trigger mechanism of such altered lipid composition, the combination and integration of lipidomics data from both engineered *Gpx4* KO mouse models will aid to identify the cause and consequence of induced ferroptotic cell death. However, further studies are necessary to uncover the underlying mechanism and link of *Gpx4* deletion and altered lipid metabolism in the MN-specific model, since the mouse model is based on the *Gpx4* KO in Mnx1 expressing cells. Beside the spinal cord MNs, Mnx1 is

also expressed in the pancreatic islet cells and is involved in both motor neuron and pancreatic beta cell development [234, 357]. The effect of possible *Gpx4* deletion in pancreatic cells was not addressed in this thesis; however, to draw a conclusion about the glucose and lipid metabolism in Mnx1-mediated KO model presented here, analysis of pancreatic tissue needs to be performed as the next step.

5.5 Transcriptome profiling of GPX4-deleted spinal cord tissue uncovers an activated immune system and impaired neuronal function

A genome-wide transcriptomic analysis was performed on spinal cord tissue of 12-months old *Gpx4$^{fl/fl;Hb9Cre}$* mice. This analysis revealed that *Chat* was found to be significantly downregulated, whereas the transcripts of *Gfap*, for example, were found to be higher in *Gpx4* KO animals. Further, the top regulated hits, including *Clec7a*, Lyz2 and *Vgf* strongly argue for an activated immune system, a decreased neuronal function and metabolic changes in *Gpx4* KO spinal cord. For instance, genes involved in the complement activation cascade, such as *C1qb*, *C1qb*, *C3ar1*, *C4a* and *C4b* were found to be significantly upregulated in the MN-specific *Gpx4* KO animals. This result underpins the finding that *Gpx4* KO leads to a progressive loss of MNs and an activated neuroinflammatory response akin to what was found in cortical neuron-specific GPX4 KO mice. Although mainly documented as a risk factor in AD, *ApoE* transcript levels were interestingly elevated in MN-specific *Gpx4* KO samples. An association of an *APOE* genotype and ALS patients was studied in different ALS patient cohorts, showing that the *APOE* gene does not directly contribute to be a higher risk for the development of ALS, however, depending on the *APOE* alleles the clinical profile may differs, whereby *APOE4* was linked to an earlier onset of ALS disease in this cohort [358, 359]. Both, several complement factors and APOE were also found to be highly abundant in the proteomics study of the cortical neuron specific *Gpx4* KO model (see 4.2). Conclusively, the activation of the complement system as a pro-inflammatory response seems to be tightly linked to the induction of neuronal ferroptotic cell death. Furthermore, the finding that APOE is highly enriched in both neuron-specific *Gpx4* KO mouse models supports the hypothesis that APOE may strongly impact on the neuroinflammatory response coinciding with both astro- and microgliosis, beyond its role to drive neurodegeneration in Aβ-, or *Tau*-dependent manner [318].

Moreover, several genes associated with calcium, glutamate and synaptogenesis signaling were found to be strongly downregulated in *Gpx4* KO tissue, including *Calm1*, *Glul* or *Grin2*. These genes code for receptors and proteins, which are essential for glutamate and calcium

homeostasis to maintain synaptic activity and signaling in MNs. The significantly lower expression levels of calcium-signaling associated genes suggest a modulation in calcium channel activity, calcium buffering capacity and loss of synapses, provoked by the loss of MN upon *Gpx4* deletion [360, 361]. One transcript being downregulated in spinal cord samples of KO animals was *Kif5a*. *Kif5a* is a member of the kinesin family of proteins and is expressed in neurons. KIF5 is a complex of KIF5A, KIF5B and KIF5C and functions as an axonal transport protein, trafficking cargos like proteins or organelles in neurons [362]. Interestingly, mutations in *Kif5a* were identified as a contributing factor in ALS even though with low penetrance, leading to the assumption that *Kif5a* is a novel ALS risk-associated gene [363]. Although the transcriptome profiling reflects only spinal cord tissue from 12-months old *Gpx4* KO and control mice, these results clearly showed an impact of MN-specific *Gpx4* deletion on an activated immune system, altered calcium signaling and a decrease in neuronal function. The signature of significantly altered genes will be helpful in the future to study the dynamic and complex profiling of gene regulation, such as *Chat*, complement factors or *ApoE* over time, in the motor-neuron specific *Gpx4* KO model and likely other animal models recapitulating ALS-disease.

5.6 Genetic and pharmacological approaches to ameliorate neuronal ferroptosis

Results presented in this thesis underline the importance of GPX4 as a guardian of ferroptosis in neuronal cells *in vivo* as they present two mouse models mimicking progressive ND phenotypes. Therefore, both GPX4 KO strains are highly suitable models to gain a better molecular understanding of this death pathway *in vivo* as a prerequisite for the development of novel ferroptosis inhibitors to efficiently combat the loss of neurons induced by ferroptosis.

Ingold *et al.* studied the relevance of selenium- versus thiol-based GPX4 catalysis in mice and isolated cells [44]. These studies showed that on one hand selenium-containing GPX4 is required for normal embryogenesis (on a congenic C57BL/6 background), while on the other hand the expression of the Cys-variant of GPX4 (Gpx4U46C) alone was sufficient to prevent TAM-inducible *Gpx4* KO mice from acute kidney injury [44]. The generation of neuron-specific *Gpx4cys/fl* mouse lines in this thesis thus aimed to address the question, whether Cys-containing GPX4 is sufficient to rescue the neurodegenerative phenotype upon *Gpx4* deletion in glutamatergic neurons of cortex as well as MN. As determined by immunohistological analyses and by measuring circulating NfL levels, these studies allowed to firmly conclude that Cys-

containing GPX4 mitigate the striking neurological phenotype in both transgenic mouse models. Considering future efforts in the development of potential gene therapies to treat NDs caused by ferroptosis, the transgenic expression of a selenium-independent variant of GPX4 might be the preferred way, as it would spare the need for the complex biosynthesis machinery required for selenoprotein expression [24, 59] [71].

Besides this, it was also studied whether the genetic loss of *Acsl4* in the *Gpx4* KO in glutamatergic neurons as well as MN may rescue the neurodegenerative phenotype in both models. ACSL4 preferentially activates PUFAs consisting of 20 carbon atoms (specifically AA and EPA), which are highly enriched in brain tissue [85, 101]. Doll and colleagues previously reported that ACSL4 is an important player in the ferroptosis cascade as its expression determines the cell's resistance towards ferroptotic cell death [28, 30]. Genetic loss or pharmacological inhibition of ACSL4 leads to an impaired activation of PUFAs and consequently PL membranes that have a much lower content of esterified PUFAs, which in turn are much more resistant to lipid peroxidation [28, 87]. It was further reported by the Conrad group that the compound class of thioazolidinediones, including rosiglitazone and the blood-brain-barrier permeable pioglitazone, which besides acting as PPAR-gamma agonist, as a side effect also inhibit ACSL4 and thus can be used as anti-ferroptotic compounds [28, 231, 364]. In this respect is it interesting to note that one study demonstrated that long-term use of pioglitazone may have neuroprotective activity in AD patients explained by an associated lower dementia incidence [365]. By studying the phenotype of ACSL4/GPX4 compound mutant mice, it was, however, found that the genetic deletion of *Acsl4* had no effect on the progression of neuronal loss and associated neuroinflammatory processes induced by neuronal *Gpx4* KO. Hence, these findings support the assumption that ACSL4 inhibitors will likely not qualify as a future therapies to treat chronic neurological disorders caused by ferroptosis. Nevertheless, it needs to be shown whether ACSL4 might be a potential target for approaches to treat acute CNS diseases, such as ischemic or hemorrhagic stroke.

A possible explanation of these results with *Acsl4* KO might be that ACSL6, which is closely related to ACSL4, might play the predominant role in CNS by activating PUFAs. In fact, ACSL6 is highly expressed in neuronal tissue and is the fatty acid ligase that preferably activates very long-chain fatty acids including DHA, which is the most abundant PUFA in brain tissue [88].

Indeed, cell-based data from our laboratory shows that ACSL6 is able to compensate for the loss of ACSL4 (Lorenz *et al.*, unpublished). Since ACSL6 is essential for embryogenesis like ACSL4 [104], the generation of compound mutant mice lacking both GPX4 and ACSL6 in neurons might be a valid approach to potentially ameliorate neurodegenerative and neuroinflammatory phenotypes elicited by the neuron-specific loss of *Gpx4*.

Lastly, it was addressed in this thesis whether the application of ferroptosis inhibitors is a viable approach to ameliorate the neuronal loss induced by GPX4 loss. To this end, novel BBB-permeable liproxstatins (developed in our institute) were used. Mechanistically liproxstatins act as RTAs by inhibiting the accumulation of toxic lipid hydroperoxides in lipid bilayer. Thereby, the aromatic amine of Lip-1 becomes oxidized and forms a nitrogen-centered radical that upon oxidation can repeatedly reduce multiple peroxyl radicals in PL bilayers whereby it regenerates itself [52, 54]. Although, Lip-1 has been repeatedly shown to inhibit ferroptotic cell death in various tissue and diseases models [15, 24], the moderate BBB permeability (unpublished data) needs to be taken into account when testing Lip-1 in neuronal ferroptotic models. This might be the reason why there was just a tendency for neuroprotective activity of Lip-1. In contrast, the *in vitro* study using ALS-patient derived MNs showed clear efficacy towards Lip treatment to inhibit RSL3-mediated ferroptotic cell death. Therefore, future studies should be geared towards next generation liproxstatins with proven BBB permeability in order to test their efficacy in various ND models including GPX4 KO models but also in other bona fide neurodegeneration models, such was the SOD1G93A tg mouse models, Tau models and Huntington's disease models.

Conclusively, the comprehensive characterization of the mouse models generated here demonstrates that ferroptotic neuronal cell death is sufficient to induce a neurodegenerative phenotype and molecular pattern reminiscent to neurological disorders in man. The data presented in this thesis corroborate GPX4 as the key regulator of ferroptosis being indispensable for neuronal survival. The spatiotemporal deletion of *Gpx4* in glutamatergic neurons causes progressive neuronal loss, eliciting a vicious cycle of a neuroinflammatory response and immune cell infiltration that finally culminates in massive cortical atrophy. The omics analysis of cortex tissue revealed striking similarities with molecular signatures characteristic of AD and other NDs, despite the absence of known risk factors or mutations in ND-associated genes in the models established in this thesis. Unlike previously reported

neuron-specific GPX4 null models (which is often associated with premature death), both mouse lines are highly valuable tools not only to investigate in details the long-term progression of dementia and ALS-like symptoms, but also to establish biomarkers of ferroptosis in neurons and to test the *in vivo* efficacy of novel ferroptosis-inhibiting drugs.

6 REFERENCES

1.   Lockshin, R.A. and C.M. Williams, *Programmed Cell Death--I. Cytology of Degeneration in the Intersegmental Muscles of the Pernyi Silkmoth.* J Insect Physiol, 1965. **11**: p. 123-33.
2.   Kerr, J.F., *Shrinkage necrosis: a distinct mode of cellular death.* J Pathol, 1971. **105**(1): p. 13-20.
3.   Galluzzi, L., et al., *Molecular mechanisms of cell death: recommendations of the Nomenclature Committee on Cell Death 2018.* Cell Death Differ, 2018. **25**(3): p. 486-541.
4.   Dolma, S., et al., *Identification of genotype-selective antitumor agents using synthetic lethal chemical screening in engineered human tumor cells.* Cancer Cell, 2003. **3**(3): p. 285-96.
5.   Yang, W.S. and B.R. Stockwell, *Synthetic lethal screening identifies compounds activating iron-dependent, nonapoptotic cell death in oncogenic-RAS-harboring cancer cells.* Chem Biol, 2008. **15**(3): p. 234-45.
6.   Seiler, A., et al., *Glutathione peroxidase 4 senses and translates oxidative stress into 12/15-lipoxygenase dependent- and AIF-mediated cell death.* Cell Metab, 2008. **8**(3): p. 237-48.
7.   Dixon, S.J., et al., *Ferroptosis: an iron-dependent form of nonapoptotic cell death.* Cell, 2012. **149**(5): p. 1060-72.
8.   Davis, J.B. and P. Maher, *Protein kinase C activation inhibits glutamate-induced cytotoxicity in a neuronal cell line.* Brain Res, 1994. **652**(1): p. 169-73.
9.   Tan, S., D. Schubert, and P. Maher, *Oxytosis: A novel form of programmed cell death.* Curr Top Med Chem, 2001. **1**(6): p. 497-506.
10.   Lewerenz, J., et al., *Oxytosis/Ferroptosis-(Re-) Emerging Roles for Oxidative Stress-Dependent Non-apoptotic Cell Death in Diseases of the Central Nervous System.* Front Neurosci, 2018. **12**: p. 214.
11.   Bannai, S., H. Tsukeda, and H. Okumura, *Effect of antioxidants on cultured human diploid fibroblasts exposed to cystine-free medium.* Biochem Biophys Res Commun, 1977. **74**(4): p. 1582-8.
12.   Eagle, H., *The specific amino acid requirements of a human carcinoma cell (Stain HeLa) in tissue culture.* J Exp Med, 1955. **102**(1): p. 37-48.
13.   Yang, W.S., et al., *Regulation of ferroptotic cancer cell death by GPX4.* Cell, 2014. **156**(1-2): p. 317-331.
14.   Ursini, F., et al., *Purification from pig liver of a protein which protects liposomes and biomembranes from peroxidative degradation and exhibits glutathione peroxidase activity on phosphatidylcholine hydroperoxides.* Biochim Biophys Acta, 1982. **710**(2): p. 197-211.
15.   Friedmann Angeli, J.P., et al., *Inactivation of the ferroptosis regulator Gpx4 triggers acute renal failure in mice.* Nat Cell Biol, 2014. **16**(12): p. 1180-91.
16.   Doll, S., et al., *FSP1 is a glutathione-independent ferroptosis suppressor.* Nature, 2019. **575**(7784): p. 693-698.
17.   Bersuker, K., et al., *The CoQ oxidoreductase FSP1 acts parallel to GPX4 to inhibit ferroptosis.* Nature, 2019. **575**(7784): p. 688-692.
18.   Yang, W.S. and B.R. Stockwell, *Ferroptosis: Death by Lipid Peroxidation.* Trends Cell Biol, 2016. **26**(3): p. 165-176.
19.   Sato, H., et al., *Cloning and expression of a plasma membrane cystine/glutamate exchange transporter composed of two distinct proteins.* J Biol Chem, 1999. **274**(17): p. 11455-8.
20.   Mandal, P.K., et al., *System x(c)- and thioredoxin reductase 1 cooperatively rescue glutathione deficiency.* J Biol Chem, 2010. **285**(29): p. 22244-53.
21.   Conrad, M. and H. Sato, *The oxidative stress-inducible cystine/glutamate antiporter, system x (c) (-) : cystine supplier and beyond.* Amino Acids, 2012. **42**(1): p. 231-46.
22.   Bannai, S., *Exchange of cystine and glutamate across plasma membrane of human fibroblasts.* J Biol Chem, 1986. **261**(5): p. 2256-63.
23.   Griffith, O.W., *Biologic and pharmacologic regulation of mammalian glutathione synthesis.* Free Radic Biol Med, 1999. **27**(9-10): p. 922-35.

24. Conrad, M., S.M. Lorenz, and B. Proneth, *Targeting Ferroptosis: New Hope for As-Yet-Incurable Diseases.* Trends Mol Med, 2021. **27**(2): p. 113-122.

25. Zheng, J., et al., *Sorafenib fails to trigger ferroptosis across a wide range of cancer cell lines.* Cell Death Dis, 2021. **12**(7): p. 698.

26. Shimada, K., et al., *Global survey of cell death mechanisms reveals metabolic regulation of ferroptosis.* Nat Chem Biol, 2016. **12**(7): p. 497-503.

27. Zou, Y., et al., *A GPX4-dependent cancer cell state underlies the clear-cell morphology and confers sensitivity to ferroptosis.* Nat Commun, 2019. **10**(1): p. 1617.

28. Doll, S., et al., *ACSL4 dictates ferroptosis sensitivity by shaping cellular lipid composition.* Nat Chem Biol, 2017. **13**(1): p. 91-98.

29. Dixon, S.J., et al., *Human Haploid Cell Genetics Reveals Roles for Lipid Metabolism Genes in Nonapoptotic Cell Death.* ACS Chem Biol, 2015. **10**(7): p. 1604-9.

30. Kagan, V.E., et al., *Oxidized arachidonic and adrenic PEs navigate cells to ferroptosis.* Nat Chem Biol, 2017. **13**(1): p. 81-90.

31. Kakhlon, O. and Z.I. Cabantchik, *The labile iron pool: characterization, measurement, and participation in cellular processes(1).* Free Radic Biol Med, 2002. **33**(8): p. 1037-46.

32. Zhang, D.L., M.C. Ghosh, and T.A. Rouault, *The physiological functions of iron regulatory proteins in iron homeostasis - an update.* Front Pharmacol, 2014. **5**: p. 124.

33. Andrews, N.C. and P.J. Schmidt, *Iron homeostasis.* Annu Rev Physiol, 2007. **69**: p. 69-85.

34. Shah, R., M.S. Shchepinov, and D.A. Pratt, *Resolving the Role of Lipoxygenases in the Initiation and Execution of Ferroptosis.* ACS Cent Sci, 2018. **4**(3): p. 387-396.

35. Ivanov, I., et al., *Molecular enzymology of lipoxygenases.* Arch Biochem Biophys, 2010. **503**(2): p. 161-74.

36. Kuhn, H., S. Banthiya, and K. van Leyen, *Mammalian lipoxygenases and their biological relevance.* Biochim Biophys Acta, 2015. **1851**(4): p. 308-30.

37. Zou, Y., et al., *Cytochrome P450 oxidoreductase contributes to phospholipid peroxidation in ferroptosis.* Nat Chem Biol, 2020. **16**(3): p. 302-309.

38. Kwon, M.Y., et al., *Heme oxygenase-1 accelerates erastin-induced ferroptotic cell death.* Oncotarget, 2015. **6**(27): p. 24393-403.

39. Sun, X., et al., *Activation of the p62-Keap1-NRF2 pathway protects against ferroptosis in hepatocellular carcinoma cells.* Hepatology, 2016. **63**(1): p. 173-84.

40. Galy, B., et al., *Iron regulatory proteins are essential for intestinal function and control key iron absorption molecules in the duodenum.* Cell Metab, 2008. **7**(1): p. 79-85.

41. Fang, X., et al., *Loss of Cardiac Ferritin H Facilitates Cardiomyopathy via Slc7a11-Mediated Ferroptosis.* Circ Res, 2020. **127**(4): p. 486-501.

42. LaVaute, T., et al., *Targeted deletion of the gene encoding iron regulatory protein-2 causes misregulation of iron metabolism and neurodegenerative disease in mice.* Nat Genet, 2001. **27**(2): p. 209-14.

43. Everett, J., et al., *Biogenic metallic elements in the human brain?* Sci Adv, 2021. **7**(24).

44. Ingold, I., et al., *Selenium Utilization by GPX4 Is Required to Prevent Hydroperoxide-Induced Ferroptosis.* Cell, 2018. **172**(3): p. 409-422 e21.

45. Goldstein, J.L. and M.S. Brown, *Regulation of the mevalonate pathway.* Nature, 1990. **343**(6257): p. 425-30.

46. Miziorko, H.M., *Enzymes of the mevalonate pathway of isoprenoid biosynthesis.* Arch Biochem Biophys, 2011. **505**(2): p. 131-43.

47. Jose Pedro Friedmann Angeli, F.P.F., Palina Nepachalovich, Lohans Puentes, Omkar Zilka, Alex Inague, Svenja Lorenz, Viktoria Kunz, Helene Nehring, Thamara Nishida Xavier da Silva, Zhiyi Chen, Sebastian Doll, Werner Schmitz, Peter Imming, Sayuri Miyamoto, Judith Klein-Seetharaman, Lokender Kumar, Thiago Cardoso Genaro-Mattos, Karoly Mirnics, Svenja Meierjohann, Matthias Kroiss, Isabel Weigand, Kurt Bommert, Ralf Bargou, Ana Garcia-Saez, Derek Pratt, Maria Fedorova, Ann Wehmann, Aline Horling, Georg Bornkamm, Marcus Conrad, *7-Dehydrocholesterol is an endogenous suppressor of ferroptosis.* Nature, October 6th, 2021.

48.   Garcia-Bermudez, J., et al., *Squalene accumulation in cholesterol auxotrophic lymphomas prevents oxidative cell death.* Nature, 2019. **567**(7746): p. 118-122.

49.   Frei, B., M.C. Kim, and B.N. Ames, *Ubiquinol-10 is an effective lipid-soluble antioxidant at physiological concentrations.* Proc Natl Acad Sci U S A, 1990. **87**(12): p. 4879-83.

50.   Kraft, V.A.N., et al., *GTP Cyclohydrolase 1/Tetrahydrobiopterin Counteract Ferroptosis through Lipid Remodeling.* ACS Cent Sci, 2020. **6**(1): p. 41-53.

51.   Jiang, X., B.R. Stockwell, and M. Conrad, *Ferroptosis: mechanisms, biology and role in disease.* Nat Rev Mol Cell Biol, 2021. **22**(4): p. 266-282.

52.   Zilka, O., et al., *On the Mechanism of Cytoprotection by Ferrostatin-1 and Liproxstatin-1 and the Role of Lipid Peroxidation in Ferroptotic Cell Death.* ACS Cent Sci, 2017. **3**(3): p. 232-243.

53.   Shah, R., K. Margison, and D.A. Pratt, *The Potency of Diarylamine Radical-Trapping Antioxidants as Inhibitors of Ferroptosis Underscores the Role of Autoxidation in the Mechanism of Cell Death.* ACS Chem Biol, 2017. **12**(10): p. 2538-2545.

54.   Conrad, M. and D.A. Pratt, *The chemical basis of ferroptosis.* Nat Chem Biol, 2019. **15**(12): p. 1137-1147.

55.   Maiorino, M., M. Conrad, and F. Ursini, *GPx4, Lipid Peroxidation, and Cell Death: Discoveries, Rediscoveries, and Open Issues.* Antioxid Redox Signal, 2018. **29**(1): p. 61-74.

56.   Dalleau, S., et al., *Cell death and diseases related to oxidative stress: 4-hydroxynonenal (HNE) in the balance.* Cell Death Differ, 2013. **20**(12): p. 1615-30.

57.   Schwarz, K. and C.M. Foltz, *Factor 3 activity of selenium compounds.* J Biol Chem, 1958. **233**(1): p. 245-51.

58.   Spallholz, J.E., L.M. Boylan, and H.S.J.A.o.t.N.Y.A.o.S. Larsen, *Advances in understanding selenium's role in the immune system.* 1990. **587**(1): p. 123-139.

59.   Hatfield, D.L., et al., *Selenium and selenocysteine: roles in cancer, health, and development.* Trends Biochem Sci, 2014. **39**(3): p. 112-20.

60.   Labunskyy, V.M., D.L. Hatfield, and V.N. Gladyshev, *Selenoproteins: molecular pathways and physiological roles.* Physiol Rev, 2014. **94**(3): p. 739-77.

61.   Roveri, A., et al., *Purification and characterization of phospholipid hydroperoxide glutathione peroxidase from rat testis mitochondrial membranes.* Biochim Biophys Acta, 1994. **1208**(2): p. 211-21.

62.   Brigelius-Flohé, R. and M. Maiorino, *Glutathione peroxidases.* Biochim Biophys Acta, 2013. **1830**(5): p. 3289-303.

63.   Flohe, L., W.A. Günzler, and H.H. Schock, *Glutathione peroxidase: a selenoenzyme.* FEBS Lett, 1973. **32**(1): p. 132-4.

64.   Toppo, S., et al., *Evolutionary and structural insights into the multifaceted glutathione peroxidase (Gpx) superfamily.* Antioxid Redox Signal, 2008. **10**(9): p. 1501-14.

65.   Kryukov, G.V., et al., *Characterization of mammalian selenoproteomes.* Science, 2003. **300**(5624): p. 1439-43.

66.   Li, C., et al., *Functional analysis of the role of glutathione peroxidase (GPx) in the ROS signaling pathway, hyphal branching and the regulation of ganoderic acid biosynthesis in Ganoderma lucidum.* Fungal Genet Biol, 2015. **82**: p. 168-80.

67.   Muthukumar, K., et al., *Glutathione peroxidase3 of Saccharomyces cerevisiae protects phospholipids during cadmium-induced oxidative stress.* Antonie Van Leeuwenhoek, 2011. **99**(4): p. 761-71.

68.   Thomas, J.P., et al., *Enzymatic reduction of phospholipid and cholesterol hydroperoxides in artificial bilayers and lipoproteins.* Biochim Biophys Acta, 1990. **1045**(3): p. 252-60.

69.   Maiorino, M., et al., *Probing the presumed catalytic triad of selenium-containing peroxidases by mutational analysis of phospholipid hydroperoxide glutathione peroxidase (PHGPx).* Biol Chem Hoppe Seyler, 1995. **376**(11): p. 651-60.

70.   Conrad, M., *Transgenic mouse models for the vital selenoenzymes cytosolic thioredoxin reductase, mitochondrial thioredoxin reductase and glutathione peroxidase 4.* Biochim Biophys Acta, 2009. **1790**(11): p. 1575-85.

71. Conrad, M. and B. Proneth, *Selenium: Tracing Another Essential Element of Ferroptotic Cell Death.* Cell Chem Biol, 2020. **27**(4): p. 409-419.

72. Brigelius-Flohe, R., et al., *Phospholipid-hydroperoxide glutathione peroxidase. Genomic DNA, cDNA, and deduced amino acid sequence.* J Biol Chem, 1994. **269**(10): p. 7342-8.

73. Maiorino, M., et al., *Distinct promoters determine alternative transcription of gpx-4 into phospholipid-hydroperoxide glutathione peroxidase variants.* J Biol Chem, 2003. **278**(36): p. 34286-90.

74. Moreno, S.G., et al., *Testis-specific expression of the nuclear form of phospholipid hydroperoxide glutathione peroxidase (PHGPx).* Biol Chem, 2003. **384**(4): p. 635-43.

75. Conrad, M., et al., *The nuclear form of phospholipid hydroperoxide glutathione peroxidase is a protein thiol peroxidase contributing to sperm chromatin stability.* Mol Cell Biol, 2005. **25**(17): p. 7637-44.

76. Pfeifer, H., et al., *Identification of a specific sperm nuclei selenoenzyme necessary for protamine thiol cross-linking during sperm maturation.* FASEB J, 2001. **15**(7): p. 1236-8.

77. Ursini, F., et al., *Dual function of the selenoprotein PHGPx during sperm maturation.* Science, 1999. **285**(5432): p. 1393-6.

78. Schneider, M., et al., *Mitochondrial glutathione peroxidase 4 disruption causes male infertility.* FASEB J, 2009. **23**(9): p. 3233-42.

79. Conrad, M., et al., *Physiological role of phospholipid hydroperoxide glutathione peroxidase in mammals.* Biol Chem, 2007. **388**(10): p. 1019-25.

80. Liang, H., et al., *Short form glutathione peroxidase 4 is the essential isoform required for survival and somatic mitochondrial functions.* J Biol Chem, 2009. **284**(45): p. 30836-44.

81. Arai, M., et al., *Mitochondrial phospholipid hydroperoxide glutathione peroxidase plays a major role in preventing oxidative injury to cells.* J Biol Chem, 1999. **274**(8): p. 4924-33.

82. Imai, H., et al., *Early embryonic lethality caused by targeted disruption of the mouse PHGPx gene.* Biochem Biophys Res Commun, 2003. **305**(2): p. 278-86.

83. Yant, L.J., et al., *The selenoprotein GPX4 is essential for mouse development and protects from radiation and oxidative damage insults.* Free Radic Biol Med, 2003. **34**(4): p. 496-502.

84. Vance, J.E., *Phosphatidylserine and phosphatidylethanolamine in mammalian cells: two metabolically related aminophospholipids.* J Lipid Res, 2008. **49**(7): p. 1377-87.

85. Choi, J., et al., *Comprehensive analysis of phospholipids in the brain, heart, kidney, and liver: brain phospholipids are least enriched with polyunsaturated fatty acids.* Mol Cell Biochem, 2018. **442**(1-2): p. 187-201.

86. Sastry, P.S., *Lipids of nervous tissue: composition and metabolism.* Prog Lipid Res, 1985. **24**(2): p. 69-176.

87. O'Donnell, V.B., et al., *Lipidomics: Current state of the art in a fast moving field.* Wiley Interdiscip Rev Syst Biol Med, 2020. **12**(1): p. e1466.

88. Lacombe, R.J.S., R. Chouinard-Watkins, and R.P. Bazinet, *Brain docosahexaenoic acid uptake and metabolism.* Mol Aspects Med, 2018. **64**: p. 109-134.

89. Bazinet, R.P. and S. Laye, *Polyunsaturated fatty acids and their metabolites in brain function and disease.* Nat Rev Neurosci, 2014. **15**(12): p. 771-85.

90. Watkins, P.A. and J.M. Ellis, *Peroxisomal acyl-CoA synthetases.* Biochim Biophys Acta, 2012. **1822**(9): p. 1411-20.

91. Firsov, A.M., et al., *Threshold protective effect of deuterated polyunsaturated fatty acids on peroxidation of lipid bilayers.* FEBS J, 2019. **286**(11): p. 2099-2117.

92. Martin, S.A., et al., *Measurement of lysophospholipid acyltransferase activities using substrate competition.* J Lipid Res, 2014. **55**(4): p. 782-91.

93. Lands, W.E., *Metabolism of glycerolipids. 2. The enzymatic acylation of lysolecithin.* J Biol Chem, 1960. **235**: p. 2233-7.

94. Kathman, S.G., et al., *Blockade of the Lysophosphatidylserine Lipase ABHD12 Potentiates Ferroptosis in Cancer Cells.* ACS Chem Biol, 2020. **15**(4): p. 871-877.

95. Soupene, E. and F.A. Kuypers, *Mammalian long-chain acyl-CoA synthetases.* Exp Biol Med (Maywood), 2008. **233**(5): p. 507-21.

96. Hisanaga, Y., et al., *Structural basis of the substrate-specific two-step catalysis of long chain fatty acyl-CoA synthetase dimer.* J Biol Chem, 2004. **279**(30): p. 31717-26.

97. Ong, W.L., et al., *Differential effects of polyunsaturated fatty acids on membrane capacitance and exocytosis in rat pheochromocytoma-12 cells.* Neurochem Res, 2006. **31**(1): p. 41-8.

98. Soupene, E., et al., *Activity of the acyl-CoA synthetase ACSL6 isoforms: role of the fatty acid Gate-domains.* BMC Biochem, 2010. **11**: p. 18.

99. Magtanong, L., et al., *Exogenous Monounsaturated Fatty Acids Promote a Ferroptosis-Resistant Cell State.* Cell Chem Biol, 2019. **26**(3): p. 420-432 e9.

100. Kuwata, H., et al., *Role of long-chain acyl-coenzyme A synthetases in the regulation of arachidonic acid metabolism in interleukin 1beta-stimulated rat fibroblasts.* Biochim Biophys Acta, 2014. **1841**(1): p. 44-53.

101. Cao, Y., et al., *Cloning, expression, and chromosomal localization of human long-chain fatty acid-CoA ligase 4 (FACL4).* Genomics, 1998. **49**(2): p. 327-30.

102. Marszalek, J.R., et al., *Long-chain acyl-CoA synthetase 6 preferentially promotes DHA metabolism.* J Biol Chem, 2005. **280**(11): p. 10817-26.

103. Fernandez, R.F., et al., *Acyl-CoA synthetase 6 enriches the neuroprotective omega-3 fatty acid DHA in the brain.* Proc Natl Acad Sci U S A, 2018. **115**(49): p. 12525-12530.

104. Hale, B.J., et al., *Acyl-CoA synthetase 6 enriches seminiferous tubules with the omega-3 fatty acid docosahexaenoic acid and is required for male fertility in the mouse.* J Biol Chem, 2019. **294**(39): p. 14394-14405.

105. Soupene, E. and F.A. Kuypers, *Multiple erythroid isoforms of human long-chain acyl-CoA synthetases are produced by switch of the fatty acid gate domains.* BMC Mol Biol, 2006. **7**: p. 21.

106. Aldrovandi, M., M. Fedorova, and M. Conrad, *Juggling with lipids, a game of Russian roulette.* Trends Endocrinol Metab, 2021. **32**(7): p. 463-473.

107. Kyle, J.E., et al., *Interpreting the lipidome: bioinformatic approaches to embrace the complexity.* Metabolomics, 2021. **17**(6): p. 55.

108. Jiang, L., et al., *Ferroptosis as a p53-mediated activity during tumour suppression.* Nature, 2015. **520**(7545): p. 57-62.

109. Sato, M., et al., *Loss of the cystine/glutamate antiporter in melanoma abrogates tumor metastasis and markedly increases survival rates of mice.* Int J Cancer, 2020. **147**(11): p. 3224-3235.

110. Cramer, S.L., et al., *Systemic depletion of L-cyst(e)ine with cyst(e)inase increases reactive oxygen species and suppresses tumor growth.* Nat Med, 2017. **23**(1): p. 120-127.

111. Badgley, M.A., et al., *Cysteine depletion induces pancreatic tumor ferroptosis in mice.* Science, 2020. **368**(6486): p. 85-89.

112. Arensman, M.D., et al., *Cystine-glutamate antiporter xCT deficiency suppresses tumor growth while preserving antitumor immunity.* Proc Natl Acad Sci U S A, 2019. **116**(19): p. 9533-9542.

113. Lim, J.K.M., et al., *Cystine/glutamate antiporter xCT (SLC7A11) facilitates oncogenic RAS transformation by preserving intracellular redox balance.* Proc Natl Acad Sci U S A, 2019. **116**(19): p. 9433-9442.

114. Hangauer, M.J., et al., *Drug-tolerant persister cancer cells are vulnerable to GPX4 inhibition.* Nature, 2017. **551**(7679): p. 247-250.

115. Viswanathan, V.S., et al., *Dependency of a therapy-resistant state of cancer cells on a lipid peroxidase pathway.* Nature, 2017. **547**(7664): p. 453-457.

116. Roth, G.A., et al., *Global Burden of Cardiovascular Diseases and Risk Factors, 1990-2019: Update From the GBD 2019 Study.* J Am Coll Cardiol, 2020. **76**(25): p. 2982-3021.

117. Alim, I., et al., *Selenium Drives a Transcriptional Adaptive Program to Block Ferroptosis and Treat Stroke.* Cell, 2019. **177**(5): p. 1262-1279 e25.

118. Jin, Y., et al., *Inhibiting ferroptosis: A novel approach for stroke therapeutics.* Drug Discov Today, 2021. **26**(4): p. 916-930.

119. Linkermann, A., et al., *Synchronized renal tubular cell death involves ferroptosis.* Proc Natl Acad Sci U S A, 2014. **111**(47): p. 16836-41.

120. Li, Q., et al., *Inhibition of neuronal ferroptosis protects hemorrhagic brain.* JCI Insight, 2017. **2**(7): p. e90777.

121. Tuo, Q.Z., et al., *Tau-mediated iron export prevents ferroptotic damage after ischemic stroke.* Mol Psychiatry, 2017. **22**(11): p. 1520-1530.

122. Devisscher, L., et al., *Discovery of Novel, Drug-Like Ferroptosis Inhibitors with in Vivo Efficacy.* J Med Chem, 2018. **61**(22): p. 10126-10140.

123. Yoshida, M., et al., *Involvement of cigarette smoke-induced epithelial cell ferroptosis in COPD pathogenesis.* Nat Commun, 2019. **10**(1): p. 3145.

124. Skouta, R., et al., *Ferrostatins inhibit oxidative lipid damage and cell death in diverse disease models.* J Am Chem Soc, 2014. **136**(12): p. 4551-6.

125. Bellinger, F.P., et al., *Glutathione Peroxidase 4 is associated with Neuromelanin in Substantia Nigra and Dystrophic Axons in Putamen of Parkinson's brain.* Mol Neurodegener, 2011. **6**(1): p. 8.

126. Hauser, D.N., et al., *Dopamine quinone modifies and decreases the abundance of the mitochondrial selenoprotein glutathione peroxidase 4.* Free Radic Biol Med, 2013. **65**: p. 419-427.

127. Do Van, B., et al., *Ferroptosis, a newly characterized form of cell death in Parkinson's disease that is regulated by PKC.* Neurobiol Dis, 2016. **94**: p. 169-78.

128. Chen, L., et al., *Ablation of the Ferroptosis Inhibitor Glutathione Peroxidase 4 in Neurons Results in Rapid Motor Neuron Degeneration and Paralysis.* J Biol Chem, 2015. **290**(47): p. 28097-28106.

129. Hambright, W.S., et al., *Ablation of ferroptosis regulator glutathione peroxidase 4 in forebrain neurons promotes cognitive impairment and neurodegeneration.* Redox Biol, 2017. **12**: p. 8-17.

130. Lau, A. and M. Tymianski, *Glutamate receptors, neurotoxicity and neurodegeneration.* Pflugers Arch, 2010. **460**(2): p. 525-42.

131. Wirth, E.K., et al., *Neuronal selenoprotein expression is required for interneuron development and prevents seizures and neurodegeneration.* FASEB J, 2010. **24**(3): p. 844-52.

132. Wirth, E.K., et al., *Cerebellar hypoplasia in mice lacking selenoprotein biosynthesis in neurons.* Biol Trace Elem Res, 2014. **158**(2): p. 203-10.

133. Ueta, T., et al., *Glutathione peroxidase 4 is required for maturation of photoreceptor cells.* J Biol Chem, 2012. **287**(10): p. 7675-82.

134. Przedborski, S., M. Vila, and V. Jackson-Lewis, *Neurodegeneration: what is it and where are we?* J Clin Invest, 2003. **111**(1): p. 3-10.

135. Hutchins, J.B. and S.W. Barger, *Why neurons die: cell death in the nervous system.* Anat Rec, 1998. **253**(3): p. 79-90.

136. Hou, Y., et al., *Ageing as a risk factor for neurodegenerative disease.* Nat Rev Neurol, 2019. **15**(10): p. 565-581.

137. Benussi, A., A. Padovani, and B. Borroni, *Phenotypic Heterogeneity of Monogenic Frontotemporal Dementia.* Front Aging Neurosci, 2015. **7**: p. 171.

138. Olszewska, D.A., et al., *Genetics of Frontotemporal Dementia.* Curr Neurol Neurosci Rep, 2016. **16**(12): p. 107.

139. Collaborators, G.B.D.D., *Global, regional, and national burden of Alzheimer's disease and other dementias, 1990-2016: a systematic analysis for the Global Burden of Disease Study 2016.* Lancet Neurol, 2019. **18**(1): p. 88-106.

140. Hippius, H. and G. Neundorfer, *The discovery of Alzheimer's disease.* Dialogues Clin Neurosci, 2003. **5**(1): p. 101-8.

141. Congdon, E.E. and E.M. Sigurdsson, *Tau-targeting therapies for Alzheimer disease.* Nat Rev Neurol, 2018. **14**(7): p. 399-415.

142. Barnham, K.J., C.L. Masters, and A.I. Bush, *Neurodegenerative diseases and oxidative stress.* Nat Rev Drug Discov, 2004. **3**(3): p. 205-14.

143. Hansson, O., *Biomarkers for neurodegenerative diseases.* Nat Med, 2021. **27**(6): p. 954-963.

144. Masters, C.L., et al., *Amyloid plaque core protein in Alzheimer disease and Down syndrome.* Proc Natl Acad Sci U S A, 1985. **82**(12): p. 4245-9.

145. Glenner, G.G. and C.W. Wong, *Alzheimer's disease: initial report of the purification and characterization of a novel cerebrovascular amyloid protein.* Biochem Biophys Res Commun, 1984. **120**(3): p. 885-90.

146. Haass, C. and D.J. Selkoe, *Cellular processing of beta-amyloid precursor protein and the genesis of amyloid beta-peptide.* Cell, 1993. **75**(6): p. 1039-42.

147. Chen, G.F., et al., *Amyloid beta: structure, biology and structure-based therapeutic development.* Acta Pharmacol Sin, 2017. **38**(9): p. 1205-1235.

148. Canevari, L., A.Y. Abramov, and M.R. Duchen, *Toxicity of amyloid beta peptide: tales of calcium, mitochondria, and oxidative stress.* Neurochem Res, 2004. **29**(3): p. 637-50.

149. Kim, T., et al., *Human LilrB2 is a beta-amyloid receptor and its murine homolog PirB regulates synaptic plasticity in an Alzheimer's model.* Science, 2013. **341**(6152): p. 1399-404.

150. Deshpande, A., et al., *A role for synaptic zinc in activity-dependent Abeta oligomer formation and accumulation at excitatory synapses.* J Neurosci, 2009. **29**(13): p. 4004-15.

151. Naveilhan, P., et al., *1,25-Dihydroxyvitamin D3 regulates the expression of the low-affinity neurotrophin receptor.* Brain Res Mol Brain Res, 1996. **41**(1-2): p. 259-68.

152. Peng, L., et al., *The chemerin receptor CMKLR1 is a functional receptor for amyloid-beta peptide.* J Alzheimers Dis, 2015. **43**(1): p. 227-42.

153. Huang, L.K., S.P. Chao, and C.J. Hu, *Clinical trials of new drugs for Alzheimer disease.* J Biomed Sci, 2020. **27**(1): p. 18.

154. Rosenblum, W.I., *Why Alzheimer trials fail: removing soluble oligomeric beta amyloid is essential, inconsistent, and difficult.* Neurobiol Aging, 2014. **35**(5): p. 969-74.

155. Makin, S., *The amyloid hypothesis on trial.* Nature, 2018. **559**(7715): p. S4-S7.

156. Fagan, A.M., et al., *Human and murine ApoE markedly alters A beta metabolism before and after plaque formation in a mouse model of Alzheimer's disease.* Neurobiol Dis, 2002. **9**(3): p. 305-18.

157. Shi, Y., et al., *ApoE4 markedly exacerbates tau-mediated neurodegeneration in a mouse model of tauopathy.* Nature, 2017. **549**(7673): p. 523-527.

158. Liu, C.C., et al., *Apolipoprotein E and Alzheimer disease: risk, mechanisms and therapy.* Nat Rev Neurol, 2013. **9**(2): p. 106-18.

159. Shi, Y. and D.M. Holtzman, *Interplay between innate immunity and Alzheimer disease: APOE and TREM2 in the spotlight.* Nat Rev Immunol, 2018. **18**(12): p. 759-772.

160. Bales, K.R., et al., *Apolipoprotein E is essential for amyloid deposition in the APP(V717F) transgenic mouse model of Alzheimer's disease.* Proc Natl Acad Sci U S A, 1999. **96**(26): p. 15233-8.

161. Holtzman, D.M., et al., *Apolipoprotein E isoform-dependent amyloid deposition and neuritic degeneration in a mouse model of Alzheimer's disease.* Proc Natl Acad Sci U S A, 2000. **97**(6): p. 2892-7.

162. Strittmatter, W.J., et al., *Isoform-specific interactions of apolipoprotein E with microtubule-associated protein tau: implications for Alzheimer disease.* Proc Natl Acad Sci U S A, 1994. **91**(23): p. 11183-6.

163. Braak, H., et al., *Staging of Alzheimer disease-associated neurofibrillary pathology using paraffin sections and immunocytochemistry.* Acta Neuropathol, 2006. **112**(4): p. 389-404.

164. Huang, Y. and R.W. Mahley, *Apolipoprotein E: structure and function in lipid metabolism, neurobiology, and Alzheimer's diseases.* Neurobiol Dis, 2014. **72 Pt A**: p. 3-12.

165. Hanger, D.P., et al., *Novel phosphorylation sites in tau from Alzheimer brain support a role for casein kinase 1 in disease pathogenesis.* J Biol Chem, 2007. **282**(32): p. 23645-54.

166. Goate, A., et al., *Segregation of a missense mutation in the amyloid precursor protein gene with familial Alzheimer's disease.* Nature, 1991. **349**(6311): p. 704-6.

167. Irizarry, M.C., et al., *APPSw transgenic mice develop age-related A beta deposits and neuropil abnormalities, but no neuronal loss in CA1.* J Neuropathol Exp Neurol, 1997. **56**(9): p. 965-73.

168. Bekris, L.M., et al., *Genetics of Alzheimer disease.* J Geriatr Psychiatry Neurol, 2010. **23**(4): p. 213-27.

169. Fernandez, C.G., et al., *The Role of APOE4 in Disrupting the Homeostatic Functions of Astrocytes and Microglia in Aging and Alzheimer's Disease.* Front Aging Neurosci, 2019. **11**: p. 14.

170. Yin, C., et al., *ApoE attenuates unresolvable inflammation by complex formation with activated C1q.* Nat Med, 2019. **25**(3): p. 496-506.

171. Fitz, N.F., et al., *Phospholipids of APOE lipoproteins activate microglia in an isoform-specific manner in preclinical models of Alzheimer's disease.* Nat Commun, 2021. **12**(1): p. 3416.

172. Itagaki, S., et al., *Relationship of microglia and astrocytes to amyloid deposits of Alzheimer disease.* J Neuroimmunol, 1989. **24**(3): p. 173-82.

173. Henneman, W.J., et al., *Hippocampal atrophy rates in Alzheimer disease: added value over whole brain volume measures.* Neurology, 2009. **72**(11): p. 999-1007.

174. Tay, T.L., et al., *A new fate mapping system reveals context-dependent random or clonal expansion of microglia.* Nat Neurosci, 2017. **20**(6): p. 793-803.

175. Deczkowska, A., et al., *Disease-Associated Microglia: A Universal Immune Sensor of Neurodegeneration.* Cell, 2018. **173**(5): p. 1073-1081.

176. Martin, E., et al., *Distinct inflammatory phenotypes of microglia and monocyte-derived macrophages in Alzheimer's disease models: effects of aging and amyloid pathology.* Aging Cell, 2017. **16**(1): p. 27-38.

177. Hickman, S., et al., *Microglia in neurodegeneration.* Nat Neurosci, 2018. **21**(10): p. 1359-1369.

178. Yuan, P., et al., *TREM2 Haplodeficiency in Mice and Humans Impairs the Microglia Barrier Function Leading to Decreased Amyloid Compaction and Severe Axonal Dystrophy.* Neuron, 2016. **90**(4): p. 724-39.

179. Krasemann, S., et al., *The TREM2-APOE Pathway Drives the Transcriptional Phenotype of Dysfunctional Microglia in Neurodegenerative Diseases.* Immunity, 2017. **47**(3): p. 566-581 e9.

180. Eng, L.F., et al., *An acidic protein isolated from fibrous astrocytes.* Brain Res, 1971. **28**(2): p. 351-4.

181. Escartin, C., et al., *Reactive astrocyte nomenclature, definitions, and future directions.* Nat Neurosci, 2021. **24**(3): p. 312-325.

182. Rodriguez, J.J., et al., *Astroglia in dementia and Alzheimer's disease.* Cell Death Differ, 2009. **16**(3): p. 378-85.

183. Talbott, E.O., A.M. Malek, and D. Lacomis, *The epidemiology of amyotrophic lateral sclerosis.* Handb Clin Neurol, 2016. **138**: p. 225-38.

184. Ragagnin, A.M.G., et al., *Motor Neuron Susceptibility in ALS/FTD.* Front Neurosci, 2019. **13**: p. 532.

185. Bhumbra, G.S. and M. Beato, *Recurrent excitation between motoneurones propagates across segments and is purely glutamatergic.* PLoS Biol, 2018. **16**(3): p. e2003586.

186. Stifani, N., *Motor neurons and the generation of spinal motor neuron diversity.* Front Cell Neurosci, 2014. **8**: p. 293.

187. Taylor, J.P., R.H. Brown, Jr., and D.W. Cleveland, *Decoding ALS: from genes to mechanism.* Nature, 2016. **539**(7628): p. 197-206.

188. Barber, S.C. and P.J. Shaw, *Oxidative stress in ALS: key role in motor neuron injury and therapeutic target.* Free Radic Biol Med, 2010. **48**(5): p. 629-41.

189. Gurney, M.E., et al., *Motor neuron degeneration in mice that express a human Cu,Zn superoxide dismutase mutation.* Science, 1994. **264**(5166): p. 1772-5.

190. Rosen, D.R., et al., *Mutations in Cu/Zn superoxide dismutase gene are associated with familial amyotrophic lateral sclerosis.* Nature, 1993. **362**(6415): p. 59-62.

191. Parone, P.A., et al., *Enhancing mitochondrial calcium buffering capacity reduces aggregation of misfolded SOD1 and motor neuron cell death without extending survival in mouse models of inherited amyotrophic lateral sclerosis.* J Neurosci, 2013. **33**(11): p. 4657-71.

192. Neumann, M., et al., *Ubiquitinated TDP-43 in frontotemporal lobar degeneration and amyotrophic lateral sclerosis.* Science, 2006. **314**(5796): p. 130-3.

193. Rademakers, R., et al., *Fus gene mutations in familial and sporadic amyotrophic lateral sclerosis.* Muscle Nerve, 2010. **42**(2): p. 170-6.

194. DeJesus-Hernandez, M., et al., *Expanded GGGGCC hexanucleotide repeat in noncoding region of C9ORF72 causes chromosome 9p-linked FTD and ALS.* Neuron, 2011. **72**(2): p. 245-56.

195. Vande Velde, C., et al., *Selective association of misfolded ALS-linked mutant SOD1 with the cytoplasmic face of mitochondria.* Proc Natl Acad Sci U S A, 2008. **105**(10): p. 4022-7.

196. Burberry, A., et al., *C9orf72 suppresses systemic and neural inflammation induced by gut bacteria.* Nature, 2020. **582**(7810): p. 89-94.

197. Tam, O.H., et al., *Postmortem Cortex Samples Identify Distinct Molecular Subtypes of ALS: Retrotransposon Activation, Oxidative Stress, and Activated Glia.* Cell Rep, 2019. **29**(5): p. 1164-1177 e5.

198. Barber, C.N. and D.M. Raben, *Lipid Metabolism Crosstalk in the Brain: Glia and Neurons.* Front Cell Neurosci, 2019. **13**: p. 212.

199. Smith, E.F., P.J. Shaw, and K.J. De Vos, *The role of mitochondria in amyotrophic lateral sclerosis.* Neurosci Lett, 2019. **710**: p. 132933.

200. Lee, J.K., et al., *Iron accumulation promotes TACE-mediated TNF-alpha secretion and neurodegeneration in a mouse model of ALS.* Neurobiol Dis, 2015. **80**: p. 63-9.

201. Gurney, M.E., et al., *Benefit of vitamin E, riluzole, and gabapentin in a transgenic model of familial amyotrophic lateral sclerosis.* Ann Neurol, 1996. **39**(2): p. 147-57.

202. Andreassen, O.A., et al., *N-acetyl-L-cysteine improves survival and preserves motor performance in an animal model of familial amyotrophic lateral sclerosis.* Neuroreport, 2000. **11**(11): p. 2491-3.

203. Graf, M., et al., *High dose vitamin E therapy in amyotrophic lateral sclerosis as add-on therapy to riluzole: results of a placebo-controlled double-blind study.* J Neural Transm (Vienna), 2005. **112**(5): p. 649-60.

204. Louwerse, E.S., et al., *Randomized, double-blind, controlled trial of acetylcysteine in amyotrophic lateral sclerosis.* Arch Neurol, 1995. **52**(6): p. 559-64.

205. Homma, T., et al., *Edaravone, a free radical scavenger, protects against ferroptotic cell death in vitro.* Exp Cell Res, 2019. **384**(1): p. 111592.

206. Jaiswal, M.K., *Riluzole and edaravone: A tale of two amyotrophic lateral sclerosis drugs.* Med Res Rev, 2019. **39**(2): p. 733-748.

207. Cunha-Oliveira, T., et al., *Oxidative Stress in Amyotrophic Lateral Sclerosis: Pathophysiology and Opportunities for Pharmacological Intervention.* Oxid Med Cell Longev, 2020. **2020**: p. 5021694.

208. Albom, M., *Tuesdays With Morrie: An old man, a young man, and life's greatest lesson*. 1st Broadway Books trade pbk. ed. ed. 1998, New York, NY : Broadway Books, 2002.: Broadway Books.

209. Crain, S.M., *Development of "organotypic" bioelectric activities in central nervous tissues during maturation in culture.* Int Rev Neurobiol, 1966. **9**: p. 1-43.

210. Crain, S.M. and E.R. Peterson, *Development of neural connections in culture.* Ann N Y Acad Sci, 1974. **228**(0): p. 6-34.

211. Thomson, J.A., et al., *Embryonic stem cell lines derived from human blastocysts.* Science, 1998. **282**(5391): p. 1145-7.

212. Takahashi, K. and S. Yamanaka, *Induction of pluripotent stem cells from mouse embryonic and adult fibroblast cultures by defined factors.* Cell, 2006. **126**(4): p. 663-76.

213. Takahashi, K., et al., *Induction of pluripotent stem cells from adult human fibroblasts by defined factors.* Cell, 2007. **131**(5): p. 861-72.

214. Yagi, T., et al., *Modeling familial Alzheimer's disease with induced pluripotent stem cells.* Hum Mol Genet, 2011. **20**(23): p. 4530-9.

215. Lee, G., et al., *Modelling pathogenesis and treatment of familial dysautonomia using patient-specific iPSCs.* Nature, 2009. **461**(7262): p. 402-6.

216. Brennand, K.J., et al., *Modelling schizophrenia using human induced pluripotent stem cells.* Nature, 2011. **473**(7346): p. 221-5.

217. Dimos, J.T., et al., *Induced pluripotent stem cells generated from patients with ALS can be differentiated into motor neurons.* Science, 2008. **321**(5893): p. 1218-21.

218. Eggan, K., *Using stem cells and reprogramming to understand disease.* Regen Med, 2008. **3**(6): p. 799-801.

219. Paquet, D., et al., *Efficient introduction of specific homozygous and heterozygous mutations using CRISPR/Cas9.* Nature, 2016. **533**(7601): p. 125-9.

220. Kwart, D., et al., *A Large Panel of Isogenic APP and PSEN1 Mutant Human iPSC Neurons Reveals Shared Endosomal Abnormalities Mediated by APP beta-CTFs, Not Abeta.* Neuron, 2019. **104**(5): p. 1022.

221. Papadimitriou, C., et al., *3D Culture Method for Alzheimer's Disease Modeling Reveals Interleukin-4 Rescues Abeta42-Induced Loss of Human Neural Stem Cell Plasticity.* Dev Cell, 2018. **46**(1): p. 85-101 e8.

222. Chiaradia, I. and M.A. Lancaster, *Brain organoids for the study of human neurobiology at the interface of in vitro and in vivo.* Nat Neurosci, 2020. **23**(12): p. 1496-1508.

223. Eglen, R.M. and T. Reisine, *Human iPS Cell-Derived Patient Tissues and 3D Cell Culture Part 2: Spheroids, Organoids, and Disease Modeling.* SLAS Technol, 2019. **24**(1): p. 18-27.

224. Veening-Griffioen, D.H., et al., *Are some animal models more equal than others? A case study on the translational value of animal models of efficacy for Alzheimer's disease.* Eur J Pharmacol, 2019. **859**: p. 172524.

225. Hanes, J., et al., *Rat tau proteome consists of six tau isoforms: implication for animal models of human tauopathies.* J Neurochem, 2009. **108**(5): p. 1167-76.

226. Kloskowska, E., et al., *Cognitive impairment in the Tg6590 transgenic rat model of Alzheimer's disease.* J Cell Mol Med, 2010. **14**(6B): p. 1816-23.

227. Gotz, J., L.G. Bodea, and M. Goedert, *Rodent models for Alzheimer disease.* Nat Rev Neurosci, 2018. **19**(10): p. 583-598.

228. LaMonte, B.H., et al., *Disruption of dynein/dynactin inhibits axonal transport in motor neurons causing late-onset progressive degeneration.* Neuron, 2002. **34**(5): p. 715-27.

229. Feng, W., et al., *Gclc deficiency in mouse CNS causes mitochondrial damage and neurodegeneration.* Hum Mol Genet, 2017. **26**(7): p. 1376-1390.

230. Chen, L., et al., *Overexpression of ferroptosis defense enzyme Gpx4 retards motor neuron disease of SOD1G93A mice.* Sci Rep, 2021. **11**(1): p. 12890.

231. Doll, S.G., *Identification of new pathway members of ferroptotic cell death.* 2017.

232. Casanova, E., et al., *A CamKIIalpha iCre BAC allows brain-specific gene inactivation.* Genesis, 2001. **31**(1): p. 37-42.

233. Erdmann, G., G. Schutz, and S. Berger, *Inducible gene inactivation in neurons of the adult mouse forebrain.* BMC Neurosci, 2007. **8**: p. 63.

234. Arber, S., et al., *Requirement for the homeobox gene Hb9 in the consolidation of motor neuron identity.* Neuron, 1999. **23**(4): p. 659-74.

235. Smedley, D., et al., *The BioMart community portal: an innovative alternative to large, centralized data repositories.* Nucleic Acids Res, 2015. **43**(W1): p. W589-98.

236. Berriz, G.F., et al., *Characterizing gene sets with FuncAssociate.* Bioinformatics, 2003. **19**(18): p. 2502-4.

237. Kulak, N.A., et al., *Minimal, encapsulated proteomic-sample processing applied to copy-number estimation in eukaryotic cells.* Nat Methods, 2014. **11**(3): p. 319-24.

238. Cox, J. and M. Mann, *MaxQuant enables high peptide identification rates, individualized p.p.b.-range mass accuracies and proteome-wide protein quantification.* Nat Biotechnol, 2008. **26**(12): p. 1367-72.

239. Cox, J., et al., *Accurate proteome-wide label-free quantification by delayed normalization and maximal peptide ratio extraction, termed MaxLFQ.* Mol Cell Proteomics, 2014. **13**(9): p. 2513-26.

240. Tyanova, S., et al., *The Perseus computational platform for comprehensive analysis of (prote)omics data.* Nat Methods, 2016. **13**(9): p. 731-40.

241. Benjamini, Y. and Y. Hochberg, *Controlling the False Discovery Rate: A Practical and Powerful Approach to Multiple Testing.* 1995. **57**(1): p. 289-300.

242. Frisch, M., et al., *LitInspector: literature and signal transduction pathway mining in PubMed abstracts.* Nucleic Acids Res, 2009. **37**(Web Server issue): p. W135-40.

243. Folch, J., M. Lees, and G.H. Sloane Stanley, *A simple method for the isolation and purification of total lipides from animal tissues.* J Biol Chem, 1957. **226**(1): p. 497-509.

244. Goracci, L., et al., *Lipostar, a Comprehensive Platform-Neutral Cheminformatics Tool for Lipidomics.* Anal Chem, 2017. **89**(11): p. 6257-6264.

245. Adams, K.J., et al., *Skyline for Small Molecules: A Unifying Software Package for Quantitative Metabolomics.* J Proteome Res, 2020. **19**(4): p. 1447-1458.

246. Pang, Z., et al., *MetaboAnalyst 5.0: narrowing the gap between raw spectra and functional insights.* Nucleic Acids Res, 2021. **49**(W1): p. W388-W396.

247. Sturn, A., J. Quackenbush, and Z. Trajanoski, *Genesis: cluster analysis of microarray data.* Bioinformatics, 2002. **18**(1): p. 207-8.

248. Du, Z.W., et al., *Generation and expansion of highly pure motor neuron progenitors from human pluripotent stem cells.* Nat Commun, 2015. **6**: p. 6626.

249. Fuchs, H., et al., *Understanding gene functions and disease mechanisms: Phenotyping pipelines in the German Mouse Clinic.* Behav Brain Res, 2018. **352**: p. 187-196.

250. Garrett, L., et al., *Conditional Reduction of Adult Born Doublecortin-Positive Neurons Reversibly Impairs Selective Behaviors.* Front Behav Neurosci, 2015. **9**: p. 302.

251. Heermann, T., et al., *Crybb2 Mutations Consistently Affect Schizophrenia Endophenotypes in Mice.* Mol Neurobiol, 2019. **56**(6): p. 4215-4230.

252. Holter, S.M., et al., *Assessing Cognition in Mice.* Curr Protoc Mouse Biol, 2015. **5**(4): p. 331-358.

253. Hölter, S.M.G., L., *High-throughput mouse phenotyping.*, in *Animal Models of Movement Disorders. Volume I*, E.L.D. Lane, S.B.*, Editor. 2011, Springer: Berlin.

254. Gailus-Durner, V., et al., *Introducing the German Mouse Clinic: open access platform for standardized phenotyping.* Nat Methods, 2005. **2**(6): p. 403-4.

255. Fuchs, H., et al., *The German Mouse Clinic: a platform for systemic phenotype analysis of mouse models.* Curr Pharm Biotechnol, 2009. **10**(2): p. 236-43.

256. Fuchs, H., et al., *Mouse phenotyping.* Methods, 2011. **53**(2): p. 120-35.

257. Zimprich, A., et al., *Analysis of locomotor behavior in the German Mouse Clinic.* J Neurosci Methods, 2018. **300**: p. 77-91.

258. Laws, N. and A. Hoey, *Progression of kyphosis in mdx mice.* J Appl Physiol (1985), 2004. **97**(5): p. 1970-7.

259. Schindelin, J., et al., *Fiji: an open-source platform for biological-image analysis.* Nat Methods, 2012. **9**(7): p. 676-82.

260. Rathkolb, B., et al., *Clinical Chemistry and Other Laboratory Tests on Mouse Plasma or Serum.* Curr Protoc Mouse Biol, 2013. **3**(2): p. 69-100.

261. Dobin, A., et al., *STAR: ultrafast universal RNA-seq aligner.* Bioinformatics, 2013. **29**(1): p. 15-21.

262. Love, M.I., W. Huber, and S. Anders, *Moderated estimation of fold change and dispersion for RNA-seq data with DESeq2.* Genome Biol, 2014. **15**(12): p. 550.

263. Kim, K.K., R.S. Adelstein, and S. Kawamoto, *Identification of neuronal nuclei (NeuN) as Fox-3, a new member of the Fox-1 gene family of splicing factors.* J Biol Chem, 2009. **284**(45): p. 31052-61.

264. Zhang, Z., et al., *Human traumatic brain injury induces autoantibody response against glial fibrillary acidic protein and its breakdown products.* PLoS One, 2014. **9**(3): p. e92698.

265. LaFleur, A.M., et al., *Role of CC chemokine CCL6/C10 as a monocyte chemoattractant in a murine acute peritonitis.* Mediators Inflamm, 2004. **13**(5-6): p. 349-55.

266. Hinojosa, A.E., et al., *Dual effects of noradrenaline on astroglial production of chemokines and pro-inflammatory mediators.* J Neuroinflammation, 2013. **10**: p. 81.

267. Bhowmick, S., et al., *Intercellular Adhesion Molecule-1-Induced Posttraumatic Brain Injury Neuropathology in the Prefrontal Cortex and Hippocampus Leads to Sensorimotor Function Deficits and Psychological Stress.* eNeuro, 2021. **8**(4).

268. McGrath, E.R., et al., *Circulating IGFBP-2: a novel biomarker for incident dementia.* Ann Clin Transl Neurol, 2019. **6**(9): p. 1659-1670.

269. Walker, D.G., et al., *Changes in CD200 and intercellular adhesion molecule-1 (ICAM-1) levels in brains of Lewy body disorder cases are associated with amounts of Alzheimer's pathology not alpha-synuclein pathology.* Neurobiol Aging, 2017. **54**: p. 175-186.

270. Yu, H., X. Liu, and Y. Zhong, *The Effect of Osteopontin on Microglia.* Biomed Res Int, 2017. **2017**: p. 1879437.

271. Abu-Rumeileh, S., et al., *CSF biomarkers of neuroinflammation in distinct forms and subtypes of neurodegenerative dementia.* Alzheimers Res Ther, 2019. **12**(1): p. 2.

272. Wang, L.Y., et al., *CXCL5 signaling is a shared pathway of neuroinflammation and blood-brain barrier injury contributing to white matter injury in the immature brain.* J Neuroinflammation, 2016. **13**: p. 6.

273. Lee, M., et al., *Tissue-specific Role of CX3CR1 Expressing Immune Cells and Their Relationships with Human Disease.* Immune Netw, 2018. **18**(1): p. e5.

274. Fujioka, H., et al., *Neural functions of matrix metalloproteinases: plasticity, neurogenesis, and disease.* Biochem Res Int, 2012. **2012**: p. 789083.

275. Witte, K., et al., *IL-28A, IL-28B, and IL-29: promising cytokines with type I interferon-like properties.* Cytokine Growth Factor Rev, 2010. **21**(4): p. 237-51.

276. Dawson, G., *Measuring brain lipids.* Biochim Biophys Acta, 2015. **1851**(8): p. 1026-39.

277. Fitzner, D., et al., *Cell-Type- and Brain-Region-Resolved Mouse Brain Lipidome.* Cell Rep, 2020. **32**(11): p. 108132.

278. Lagace, T.A., *Phosphatidylcholine: Greasing the Cholesterol Transport Machinery.* Lipid Insights, 2015. **8**(Suppl 1): p. 65-73.

279. Law, S.H., et al., *An Updated Review of Lysophosphatidylcholine Metabolism in Human Diseases.* Int J Mol Sci, 2019. **20**(5).

280. Hannun, Y.A. and L.M. Obeid, *The Ceramide-centric universe of lipid-mediated cell regulation: stress encounters of the lipid kind.* J Biol Chem, 2002. **277**(29): p. 25847-50.

281. Hannun, Y.A. and L.M. Obeid, *Principles of bioactive lipid signalling: lessons from sphingolipids.* Nat Rev Mol Cell Biol, 2008. **9**(2): p. 139-50.

282. Kitatani, K., J. Idkowiak-Baldys, and Y.A. Hannun, *The sphingolipid salvage pathway in ceramide metabolism and signaling.* Cell Signal, 2008. **20**(6): p. 1010-8.

283. Castellanos, D.B., et al., *Brain lipidomics as a rising field in neurodegenerative contexts: Perspectives with Machine Learning approaches.* Front Neuroendocrinol, 2021. **61**: p. 100899.

284. Lewerenz, J., P. Maher, and A. Methner, *Regulation of xCT expression and system x (c) (-) function in neuronal cells.* Amino Acids, 2012. **42**(1): p. 171-9.

285. Rogers, D.C., et al., *Behavioral and functional analysis of mouse phenotype: SHIRPA, a proposed protocol for comprehensive phenotype assessment.* Mamm Genome, 1997. **8**(10): p. 711-3.

286. Bahney, J. and C.S. von Bartheld, *The Cellular Composition and Glia-Neuron Ratio in the Spinal Cord of a Human and a Nonhuman Primate: Comparison With Other Species and Brain Regions.* Anat Rec (Hoboken), 2018. **301**(4): p. 697-710.

287. Arvanitakis, Z., R.C. Shah, and D.A. Bennett, *Diagnosis and Management of Dementia: Review.* JAMA, 2019. **322**(16): p. 1589-1599.

288. Steinacker, P., et al., *Neurofilaments in the diagnosis of motoneuron diseases: a prospective study on 455 patients.* J Neurol Neurosurg Psychiatry, 2016. **87**(1): p. 12-20.

289. Benzing, W.C., et al., *Evidence for glial-mediated inflammation in aged APP(SW) transgenic mice.* Neurobiol Aging, 1999. **20**(6): p. 581-9.

290. Heneka, M.T., et al., *Focal glial activation coincides with increased BACE1 activation and precedes amyloid plaque deposition in APP[V717I] transgenic mice.* J Neuroinflammation, 2005. **2**: p. 22.

291. Chun, H., et al., *Severe reactive astrocytes precipitate pathological hallmarks of Alzheimer's disease via H2O2(-) production.* Nat Neurosci, 2020. **23**(12): p. 1555-1566.

292. Chatterjee, P., et al., *Plasma glial fibrillary acidic protein is elevated in cognitively normal older adults at risk of Alzheimer's disease.* Transl Psychiatry, 2021. **11**(1): p. 27.

293. Oeckl, P., et al., *Glial Fibrillary Acidic Protein in Serum is Increased in Alzheimer's Disease and Correlates with Cognitive Impairment.* J Alzheimers Dis, 2019. **67**(2): p. 481-488.

294. Simpson, J.E., et al., *Astrocyte phenotype in relation to Alzheimer-type pathology in the ageing brain.* Neurobiol Aging, 2010. **31**(4): p. 578-90.

295. Rodriguez, J.J., et al., *Enriched environment and physical activity reverse astrogliodegeneration in the hippocampus of AD transgenic mice.* Cell Death Dis, 2013. **4**: p. e678.

296. Kriegstein, A. and A. Alvarez-Buylla, *The glial nature of embryonic and adult neural stem cells.* Annu Rev Neurosci, 2009. **32**: p. 149-84.

297. Butovsky, O., et al., *Identification of a unique TGF-beta-dependent molecular and functional signature in microglia.* Nat Neurosci, 2014. **17**(1): p. 131-43.

298. Mrdjen, D., et al., *High-Dimensional Single-Cell Mapping of Central Nervous System Immune Cells Reveals Distinct Myeloid Subsets in Health, Aging, and Disease.* Immunity, 2018. **48**(2): p. 380-395 e6.

299. Friedman, B.A., et al., *Diverse Brain Myeloid Expression Profiles Reveal Distinct Microglial Activation States and Aspects of Alzheimer's Disease Not Evident in Mouse Models.* Cell Rep, 2018. **22**(3): p. 832-847.

300. Spiller, K.J., et al., *Microglia-mediated recovery from ALS-relevant motor neuron degeneration in a mouse model of TDP-43 proteinopathy.* Nat Neurosci, 2018. **21**(3): p. 329-340.

301. Wang, Y., et al., *TREM2 lipid sensing sustains the microglial response in an Alzheimer's disease model.* Cell, 2015. **160**(6): p. 1061-71.

302. Keren-Shaul, H., et al., *A Unique Microglia Type Associated with Restricting Development of Alzheimer's Disease.* Cell, 2017. **169**(7): p. 1276-1290 e17.

303. Steinacker, P., et al., *Chitotriosidase (CHIT1) is increased in microglia and macrophages in spinal cord of amyotrophic lateral sclerosis and cerebrospinal fluid levels correlate with disease severity and progression.* J Neurol Neurosurg Psychiatry, 2018. **89**(3): p. 239-247.

304. Prinz, M. and J. Priller, *The role of peripheral immune cells in the CNS in steady state and disease.* Nat Neurosci, 2017. **20**(2): p. 136-144.

305. Croese, T., G. Castellani, and M. Schwartz, *Immune cell compartmentalization for brain surveillance and protection.* Nat Immunol, 2021. **22**(9): p. 1083-1092.

306. Janda, E., L. Boi, and A.R. Carta, *Microglial Phagocytosis and Its Regulation: A Therapeutic Target in Parkinson's Disease?* Front Mol Neurosci, 2018. **11**: p. 144.

307. Galloway, D.A., et al., *Corrigendum: Phagocytosis in the Brain: Homeostasis and Disease.* Front Immunol, 2019. **10**: p. 1575.

308. Laurent, C., et al., *Hippocampal T cell infiltration promotes neuroinflammation and cognitive decline in a mouse model of tauopathy.* Brain, 2017. **140**(1): p. 184-200.

309. Geisert, E.E., Jr., H.G. Johnson, and L.I. Binder, *Expression of microtubule-associated protein 2 by reactive astrocytes.* Proc Natl Acad Sci U S A, 1990. **87**(10): p. 3967-71.

310. Dehmelt, L. and S. Halpain, *The MAP2/Tau family of microtubule-associated proteins.* Genome Biol, 2005. **6**(1): p. 204.

311. Chen, F., et al., *Clusterin secreted from astrocyte promotes excitatory synaptic transmission and ameliorates Alzheimer's disease neuropathology.* Mol Neurodegener, 2021. **16**(1): p. 5.

312. Foster, E.M., et al., *Clusterin in Alzheimer's Disease: Mechanisms, Genetics, and Lessons From Other Pathologies.* Front Neurosci, 2019. **13**: p. 164.

313. Koch, S., et al., *Characterization of four lipoprotein classes in human cerebrospinal fluid.* J Lipid Res, 2001. **42**(7): p. 1143-51.

314. Koch, M., et al., *Apolipoproteins and their subspecies in human cerebrospinal fluid and plasma.* Alzheimers Dement (Amst), 2017. **6**: p. 182-187.

315. Viard, I., et al., *Clusterin gene expression mediates resistance to apoptotic cell death induced by heat shock and oxidative stress.* J Invest Dermatol, 1999. **112**(3): p. 290-6.

316. Trougakos, I.P. and E.S. Gonos, *Regulation of clusterin/apolipoprotein J, a functional homologue to the small heat shock proteins, by oxidative stress in ageing and age-related diseases.* Free Radic Res, 2006. **40**(12): p. 1324-34.

317. Castellano, J.M., et al., *Human apoE isoforms differentially regulate brain amyloid-beta peptide clearance.* Sci Transl Med, 2011. **3**(89): p. 89ra57.

318. Tzioras, M., et al., *Invited Review: APOE at the interface of inflammation, neurodegeneration and pathological protein spread in Alzheimer's disease.* Neuropathol Appl Neurobiol, 2019. **45**(4): p. 327-346.

319. Farber, K., et al., *C1q, the recognition subcomponent of the classical pathway of complement, drives microglial activation.* J Neurosci Res, 2009. **87**(3): p. 644-52.

320. Lynch, N.J., et al., *Microglial activation and increased synthesis of complement component C1q precedes blood-brain barrier dysfunction in rats.* Mol Immunol, 2004. **40**(10): p. 709-16.

321. Klavins, K., et al., *The ratio of phosphatidylcholines to lysophosphatidylcholines in plasma differentiates healthy controls from patients with Alzheimer's disease and mild cognitive impairment.* Alzheimers Dement (Amst), 2015. **1**(3): p. 295-302.

322. Fonteh, A.N., et al., *Accumulation of Cerebrospinal Fluid Glycerophospholipids and Sphingolipids in Cognitively Healthy Participants With Alzheimer's Biomarkers Precedes Lipolysis in the Dementia Stage.* Front Neurosci, 2020. **14**: p. 611393.

323. Nayeem, M.A., *Role of oxylipins in cardiovascular diseases.* Acta Pharmacol Sin, 2018. **39**(7): p. 1142-1154.

324. Shearer, G.C. and J.W. Newman, *Impact of circulating esterified eicosanoids and other oxylipins on endothelial function.* Curr Atheroscler Rep, 2009. **11**(6): p. 403-10.

325. Rajamani, A., et al., *Oxylipins in triglyceride-rich lipoproteins of dyslipidemic subjects promote endothelial inflammation following a high fat meal.* Sci Rep, 2019. **9**(1): p. 8655.

326. Borkowski, K., et al., *Association of plasma and CSF cytochrome P450, soluble epoxide hydrolase, and ethanolamide metabolism with Alzheimer's disease.* Alzheimers Res Ther, 2021. **13**(1): p. 149.

327. Bazan, N.G., V. Colangelo, and W.J. Lukiw, *Prostaglandins and other lipid mediators in Alzheimer's disease.* Prostaglandins Other Lipid Mediat, 2002. **68-69**: p. 197-210.

328. Nguyen, T.B., et al., *DGAT1-Dependent Lipid Droplet Biogenesis Protects Mitochondrial Function during Starvation-Induced Autophagy.* Dev Cell, 2017. **42**(1): p. 9-21 e5.

329. Ioannou, M.S., et al., *Neuron-Astrocyte Metabolic Coupling Protects against Activity-Induced Fatty Acid Toxicity.* Cell, 2019. **177**(6): p. 1522-1535 e14.

330. Marschallinger, J., et al., *Lipid-droplet-accumulating microglia represent a dysfunctional and proinflammatory state in the aging brain.* Nat Neurosci, 2020. **23**(2): p. 194-208.

331. Liu, L., et al., *Glial lipid droplets and ROS induced by mitochondrial defects promote neurodegeneration.* Cell, 2015. **160**(1-2): p. 177-90.

332. Hauser, P.S., V. Narayanaswami, and R.O. Ryan, *Apolipoprotein E: from lipid transport to neurobiology.* Prog Lipid Res, 2011. **50**(1): p. 62-74.

333. Qi, G., et al., *ApoE4 Impairs Neuron-Astrocyte Coupling of Fatty Acid Metabolism.* Cell Rep, 2021. **34**(1): p. 108572.

334. Cutler, R.G., et al., *Involvement of oxidative stress-induced abnormalities in ceramide and cholesterol metabolism in brain aging and Alzheimer's disease.* Proc Natl Acad Sci U S A, 2004. **101**(7): p. 2070-5.

335. Satoi, H., et al., *Astroglial expression of ceramide in Alzheimer's disease brains: a role during neuronal apoptosis.* Neuroscience, 2005. **130**(3): p. 657-66.

336. El Alwani, M., et al., *Bioactive sphingolipids in the modulation of the inflammatory response.* Pharmacol Ther, 2006. **112**(1): p. 171-83.

337. de Wit, N.M., et al., *Astrocytic ceramide as possible indicator of neuroinflammation.* J Neuroinflammation, 2019. **16**(1): p. 48.

338. Dong, Y., et al., *Oxidized phosphatidylcholines found in multiple sclerosis lesions mediate neurodegeneration and are neutralized by microglia.* Nat Neurosci, 2021. **24**(4): p. 489-503.

339. Ichiyanagi, N., et al., *Establishment of In Vitro FUS-Associated Familial Amyotrophic Lateral Sclerosis Model Using Human Induced Pluripotent Stem Cells.* Stem Cell Reports, 2016. **6**(4): p. 496-510.

340. Fujimori, K., et al., *Modeling sporadic ALS in iPSC-derived motor neurons identifies a potential therapeutic agent.* Nat Med, 2018. **24**(10): p. 1579-1589.

341. Ericson, J., et al., *Two critical periods of Sonic Hedgehog signaling required for the specification of motor neuron identity.* Cell, 1996. **87**(4): p. 661-73.

342. Ferrera, L., et al., *An Italian dominant FALS Leu144Phe SOD1 mutation: genotype-phenotype correlation.* Amyotroph Lateral Scler Other Motor Neuron Disord, 2003. **4**(3): p. 167-70.

343. Corcia, P., et al., *Respiratory onset in an ALS family with L144F SOD1 mutation.* J Neurol Neurosurg Psychiatry, 2011. **82**(7): p. 747-9.

344. Verde, F., et al., *Neurofilament light chain in serum for the diagnosis of amyotrophic lateral sclerosis.* J Neurol Neurosurg Psychiatry, 2019. **90**(2): p. 157-164.

345. Khalil, M., et al., *Serum neurofilament light levels in normal aging and their association with morphologic brain changes.* Nat Commun, 2020. **11**(1): p. 812.

346. Schiaffino, S. and C. Reggiani, *Fiber types in mammalian skeletal muscles.* Physiol Rev, 2011. **91**(4): p. 1447-531.

347. Ahmetov, II, O.L. Vinogradova, and A.G. Williams, *Gene polymorphisms and fiber-type composition of human skeletal muscle.* Int J Sport Nutr Exerc Metab, 2012. **22**(4): p. 292-303.

348. Biering-Sorensen, B., et al., *Muscle after spinal cord injury.* Muscle Nerve, 2009. **40**(4): p. 499-519.

349. Blaauw, B., S. Schiaffino, and C. Reggiani, *Mechanisms modulating skeletal muscle phenotype.* Compr Physiol, 2013. **3**(4): p. 1645-87.

350. Albers, P.H., et al., *Human muscle fiber type-specific insulin signaling: impact of obesity and type 2 diabetes.* Diabetes, 2015. **64**(2): p. 485-97.

351. Ceddia, R.B., W.N. William, Jr., and R. Curi, *Comparing effects of leptin and insulin on glucose metabolism in skeletal muscle: evidence for an effect of leptin on glucose uptake and decarboxylation.* Int J Obes Relat Metab Disord, 1999. **23**(1): p. 75-82.

352. Newsholme, E.A. and G. Dimitriadis, *Integration of biochemical and physiologic effects of insulin on glucose metabolism.* Exp Clin Endocrinol Diabetes, 2001. **109 Suppl 2**: p. S122-34.

353. Dorst, J., et al., *Patients with elevated triglyceride and cholesterol serum levels have a prolonged survival in amyotrophic lateral sclerosis.* J Neurol, 2011. **258**(4): p. 613-7.

354. Hartmann, H., et al., *Cholesterol dyshomeostasis in amyotrophic lateral sclerosis: cause, consequence, or epiphenomenon?* FEBS J, 2021.

355. Cutler, R.G., et al., *Evidence that accumulation of ceramides and cholesterol esters mediates oxidative stress-induced death of motor neurons in amyotrophic lateral sclerosis.* Ann Neurol, 2002. **52**(4): p. 448-57.

356. Chaves-Filho, A.B., et al., *Alterations in lipid metabolism of spinal cord linked to amyotrophic lateral sclerosis.* Sci Rep, 2019. **9**(1): p. 11642.

357. Li, H., et al., *Selective agenesis of the dorsal pancreas in mice lacking homeobox gene Hlxb9.* Nat Genet, 1999. **23**(1): p. 67-70.

358. Moulard, B., et al., *Apolipoprotein E genotyping in sporadic amyotrophic lateral sclerosis: evidence for a major influence on the clinical presentation and prognosis.* J Neurol Sci, 1996. **139 Suppl**: p. 34-7.

359. Zetterberg, H., et al., *Association of APOE with age at onset of sporadic amyotrophic lateral sclerosis.* J Neurol Sci, 2008. **273**(1-2): p. 67-9.

360. Grosskreutz, J., L. Van Den Bosch, and B.U. Keller, *Calcium dysregulation in amyotrophic lateral sclerosis.* Cell Calcium, 2010. **47**(2): p. 165-74.

361. Wienecke, J., et al., *Global gene expression analysis of rodent motor neurons following spinal cord injury associates molecular mechanisms with development of postinjury spasticity.* J Neurophysiol, 2010. **103**(2): p. 761-78.

362. Kanai, Y., et al., *KIF5C, a novel neuronal kinesin enriched in motor neurons.* J Neurosci, 2000. **20**(17): p. 6374-84.

363. Nicolas, A., et al., *Genome-wide Analyses Identify KIF5A as a Novel ALS Gene.* Neuron, 2018. **97**(6): p. 1268-1283 e6.

364. Kim, J.H., T.M. Lewin, and R.A. Coleman, *Expression and characterization of recombinant rat Acyl-CoA synthetases 1, 4, and 5. Selective inhibition by triacsin C and thiazolidinediones.* J Biol Chem, 2001. **276**(27): p. 24667-73.

365. Heneka, M.T., A. Fink, and G. Doblhammer, *Effect of pioglitazone medication on the incidence of dementia.* Ann Neurol, 2015. **78**(2): p. 284-94.

APPENDIX

Immune cells
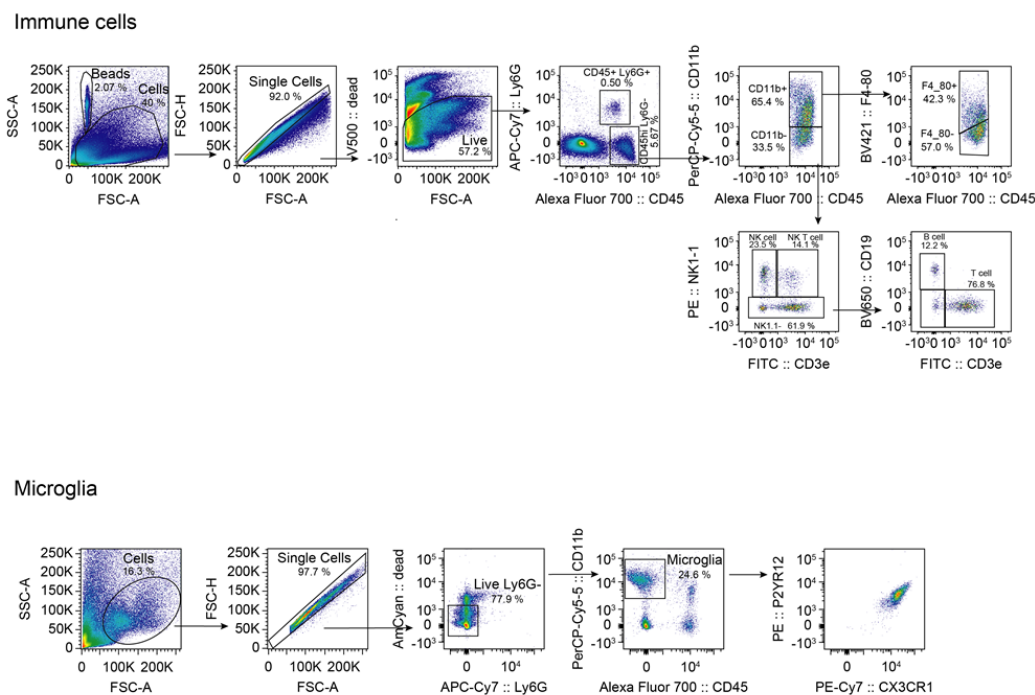
Microglia

Figure 33| Flow cytometry gating strategy for immune cells and microglia

Description of Excel files, accompanied under:

https://nc-mcd.helmholtz-muenchen.de/nextcloud/s/MY2wtT5sjy4NCKi

<u>Supplementary Table 1</u>. Normalized log2 transformed intensities of proteins from *Gpx4* knockout (KO) and wild type (WT) samples in the cortex including results of the one-way ANOVA and protein annotations.

<u>Supplementary Table 2.</u> Enrichment of differentially regulated proteins from one-way ANOVA in the category biological process of the gene ontology (GO) based on the GeneRanker analysis (Genomatix). Rows are highlighted that include important annotation terms related to *Gpx4* KO with respect to "neuron development", "response to stress", "response to oxidative stress", "fatty acid metabolic process" and "immune system process" which are affected by changed protein levels.

<u>Supplementary Table 3</u>. Enrichment of differentially regulated proteins from one-way ANOVA in the category disease (Genomatix Literature Mining) based on the GeneRanker analysis (Genomatix). Rows are highlighted that include important annotation terms related to *Gpx4*

KO with respect to "ALZHEIMER'S DISEASE", "NEURODEGENERATIVE DISORDERS", and "DEMENTIA" which are affected by changed protein levels.

Supplementary Table 4. Enrichment of differentially regulated proteins from one-way ANOVA in the category MeSH disease based on the GeneRanker analysis (Genomatix). Rows are highlighted that include important annotation terms related to *Gpx4* KO with respect to "Neurodegenerative Diseases", "Brain Diseases", "Central Nervous System Diseases", "Dementia", and "Alzheimer Disease" which are affected by changed protein levels.

Supplementary Table 5.Result of t-tests of *Gpx4* knockout (KO) versus wild type (WT) samples 1 week after KO induction. Significantly changed proteins (column p.adj_KO1w_vs_WT1w < 0.05) are highlighted.

Supplementary Table 6.Result of t-tests of *Gpx4* knockout (KO) versus wildtype (WT) samples 2 week after KO induction. Significantly changed proteins (column p.adj_KO2w_vs_WT2w < 0.05) are highlighted.

Supplementary Table 7.Result of t-tests of *Gpx4* knockout (KO) versus wildtype (WT) samples 4 week after KO induction. Significantly changed proteins (column p.adj_KO4w_vs_WT4w < 0.05) are highlighted.

Supplementary Table 8 Normalized data matrix of *Gpx4* knockout (KO) versus wildtype (WT) cortex samples of week 1, week 2, and week 4.

Supplementary Table 9. Gene-level analysis with deseq2 after removing genes with low counts. The p-values attained by the Wald test are corrected for multiple testing using the Benjamini and Hochberg method (padj). Significant genes were defined by padj<0.1 or more stringent by padj < 0.05. Also, raw p-values <0.01 were used to define a set of regulated genes. Gene sets were filtered for normalized counts >5 in at least one group.

Supplementary Table 10. Complete result lists for significantly enriched canonical pathways through the use of QIAGEN's Ingenuity Pathway Analysis software (IPA®, QIAGEN Redwood City, www.qiagen.com/ingenuity). Z-scores >2 (<-2) indicate activated (inactivated) terms.

ACKNOWLEDGEMENT

AFFIDAVIT

I hereby declare that the dissertation titled "Disentangling the *in vivo* role of ferroptosis in neurodegeneration" prepared under the guidance and supervision of Prof. Dr. Wolfgang Wurst, head of the Institute of Developmental Genetics, and submitted to the degree-awarding institution TUM School of Life Sciences is my own, original work undertaken in partial fulfillment of the requirements for the doctoral degree. I have made no use of sources, materials or assistance other than those specified in §6 (6) and (7), clause 2.

[ ] I have not employed the services of an organization that provides dissertation supervisors in return for payment or that fulfills, in whole or in part, the obligations incumbent on me in connection with my dissertation.

[ ] I have not submitted the dissertation, either in the present or a similar form, as part of another examination process.

[ ] The degree-awarding institution TUM School of Life Sciences has approved prior publication of the dissertation.

[ ] I have not yet been awarded the desired doctoral degree nor have I failed the last possible attempt to obtain the desired degree in a previous doctoral program.

I am familiar with the public available Regulations for the Award of Doctoral Degrees of TUM, in particular §28 (Invalidation of doctoral degree) and §29 (Revocation of doctoral degree). I am aware of the consequences of filing a false affidavit.

[ ] I agree,   [ ] I do not agree that my personal data is stored in the TUM alumni database.

Freising, 26.01.2022

Svenja Maria Lorenz